ICTRS 2013

Second International Conference on

Telecommunications and Remote Sensing

Proceedings

Noordwijkerhout, The Netherlands 11-12 July, 2013

Organized by:

CREST

Under the anspices of:

U.R.S.I.

In Cooperation with:

ARISTOTLE UNIVERSITY OF THESSALONIKI

AMAKOTA

ICTRS 2013

PROCEEDINGS

of the 2nd International Conference
on Telecommunications and Remote Sensing

Noordwijkerhout, The Netherlands
11-12 July, 2013

Organized by

IICREST - Interdisciplinary Institute for Collaboration and Research on Enterprise Systems and Technology

In Cooperation with

Aristotle University of Thessaloniki

AMAKOTA Ltd.

Under the Auspices of

URSI – International Union of Radio Science

Edited by Blagovest Shishkov

Graphics Production

Bozhana Yankova, Bulgaria

Printed in Bulgaria

ISBN: 978-989-8565-57-0

Depósito Legal: 360186/13

http://www.ictrs.org

secretariat@iicrest.org

BRIEF CONTENTS

KEYNOTE SPEAKERS

Hristo Kabakchiev

Sofia University "St. Kl. Ohridski"

Bulgaria

Kazuya Kobayashi

Chuo University

Japan

CHAIR AND PROGRAM COMMITTEE

CHAIR

Blagovest Shishkov, Bulgarian Academy of Sciences, Bulgaria

PROGRAM COMMITTEE

Oleksiy Agapitov, Taras Shevchenko Kyiv National University, Ukraine
Catherine Algani, CNAM, France
Mauro Assis, Brazilian Committee of URSI, Brazil
Krassimir Atanassov, BAS, Bulgaria
Boncho Balabanov, NBU, Bulgaria
Vera Behar, BAS, Bulgaria
Maurice Bellanger, CNAM, France
Lyubka Doukovska, BAS, Bulgaria
Yoshiharu Fuse, USEF, Japan
Ivan Garvanov, BAS, Bulgaria
Mihail Iliev, University of Ruse "Angel Kanchev", Bulgaria
Hristo Kabakchiev, Sofia University "St. Kl. Ohridski", Bulgaria
Dorina Kabakchieva, UNWE, Bulgaria
Kazuya Kobayashi, Chuo University, Japan
Mesut Kartal, Istanbul Technical University, Turkey
Mohamed Latrach, ESEO, France
Andon Lazarov, Bourgas Free University, Bulgaria
Frank Little, Texas A & M University, USA
Marco Luise, University of Pisa, Pisa, Italy
Olga Maltseva, Institute of Physics Southern Federal University, Russia
Andrea Massa, University of Trento, Italy
Galia Marinova, Technical University of Sofia, Bulgaria

PROGRAM COMMITTEE (CONT.)

Wolfgang Mathis, Leibniz Universität Hannover , Germany

Lyudmila Mihaylova, Lancaster University, UK

T**omohiko Mitani**, Research Institute for Sustainable Humanosphere, Japan

Tadao Nagatsuma, Osaka University, Japan

Shoichi Narahashi, NTT Docomo, Japan

Marin Nenchev, Technical University - Sofia, Bulgaria

Eugene Nickolov, BAS, Bulgaria

Martin O'droma, University of Limerick, Ireland

Takashi Ohira, Toyohashi University of Technology, Japan

Jaques Palicot, SUPELEC, IETR, France

Hermann Rohling, Hamburg University of Technology, Germany

Sana Salous, Durham University, UK

Hamit Serbest, Cukurova University, Turkey

Naoki Shinohara, Kyoto University, Japan

Boris Shishkov, IICREST, Bulgaria

Alexander Shmelev, Radiotechnical Institute by Acad. A.L.Mints, Russia

Angela Slavova, BAS, Bulgaria

Jun-Ichi Takada, Tokyo Institute of Technology, Japan

Hiroyuki Tsuji, NIICT, Japan

Marten Van Sinderen, University of Twente, The Netherlands

Satoshi Yagitani, Kanazawa University, Japan

Tsuneki Yamasaki, Nihon University, Japan

BEST PAPERS SELECTION

The authors of around three selected ICTRS'13 best papers will be invited to submit revised and extended versions of their papers to a special issue of the international journal

ANNALS OF TELECOMMUNICATIONS

FOREWORD

This book contains the proceedings of ICTRS 2013 - the Second International Conference on Telecommunications and Remote Sensing, held in Noordwijkerhout, The Netherlands, on July 11-12, 2013. The proceedings consist of 20 high-quality research and experience papers that have not been published previously.

The Conference was organized and sponsored by the Interdisciplinary Institute for Collaboration and Research on Enterprise Systems and Technology (IICREST), in cooperation with Aristotle University of Thessaloniki and AMAKOTA Ltd.

ICTRS 2013 is performed under the auspices of the International Union of Radio Science (URSI). Further, the conference covers topics relevant to the work in a number of URSI Commissions, namely Commission A, Commission B, Commission C, Commission D, Commission E, Commission F, Commission G, Commission K, as well as topics relating to Space Solar Power System (SSPS). All this has inspired and influenced the scientific program of the conference that is concerned with the international developments and applications in the following directions:

(i) Radio-Communications and Signal Processing
(ii) Electronics and Photonics
(iii) Electromagnetic Environment and Interference
(iv) Solar Power Satellite Systems
(v) Remote Sensing
(vi) Electromagnetic Fields and Waves
(vii) Context Awareness

As seen from the above areas, the first four ones are mainly concerned with Telecommunications, while the others are mainly concerned with Remote Sensing and Context Awareness. This research orientation as well as the ICTRS'12 'heritage' clearly show that even though ICTRS has adopted the URSI research agenda, it is also spreading its influence to a broader audience including all those researchers and practitioners who are interested in the topics of the conference. It is seen as well that since the start in 2012 well until now, we have been successful in establishing a small but focused Community of experienced academicians and practitioners who are inspiring the ICTRS developments. These developments are considered useful not only for URSI but also in general for the Telecommunications Community.

Considering two types of submissions, namely invited submissions and regular submissions, we have selected, based on a review process driven by rigorous quality standards, 20 papers. 17 of these papers were selected for a 30-minutes oral presentation (Full Papers) and 3 papers were selected for a 20-minutes oral presentation (Short Papers). The results of the current event and the previous one are comparable - this indicates for stable development which we aim at sustaining and reinforcing in the future.

FOREWORD (CONT.)

Further, the authors of around three selected best papers will be invited to submit revised and extended versions of their papers to a special issue of the International Journal ANNALS OF TELECOMMUNICATIONS.

The published papers are a good selection representing work concerning different relevant topics, including: Intelligent Methods of Radio Signals and Systems; Wave Propagation and Remote Sensing; Solar Power Satellite Systems; Context Awareness; etc.

The high quality of the ICTRS 2013 program is enhanced by two keynote lectures, delivered by distinguished guests who are renowned experts in their fields, including (alphabetically): Hristo Kabakchiev (Sofia University "St. Kl. Ohridski", Bulgaria) and Kazuya Kobayashi (Chuo University, Japan). In addition, the current Keynote Lecturers and a '12 Keynote Lecturer, namely: Naoki Shinohara (Kyoto University, Japan) will take part in a panel discussion. Finally, an outstanding researcher from BGU, Israel, Dan Censor will lead a discussion session that focuses on different aspects that concern Relativity Theory. These high points in the conference program would contribute to positioning ICTRS as a high quality event driven by a stable and motivated community.

Building an interesting and successful program for the conference required the dedicated efforts of many people. We must thank the authors, whose research efforts are recorded here. We turn with special gratitude also to the Keynote Lecturers and the Program Committee for their support and enthusiasm. We thank SCITEPRESS for their willingness to publish the current proceedings. Last but not least, we would like to express our gratitude to the representatives of IICREST and AMAKOTA Ltd. for doing all necessary preparations for a stimulating and productive event – we would be happy if IICREST continues with organizing further editions of ICTRS, under the auspices of URSI! I would like to also mention the excellent collaboration on compiling the current proceedings with Canka Petrova who worked on behalf of IICREST in close collaboration with the Publisher, SCITEPRESS.

We wish you all an inspiring conference and enjoyable stay in the beautiful Noordwijk area of The Netherlands. We look forward to seeing you next year in Luxembourg, for the Third International Conference on Telecommunications and Remote Sensing (ICTRS 2014), details of which will be made available at http://www.ictrs.org.

Blagovest Shishkov
Bulgarian Academy of Sciences
President of Bulgarian URSI Committee
Chair of ICTRS 2013

CONTENTS

KEYNOTE SPEAKERS

RADAR CROSS SECTION OF A FINITE PARALLEL-PLATE WAVEGUIDE WITH FOUR-LAYER MATERIAL LOADING

Kazuya Kobayashi
Department of Electrical, Electronic, and Communication Engineering, Chuo University
1-13-27 Kasuga, Bunkyo-ku, Tokyo 112-8551, Japan
kazuya@tamacc.chuo-u.ac.jp

Keywords: Wiener-Hopf technique, canonical problems, scattering and diffraction, radar cross section, cavities

Abstract: A rigorous radar cross section analysis is carried out for a finite parallel-plate waveguide with four-layer material loading using the Wiener-Hopf technique. Exact and approximate solutions of the Wiener-Hopf equations are obtained, and the scattered field is evaluated analytically. Numerical examples on the radar cross section (RCS) are presented for various physical parameters and far-field scattering characteristics of the waveguide are discussed in detail.

1 INTRODUCTION

The analysis of electromagnetic scattering by open-ended metallic waveguide cavities is an important subject in the prediction and reduction of the radar cross section (RCS) of a target. This problem serves as a simple model of duct structures such as jet engine intakes of aircrafts and cracks occurring on surfaces of general complicated bodies. Some of the diffraction problems involving two- and three-dimensional (2-D and 3-D) cavities have been analyzed thus far based on high-frequency techniques and numerical methods (Lee and Ling, 1989; Ling et al., 1989; Pathak and Burkholder, 1989; Pathak and Burkholder, 1993; Ohnuki and Hinata, 1998). It appears, however, that the solutions due to these approaches are not uniformly valid for arbitrary dimensions of the cavity. Therefore it is desirable to overcome the disadvantages of the previous works to obtain solutions which are uniformly valid in arbitrary cavity dimensions.

The Wiener-Hopf technique (Noble, 1958) is known as a powerful, rigorous approach for analyzing scattering and diffraction problems involving canonical geometries. In the previous papers (Okada et al., 2002a; Okada et al., 2002b), we have considered a finite parallel-plate waveguide with three-layer material loading as a geometry that can form cavities, and carried out a Wiener-Hopf analysis of the plane wave diffraction. As a result, it has been verified that our final solutions are valid for broad frequency range and can be used as reference solutions.

In this paper, we shall consider a finite parallel-plate waveguide with four-layer material loading as a generalization to the geometry in our previous papers (Okada et al., 2002a; Okada et al., 2002b), and analyze the plane wave diffraction using the Wiener-Hopf technique. for *E* and *H* polarizations. The analytical details are presented only for the *E*-polarized case, whereas numerical results will be shown for both polarizations. Main results of this paper are already published elsewhere (Zheng and Kobayashi, 2008; Shang and Kobayashi, 2008).

The time factor is assumed to be $e^{-i\omega t}$ and suppressed throughout this paper.

2 FORMULATION OF THE PROBLEM

We consider the diffraction of an *E*-polarized plane wave by a finite parallel-plate waveguide with four-layer material loading as shown in Figure 1, where *E* polarization implies that the incident electric field is parallel to the y-axi, and $-L<D_1<D_2<D_3<D_4<D_5<L$. The waveguide plates are perfectly conducting and of zero thickness, and the material layers I $(D_1<z<D_2)$, II $(D_2<z<D_3)$, III $(D_3<z<D_4)$, and IV $(D_4<z<D_5)$ are characterized by the

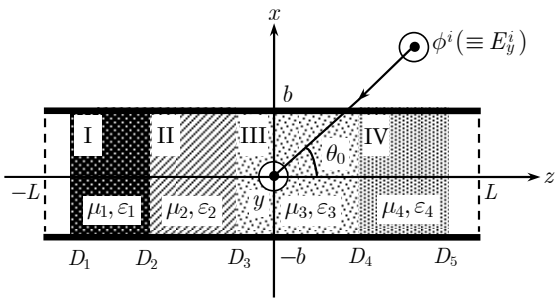

Figure 1: Geometry of the waveguide.

relative permittivity ε_m and the relative permeability μ_m for $m=1,2,3,$ and $4,$ respectively. In view of the geometry and the characteristics of the incident field, this is a 2-D problem.

Let us define the total electric field $\phi^t(x,z)$ $[\equiv E_y^t(x,z)]$ by

$$\phi^t(x,z) = \phi^i(x,z) + \phi(x,z), \tag{1}$$

where $\phi^i(x,z)$ is the incident field given by

$$\phi^i(x,z) = e^{-ik(x\sin\theta_0 + z\cos\theta_0)} \tag{2}$$

for $0 < \theta_0 < \pi / 2$ with $k[\equiv \omega(\varepsilon_0\mu_0)^{1/2}]$ being the free-space wavenumber. The total field $\phi^t(x,z)$ satisfies the 2-D Helmholtz equation

$$\left[\frac{\partial^2}{\partial x^2} + \frac{\partial^2}{\partial z^2} + \mu(x,z)\varepsilon(x,z)k^2\right]\phi^t(x,z) = 0, \tag{3}$$

where

$$\mu(x,z) = \begin{cases} \mu_1 \text{ (layer I)} \\ \mu_2 \text{ (layer II)} \\ \mu_3 \text{ (layer III)} \\ \mu_4 \text{ (layer IV)} \\ 1 \text{(otherwise)} \end{cases}, \tag{4}$$

$$\varepsilon(x,z) = \begin{cases} \varepsilon_1 \text{ (layer I)} \\ \varepsilon_2 \text{ (layer II)} \\ \varepsilon_3 \text{ (layer III)} \\ \varepsilon_4 \text{ (layer IV)} \\ 1 \text{(otherwise)} \end{cases}. \tag{5}$$

We assume that the vacuum is slightly lossy as in $k = k_1 + ik_2$ with $0 < k_2 \ll k_1$. The solution for real k is obtained by letting $k_2 \to +0$ at the end of analysis. Let us define the Fourier transform of $\phi(x,z)$ in (1) with respect to z as

$$\Phi(x,\alpha) = (2\pi)^{-1/2}\int_{-\infty}^{\infty}\phi(x,z)e^{i\alpha z}dz, \tag{6}$$

where $\alpha = \mathrm{Re}\,\alpha + i\,\mathrm{Im}\,\alpha$ $(\equiv \sigma + i\tau)$. In view of the radiation condition, it is found that $\Phi(x,\alpha)$ is regular in the strip $|\tau| < k_2\cos\theta_0$ of the complex α-plane.

Taking appropriate Fourier transforms of (3) and solving the resultant transformed wave equations, we derive a scattered field expression in the transform domain as in

$$\begin{aligned}\Phi(x,\alpha) &= \Psi(\pm b,\alpha)e^{\mp\gamma(x\mp b)} \quad \text{for } x \gtrless \pm b, \\ &= \Psi(b,\alpha)\frac{\sinh\gamma(x+b)}{\sinh 2\gamma b} - \Psi(-b,\alpha)\frac{\sinh\gamma(x-b)}{\sinh 2\gamma b} \\ &\quad -\frac{1}{b}\sum_{n=1}^{\infty}\frac{1}{\alpha^2+\gamma_n^2} \\ &\quad \cdot\left[e^{i\alpha D_5}c_{5n}^{+}(\alpha) - e^{i\alpha D_1}c_{1n}^{-}(\alpha)\right] \\ &\quad \cdot\sin\frac{n\pi}{2b}(x+b) \\ &\quad -\frac{1}{b}\sum_{m=1}^{4}\sum_{n=1}^{\infty}\frac{1}{\alpha^2+\Gamma_{mn}^2} \\ &\quad \cdot\left[e^{i\alpha D_m}c_{mn}^{+}(\alpha) - e^{i\alpha D_{m+1}}c_{m+1,n}^{-}(\alpha)\right] \\ &\quad \cdot\sin\frac{n\pi}{2b}(x+b) \quad \text{for } |x| < b,\end{aligned} \tag{7}$$

where

$$\begin{aligned}\Psi(\pm b,\alpha) = (1/2)\big\{&e^{-i\alpha L}\left[U_-(\alpha) \pm V_-(\alpha)\right] \\ &+ e^{i\alpha L}\left[U_{(+)}(\alpha) \pm V_{(+)}(\alpha)\right]\big\},\end{aligned} \tag{8}$$

$$\gamma = (\alpha^2 - k^2)^{1/2}, \quad \mathrm{Re}\,\gamma > 0, \tag{9}$$

$$\gamma_n = [(n\pi / 2b)^2 - k^2]^{1/2}, \tag{10}$$

$$\Gamma_{mn} = [(n\pi / 2b)^2 - k_m^2]^{1/2} \tag{11}$$

with $k_m = (\mu_m\varepsilon_m)^{1/2}k$. It can be shown that the coefficients $c_{mn}^{\pm}(\alpha)$ in (7) are expressed in terms of the functions $U_-(\alpha)$, $U_{(+)}(\alpha)$, $V_-(\alpha)$, and $V_{(+)}(\alpha)$ (Zheng and Kobayashi, 2008).

We now differentiate (7) with respect to x and set $x = b \pm 0, -b \pm 0$ in the results. Carrying out some manipulations by using boundary conditions, it follows that $U_-(\alpha)$, $U_{(+)}(\alpha)$, $V_-(\alpha)$, and $V_{(+)}(\alpha)$ satisfy

$$J_1^d(\alpha) = -\frac{e^{-i\alpha L}U_-(\alpha) + e^{i\alpha L}U_{(+)}(\alpha)}{M(\alpha)}$$

$$- \sum_{n=1,\text{odd}}^{\infty} \frac{n\pi}{b^2}\left[\frac{e^{i\alpha D_5}c_{5n}^{+}(\alpha) - e^{i\alpha D_1}c_{1n}^{-}(\alpha)}{\alpha^2 + \gamma_n^2} + \sum_{m=1}^{4} \frac{e^{i\alpha D_m}c_{mn}^{+}(\alpha) - e^{i\alpha D_{m+1}}c_{m+1,n}^{-}(\alpha)}{\alpha^2 + \Gamma_{mn}^2}\right], \quad (12)$$

$$J_1^s(\alpha) = -\frac{e^{-i\alpha L}V_{-}(\alpha) + e^{i\alpha L}V_{(+)}(\alpha)}{N(\alpha)} + \sum_{n=2,\text{even}}^{\infty} \frac{n\pi}{b^2}\left[\frac{e^{i\alpha D_5}c_{5n}^{+}(\alpha) - e^{i\alpha D_1}c_{1n}^{-}(\alpha)}{\alpha^2 + \gamma_n^2} + \sum_{m=1}^{4} \frac{e^{i\alpha D_m}c_{mn}^{+}(\alpha) - e^{i\alpha D_{m+1}}c_{m+1,n}^{-}(\alpha)}{\alpha^2 + \Gamma_{mn}^2}\right], \quad (13)$$

where $J_1^{d,s}(\alpha)$ are unknown functions corresponding to surface currents induced on the waveguide plates, and $M(\alpha)$ and $N(\alpha)$ are kernel functions defined by

$$M(\alpha) = \gamma^{-1}e^{-\gamma b}\cosh\gamma b, \quad (14)$$

$$N(\alpha) = \gamma^{-1}e^{-\gamma b}\sinh\gamma b. \quad (15)$$

Equations (12) and (13) are the simultaneous Wiener-Hopf equations, which can be solved via the factorization and decomposition procedure.

3 SOLUTION OF THE WIENER-HOPF EQUATIONS

The kernel functions $M(\alpha)$ and $N(\alpha)$ defined by (14) and (15) are factorized as (Noble, 1958)

$$M(\alpha) = M_{+}(\alpha)M_{-}(\alpha), \quad (16)$$

$$N(\alpha) = N_{+}(\alpha)N_{-}(\alpha), \quad (17)$$

where

$$M_{+}(\alpha)[= M_{-}(-\alpha)] = (\cos kb)^{1/2}e^{i\pi/4}(k+\alpha)^{-1/2} \cdot \exp\left\{(i\gamma b \,/\, \pi)\ln[(\alpha-\gamma)\,/\,k]\right\} \cdot \exp\left\{(i\alpha b \,/\, \pi)[1 - C + \ln(\pi \,/\, kb) + i\pi \,/\, 2]\right\} \cdot \prod_{n=1,\text{odd}}^{\infty}(1 + \alpha \,/\, i\gamma_n)e^{2i\alpha b/n\pi}, \quad (18)$$

$$N_{+}(\alpha)[= N_{-}(-\alpha)] = (\sin kb \,/\, k)^{1/2} \exp\left\{(i\gamma b \,/\, \pi)\ln[(\alpha-\gamma)\,/\,k]\right\} \cdot \exp\left\{(i\alpha b \,/\, \pi)[1 - C + \ln(2\pi \,/\, kb) + i\pi \,/\, 2]\right\} \cdot \prod_{n=2,\text{even}}^{\infty}(1 + \alpha \,/\, i\gamma_n)e^{2i\alpha b/n\pi} \quad (19)$$

with $C\,(= 0.57721566\cdots)$ being Euler's constant.

We multiply both sides of (12) and (13) by the functions $e^{\pm i\alpha L}M_{\pm}(\alpha)$ and $e^{\pm i\alpha L}N_{\pm}(\alpha)$, respectively, and decompose the resultant equations using the edge condition. After some manipulations, we obtain that

$$\left.\begin{matrix} U_{-}(\alpha) \\ U_{(+)}(\alpha) \end{matrix}\right\} = b^{1/2}M_{\mp}(\alpha) \cdot \left[\pm\left\{\begin{matrix} A_u \\ B_u \end{matrix}\right\}\frac{1}{b(\alpha - k\cos\theta_0)} + \frac{J_u^{(1),(2)}(\alpha)}{b^{1/2}} \mp \sum_{n=2}^{\infty}\frac{e^{-2\gamma_{2n-3}(L\pm D_{1,5})}X_{2n-3}^{\mp}a_n p_n u_n^{\mp}}{b(\alpha \mp i\gamma_{2n-3})} \mp \sum_{n=2}^{\infty}\frac{e^{-\gamma_{2n-3}(2L+D_1-D_5)}Y_{2n-3}^{\mp}a_n p_n u_n^{\pm}}{b(\alpha \mp i\gamma_{2n-3})}\right], \quad (20)$$

$$\left.\begin{matrix} V_{-}(\alpha) \\ V_{(+)}(\alpha) \end{matrix}\right\} = b^{1/2}N_{\mp}(\alpha) \cdot \left[\mp\left\{\begin{matrix} A_v \\ B_v \end{matrix}\right\}\frac{1}{b(\alpha - k\cos\theta_0)} + \frac{J_v^{(1),(2)}(\alpha)}{b^{1/2}} \mp \sum_{n=2}^{\infty}\frac{e^{-2\gamma_{2n-2}(L\pm D_{1,5})}X_{2n-2}^{\mp}b_n q_n v_n^{\mp}}{b(\alpha \mp i\gamma_{2n-2})} \mp \sum_{n=2}^{\infty}\frac{e^{-\gamma_{2n-2}(2L+D_1-D_5)}Y_{2n-2}^{\mp}b_n q_n v_n^{\pm}}{b(\alpha \mp i\gamma_{2n-2})}\right], \quad (21)$$

where

$$a_n = [(2n-3)\pi \,/\, 2]^2 \,/\, bi\gamma_{2n-3}, \quad (22)$$

$$b_n = [(n-1)\pi]^2 \,/\, bi\gamma_{2n-2}, \quad (23)$$

$$p_n = b^{-1/2}M_{+}(i\gamma_{2n-3}), \quad (24)$$

$$q_n = b^{-1/2}N_{+}(i\gamma_{2n-2}), \quad (25)$$

$$u_n^{-} = b^{-1}U_{-}(-i\gamma_{2n-3}), \quad (26)$$

$$u_n^{+} = b^{-1}U_{(+)}(i\gamma_{2n-3}), \quad (27)$$

$$v_n^{-} = b^{-1}V_{-}(-i\gamma_{2n-2}), \quad (28)$$

$$v_n^{+} = b^{-1}V_{(+)}(i\gamma_{2n-2}), \quad (29)$$

$$\left.\begin{matrix} J_u^{(1)}(\alpha) \\ J_u^{(2)}(\alpha) \end{matrix}\right\} = \frac{1}{\pi i}\int_k^{k+i\infty} e^{2i\beta L}M_{+}(\beta) \cdot \frac{(\beta^2 - k^2)^{1/2}}{\beta \mp \alpha}\left\{\begin{matrix} U_{(+)}(\beta) \\ U_{-}(-\beta) \end{matrix}\right\}d\beta, \quad (30)$$

$$\left.\begin{matrix} J_v^{(1)}(\alpha) \\ J_v^{(2)}(\alpha) \end{matrix}\right\} = \frac{1}{\pi i}\int_k^{k+i\infty} e^{2i\beta L} N_+(\beta) \cdot \frac{(\beta^2-k^2)^{1/2}}{\beta \mp \alpha} \left\{\begin{matrix} V_{(+)}(\beta) \\ V_-(-\beta) \end{matrix}\right\} d\beta, \quad (31)$$

$$\left.\begin{matrix} A_u \\ B_u \end{matrix}\right\} = \frac{(2b)^{1/2} e^{\pm ikL\cos\theta_0}\cos(kb\sin\theta_0)}{\pi^{1/2} i M_{\mp}(k\cos\theta_0)}, \quad (32)$$

$$\left.\begin{matrix} A_v \\ B_v \end{matrix}\right\} = \frac{(2b)^{1/2} e^{\pm ikL\cos\theta_0}\sin(kb\sin\theta_0)}{\pi^{1/2} N_{\mp}(k\cos\theta_0)}. \quad (33)$$

The coefficients $X_n^{\pm}$ and $Y_n^{\pm}$ in (20) and (21) are expressed using some lengthy equations and hence, their definition is omitted here.

Equations (20) and (21) provide the exact solutions of the Wiener-Hopf equations (12) and (13), respectively, but they are formal since the infinite series with the unknown coefficients $u_n^{\pm}$ and $v_n^{\pm}$ for $n=2,3,4,\cdots$ as well as the branch-cut integrals $J_u^{(1),(2)}(\alpha)$ and $J_v^{(1),(2)}(\alpha)$ with the unknown integrands $U_-(\alpha)$, $U_{(+)}(\alpha)$, $V_-(\alpha)$, and $V_{(+)}(\alpha)$ are involved. Therefore, it is required to develop approximation procedures for an explicit solution.

In order to obtain approximate solutions of the Wiener-Hopf equations, we shall apply the method based on a rigorous asymptotics established by the author (Kobayashi, 2013). For the infinite series with unknown coefficients, we can derive highly accurate, approximate expressions by taking into account the edge condition explicitly. For the branch-cut integrals with unknown integrands, we assume that the waveguide length is large compared with the incident wavelength and derive high-frequency asymptotic expressions of the branch-cut integrals. Based on these results, approximate solutions of the Wiener-Hopf equations, efficient for numerical computation, are explicitly derived, which involves a numerical solution of appropriate matrix equations.

4 SCATTERED FIELD

The scattered field in the real space can be derived by taking the inverse Fourier transform of (7) according to

$$\phi(x,z) = (2\pi)^{-1/2}\int_{-\infty+ic}^{\infty+ic} \Phi(x,\alpha) e^{-i\alpha z} d\alpha, \quad (34)$$

where $|c| < k_2\cos\theta_0$. Introducing the cylindrical coordinate

$$x = \rho\sin\theta,\ z = \rho\cos\theta,\ 0 < |\theta| < \pi \quad (35)$$

and applying the saddle point method, an asymptotic expression of the scattered field outside the waveguide is derived as

$$\phi(\rho,\theta) \sim \pm\Psi(\pm b, -k\cos\theta)k\sin\theta \cdot e^{\pm ikb\sin\theta}\frac{e^{i(k\rho-\pi/4)}}{(k\rho)^{1/2}},\ x \gtrless \pm b \quad (36)$$

for $k\rho \to \infty$. The field inside the waveguide is evaluated in closed form by computing the residue series of (34), but will not be discussed here.

5 NUMERICAL RESULTS AND DISCUSSION

We shall now investigate the scattering mechanism via numerical results of the RCS for various physical parameters. Figures 2(a,b,c) and 2(d,e,f) show the monostatic RCS as a function of incident angle θ_0 for *E* and *H* polarizations, respectively. In order to investigate the scattering mechanism over a broad frequency range, we have carried out numerical computation for three typical values of the normalized waveguide aperture width $kb = 3.14,\ 15.7,$ and 31.4. The ratio of the waveguide length $2L$ to the waveguide width $2b$ has been chosen as $L\ /\ b = 1.0$.

In numerical computation, we have considered the case where layer I $(D_1 < z < D_2)$ is filled with perfect conductors so that two cavity regions are formed at the left $(-L < z < D_1)$ and right $(D_2 < z < L)$ sides of the waveguide. We have chosen the depth of the left and right cavities as $t_{\mathrm{L}}(= D_1 + L) = 0.6L$ and $t_{\mathrm{R}}(= L - D_2) = L$, respectively so that the thickness of layer I (perfect conductors) becomes $t_{\mathrm{PEC}}(= D_2 - D_1) = 0.4L$. In order to investigate the effect of the three-layer material loading, we have considered the case where layers II-IV in the right cavity are composed of Emerson & Cuming AN-73 (Lee and Ling, 1989) with the material constants being:

$\varepsilon_2 = 3.14 + i10.0, \mu_2 = 1.0, \varepsilon_3 = 1.6 + i0.9, \quad \mu_3 = 1.0,$ $\varepsilon_4 = 1.4 + i0.35, \mu_4 = 1.0$ and the layer thickness

being $D_3 - D_2 = D_4 - D_3 = D_5 - D_4 (= t_{3\text{layer}} / 3)$. We have also considered the two-layer case where layer IV of Emerson & Cuming AN-73 is removed,

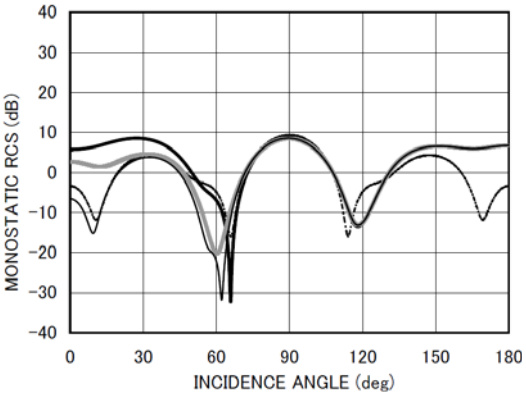

(a) E polarization, $kb = 3.14$.

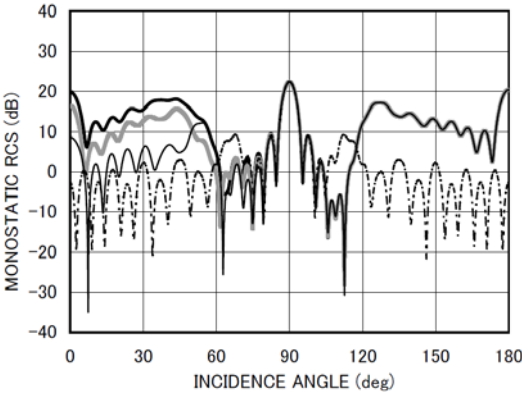

(b) E polarization, $kb = 15.7$.

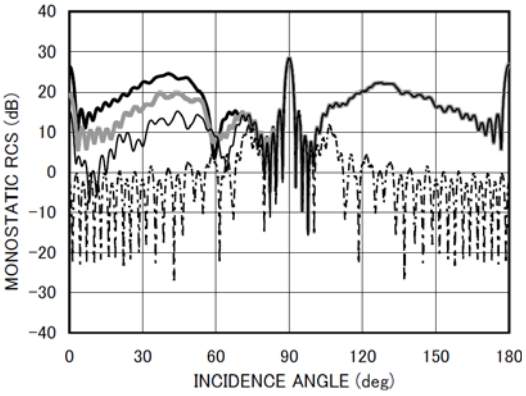

(c) E polarization, $kb = 31.4$.

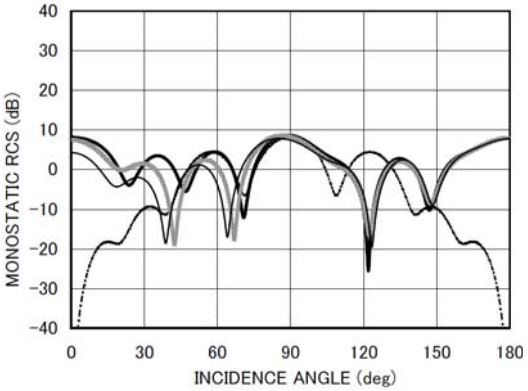

(d) H polarization, $kb = 3.14$.

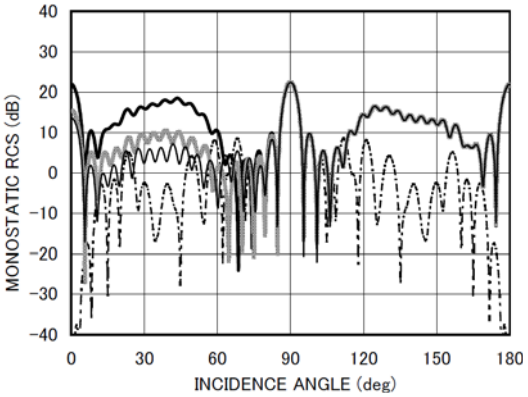

(e) H polarization, $kb = 15.7$.

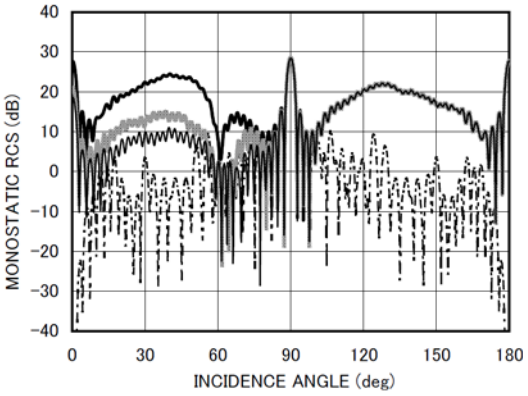

(f) H polarization, $kb = 31.4$.

Figure 2: Monostatic RCS for $L / b = 1.0$. : empty waveguide (layers I-IV: vacuum). : cavity with no loading (layer I: perfect conductor; layers II-IV: vacuum; $t_{\text{L}} = 0.6L$, $t_{\text{PEC}} = 0.4L$, $t_{\text{R}} = L$). : cavity with two-layer loading (layer I: perfect conductor; layer II: $\varepsilon_2 = 3.14 + i10.0$, $\mu_2 = 1.0$; layer III: $\varepsilon_3 = 1.6 + i0.9$, $\mu_3 = 1.0$; layer IV: vacuum; $t_{\text{L}} = 0.6L$, $t_{\text{PEC}} = 0.4L$, $t_{\text{R}} = L$, $t_{2\text{layer}} = 0.4L$) .: cavity with three-layer loading (layer I: perfect conductor; layers II-IV: Emerson & Cuming AN-73; $t_{\text{L}} = 0.6L$, $t_{\text{PEC}} = 0.4L$, $t_{\text{R}} = L$, $t_{3\text{layer}} = 0.6L$).

namely, $\varepsilon_2 = 3.14 + i10.0, \mu_2 = 1.0, \varepsilon_3 = 1.6 + i0.9, \mu_3 = 1.0, \varepsilon_4 = \mu_4 = 1.0,$ and $D_3 - D_2 = D_4 - D_3 (= t_{2\text{layer}} / 2)$. The thickness of the two- and three-layer materials has been taken as $t_{2\text{layer}} = 0.4L$ and $t_{3\text{layer}} = 0.6L,$ respectively. In addition, the results for an empty parallel-plate waveguide $(\varepsilon_n = \mu_n = 1.0, n = 1,2,3,4)$ have also been plotted for comparison.

It is seen from Figure 2 that all the monostatic RCS results show sharp peaks at $\theta_0 = 90°$, which correspond to the specular reflection from the upper waveguide plate at $x = b$. Due to the geometrical symmetry, the RCS curves for the empty parallel-plate waveguide (no material loading) are symmetrical around the main lobe direction at $\theta_0 = 90°$. For fairly large cavities with no material loading, the RCS takes close values at $\theta_0 = 0°, 90°, 180°$ as seen from Figures 2(b,c) for *E* polarization and Figures 2(e,f) for *H* polarization, since contributions to the backscattered far field at high frequencies mainly come from the reflected waves from the perfectly conducting surfaces at $x = b$ and $z = D_1, D_2$.

We find from the four curves for fixed kb and polarization in Figure 2 that the RCS characteristics show close features near the main lobe direction $80° < \theta_0 < 100°$. This is due to the fact that main contributions to the backscattered far field arise from exterior features of the waveguide, not depending on features inside the waveguide. We also notice from the results of the three cavities for fixed kb and polarization that the RCS characteristics for $90° < \theta_0 < 180°$ are nearly identical to each other, since the cavity formed at the right side of the waveguide is then invisible from the incident direction and the backscattered far field is not affected by the interior geometries of the right cavity.

We now investigate the effect of material loading inside the right cavity. For the cavity with no material loading, the RCS shows large values over the range $0° < \theta_0 < 60°$ due to interior irradiation, whereas the irradiation is reduced for the case of material loading. By comparing the RCS results for material-loaded cavities between the two-layer case and the three-layer case (Emerson & Coming AN-73), we see better RCS reduction in the case of the cavity with three-layer loading for all chosen kb.

Let us now make comparisons of the monostatic RCS between different polarizations, and investigate the differences in the backscattering characteristics depending on the incident polarization. Comparing the RCS curves in Figures 2(a,b,c) for *E* polarization with those in Figures 2(d,e,f) for *H* polarization, we see differences in all numerical examples. In particular, the monostatic RCS for *H* polarization oscillates rapidly in comparison to the *E*-polarized case. This difference is due to the fact that the effect of edge diffraction depends on the incident polarization. We also see that, if the cavity aperture opening is small as in $kb = 3.14,$ there are great differences in the RCS characteristics between *E* and *H* polarizations except near the main lobe direction $\theta_0 = 90°$. This is because the diffraction phenomena at low frequencies strongly depend on the incident polarization. It is also found that, with an increase of the cavity opening, the RCS exhibits close features for both polarizations.

6 CONCLUSIONS

In this paper, we have considered a finite parallel-plate waveguide with four-layer loading as a generalization to the geometry treated in our previous papers (Okada et al., 2002a; Okada et al., 2002b), and analyzed rigorously the plane wave diffraction for both *E* and *H* polarizations by means of the Wiener-Hopf technique. We have presented illustrative numerical examples of the RCS for various physical parameters to discuss the far field scattering characteristics in detail. In particular, it has been shown that the four-layer material loading gives rise to a better RCS reduction compared with the three-layer case analyzed in our previous papers. The results can be used as a reference solution for validating approximate approaches.

REFERENCES

Lee, S.-W. and Ling, H. (1989). Data book for cavity RCS: version 1. *Technical Report., University of Illinois*, No. SWL 89-1.

Ling, H., Chou, R.-C., and Lee, S.-W. (1989). Shooting and bouncing rays: calculating the RCS of an arbitrary

shaped cavity. *IEEE Transactions on Antennas and Propagation*, 37, 194-205.

Pathak, P. H. and Burkholder, R. J. (1989). Modal, ray, and beam techniques for analyzing the EM scattering by open-ended waveguide cavities. *IEEE Transactions on Antennas and Propagation*, 37, 635-647.

Pathak, P. H. and Burkholder, R. J. (1993). A reciprocity formulation for the EM scattering by an obstacle within a large open cavity. *IEEE Transactions on Microwave Theory and Techniques*, 41, 702-707.

Ohnuki, S. and Hinata, T. (1998). Radar cross section of an open-ended rectangular cylinder with an iris inside the cavity. *IEICE Trans. Electron*., E81-C, 1875-1880.

Noble, B. (1958). *Methods Based on the Wiener-Hopf Technique for the Solution of Partial Differential Equations*, London: Pergamon.

Okada, S., Koshikawa, S., and Kobayashi K. (2002a). Wiener-Hopf analysis of the plane wave diffraction by a finite parallel-plate waveguide with three-layer material loading: part I. the case of E polarization. *Telecommunications and Radio Engineering*, 58, 53-65.

Okada, S., Koshikawa, S., and Kobayashi K. (2002b). Wiener-Hopf analysis of the plane wave diffraction by a finite parallel-plate waveguide with three-layer material loading: part II. the case of H polarization. *Telecommunications and Radio Engineering*, 58, 66-75.

Zheng, J. P. and Kobayashi, K. (2008). Plane wave diffraction by a finite parallel-plate waveguide with four-layer material loading: part I - the case of E polarization. *Progress In Electromagnetics Research B*, 6, 1-36.

Shang, E. H. and Kobayashi, K. (2008). Plane wave diffraction by a finite parallel-plate waveguide with four-layer material loading: part II - the case of H polarization. *Progress In Electromagnetics Research B*, 6, 267-294.

Kobayashi, K. (2013). Solutions of wave scattering problems for a class of the modified Wiener-Hopf geometries. *IEEJ Transactions on Fundamentals and Materials*, 133, 233-241 (*invited paper*).

BRIEF BIOGRAPHY

Kazuya Kobayashi received his B.S., M.S., and Ph.D. degrees, all in electrical engineering, from Waseda University, Tokyo, Japan in 1977, 1979, and 1982, respectively. In 1982, he joined the Department of Electrical, Electronic, and Communication Engineering, Chuo University, Tokyo, Japan, where he is currently a Professor. Dr. Kobayashi held the Visiting Professor position at various institutions including, University of Wisconsin-Madison, Madison, Wisconsin, U.S.A. (1987-1988), Institute of Radiophysics and Electronics of the National Academy of Sciences of Ukraine, Kharkov, Ukraine (2001), and Karpenko Physico-Mechanical Institute of the National Academy of Sciences of Ukraine, Lvov, Ukraine (2001). He has been Adjunct Professor at The Electromagnetics Academy at Zhejiang University, Hangzhou, China since 2004. Dr. Kobayashi received V. G. Sologub Prize (equivalent to Best Paper Award) at the “1998 International Conference on Mathematical Methods in Electromagnetic Theory” (MMET*98) held in Kharkov, Ukraine in 1998. Dr. Kobayashi is registered as a Member of the Science Council of Japan (SCJ), Japan and a Fellow of The Electromagnetics Academy, U.S.A. He has been the President of the Japan National Committee of the International Union of Radio Science (URSI) since 2008. His research area includes, developments of rigorous mathematical techniques as applied to electromagnetic wave problems, integral equations, boundary value problems, special functions, radar cross section, and scattering and diffraction.

SIGNAL PROCESSING FOR RADAR AND GPS IN BISTATIC FORWARD SCATTERING SYSTEMS

Hristo Kabakchiev
Faculty of Mathematics & Informatics,Sofia University, 15 Tsar Osvoboditel Blvd., Sofia, Bulgaria
ckabakchiev@yahoo.com

Abstract: In the Radar System, if the transmitter and receiver are collocated, this configuration is known as a Monostatic Radar Systems (MRS). In contrast, if the transmitter and receiver are separate, the systems are known as a Bistatic Radar Systems (BRS). The other type of Bistatic Radar Systems with a non-cooperative transmitter is a specific case of Passive Bistatic Radar Systems (PBRS), which exploits broadcast and communications signals as 'illuminators of opportunity'. For example where the signals from of the GPS system are exploited, this system is known as GPS PBRS. Currently, there is increased interest in Bistatic Radar Systems using Radar and GPS signals and, in particular, in systems operating at large bistatic angles where the effect of electromagnetic wave Forward Scattering (FS) occurs. This FS area is characterised by a gain in the target radar cross section and is restricted by the narrow corridor along the baseline, i.e. the line between the transmitter and the receiver separated by distance. However, this BFSRS and GPS PBFSRS has some fundamental limitations, which are the absence of range resolution and operation within very narrow angles. On the other hand, these systems may be used for the effective detection and tracking of targets moving in the FS area. Regardless of the large number of possible constraints, BFSRS and GPS PBFSRS may outperform traditional Monostatic Radar Systems in some situations, e.g. low profile, low speed and stealth targets (people, inflatable boats, and vehicles), as well as detection in a cluttered and complex environment (forest, urban, maritime). Several applications of this BFSRS and GPS PBFSRS for detection, estimation and classification of flying and moving objects in conditions of different clutter and jamming are consider. Signal models for Radar and GPS and Signal Processing for BFSRS and GPS PBFSRS are described. Results of numerical experiments are presented.

BRIEF BIOGRAPHY

Hristo Kabakchiev is a professor at the Faculty of Mathematics and Informatics, Sofia University "St. Kl. Ohridski", Bulgaria, and the leader of the "Signal Processing" research group at the Institute of Information and Communication Technologies, Bulgarian Academy of Sciences. Since 1989 he has been involved in signal processing applied research, including the development of a Bulgarian Coastal Radar for Long Surface for Marine Target Detection, ATC Radar for Low Flying Targets, Space Time Adaptive Processor for MTD LFM Radar (radar signal processors developed for the Bulgarian army), and Step Frequency Digital Ground Penetrating Radar.

His current research interests include GPS acquisition processing at the software GPS receiver for broadband and pulse jamming suppression by using adaptive beam-forming processing with MVDR approach, CFAR detection at the cross-correlator output, non–coherent integration at the output of the receiver with CFAR detection, binary integration after CFAR thresholding.

Full Papers

FREQUENCY SPECTRUM OF THE WAVE BACKSCATTERED TO TRANSCEIVER MOVING TOWARDS ROUGH SURFACE

Alexander B. Shmelev
Radiotechnical Institute by Academician A.L.Mints, 8 Marta Str.,Bld.10-1, Moscow, 127083, Russia
abshmelev@yahoo.com

Keywords: Frequency spectrum, randomly rough surface, aerospace vehicle, incident wave, scattered field, characteristic function, correlation function, normal distribution.

Abstract: Frequency spectrum of the wave scattered by randomly rough surface back to transceiver located on aerospace vehicle moving towards the surface is evaluated and investigated in explicit form. Kirchhoff's (physical optics) method is applied for scattered field evaluation. It is assumed that transceiver irradiates directive spherical wave illuminating circled area on the surface. Distribution of the rough surface height is assumed to be normal with isotropic Gaussian correlation function. Application the effective approximation formula for characteristic functions difference in integrand gives rise to spectrum evaluation for arbitrary height of surface irregularities. Frequency spectrum is shown to exist in two forms. The first one is represented by monotonic curve, depending on correlation distance of the rough surface. The second form includes one maximum, which position and amplitude are related with the roughness' mean square slope. On the parameter plane the curve is plotted which separates regions with abovementioned spectrum forms.

1 INTRODUCTION

The purpose of this paper is theoretical evaluation frequency spectrum of radiowave backscattered to transceiver moving towards randomly rough surface. This situation occurs, for example, before spacecraft landing on the Moon or planet surface. Irregularities of such surfaces are formed by natural factors and may be described as random fields. Frequency spectrum provides information about statistical characteristics of rough surface, such as correlation distance, mean square height and slope of its irregularities.

The scattering problem on randomly rough surface may be formulated as follows. Let scalar (sound) or vector (electromagnetic) wave fall on the surface S separating two media. The surface is described by equation $z = \zeta(x, y, t)$, where ζ is random function of coordinates x, y and time t. It is required to establish relation between statistical parameters of rough surface and characteristics of scattered field. Approaches to this problem as well as results obtained were described in literature at various times (Beckman and Spizzichino, 1963), (Bass and Fuks, 1972), (Shmelev, 1972). Nevertheless this problem is actual up to now because of application peculiarity variety.

We use in this paper Kirchhoff's (physical optics) method – the most developed and effective in wave scattering problems. It is based on assumption that reflection of incident wave at every point of rough surface locally obeys geometric optics laws. This means that our consideration is restricted to rather smooth and gentle irregularities, which curvature radius is large in comparison with wave length. We don't take into account shadowing effects, so surface slopes are assumed to be not too sharp.

The problem solution by Kirchhoff's method is used to include two stages. At the first stage dynamical part of the problem is considered. General expression for wave field diffracted on the surface S is composed in Kirchhoff's approximation. The surface height is described herein by arbitrary function $z = \zeta(x, y, t)$. At the second stage this function is declared to be random and various statistical characteristics of scattered field, such as middle value, average intensity, correlation function etc., are evaluated by averaging over rough surfaces ensemble. In this paper we are interested in frequency spectrum of backscattered field when transceiver is moving towards rough surface (in

vertical direction). Analogous problem in the case when transceiver is moving along rough surface (in horizontal direction) was studied earlier (Shmelev, 1973). More accurate explicit results may be obtained in the case under consideration.

2 DYNAMICAL PART

For the sake of simplicity we consider scalar (sound) waves taking in mind that vector character of electromagnetic wave acts on polarization but not on spectrum shape. Let the directional spherical wave

$$\Phi(\mathbf{r}) = \frac{F(\mathbf{n}_r)}{|\mathbf{r}-\mathbf{R}_0|} e^{ik|\mathbf{r}-\mathbf{R}_0|} \qquad (1)$$

fall on the rough surface S which height $z = \zeta(x, y)$ diverges from the mean plane $z = \langle \zeta(x, y) \rangle = 0$ denoted by S_0. The wave number in upper medium is $k = \omega/c$, directivity pattern of transmitter is $F(\mathbf{n}_r)$, where $\mathbf{n}_r = \dfrac{\mathbf{r}-\mathbf{R}_0}{|\mathbf{r}-\mathbf{R}_0|}$, $\mathbf{R}_0$ - transmitter position vector.

At first we consider motionless surface S. Its movement towards transceiver will be taken into account in quasi-static approximation by time dependence restoration in final expression for diffracted field. This approximation is valid if transmitter velocity is small in comparison with light velocity $v \ll c$. Geometric scheme of the wave scattering problem is shown on Figure 1 for general case of spaced transmitter Q and receiver P.

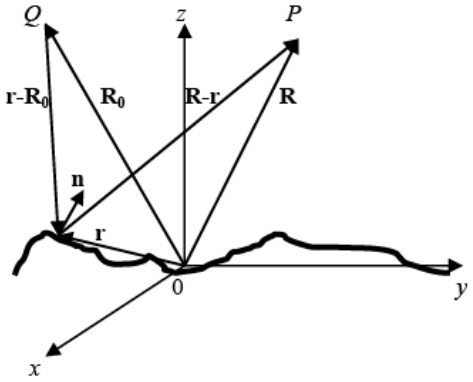

Figure 1: The scattering problem geometry for spaced transmitter and receiver.

Here $\mathbf{R_0}$ and $\mathbf{R}$ are transmitter Q and receiver P position vectors, $\mathbf{r} = (x, y, \zeta(x, y)) = (\mathbf{r}_\perp, \zeta)$ is radius -vector of rough surface point, $\mathbf{n}$ - surface normal at this point.

Diffracted field at observation point P is related with values of the field φ and its normal derivative $\partial\varphi/\partial n$ on the rough surface S by Green's formula

$$\varphi(\mathbf{R}) = \frac{1}{4\pi}\int_S \left(\varphi \frac{\partial}{\partial n}\frac{e^{ik|\mathbf{R}-\mathbf{r}|}}{|\mathbf{R}-\mathbf{r}|} - \frac{\partial\varphi}{\partial n}\frac{e^{ik|\mathbf{R}-\mathbf{r}|}}{|\mathbf{R}-\mathbf{r}|} \right) dS . \qquad (2)$$

In Kirchhoff's approximation following relations are valid at the every point of surface S

$$\varphi = V\Phi, \quad \frac{\partial\varphi}{\partial n} = -V\frac{\partial\Phi}{\partial n}, \qquad (3)$$

where $V = V(\mathbf{r}, \mathbf{n})$ is local Fresnel reflection coefficient. Substitution (1) and (3) into (2) gives

$$\varphi(\mathbf{R}) = \frac{1}{4\pi}\int_S V \frac{\partial}{\partial n}\left[\frac{F(\mathbf{n}_r) e^{ik|\mathbf{r}-\mathbf{R}_0| + ik|\mathbf{R}-\mathbf{r}|}}{|\mathbf{R}-\mathbf{r}|\cdot|\mathbf{r}-\mathbf{R}_0|} \right] dS . \qquad (4)$$

Let us assume now that transmitter and receiver are situated far enough from the rough surface, so that $R, R_0 \gg \lambda, \sigma, k\sigma^2$, where σ is mean square height of surface irregularities and $\lambda = 2\pi/k$ - wave length. Then we separate two types of multipliers in (4) – rapidly oscillating exponent and slowly varying functions weakly dependent on rough surface height $\zeta(\mathbf{r}_\perp)$. Setting $\zeta = 0$ in this functions, keeping linear with respect to ζ terms in exponent power expansion and changing integration over surface S by integration over middle plane S_0, we come to known expression for diffracted field

$$\varphi(\mathbf{R}) = \frac{i}{4\pi}\int_{S_0} VF(\mathbf{n}_{01}) \frac{e^{ikR_{01} + ikR_1}}{R_{01}R_1}\frac{q^2}{q_z} e^{iq_z\zeta}\, d^2\mathbf{r}_\perp , \qquad (5)$$

where $\mathbf{r}_\perp = (x, y, 0)$, $\mathbf{R}_{01} = \mathbf{r}_\perp - \mathbf{R}_0$, $\mathbf{R}_1 = \mathbf{R} - \mathbf{r}_\perp$, $\mathbf{n}_{01} = \mathbf{R}_{01}/R_{01}$, $\mathbf{n}_1 = \mathbf{R}_1/R_1$ and $\mathbf{q} = k(\mathbf{n}_{01} - \mathbf{n}_1)$ is the scattering vector.

Let us now take into consideration motion of the rough surface along z-axis with the constant velocity v. In quasi-static approximation we have to set in (5) $\zeta = \zeta(\mathbf{r}_\perp, t) = \zeta(\mathbf{r}_\perp) + vt$. In addition we assume that surface S is absolutely reflecting (V=1) – absolutely rigid in acoustics or perfectly conductive in electrodynamics. This removes influence of surface

material properties on spectrum under investigation. Solution of dynamical part of the problem takes on final form

$$\varphi = \frac{i\,\mathrm{e}^{i\omega_0 t}}{4\pi}\int\limits_{S_0} F\left(\mathbf{n}_{01}\right)\frac{\mathrm{e}^{ik\left(R_{01}+R_1\right)}}{R_{01}R_1}\frac{q^2}{q_z}\mathrm{e}^{iq_z\zeta(\mathbf{r}_\perp)+iq_z vt}\,d^2\mathbf{r}_\perp . \quad (6)$$

This expression provides basis for further evaluation statistical characteristics of diffracted field.

3 AVERAGE FIELD

Averaging expression (6) over ensemble of random field $\zeta\left(\mathbf{r}_\perp\right)$ realizations leads to average value of diffracted field

$$\left\langle\varphi\right\rangle = \frac{i\,\mathrm{e}^{i\omega_0 t}}{4\pi}\int\limits_{S_0} F\frac{\mathrm{e}^{ik\left(R_{01}+R_1\right)}}{R_{01}R_1}\frac{q^2}{q_z}f_{1\zeta}\left(q_z\right)\mathrm{e}^{iq_z vt}\,d^2\mathbf{r}_\perp , \quad (7)$$

where corner brackets denote averaging operation, $f_{1\zeta}\left(q_z\right)=\left\langle\exp\left(iq_z\zeta\right)\right\rangle$ is characteristic function of the rough surface *S*. We suppose that random field $\zeta\left(\mathbf{r}_\perp\right)$ is statistically homogeneous.

Evaluation this integral by means of stationary phase technique gives physically transparent result

$$\left\langle\varphi(\mathbf{R},t)\right\rangle = f_{1\zeta}(q_{zs})\varphi^{(0)}(\mathbf{R})\exp\left(iq_{zs}vt\right), \quad (8)$$

where $q_{zs}=2k\cos\theta_s$ is *z*-component of scattering vector at stationary point coinciding with the point of mirror reflection from the mean plane S_0. This point is chosen to be origin of coordinates. Incidence angle at stationary point is denoted by θ_s. The field mirrored from the plane S_0 is designated as $\varphi^{(0)}\left(\mathbf{R}\right)$.

Average field is interpreted like coherent part of diffracted field. Multiplier $f_{1\zeta}\left(q_{zs}\right)$ is effective reflection coefficient of average field. If surface height is distributed under Gaussian law, it has the form

$$f_{1\zeta}(q_{zs}) = \exp\left(-2k^2\sigma^2\cos^2\theta_s\right) = \mathrm{e}^{-\Delta^2/2}, \quad (9)$$

where $\Delta = 2k\sigma\cos\theta_s$ is the Rayleigh parameter characterizing degree of surface roughness.

Doppler shift of average field is equal to

$$\Delta\omega = q_{zs}v = 2kv\cos\theta_s . \quad (10)$$

Backscattering case follows by setting $\theta_s = 0$ in formulas obtained.

4 SCATTERED FIELD

Scattered field is meant to be diffracted field minus its average value $\Delta\varphi=\varphi-\left\langle\varphi\right\rangle$. Let us evaluate temporal correlation function of the scattered field $\psi\left(t-t'\right)=\left\langle\Delta\varphi\left(\mathbf{R},t\right)\cdot\Delta\varphi^*\left(\mathbf{R},t'\right)\right\rangle$. Using (6) and (7) we obtain

$$\psi\left(\tau\right) = \frac{\mathrm{e}^{i\omega_0\tau}}{16\pi^2}\int\limits_{S_0}\frac{\left|F\left(\mathbf{n}_{01}\right)\right|^2 q^4}{R_{01}^2R_1^2q_z^2}J\left(\mathbf{q}\right)\mathrm{e}^{iq_z v\tau}\,d^2\mathbf{r}_\perp , \quad (11)$$

where

$$J\left(\mathbf{q}\right) = \int\limits_{-\infty}^{\infty}\left[\,f_{2\zeta}\left(q_z,-q_z,\boldsymbol{\rho}\right)-\left|f_{1\zeta}\left(q_z\right)\right|^2\right]\mathrm{e}^{i\mathbf{q}_\perp\boldsymbol{\rho}}\,d^2\boldsymbol{\rho} , \quad (12)$$

$f_{2\zeta}\left(u,w,\boldsymbol{\rho}\right)=\left\langle\exp\left[iu\zeta\left(\mathbf{r}_\perp\right)+iw\zeta\left(\mathbf{r}_\perp+\boldsymbol{\rho}\right)\right]\right\rangle$ is two-dimensional characteristic function of the rough surface.

Integral $J\left(\mathbf{q}\right)$ is well studied in cited literature. There are known its explicit expressions for irregularities distributed under Gaussian law. In the case of small irregularities in comparison with the wave length $\delta=\left(k\sigma\right)^2\ll 1$ and Gaussian spatial correlation coefficient $K\left(\rho\right)=\exp\left(-\rho^2/l^2\right)$ with the single correlation distance *l* this expression has the form

$$J\left(\mathbf{q}\right) = \pi\sigma^2l^2q_z^2\exp\left(-q_\perp^2l^2/4\right), \quad \delta\ll 1 . \quad (13)$$

In the opposite case of high irregularities $\delta\gg 1$ and arbitrary spatial single-scale correlation function integral *J* equals to

$$J\left(\mathbf{q}\right) = \frac{4\pi}{\beta q_z^2}\exp\left(-\frac{q_\perp^2}{\beta q_z^2}\right), \quad \delta\gg 1 , \quad (14)$$

where parameter $\beta=\sigma_s^2=-2\sigma^2K''\left(0\right)=4\sigma^2/l^2$ characterizes mean-square slope of the surface roughness.

In this paper we use the integral J evaluation technique valid for arbitrary values of parameter δ, i.e. for arbitrary height of surface irregularities. It is based on approximation formula

$$\exp\left[-\gamma\left(1-\mathrm{e}^{-x^2}\right)\right]-\mathrm{e}^{-\gamma}\simeq\left(1-\mathrm{e}^{-\gamma}\right)\exp\left(-\frac{\gamma x^2}{1-\mathrm{e}^{-\gamma}}\right), \quad (15)$$

where γ is positive parameter. This approximation was studied in detail in (Vinogradov and Shmelev, 2008).

Let us assume that the surface height is distributed under Gaussian law with Gaussian spatial correlation coefficient $K(\boldsymbol{\rho})=\exp\left(-\rho_x^2/l_x^2-\rho_y^2/l_y^2\right)$ taking into consideration possible non-isotropy of surface irregularities. Difference of characteristic functions in integrand (12) may be represented in accordance with (15) by following expression

$$\begin{aligned} &f_{2\zeta}(q_z,-q_z,\boldsymbol{\rho})-\left|f_{1\zeta}(q_z)\right|^2= \\ &=\exp\left[-q_z^2\sigma^2\left(1-\mathrm{e}^{-\rho_x^2/l_x^2-\rho_y^2/l_y^2}\right)\right]-\exp\left(-q_z^2\sigma^2\right)\simeq \\ &\simeq\left(1-\mathrm{e}^{-q_z^2\sigma^2}\right)\exp\left(-\rho_x^2/l_{\Phi x}^2-\rho_y^2/l_{\Phi y}^2\right), \end{aligned} \quad (16)$$

where effective correlation distances have the values

$$l_{\Phi x}^2=\frac{l_x^2}{q_z^2\sigma^2}\left(1-\mathrm{e}^{-q_z^2\sigma^2}\right), \quad l_{\Phi y}^2=\frac{l_y^2}{q_z^2\sigma^2}\left(1-\mathrm{e}^{-q_z^2\sigma^2}\right), \quad (17)$$

dependent on wave length.

Substitution (16)-(17) into (12) and immediate evaluation of the integral lead to result

$$J(\mathbf{q})\simeq\pi l_{\Phi x}l_{\Phi y}\left(1-\mathrm{e}^{-q_z^2\sigma^2}\right)\exp\left(-\frac{q_x^2l_{\Phi x}^2+q_y^2l_{\Phi y}^2}{4}\right). \quad (18)$$

In the case of statistically isotropic surface we have to set $l_x=l_y=l$. This gives

$$\begin{aligned} J(\mathbf{q})&=\pi l_\Phi^2\left(1-\mathrm{e}^{-q_z^2\sigma^2}\right)\exp\left(-\frac{q_\perp^2l_\Phi^2}{4}\right), \\ l_\Phi^2&=\frac{l^2}{q_z^2\sigma^2}\left(1-\mathrm{e}^{-q_z^2\sigma^2}\right). \end{aligned} \quad (19)$$

In limiting cases of small and high irregularities these expressions lead to (13) and (14).

Let us consider now backscattering case, when transmitter and receiver positions coincide, i.e. $\mathbf{R}=\mathbf{R}_0=(0,0,Z)$. Let rough surface be statistically isotropic, and multiplier describing antenna pattern be in the form

$$\left|F(\mathbf{n}_{01})\right|^2=\begin{cases}1, & \text{if } r_\perp\le a,\\ 0, & \text{if } r_\perp>a,\end{cases} \quad (20)$$

where a is radius of illuminated area on the mean plane S_0. Transformation to polar coordinates in integrand (11) gives then required expression for temporal correlation function of backscattered field

$$\psi(\tau)=\frac{\mathrm{e}^{i\omega_0\tau}}{16\pi^2}\int_0^{2\pi}d\varphi\int_0^a r_\perp dr_\perp\,\frac{q^4}{R_{01}^2R_1^2q_z^2}J(\mathbf{q})\mathrm{e}^{iq_zv\tau}, \quad (21)$$

where following relations are valid:

$$\begin{aligned} &\mathbf{R}_{01}=-\mathbf{R}_1=(\mathbf{r}_\perp,-Z), \quad R_1^2=R_{01}^2=r_\perp^2+Z^2, \\ &\mathbf{q}=2k\mathbf{n}_{01}=2k\frac{(\mathbf{r}_\perp,-Z)}{\sqrt{r_\perp^2+Z^2}}, \quad q^2=4k^2, \\ &l_\Phi^2=\frac{l^2\left(r_\perp^2+Z^2\right)}{4k^2\sigma^2Z^2}\left[1-\exp\left(-\frac{4k^2\sigma^2Z^2}{r_\perp^2+Z^2}\right)\right]. \end{aligned} \quad (22)$$

5 FREQUENCY SPECTRUM

As is known, frequency spectrum may be evaluated by Fourier transformation of temporal correlation function

$$G(\omega)=\int_{-\infty}^{\infty}\psi(\tau)\mathrm{e}^{i\omega\tau}\,d\tau. \quad (23)$$

Insertion (21), (22) into (23) and application of δ-function integral representation $\delta(\omega)=\frac{1}{2\pi}\int_{-\infty}^{\infty}\mathrm{e}^{i\omega\tau}\,d\tau$ gives following expression for frequency spectrum of backscattered field

$$G(\omega)=\frac{1}{4}\int_0^a\frac{q^4J(\mathbf{q})}{R_{01}^2R_1^2q_z^2}\delta(\omega-\omega_0-q_zv)\,r_\perp dr_\perp. \quad (24)$$

Introducing new integration variable $x=q_zv=-\frac{2kvZ}{\sqrt{Z^2+r_\perp^2}}$ and performing integration of

δ-function, we obtain frequency spectrum of backscattered field in explicit form

$$G(\Omega)=\frac{\pi\left(1-e^{-\delta\Omega^2}\right)^2}{2kvZ^2\beta\Omega^3}\exp\left[\frac{\left(\Omega^2-1\right)}{\beta\Omega^2}\left(1-e^{-\delta\Omega^2}\right)\right]. \quad (25)$$

Dimensionless frequency $\Omega=\frac{\omega-\omega_0}{2kv}=\frac{\Delta\omega}{2kv}$ varies within $\cos\theta\le\Omega\le 1$, where angle 2θ is the beam width of transmitter, so that $\tan\theta=a/Z$. Beyond this interval $G(\Omega)\equiv 0$. Physically this means that frequency spectrum includes all possible Doppler shifts of scattered field – from maximum $\Delta\omega_{max}=2kv$ in vertical direction till minimum $\Delta\omega_{min}=2kv\cos\theta$ in direction of illuminated area border.

To avoid dependence on inessential parameters let us consider spectrum normalized to its value at Ω=1, i.e. $G_0(\Omega)=G(\Omega)/G(1)$:

$$G_0(\Omega)=\frac{\left(1-e^{-\delta\Omega^2}\right)^2}{\left(1-e^{-\delta}\right)^2\Omega^3}\exp\left[\frac{\left(\Omega^2-1\right)}{\beta\Omega^2}\left(1-e^{-\delta\Omega^2}\right)\right]. \quad (26)$$

Analysis of this expression shows that there exist two forms of frequency spectrum. The first one is represented by monotonic curve, depending on correlation distance of the rough surface. The second form includes one maximum, which position and amplitude are related with irregularities mean square slope. Typical examples of these spectrum forms are shown on Figures 2 and 3.

Regions on the plane (δ,β) corresponding to one or another form of spectrum differ in sign of derivative $G_0'(1)$. Region, where $G_0'(1)>0$, corresponds to the first form and region, where $G_0'(1)<0$, – to the second form. The curve corresponding to $G_0'(1)=0$ separates these two regions. Simple calculations using (26) lead to equation of this curve plotted on Figure 4:

$$\beta=\frac{2\left(1-e^{-\delta}\right)^2}{3-(3+4\delta)e^{-\delta}}. \quad (27)$$

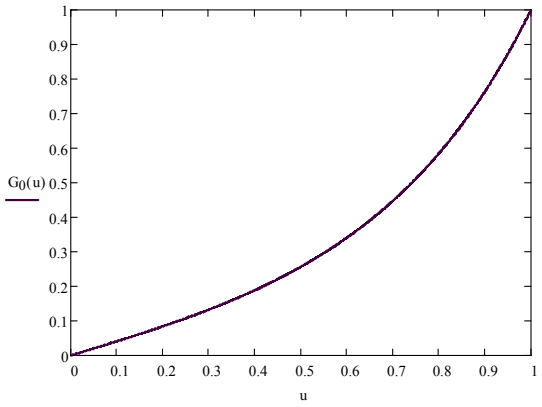

Figure 2: The first form of frequency spectrum for parameter values δ=0.1, β=0.1.

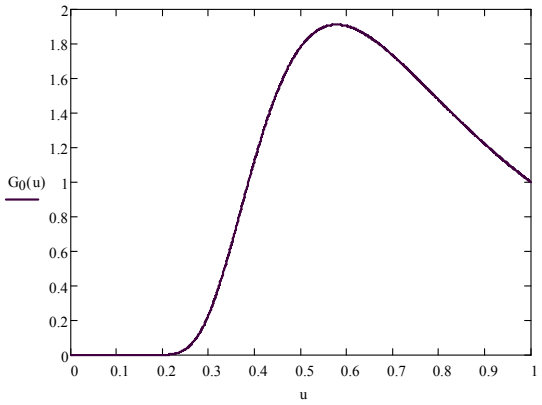

Figure 3: The second form of frequency spectrum for parameter values δ=100, β=2.

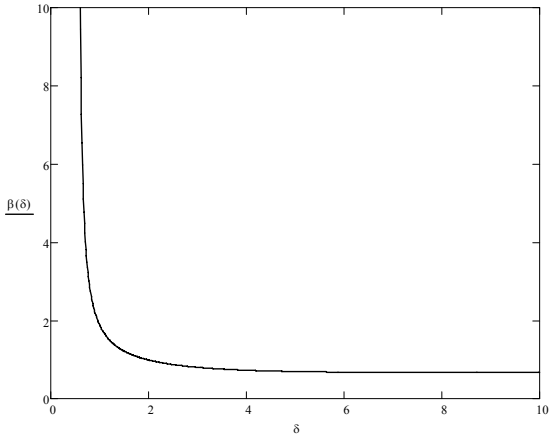

Figure 4: The curve separating regions with the first (under the curve) and the second (above the curve) forms of spectrum.

The first spectrum form results in the case when irregularities are rather small $(\delta < 1)$ or gentle $(\beta < 0.7)$. High and sharp irregularities lead to the second form of spectrum.

In the case of extreme low roughness $(\delta \ll 1)$ expression (26) is simplified to

$$G_0(\Omega) \simeq \Omega \cdot \exp\left[-\alpha\left(1-\Omega^2\right)\right], \quad \delta \ll 1, \quad (28)$$

where $\alpha = \delta/\beta = (kl)^2$ is mean square correlation distance in the scale of wave length. Differentiation (28) gives relation

$$\alpha = \frac{G_0'(1)-1}{2}, \quad (29)$$

which may be used for experimental estimation of parameter α.

In the opposite case of very high roughness $(\delta \gg 1)$ expression (26) takes on the form

$$G_0(\Omega) = \frac{1}{\Omega^3}\exp\left[-\frac{\left(1-\Omega^2\right)}{\beta\Omega^2}\right], \quad \delta \gg 1. \quad (30)$$

For sharp irregularities $(\beta > 0.67)$ it describes the second spectrum form having maximum at $\Omega_m = \sqrt{2/(3\beta)}$. Thus position of maximum carries information on mean square slope of the rough surface β. Additional information on this parameter contains height of this maximum

$$G_0(\Omega_m) = \left(\frac{3\beta}{2}\right)^{3/2} \cdot \exp\left(-\frac{3\beta-2}{2\beta}\right). \quad (31)$$

This function is plotted on Figure 5.

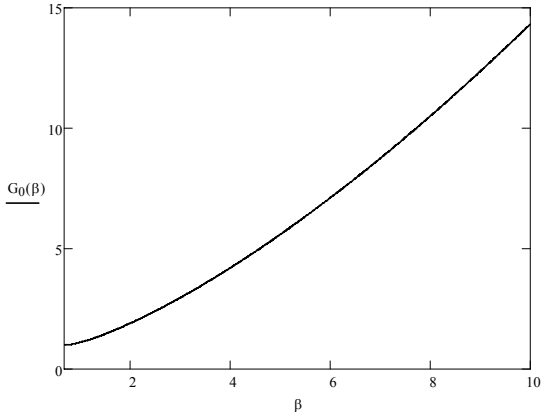

Figure 5: View of the function (31).

6 CONCLUSIONS

Proposed evaluation the frequency spectrum of the wave backscattered from rough surface in explicit form and for arbitrary roughness height lets us establish detailed relations between spectrum parameters and statistical characteristics of the surface. Results obtained may be useful for further development of rough surfaces remote sensing technique.

REFERENCES

Beckman, P. and Spizzichino, A., 1963. *The Scattering of Electromagnetic Waves from Rough Surfaces*. Pergamon Press. New York.

Bass, F.G. and Fuks, I.M., 1972. *Wave Scattering on Statistically Rough Surface*. Nauka Press. Moscow. (In Russian).

Shmelev, A.B., 1972. *Wave Scattering by Statistically Uneven Surfaces.* American Institute of Physics Incorporated: Soviet Physics Uspekhi, 15, 173-183.

Shmelev, A.B., 1973. *The Frequency Spectrum of a Sound Field Scattered by a Uniformly Moving Rough Surface.* Izvestiya VUZov (Radiofizika), 16, 54-61. (In Russian).

Vinogradov, A.G. and Shmelev, A.B., 2008. *Wave Scattering by a Rough Surface in Random Inhomogeneous Medium.* Radiotechnika Press: Electromagnetic Waves and Electronic Systems, 13(9), 38-45. (In Russian).

IN-SITU MEASUREMENT AND VISUALIZATION OF ELECTROMAGNETIC FIELDS

Satoshi Yagitani, Mitsunori Ozaki
Institute of Science and Engineering, Kanazawa University, Kakuma-machi, Kanazawa, Japan
yagitani@is.t.kanazawa-u.ac.jp, ozaki@is.t.kanazawa-u.ac.jp

Yoshiyuki Yoshimura, Hirokazu Sugiura
Industrial Research Institute of Ishikawa, 2-1 Kuratsuki, Kanazawa, Japan
yyoshi@irii.jp, h-sugiura@irii.jp

Keywords: Electromagnetic fields, Radio-frequency fields, Measurement, Visualization, EMC, Absorber.

Abstract: In-situ monitoring of electromagnetic field distributions is useful for localizing and identifying EM noise sources, as well as for evaluating actual antenna characteristics. A couple of new techniques developed for in-situ measurement and visualization of electromagnetic fields are reported. At first, visualization of EM field distributions measured by a freehand scanning sensor on a live video image is described. Secondly, imaging of 2-d RF field distributions incident on a metamaterial absorber is explained. Then, in-situ visualization techniques for EM vectors and RF polarizations are discussed. Such techniques are expected to be quite useful for measuring EM field distributions in various scenarios in the fields of EMC, antennas and propagation.

1 INTRODUCTION

In-situ measurement of the actual spatial distributions of electromagnetic (EM) field is useful for localizing and identifying EM noise sources in electric or electronic equipment under actual operating conditions, as well as for evaluating the performance of antennas in wireless communication devices used in real environments. Conventionally, the spatial distributions of the EM field have been measured by scanning the plane/volume of interest with a sensor or sensor array. So far there have been proposed and developed a wide variety of mapping and cartography systems of EM distributions from the viewpoint of EMC/EMI. For radio-frequency (RF) fields from tens of MHz up to tens of GHz, various kinds of sensor-scanning systems have been developed to measure RF emissions from electronic devices and systems, individual PCBs, and even onboard VLSI chips. In these systems, for example, an electric field probe (Dutta et al., 1999), a magnetic loop probe (Haelvoet et al, 1996), a magnetic sensor array (Yamaguchi et al., 1999), and an electromagnetic field probe (Kazama and Arai, 2002) have been used with mechanically-scanning systems (Baudry et al., 2007), which have measured and visualized RF near-field distributions. A 2-d dense array of thousands of loop sensors for near-field distribution imaging (without the need for scanning) has also been available (Fan, 2009). The near-field distributions have been used to identify radiated emission sources (Laurin et al., 2001) and to predict far-field noise radiation (Shi et al., 2004). Another study has measured Fresnel near-field distributions to holographically localize RF leakage points for example from a shielded door (Kitayoshi and Sawaya, 1999) and from the surface of spacecraft (Chen et al., 2012).

It is noted that for dc to low-frequency magnetic field application, there have been independently developed the imaging systems such as “magnetovision” with scanning 1d and 2d magnetoresistive (MR) sensor arrays, to obtain principally dc magnetic field images, for example for investigation of magnetized materials (Tumanski and Liszka, 2002; Tumanski and Baranowski, 2006).

Another unique RF field imaging technique has been proposed which employs an infrared (IR)

thermogram (Norgard and Musselman, 2004). An RF field impinging on a lossy screen is absorbed and creates a temperature rise there corresponding to a map of absorbed power distribution, which is taken by an IR camera. A "live electro-optic (EO) imaging" system has employed an ultra-parallel photonic heterodyne technique to take a video image of electric near-field distribution applied on an EO crystal plate at microwave frequencies (Sasagawa et al., 2007). The electric fields more than tens of GHz were down-converted and lively displayed at 30 frames/second as a 2d image with 100x100 pixels.

Generally these techniques give accurate cartographic mapping and images of EM fields, but require specific sensor scanning devices or imaging systems. In constrast, the authors' group have been developing compact in-situ measurement and visualization techniques for EM fields, which could be used to capture an intuitive view of EM distributions existing in actual environments. In this paper a couple of developed techniques to measure and visualize EM field distributions are reported.

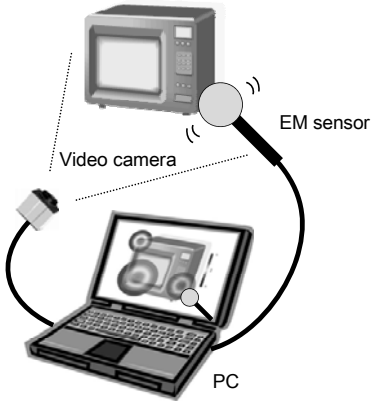

Figure 1: EM field distribution imager.

2 EM FIELD MEASUREMENT AND VISUALIZATION ON A VIDEO IMAGE

2.1 EM Field Distribution Imager

The "EM field distribution imager" illustrated in Figure 1 measures and visualizes in-situ EM field distributions on a live video image of the real world. The image of an EM sensor is taken by a single video camera. Image processing is applied on a PC and the location of the sensor is identified on each frame of the video image, where the sensor location is painted with the color representing the EM field intensity actually measured by the sensor itself. By freely scanning the sensor by hand, the image of the in-situ field distribution is gradually showing up along the sensor trajectory as a color map on the video image. Figure 2 shows an example of the RF field (1.9 GHz) visualization around a mobile phone. A sleeve dipole antenna was put inside a yellow acrylic spherical cover of 10 cm diameter. A video camera was placed 1 m away from the cell phone put on a tripod in an office room. Here the 3d location of the sensor was identified by extracting the yellow circle on the image, the center and size of which gave information on the sensor's lateral and depth location relative to the camera. Along the freely scanned trajectory an intensity map of the RF filed was created, which exhibited a standing-wave pattern possibly caused by reflection at the wall or floor. With this system one can scan the space of interest while watching the video image, to obtain an intuitive view of EM field distribution, in every situation wherever the video camera and the sensor can be carried in.

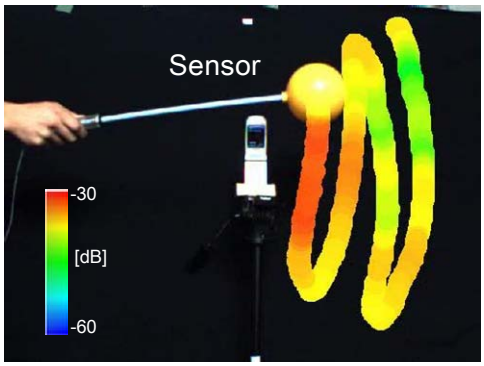

Figure 2: RF field imaging around a mobile phone.

This kind of freehand-scanning method has been developed also by other researchers, based on magnetic tracking, optical tracking and IR tracking, for the investigation of the low-frequency magnetic noise emitted from electrical appliance (Sato et al., 2010; Sato et al., 2012).

2.2 Magnetic Field Vector Imaging and Source Current Estimation

Even with a single video camera, this system can determine the sensor's 3d orientation in addition to its 3d location, by putting a specific marking on the spherical sensor cover. One way is to paint three marks with different colors indicating the three axial directions of the internal sensor, which are

recognized on the video image to calculate the sensor orientation. This makes it possible to measure EM vector directions when we use an EM vector sensor. Figure 3 (a) shows an example of the magnetic field vectors measured and visualized around a 45x45-cm square loop antenna (10 kHz, 63 mA-Turns), where the 2d projection of the measured 3d vectors are plotted with length and color indicating the field intensity. Though not shown here a tri-axial magnetic search-coil sensor was used; three 10-cm-long uni-axial sensors were placed orthogonally with each other, covered by a 15-cm acrylic sphere. A perpendicular plane 1 m away from the camera (and 9 cm in front of the loop plane) was manually scanned by the sensor. Measurement was done at 7x7=49 points on a 60x60 cm area. Compared with theoretically calculated values, the measured errors in intensity and vector direction of the magnetic field were less than 10% and 10 degrees, respectively. These errors were caused by the errors in location (3 cm) and in orientation (a few degrees) of the sensor which was identified on a 640x480-pixel video image.

From the measured magnetic field vectors the source current distributions were estimated by the GVSPM method on the plane including the loop source (Yagitani et al., 2007). Figures 3 (b) and (c) plot the estimated source current vectors and amplitudes on the loop plane. The estimated current vectors are visualized on the real image of the loop source, where the estimated current is practically reconstructed along the actual square route of the loop current. Thus, the free-scanning system is expected to contribute not only to imaging of EM field distributions but also estimating their sources.

2.3 EM Imaging by Smartphone and Tablet PC

The measurement and visualization technique has also been implemented onto a smartphone and tablet PC. Figure 4 shows an example of a low frequency (60 Hz) magnetic field distribution around an electric cooker, which was measured by a magnetic sensor with an augmented reality (AR) tag attached, and visualized on a smartphone screen. With these up-to-date devices, built-in cameras are used to take a video image, while they can easily communicate with the sensors through wireless links. Furthermore an open-source AR software makes it easy to implement the sensor identification capability on the video image in a smartphone/tablet app.

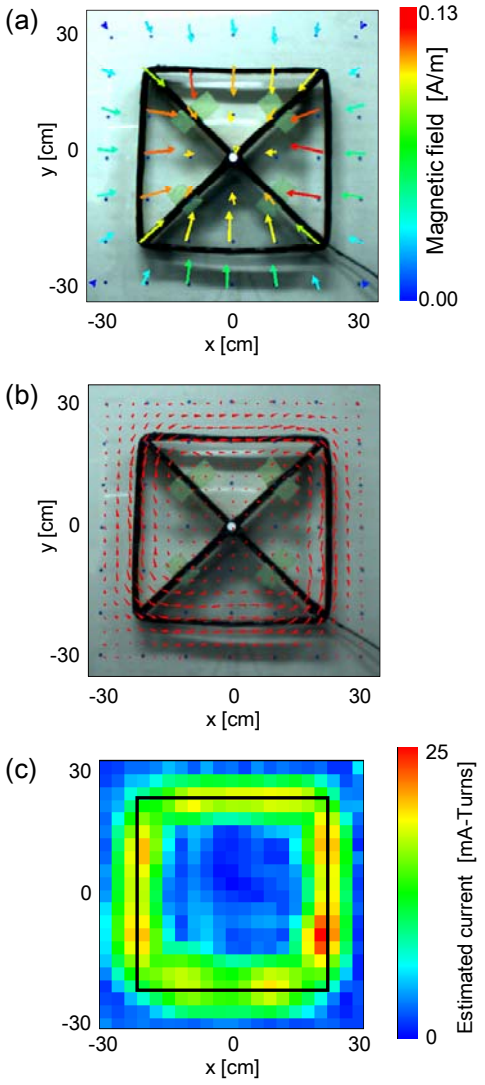

Figure 3: Low-frequency magnetic field vectors and estimated current distribution: (a) measured magnetic field vector distribution, (b) estimated current vectors, (c) estimated current amplitude distribution.

Figure 4: Low-frequency magnetic fields from an electric cooker, measured by a magnetic sensor with an AR tag attached, and visualized on a smartphone screen.

3 RF FIELD DISTRIBUTION IMAGER USING METAMATERIAL ABSORBER

3.1 Metamaterial Absorber

It has been proposed that a metamaterial absorber could be used for monitoring 2d power distributions of a radio-frequency (RF) wave incident on the absorber surface (Yagitani et al., 2011a). The metamaterial absorber was designed by employing a mushroom-type electromagnetic band-gap (EBG) structure used as a high-impedance surface (alternatively called an artificial magnetic conductor). As shown in Figure 5 (a), a 2d matrix of dense square metal patches formed on a dielectric substrate were connected to the ground plane through vias. Lumped resistors interconnecting the square patches were placed on the surface to absorb the incident wave (Gao et al., 2005). A simple equivalent circuit based on the transmission line model for the absorber is shown in Figure 5 (b); the capacitance C is formed between the adjacent patches whereas the inductance L comes from the wave propagation (transmission line) inside the substrate (Luukkonen et al., 2009). At the resonance frequency the LC impedance becomes infinite so that the surface resistance R absorbs the incident wave if R is matched with the free space wave impedance, 377 Ω, for normal incidence. Figure 5 (c) shows the reflection and absorption characteristics; the maximum absorption (minimum reflection) occurs at the resonance frequency. Since L and C are determined by the metamaterial structure, varactor diodes were inserted parallel to the resistors to make the resonance (absorption) frequency tunable (Mias and Yap, 2007).

3.2 RF Power Distribution Measurement

The configuration of this kind of metamaterial absorber makes it possible to directly measure the amounts of power absorbed (or consumed) by the individual lumped resistors. As in Figure 6, an RF power detector can be attached to each resistor and measure the absorbed power. A 2d array of power detectors attached to the lumped resistors are used to capture the 2d image of the RF power incident and absorbed on the surface. The amount of power absorbed by each resistor is dependent on the incident polarization; the incoming RF waves with the electric field polarized in the x- and y-directions are absorbed by the resistors connecting the adjacent patches in the x- and y-directions, respectively. In either case, the power absorbed by each resistor is considered to be the Poynting flux of the incident wave multiplied by the area of one unit cell. Thus, the information on the incident polarization is obtained by the power detectors individually attached to the x- and y-resistors.

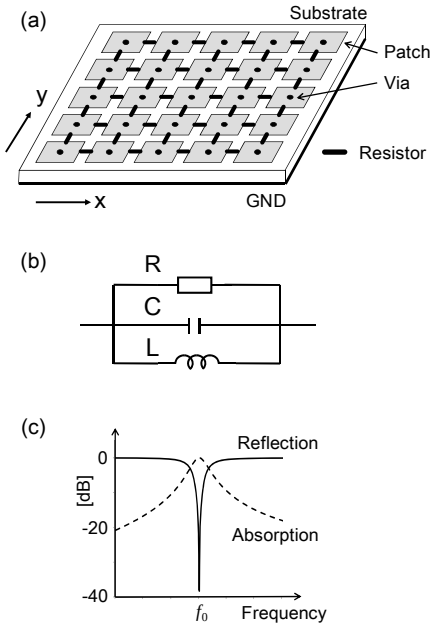

Figure 5: A metamaterial absorber: (a) basic structure, (b) equivalent circuit, and (c) reflection and absorption characteristics.

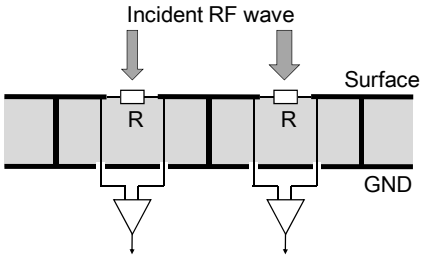

Figure 6: Measurement of absorbed RF power

A metamaterial absorber was designed and fabricated which was made tunable between 700 MHz and 2.7 GHz (Yagitani et al., 2011a). A 33x33 array of square unit cell were formed on an FR-4 substrate of 347 mm square and 1.6 mm thick. The size of each patch was 10 mm and the gap between the adjacent patches was 0.5 mm. Lumped resistors (620 Ω) and RF varactor diodes (Infineon BB833)

were inserted in parallel between the patches. The equivalent circuit model of the absorber is given in Figure 7, where C_D, L_D and R_D are the stray capacitance, stray inductance and resistance of a varactor diode, respectively, and R_{loss} represents the dielectric loss of the substrate. Detailed analysis of such a circuit was made to reveal that even a small varactor resistance (a few Ohms) is translated to a larger surface resistance which severely degrades the absorption performance especially at lower frequencies (Yagitani et al., 2011b). The performance of the absorber is shown in Figure 8 (with data taken from Yagitani et al., 2011a), where a black solid line, a gray line and a broken line represent the measured profile, the profiles obtained by equivalent-circuit analysis and EM simulation (CST MW-STUDIO), respectively. These profiles practically agree with each other. The symbols A, B, C and D correspond to the varactor capacitances of 3.35 pF, 1.72 pF, 1.09 pF and 0.72 pF, respectively. Here the lumped resistors had been chosen as 620 Ω so that the maximum absorption was obtained at 2.62 GHz.

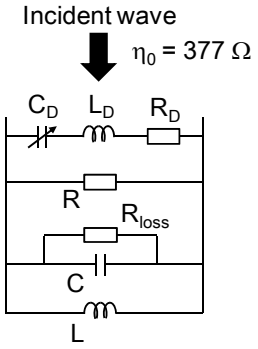

Figure 7: Equivalent circuit model of the fabricated metamaterial absorber.

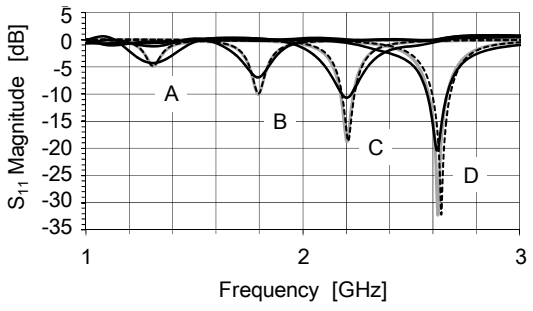

Figure 8: Absorption performance of the fabricated metamaterial absorber (data from Yagitani et al., 2011a).

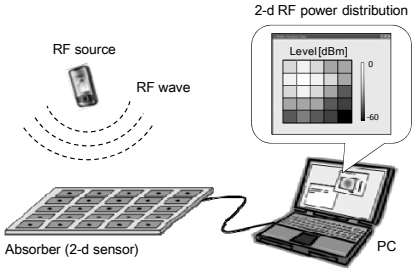

Figure 9: RF power distribution imager.

Using the fabricated absorber an RF power imager was developed, as schematically illustrated in Figure 9. The RF power distribution incident on the surface was detected by an array of power detectors attached on the backside of the absorber. An array of 64 power detectors were arranged in a 8x8 matrix to measure the *x*-polarization, whereas another array of 64 detectors were placed for the *y*-polarization. A logarithmic power detector (Analog Devides, ADL5513) was used, which measures the power in the range from -70 dBm to +10 dBm between 1 MHz and 4 GHz. The detected RF power distribution was A/D converted, transferred to a PC and displayed as a 2d color map at 30 images/second.

With this system, RF power distributions radiated from a standard dipole antenna were measured in the experimental setup shown in Figure 10 (a). A horizontally polarized radio wave (0 dBm) at 2.2 GHz was transmitted from the antenna placed at a distance d from the absorber. Figure 10 (b) plots the measured power distribution of horizontal polarization at d = 10 cm. An elliptic power distribution corresponding to the directivity of the horizontal dipole was captured. The power distributions along the *x*- and *y*-axes are compared with the theoretical values in Figure 10 (c), which were calculated according to the previous work (Yagitani et al., 2011a). Here each power detector had been calibrated by an almost far-field and plane-wave pattern, created by the transmitting antenna placed at d = 80 cm. For distances of d = 30 cm and 50 cm, the measured profiles practically agree with the theoretical curves. At a distance of 10 cm, however, the measured profiles became weaker than the theoretical ones. This would be caused by that at this short distance the radiated field did not completely become a far-field so that impedance mismatch caused the reflection from the absorber surface. More rigorous treatment for near-field spherical wave incidence is needed to quantitatively discuss the accuracy of power distributions at such a short distance.

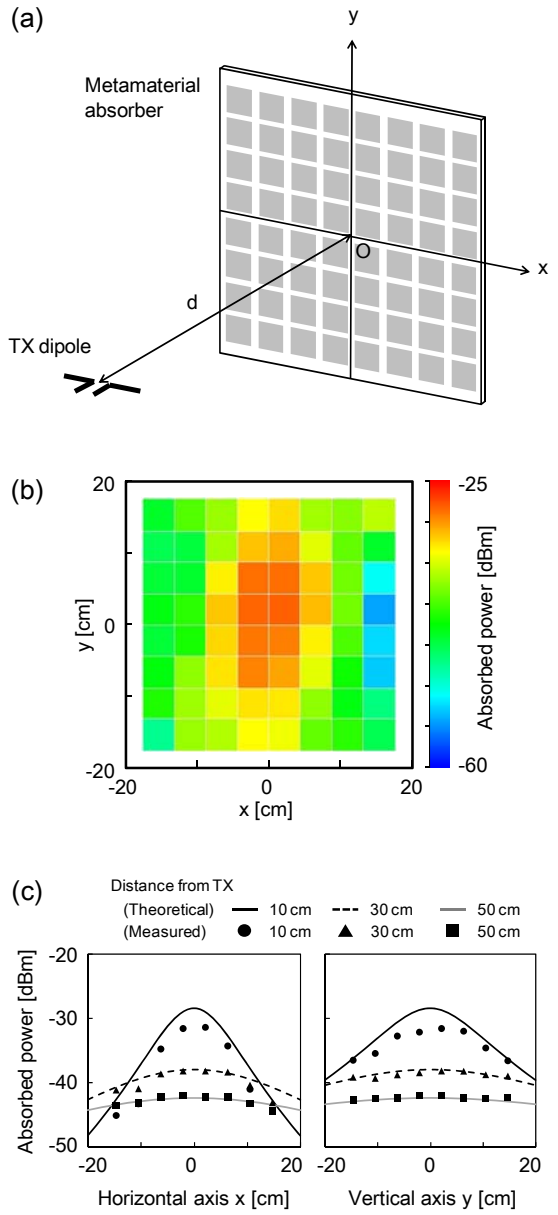

Figure 10: Measurement of RF power distribution: (a) experimental setup, (b) power distribution at 10 cm from the transmitter, and (c) horizontal and vertical profiles of power distribution.

3.3 RF Amplitude and Phase Distribution Measurement

On the basis of the developed technique, RF amplitude and phase distributions can also be obtained. By measuring the amplitude and phase of the voltages induced on each individual resistor, we are able to calculate those of the electric field incident upon it. This has been quantitatively confirmed by simulation (Yagitani et al., 2013). However, it was revealed that edge reflection from a finite-sized absorber created a specific interference pattern on the amplitude and phase profiles on the absorber surface, thereby degrading the accuracy of the measurement. Though the interference pattern depended on the absorber size and frequency, generally the central area of the absorber had the highest measurement accuracy (less than 10% errors). Reduction in the edge reflection should be desired for practical use of this technique.

One application of amplitude and phase measurement is polarization identification. As explained in Section 3.2, the metamaterial absorber measures independently two orthogonal polarizations in the *x*- and *y*-directions. From the phase information in addition to the amplitude, linear, circular and elliptical polarizations are identified, including their major and minor axial directions as well as their sense of polarization, i.e., right- or left-handed (see also Section 4.2).

Another application is the direction finding and localization of RF sources. Ideally, when an incident RF wave is completely absorbed, each individual resistor (being as an amplitude and phase sensor) does not act as a scatterer so that no mutual coupling between the resistors is expected. Therefore the matrix of resistors on the absorber would work as an ideal antenna array. The present technique could be applied to obtaining the directions-of-arrival (DOAs) of the incoming RF signals from far sources, invoking various DOA estimation techniques such as MUSIC, ESPRIT, and others. The estimated source directions could even be visualized on a real image (Kwakkernaat et al., 2008). Source localization will be realized also for near-field sources. The near-field localization techniques such as radio holography (Kitayoshi and Sawaya, 1999), MUSIC (Kato et al., 2005) and SPM (Yoshimoto et al., 2005) could be used to obtain source locations and shapes, along with source visualization (Taira et al., 2004).

4 IN-SITU VISUALIZATION OF ELECTROMAGNETIC FIELDS

In general, an EM sensor measures an EM field and converts it to electric signals, which are then transferred to receivers, and processed and displayed on a PC when necessary. The authors have been working to develop the EM sensor having the capability of visualizing the measured field

immediately adjacent to the sensor itself, thereby one could intuitively figure out the in-situ field properties such as the intensity, vector direction and polarization. In this chapter new techniques under development based on this concept are described.

4.1 Electromagnetic Vector Compass

One example of such a system is an "Electromagnetic Vector Compass." The 3d vector direction of the in-situ EM field measured by an EM vector sensor is displayed on the surface of the sensor housing itself, as illustrated in Figure 11. Figure 12 shows a prototype of the vector compass for low-frequency AC magnetic field. A tri-axial search coil sensor is used to measure magnetic field vectors, which are processed by built-in receivers and displayed on an OLED screen attached on each of the six surfaces of the cubic housing. The screen on each surface plots an arrow representing the projection of the measured 3d vectors onto that surface. Just like an ordinary magnetic compass (for dc magnetic field), it displays in-situ EM vectors in real-time. With this kind of compact sensor one is able to observe the magnetic vectors in his/her hand, just at the point of measurement.

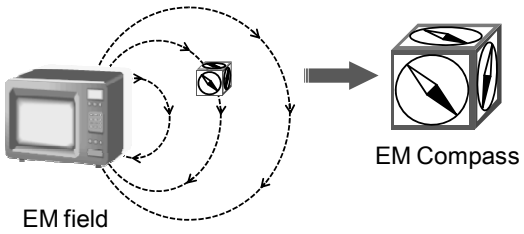

Figure 11: Electromagnetic vector compass.

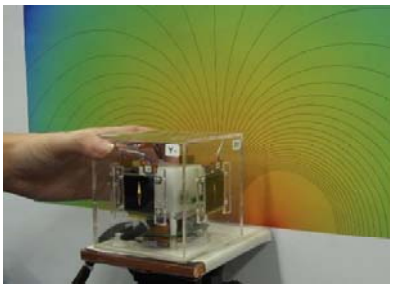

Figure 12: AC magnetic vector compass.

4.2 In-situ RF imaging Screen

In-situ visualization of RF fields is more difficult, since the sensor itself, cables, receivers and displays may reflect, scatter and disturb the field of interest. As explained in Chapter 3, we have developed a metamaterial absorber capable of measuring incident RF power, amplitude and phase distributions. If the absorber is made of transparent materials and a display screen is placed just behind it, we would be able to construct an "in-situ RF imaging screen" as illustrated in Figure 13. The 2d distribution of RF field absorbed on the surface is measured by embedded power (or amplitude and phase) detectors, which is transferred to the display and immediately visualized there. Thus the image of RF field is visualized in-situ, just as if a wall is illuminated by a flashlight.

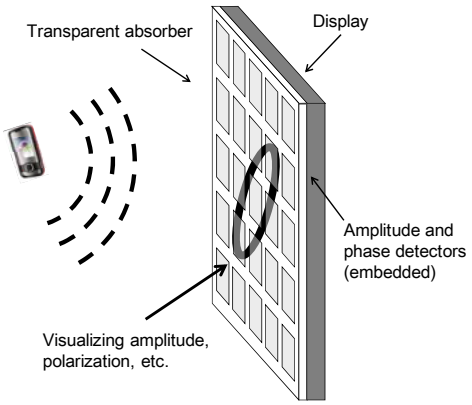

Figure 13: In-situ RF imaging screen.

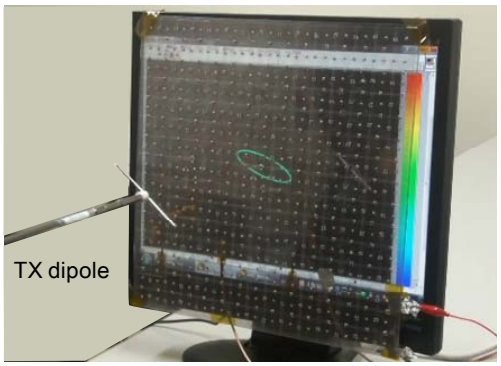

Figure 14: In-situ visualization of RF polarization.

A transparent absorber was fabricated, employing a transparent acrylic substrate and a transparent sheet of fine metal mesh. Transparent resistive films usually used to realize transparent absorbers (e.g., Haruta et al., 2000) were not adopted here because they have resistivity to absorb the RF field by themselves, whereas in the present absorber the RF power should be dissipated mainly in the lumped resistors. The size of the absorber was 30 cm square with 2-mm thickness. On the backside of the absorber amplitude and phase detectors were attached to measure two orthogonal polarizations.

Figure 14 shows a preliminary demonstration of in-situ visualization of polarization. A 1.7-GHz wave was transmitted from a dipole antenna and measured by the transparent absorber. The measured polarization at the center of the absorber was plotted on a PC display placed just behind the absorber. In this case the transmitted wave became an elliptically polarized, possibly due to the reflection from the table or cables.

5 CONCLUSIONS

Various in-situ measurement and visualization techniques and systems for EM fields were reported which have been developed by the authors' group. Using the developed systems, the EM fields can be captured and visualized in situ and in real-time. Such systems are expected to be quite useful for measuring EM field distributions in various scenarios in the fields of EMC, antennas and propagation. The systems could be applicable to quick noise measurement at the development stage of electric or electronic equipment, as well as to the in-situ measurement of EM field distributions in the actual environments such as offices, factories, cars, trains and airplanes. Last but not least, such visualization techniques could contribute to education in electromagnetics and radio engineering, where students will be able to virtually observe the actual EM fields in various situations.

ACKNOWLEDGEMENTS

The authors would like to thank (ex-) students of Kanazawa University: Messrs. Y. Yamanaka, T. Shimizu, S. Morita, K. Katsuda, E. Tanaka, R. Tanaka, M. Nojima, S. Shiraki, T. Nakagawa, T. Sunahara, D. Hiraki, K. Iwasaki, N. Fukuoka and H. Maeda for their help with design, fabrication and measurement of the EM and RF measurement and imaging systems.

REFERENCES

Baudry, D., Arcambal, C., Louis, A., Mazari, B., Eudeline, P., 2007. Applications of the near-field techniques in EMC investigations, *IEEE Trans. Electromagnetic Compatibility*, vol.49, no.3, pp.485-493.

Chen, H., Zhang, H., Ni, Z., Li, R., 2012. Research on imaging detection of RF leakage on the surface of spacecraft, *Proc. 2012 Int. Symp. EMC (EMC EUROPE)*, pp.1-4.

Dutta, S. K., Vlahacos, C. P., Steinhauer, D. E., Thanawalla, A. S., Feenstra, B. J., Wellstood, F. C., Anlage, S. M., Newman, H. S., 1999. Imaging microwave electric fields using a near-field scanning microwave microscope, *Applied Physics Letters*, vol.74, no.1, pp.156-158.

Fan, H., 2009. Far field radiated emission prediction from magnetic near field magnitude-only measurements of PCBs by Genetic Algorithm, *Proc. IEEE Int. Symp. EMC*, pp.321-324.

Gao, Q., Yin, Y., Yan, D.-B., Yuan, N.-C., 2005. A novel radar-absorbing-material based on EBG structure, *Microwave and Optical Technology Letters*, vol.47, no.3, pp.228-230.

Haelvoet, K., Criel, S., Dobbelaere, F., Martens, L., De Langhe, P., De Smedt, R., 1996. Near-field scanner for the accurate characterization of electromagnetic fields in the close vicinity of electronic devices and systems, *Proc. IEEE Instrumentation and Measurement Technology Conf.*, pp.1119-1123.

Haruta, M., Wada, K., Hashimoto, O., 2000. Wideband wave absorber at X frequency band using transparent resistive film, *Microwave and Optical Technology Letters*, vol.24, no.4, pp.223-226.

Kato, T., Taira, K., Sawaya, K., Sato, R., 2005. Estimation of short range multiple coherent source location by using MUSIC algorithm, *IEICE Trans. Commun.*, vol.E88-B, no.8, pp.3317-3320.

Kazama, S., Arai, K. I., 2002. Adjacent electric field and magnetic field distribution measurement system, *Proc. IEEE Int. Symp. EMC*, vol.1, pp.395–400.

Kitayoshi, H., Sawaya, K. 1999. Electromagnetic-wave visualization for EMI using a new holographic method, *Electronics and Communications in Japan, Part 1*, vol.82, no.8, pp.52-60.

Kwakkernaat, M. R. J. A. E., de Jong, Y. L. C., BuItitude, R. J. C., Herben, M. H. A. J., 2008. High-resolution angle-of-arrival measurements on physically-nonstationary mobile radio channels, *IEEE Trans. Antennas and Propagation*, vol.AP-56, no.8, pp. 2720-2729.

Laurin, J. J., Ouardhiri, Z., Colinas, J., 2001. Near-field imaging of radiated emission sources on printed-circuit boards, *Proc. IEEE Int. Symp. EMC*, vol.1, pp.368-373.

Luukkonen, O., Costa, F., Simovski, C. R., Monorchio, A., Tretyakov, S. A., 2009. A thin electromagnetic absorber for wide incidence angles and both polarizations, *IEEE Trans. Antennas and Propagation*, vol.57, no.10, pp.3119-3125.

Mias, C., Yap, J. H., 2007. A varactor-tunable high impedance surface with a resistive-lumped-element biasing grid, *IEEE Trans. Antennas and Propagation*, vol.55, no.7, pp.1955-1962.

Norgard, J., Musselman, R., 2004. CEM code validation using infrared thermograms, *Proc. 2004 Int. Symp. EMC*, pp.637-640.

Sasagawa, K., Kanno, A., Kawanishi, T., Tsuchiya, M., 2007. Live electrooptic imaging system based on ultraparallel photonic heterodyne for microwave near-fields, *IEEE Trans. Microwave Theory Tech.*, vol.55, no.12, pp.2782-2791.

Sato, K., Miyata, N., Kamimura, Y., Yamada, Y., 2010. A freehand scanning method for measuring EMF distributions using magnetic tracker, *IEICE Trans. Commun.*, vol.E93-B, no.7, pp.1865-1868.

Sato, K., Kawata, H., Kamimura, Y., 2012. A freehand scanning method for measuring EMF distributions, *IEICE Trans. Commun.*, vol.J95-B, No.2, pp.293-301. (in Japanese)

Shi, J., Cracraft, M. A., Zhang, J., DuBroff, R. E., Slattery, K., 2004. Using near-field scanning to predict radiated fields, *Proc. IEEE Int. Symp. EMC*, pp.14-18.

Taira, K., Kato, T., Sawaya, K., Sato, R., 2004. Estimation of source location of leakage field from transformer-type microwave oven, *Proc. 2004 Int. Symp. EMC*, vol.2, pp.489-493.

Tumanski, S., Liszka, A., 2002. The methods and devices for scanning of magnetic fields, *J. Magnetism and Magnetic Materials*, vol.242–245, pp.1253–1256.

Tumanski, S., Baranowski, S., 2006. Magnetic sensor array for investigations of magnetic field distribution, *J. Electrical Engineering*, vol.57, no.8/S, pp.185-188.

Yagitani, S., Okumura, E., Nagano, I., Yoshimura, Y., 2007. Localization of low-frequency source current distributions, *Proc. 2007 Int. Symp. Antennas and Propagation*, pp.89-92.

Yagitani, S., Katsuda, K., Nojima, M., Yoshimura, Y., Sugiura, H., 2011a. Imaging radio-frequency power distributions by an EBG absorber, *IEICE Trans. Commun.*, vol.E94-B, no.8, pp.2306-2315.

Yagitani, S., Katsuda, K., Tanaka, R., Nojima, M., Yoshimura, Y., Sugiura, H., 2011b. A tunable EBG absorber for radio-frequency power imaging, *Proc. 30th URSI GASS*, 4 pages.

Yagitani, S., Sunahara, T., Nakagawa, T., Hiraki, D., Yoshimura, Y., Sugiura, H., 2013. Radio-frequency field measurement using thin artificial magnetic conductor absorber, *Proc. 2013 Int. Symp. Electromagnetic Theory*, 4 pages.

Yamaguchi, M., Yabukami, S., Yurugi, H., Nakada, K., Arai, K. I., Itagaki, A., Itagaki, K., Saito, N., Fuda, K., Watanabe, M., Takahashi, H., Tamogami, T., Sakurada, Y., 1999. Two dimensional electromagnetic noise imaging system using planar shielded-loop coil array, *Proc. 1999 Int. Symp. EMC*, pp.51-54.

Yoshimoto, Y., Taira, K., Sawaya, K., Sato, R., 2005. Estimation of multiple coherent source locations by using SPM method combined with signal subspace fitting technique, *IEICE Trans. Commun.*, vol.E88-B, no.8, pp.3164-3169.

ANALYSIS OF ELECTROMAGNETIC FIELDS IN INHOMOGENEOUS MEDIA BY FOURIER SERIES EXPANSION METHODS－THE CASE OF A DIELECTRIC CONSTANT MIXED A POSITIVE AND NEGATIVE REGIONS

Tsuneki Yamasaki [1]
[1] Department of Electrical Engineering, College of Science and Technology, Nihon University
yamasaki@ele.cst.nihon-u.ac.jp

Keywords: Inhomogeneous and negative medium, Improved Fourier series expansion, Electromagnetic wave.

Abstract: In this paper, we propose a new method for the electromagnetic fields with inhomogeneous media mixed the positive and negative regions which is the combination of improved Fourier series expansion method using the extrapolation method. Numerical results are given for the power reflection and transmission coefficient, the energy absorption, the electromagnetic fields, and the power flow in the inhomogeneous medium mixed the positive and negative regions including the case when the permittivity profiles touches zero for the TM wave. The results of our method are in good agreement with exact solution which is obtained by MMA.

1 INTRODUCTION

Recently, the scattering and guiding problems of the inhomogeneous media have been of considerable interest, such as optical fiber gratings , photonic bandgap crystals , frequency selective devices, and a negative medium(Caloz et al.,2004). In the negative medium, such as a plasma (Freidberg et al.,1972) or a metallic grating(Yasuura et al.,1986), the permittivity has both positive and negative regions.

One of the methods that are commonly employed in solving the problems in an inhomogeneous medium is the homogeneous multilayer approximation method (HMA). Although the method is widely known and is proved to solve the electromagnetic fields in inhomogeneous media, it cannot be applied to the positive and negative regions with oblique angle of incidences in TM wave.

Yamaguchi and Hosono(Yamaguchi et al.,1982) pointed out this difficulty and applied the modified multilayer approximation method(MMA) to this problem. However MMA cannot be applied to the case when the permittivity profiles touches zero. In this case, HMA cannot also obtaine the electromagnetic fields even if the loss term of the permittivity tends to zero.

In this paper, we propose a new method for the electromagnetic fields with inhomogeneous media mixed the positive and negative regions which is the combination of improved Fourier series expansion method(Yamasaki et al.,1984) using the extrapolation method.

K.F.Casey(Casey ,1972) has presented a Fourier series expansion method to get the rigorous solution in inhomogeneous madia. However, they did not present any numerical results for the sinusoidally stratified plasma media whose permittivity had the only positive region(Casey et al.,1969).

Numerical results are given for the power reflection and transmission coefficient, the energy absorption, the electromagnetic fields, and the power flow in the inhomogeneous medium mixed the positive and negative regions including the case when the permittivity profiles touches zero for the TM wave. The results of our method are in good agreement with exact solution which is obtained by MMA.

2 METHOD OF ANALYSIS

We consider an inhomogeneous medium mixed the positive and negative regions as shown in Fig.1. The structure is uniform in the *y*-direction and the permittivity $\varepsilon_2(z)$ has zero at $z = z_1$ and $z = z_2$ (see Fig.1(b)) . The permeability is assumed to be μ_0 . The time dependence is exp(–*iωt*) and suppressed throughout.

In the formulation, the TM wave (the magnetic field has only the *y*-component) is discussed. When the TM wave is assumed to be incident from $z < 0$ at the angle θ_0, the magnetic fields in the regions $S_1(z \le 0)$ and $S_3(z \ge d)$ are expressed(Yamasaki et al.,1984) as

$\underline{S_1(z \le 0)}$:

$$H_y^{(1)} = e^{ik_1(x\sin\theta_0 + z\cos\theta_0)} + Re^{ik_1(x\sin\theta_0 - z\cos\theta_0)}, \qquad (1)$$

$$k_1 \triangleq \omega\sqrt{\varepsilon_1\mu_0} = k_0\sqrt{\varepsilon_1/\varepsilon_0},\ k_0 \triangleq 2\pi/\lambda,$$

$\underline{S_3(z \ge d)}$:

$$H_y^{(3)} = Te^{i\{k_1 x\sin\theta_0 + k_{3z}(z-d)\}}, \qquad (2)$$

$$k_{3x} \triangleq \sqrt{k_3^{\,2} - (k_1\sin\theta_0)^2}\ ,\ j = 1, 3$$

where λ is the wavelength in free space, R ,and T are the reflection and transmission coefficient to be determined by boundary conditions.

The inhomogeneous layer ($0 < z < d$) consists of periodically stratified layers which is the iteration of the permittivity $\varepsilon_d(z)[=\varepsilon_2(z)]$ in the original region ($0 < z < d$;see Fig.2)(Yamasaki et al.,1984). The modal component of magnetic field can be written as $H_y^{(2)} = H(z)e^{ik_1 x\sin\theta_0}$, and $H(z)$ must satisfy the following wave equation (Yamasaki et al.,1984)

$$\frac{d^2H(z)}{dz^2} - \frac{1}{\varepsilon_d(z)}\frac{d\varepsilon_d(z)}{dz}\frac{dH(z)}{dz} + \left[k_0^2\varepsilon_d(z)/\varepsilon_0 - (k_1\sin\theta_0)^2\right]H(z) = 0. \qquad (3)$$

In the lossless case in $\varepsilon_d(z)$, the singularity appears in the second term in Eq.(3).
Taking into account the Floquet's theorem, $H(z)$ can be approximated by the finite Fourier series as

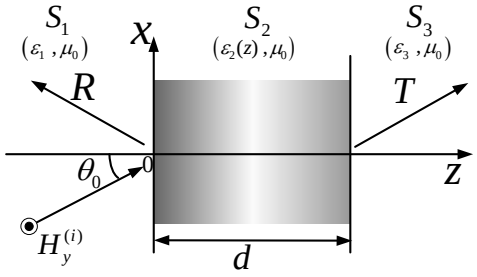

(a) Coodinate system

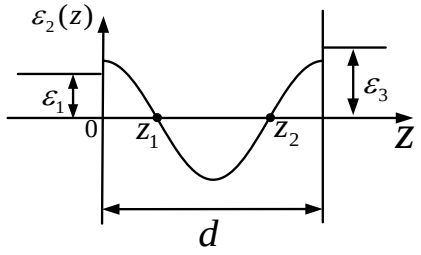

(b)Distribution of dielectric constant

Fig.1 Structure of the inhomogeneous medium mixed the positive and negative region.

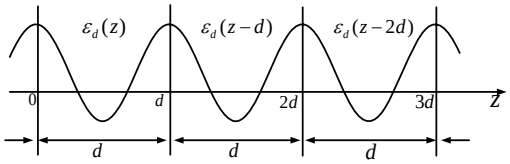

Fig 2. Periodically inhomogeneous layers

$$H(z) = e^{ihz}\sum_{n=-N}^{N} u_n e^{i2\pi nz/d} \qquad (4)$$

To the obtain the correct solution in the analysis of lossless case, $\varepsilon_d(z)$ is including the loss term σ (Yamasaki et al.,2004,2005(a),(b))

$$\tilde{\varepsilon}_d(z)/\varepsilon_0 \triangleq \varepsilon_d(z)/\varepsilon_0 + i\sigma\ (\sigma \ge 0). \qquad (5)$$

Substituting Eqs.(5) and (4) into Eq.(3), and multiplying both side by $\tilde{\varepsilon}_d(z)e^{-i2\pi mz/d}$,and rearranging after integrating with respect to z in the interval $0 < z < d$ .We get the following equation in regard to h (Yamasaki et al.,1984)

$$h^2\mathbf{MU} + h\mathbf{CU} + \mathbf{KU} = 0\ , \qquad (6)$$

where

$\mathbf{U}^{(l)} \triangleq \left[u_{-N}, \cdots, u_0, \cdots u_N\right]^T$, T : *transpose*

$\mathbf{M} \triangleq \left[\eta_{m,n}\right]$, $\mathbf{C} \triangleq \left[\zeta_{m,n}\right]$, $\mathbf{K} \triangleq \left[\gamma_{m,n}\right]$,

$\zeta_{n,m} \triangleq \dfrac{2\pi}{d}\{2n + (n-m)\}\eta_{n,m}\}$,

$$\gamma_{n,m} \triangleq [\left(\frac{2\pi}{d}\right)^2 (n^2 + n(n-m)) + (k_0 \sin\theta_0)^2]\eta_{n,m} - \xi_{n,m},$$

$$m,n = (-N,\cdots,0,\cdots,N), \quad (7)$$

$$\eta_{n,m} \triangleq \frac{1}{d}\int_0^d \{\tilde{\varepsilon}_d(z)/\varepsilon_0\} e^{i2\pi(n-m)z/p} dz,$$

$$\xi_{n,m} \triangleq \frac{k_0^2}{d}\int_0^d \{\tilde{\varepsilon}_d(z)/\varepsilon_0\}^2 e^{i2\pi(n-m)z/p} dz.$$

Letting $\mathbf{V} \triangleq h\mathbf{U}$ and modifying Eq.(6), it is reduced to the following conventional eigenvalue equation

$$\mathbf{AW} = h\mathbf{W}, \quad (8)$$

$$\mathbf{A} \triangleq \begin{bmatrix} \mathbf{0} & \mathbf{1} \\ -\mathbf{M}^{-1}\mathbf{K} & -\mathbf{M}^{-1}\mathbf{C} \end{bmatrix},$$

$$\mathbf{W} \triangleq \begin{bmatrix} \mathbf{U} \\ \mathbf{V} \end{bmatrix},$$

where **1** is unit vectore and $\mathbf{M}^{-1}$ is inverse matrix of **M.**

When it gets an eigenvalue $h_0 (= \beta + i\alpha \ ; \alpha \geq 0)$ obtained Eq.(8) for $N \to \infty$, $-h_0 (= -\beta - i\alpha)$ is the solution, and $(\pm h_0 \pm 2\pi n/d)$ are also solutions(Yamasaki et al.,1984). Therefore we selected h_0 by convergence characteristics of $(\pm h_0 \pm 2\pi n/d)$ in section of numerical analysis.

In the lossless case for $\sigma \to 0$, we can get the eigenvalue h_{EV} according to the following extrapolation equation ($a_0 \triangleq h_{\mathrm{EV}}$) in regard to the loss parameters $\sigma_j (j = 1 \sim 3)$ (Yamasaki et al.,2004,2005(a),(b))

$$h_0(\sigma_j) = a_0 + a_1 \cdot \sigma_j + a_3 \cdot (\sigma_j)^2 \ ; j = 1 \sim 3. \quad (9)$$

In the same manner, the eigenvectors $u_n^{(\mathrm{EV})}$ are also obtained by the following extrapolation equation ($b_0 \triangleq u_n^{(\mathrm{EV})}$) in regard to the loss parameters $\sigma_j (j = 1 \sim 3)$ (Yamasaki et al.,2004,2005(a),(b))

$$u_n^{(EV)}(\sigma_j) = b_0 + b_1 \cdot \sigma_j + b_3 \cdot (\sigma_j)^2 \ ; j = 1 \sim 3 \quad (10)$$

$S_2 (0 < z < d)$:

Using h_{EV} and $-h_{EV}$, and the corresponding eigenvectors $u_n^{(\mathrm{EV})}$ and $u_n^{(\text{-EV})}$, the electromagnetic fields in the inhomogeneous layer $(0 < z < d)$ are expanded by a finite Fourier series(Yamasaki et al., 2004, 2005(a),(b))

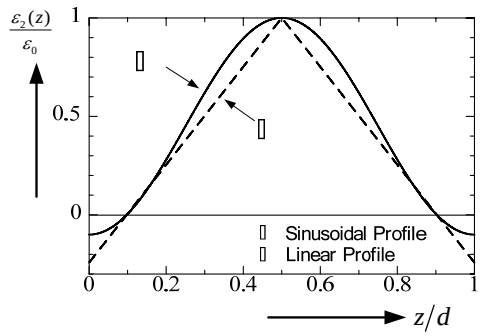

Fig.3 A profile of ① Eq.(15) and ② Eq.(16)

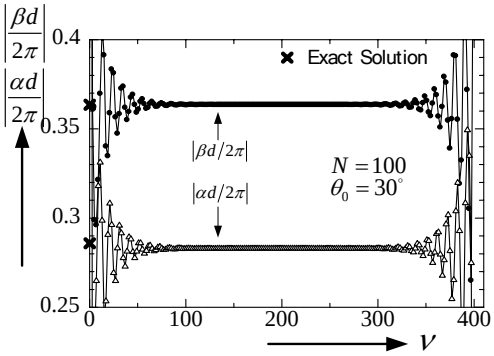

(a)Sinusoidal Profile case

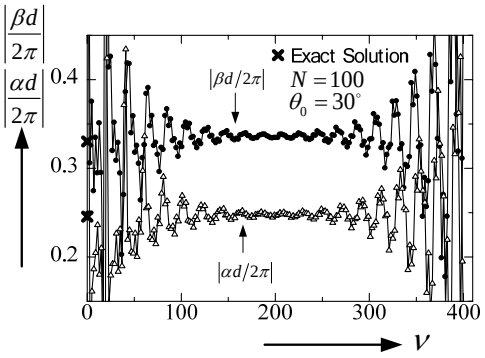

(b)Linear Profile case

Fig.4 $|\beta d/2\pi| and |\alpha d/2\pi|$ *vs.* ν

$$H_y^{(2)} = e^{ik_1 \sin\theta_0 x}[t_\nu^{(2)} e^{ih_{EV}z} f_{EV}(z) + r_\nu^{(2)} e^{-ih_{(-EV)}z} f_{(-EN)}(z)], \quad (11)$$

$$f_{EV}(z) \triangleq \sum_{n=-N}^{N} u_n^{(EV)} e^{i\frac{2\pi n}{d}z},$$

$$f_{(-EV)}(z) \triangleq \sum_{n=-N}^{N} u_n^{(-EV)} e^{i\frac{2\pi n}{d}z},$$

$$E_x^{(2)} = \{-i\omega\varepsilon(z)\}^{-1} \partial H_y^{(2)} / \partial z, \quad (12)$$

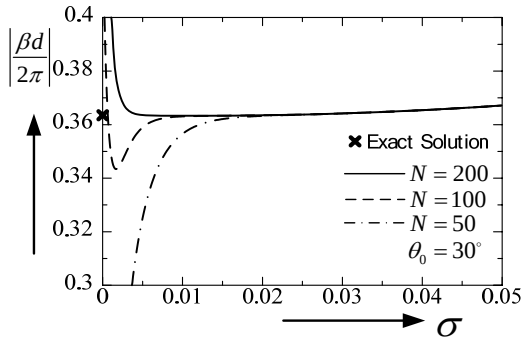

(a) $\left|\beta d/2\pi\right|$

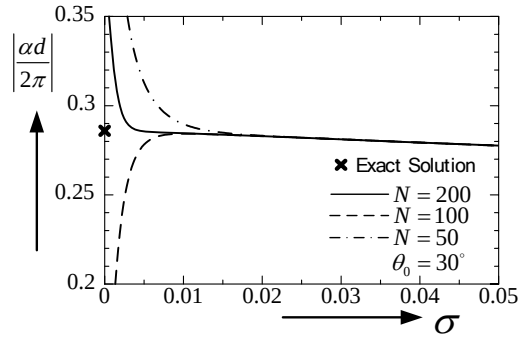

(b) $\left|\alpha d/2\pi\right|$

Fig.5 $\left|\beta d/2\pi\right| and \left|\alpha d/2\pi\right|$ *vs.* σ.

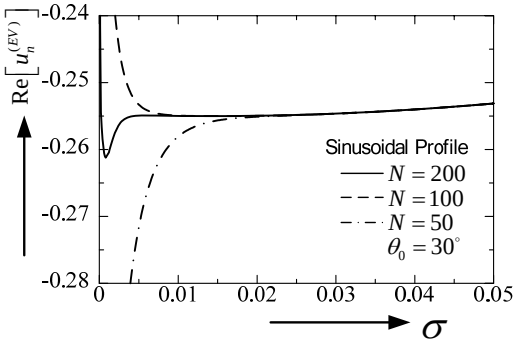

(a) $\mathrm{Re}\left[u_n^{(EV)}\right]$

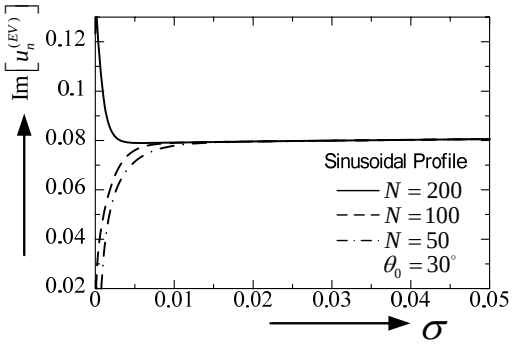

(b) $\mathrm{Im}\left[u_n^{(EV)}\right]$

Fig.6 $\mathrm{Re}\left[u_n^{(EV)}\right] and \mathrm{Im}\left[u_n^{(EV)}\right]$ *vs.* σ

where, $t_v^{(2)}$ and $r_v^{(2)}$ are unknown coefficients which satisfy the boundary conditions.
Using the boundary conditions and $T(=T_{EV})$ can be obtained by (the following equation):

$$R_{EV}(N) = T_{EV}(N) - 1,$$

$$T_{EV}(N) = 2[f_{EV}(d)D - f_{(-EV)}(d)C]/(AD - CD), \tag{13}$$

where,

$$A \triangleq f_{EV}(0) + \frac{\varepsilon_1 F_1}{\varepsilon_d(0) k_1 \cos\theta_0},$$

$$B \triangleq f_{(-EV)}(0) + \frac{\varepsilon_1 F_2}{\varepsilon_d(0) k_1 \cos\theta_0},$$

$$C \triangleq f_{EV}(d) - \frac{\varepsilon_3 F_1}{\varepsilon_d(d) k_{3x}} e^{ih_{EV}d}, \tag{14}$$

$$D \triangleq f_{(-EV)}(d) - \frac{\varepsilon_3 F_2}{\varepsilon_d(d) k_{3x}} e^{-ih_{EV}d}$$

$$F_1 \triangleq \sum_{n=-N}^{N} \left(\frac{2\pi n}{d} + h_{EV}\right) u_n^{(EV)},$$

$$F_2 \triangleq \sum_{n=-N}^{N} \left(\frac{2\pi n}{d} - h_{EV}\right) u_n^{(-EV)}.$$

3 NUMERICAL ANALYSIS

We consider the following two profiles(see Fig.3):
(1)Sinusoidal profile:

$$\varepsilon_2(z)/\varepsilon_0 = \varepsilon_A\{1 - \delta\cos(2\pi z/d)\} \tag{15}$$

(2)Linear profile:

$$\frac{\varepsilon_2(z)}{\varepsilon_0} = \begin{cases} \varepsilon_2(\min) + [\varepsilon_2(\max) - \varepsilon_2(\min)]\frac{2}{d}z : 0 < z \le \frac{d}{2} \\ \varepsilon_2(\min) + [\varepsilon_2(\max) - \varepsilon_2(\min)]\frac{2}{d}(z-d) : \frac{d}{2} \le z < 1 \end{cases} \tag{16}$$

where,

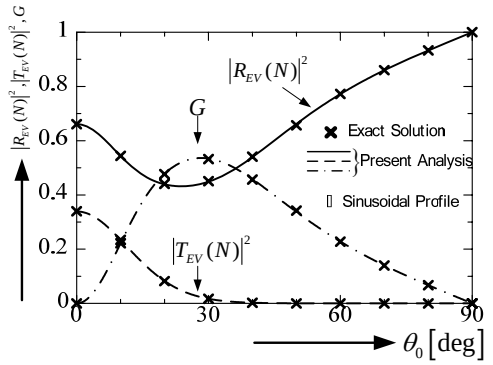

(a) Sinusoidal Profile case

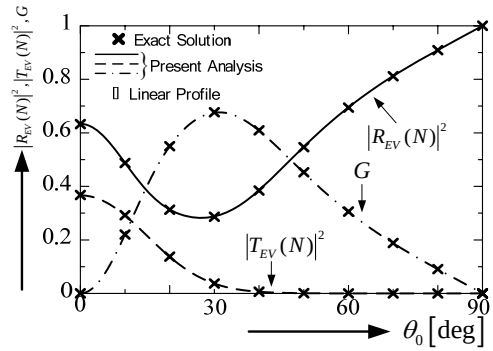

(b) Linear Profile case

Fig.7 $|R_{EV}(N)|^2$ *and* $|T_{EV}(N)|^2$ *and* G^2 *vs.* θ_0

$$\varepsilon_A \triangleq \frac{[\varepsilon_2(\max)+\varepsilon_2(\min)]}{2},$$
$$\delta \triangleq \frac{[\varepsilon_2(\max)-\varepsilon_2(\min)]}{[\varepsilon_2(\max)+\varepsilon_2(\min)]},$$

It has two zero points at $z_1/d \cong 0.0975$ and $z_2/d \cong 0.9025$ for both profiles. The values of parameters chosen are $\varepsilon_1 = \varepsilon_3 = \varepsilon_0$, $\varepsilon_2(\max) = 1$ and $\sqrt{A}\lambda/d = 0.8$. $\varepsilon_2(\min) = -0.1$ is the sinusoidal case and $\varepsilon_2(\min) \cong -0.242236$ is the linear case.

Figures 4(a) and 4(b) show the convergence of complex propagation constants $|\beta d/(2\pi)|$ and $|\alpha d/(2\pi)|$ to normalize $h_{\mathrm{EV}}(=\beta+i\alpha)$ with $N=100$, $\sigma=0.01$, and $\theta_0 = 30^0$ for the mode number $\nu = 1 \sim 2(2N+1)$. In these Figures, cross points (×) are the exactsolution which is obtained by the following characteristic equation in regard to h (Hosono ,1973)

$$\cos(hd) = (A_S + D_S)/2, \qquad (17)$$

where, A_S and D_S are the following Matrix

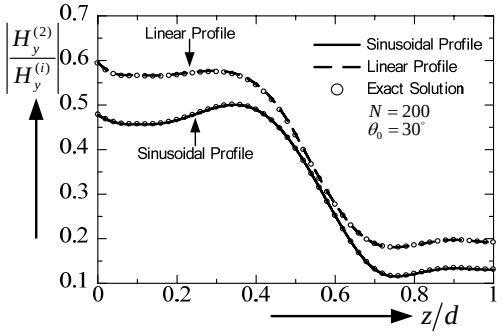

(a) $\left|H_y^{(2)}/H_y^{(i)}\right|$

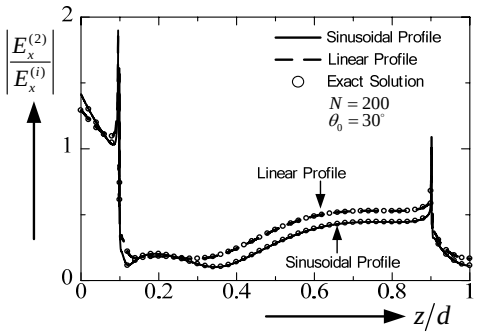

(b) $\left|E_x^{(2)}/E_x^{(i)}\right|$

Fig.8 $\left|H_y^{(2)}/H_y^{(i)}\right|$ *and* $\left|E_x^{(2)}/E_x^{(i)}\right|$ *vs.* z/d

elements can be written using the Floquet's theorem

$$\begin{bmatrix} H_y^{(2)} \\ E_x^{(2)} \end{bmatrix}_{z=0} = \begin{bmatrix} A_S & B_S \\ C_S & D_S \end{bmatrix} \begin{bmatrix} H_y^{(2)} \\ E_x^{(2)} \end{bmatrix}_{z=d} = e^{\mp jhd} \begin{bmatrix} H_y^{(2)} \\ E_x^{(2)} \end{bmatrix}_{z=d} \qquad (18)$$

In Eq.(18),the magnetic fields $H_y^{(2)}$ are expanded by a finite power series(Budden ,1961) which are approximated by the linear profile including $\varepsilon_2(z) = 0$ as follows(Yamaguchi et al., 1982, Budden ,1961):

$$H_y^{(2)} \triangleq e^{ik_1 \sin\theta_0 x}\left[t_\nu^{(2)} w_1(Z) + r_\nu^{(2)} w_2(Z)\right], \qquad (19)$$

where

$$Z \triangleq \left(\frac{k_0^2}{\varepsilon_0 d\,\varepsilon_2(z)/dz}\right)^{2/3} \cdot \varepsilon_2(z),$$

$$w_1(Z) = \sum_{n=0}^{M} a_n Z^n;\ a_0 = 1,\ a_1 = 0,\ a_n = \frac{cb_{n-2} - b_{n-3}}{n(n+2)};$$

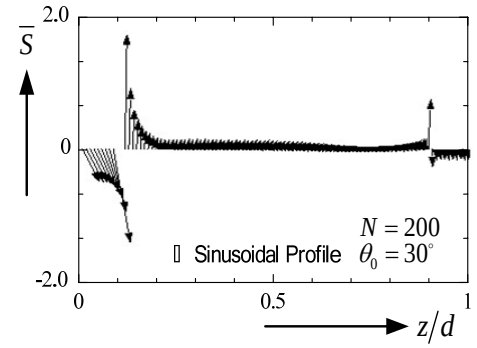

(a) Poynting Vector $\overline{S}$

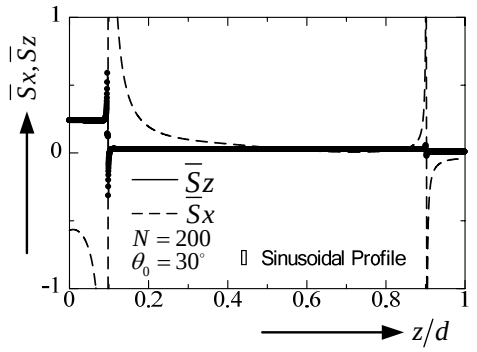

(b) Poynting Vector $\overline{S}x, \overline{S}z$

Fig .9 Poynting Vector of Sinusoidal Profile

$$w_2(Z) = (\frac{c}{2}\log Z)w_1(Z) + \sum_{n=0}^{M} b_n Z^n \ ;\ b_0 = 1\ , b_1 = 0\ , b_2 = 0,$$

$$b_n = \frac{cb_{n-2} - b_{n-3} - c(n-1)}{n(n-2)};\ c = k_0^2 \sin^2\theta_0 / \left(k_0^2 d\varepsilon_2(z)/dz\right)^{\frac{2}{3}}.$$

From Figure 4, the modal number chosen is $\nu = 2N+1$ (=201) gives good convergence in comparison with the exact solution which is obtained for $M = 1000$ in Eq.21. The values of exact solution are $|\beta d/(2\pi)| \cong 0.3635$ and $|\alpha d/(2\pi)| \cong 0.2859$ for the sinusoidal profile, and $|\beta d/(2\pi)| \cong 0.3303$ and $|\alpha d/(2\pi)| \cong 0.2454$ for the linear profile. The convergence tendency of the sinusoidal profile is faster than that of the linear profile. Figures 5(a) and 5(b) show the $|\beta d/(2\pi)|$ and $|\alpha d/(2\pi)|$ for various values of loss term σ at the modal number $\nu(=2N+1)$ in the sinusoidal profile. The results of the present method seem to be difficult when σ tends to zero for increasing modal truncation number N, but the true value can be obtained by extrapolation method.

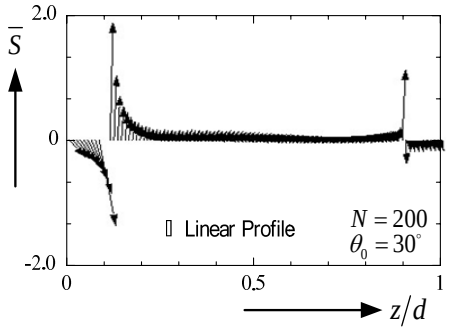

(a) Poynting Vector $\overline{S}$

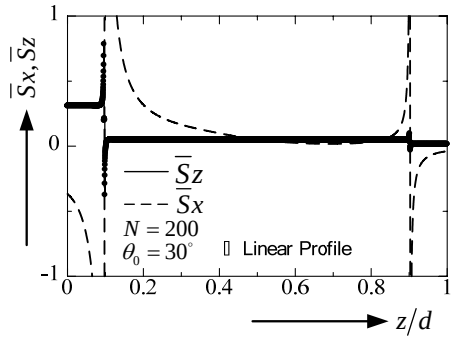

(b) Poynting Vector $\overline{S}x, \overline{S}z$

Fig.10 Poynting Vector of Linear Profile

Figures 6(a) and 6(b) show the eigenvectors $u_n^{(\mathrm{EV})}$ ($\mathrm{Re}\left[u_n^{(EV)}\right]$ and $\mathrm{Im}\left[u_n^{(EV)}\right]$) for various values of loss term σ at the same conditions as in Fig.5 for the sinusoidal profile. From Figure 6, the true value of the eigenvectors $u_n^{(\mathrm{EV})}$ can be obtained by the extrapolation method for $N \geq 200$. On the other hand, the case of linear profile, the convergence tendency is slower than that of sinusoidal profile. But the extrapolation method is also effective for $N \geq 200$

Figures 7(a) and 7(b) show the power reflection coefficient $|R_{EV}(N)|^2$ the power transmission coefficient $|T_{EV}(N)|^2$, and the power loss of energy difference $G[\triangleq 1 - |R_{EV}(N)|^2 - |T_{EV}(N)|^2]$ for various values of incident angle θ_0 using the extrapolation method to select the loss term at $\sigma_1 = 0.01$, $\sigma_2 = 0.02$,and $\sigma_3 = 0.03$ .The results of the present method are in good agreement with those of exact solutions. The relative error to the exact

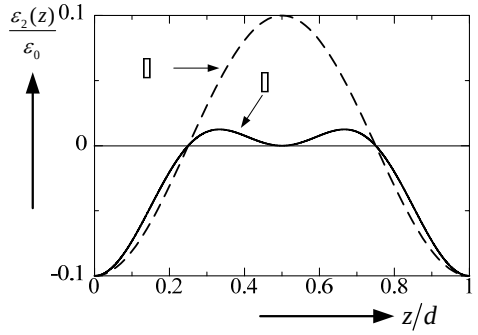

Fig.11 A profile of ① Eq.(16) and ②Eq.(22)

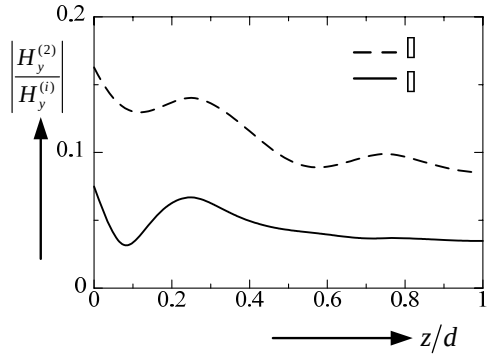

(a) $\left|H_y^{(2)}/H_y^{(i)}\right|$

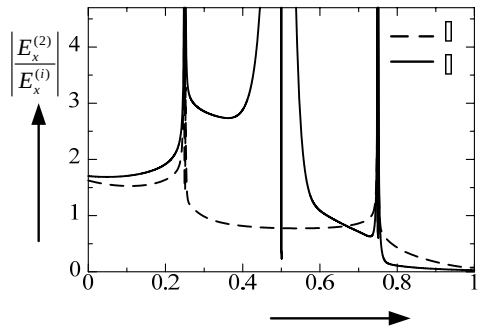

(b) $\left|E_x^{(2)}/E_x^{(i)}\right|$

Fig.12 $\left|H_y^{(2)}/H_y^{(i)}\right|$ and $\left|E_x^{(2)}/E_x^{(i)}\right|$ *vs.* z/d

solutions is about 0.02% for the sinusoidal profile and 0.2% for the linear profile when the modal truncation number chosen is $N = 200$. From Figure 7, the energy absorption G is nonzero even if the medium is lossless case.

Figures 8(a) and 8(b) show the normalized magnetic fields $|H_y^{(2)}/H_y^{(i)}|$ and the normalized electric fields $|E_x^{(2)}/E_x^{(i)}|$ for various values of z/d at $\theta_0 = 30^\circ$ for $N = 200$ using the extrapolation method in Fig.5 and Fig.6. From Fig.8, the results of the present method are in good agreement with those of exact solutions. In the sinusoidal case, $|H_y^{(2)}/H_y^{(i)}|$ is about constant rather than that of the linear case in $0 \le z/d < 0.4$. This is attributed to the effect of the profile and the angle of incidence θ_0.

On the other hand, the characteristic tendency of $|E_x^{(2)}/E_x^{(i)}|$ is about same in both profiles, and the effects of singularities are clearly seen at $z_1/d \cong 0.0975$ and 0.9025, but it has the limited value at this point because of $\partial H_y^{(2)}(z_1 \text{ or } z_2)/\partial z = 0$,

$$f_E(z) \triangleq \left|E_x^{(2)} / E_x^{(i)}\right| = \lim_{z \to z_1, z_2} \left| \frac{\partial H_y^{(2)}(z)/\partial z}{d\varepsilon_2(z)/dz} \right|. \tag{20}$$

In the Fig.8(b), the limiting values are $f_E(z_1) \cong 0.6096$ and $f_E(z_2) \cong 0.4152$.

Figures 9 and 10 show the Poynting vectors of $\overline{S}$, $\overline{S}_x$, and $\overline{S}_z$ for various values of z/d in the inhomogeneous region with the same parameters as in Fig.8 for both profiles. The definition of Poynting vector is as follows:

$$\overline{S} = \overline{S}_x \mathbf{i} + \overline{S}_z \mathbf{j},$$
$$\overline{S}_x \triangleq -\mathrm{Re}\left[E_z \times H_y^*\right]/2, \tag{21}$$
$$\overline{S}_z \triangleq \mathrm{Re}\left[E_x \times H_y^*\right]/2.$$

where, $\mathbf{i}$ and $\mathbf{j}$ are unit vectors in the direction of x axis and z axis, respectively.

From Figs.9 and 10, we see the following features:

(1)The effect of a positive and negative medium are more significant at $z_1/d \cong 0.0975$ and $z_2/d \cong 0.9025$, so that the direction reverses to the power flow $\overline{S}$ at that points.

(2) In the sinusoidal case, $\overline{S}_z$ has the limited values at points of zeros $z_1/d \cong 0.0975$ and $z_2/d \cong 0.9025$, so that $\overline{S}_z(z_1) \cong 0.1300$ and $\overline{S}_z(z_2) \cong 0.0166$, respectively.

On the other hand, $\overline{S}_z(z_1) \cong 0.21245$ and $\overline{S}_z(z_2) \cong 0.03396$ at those points for the linear case. The energy of these points are absorbed.

(3) $\overline{S}_x$ becomes infinite and the sign is reversed at the singularities $z_1/d \cong 0.0975$ and $z_2/d \cong 0.9025$.

In the investigation of above results, our methods can be applied to the positive and negative medium and have good accuracy of the electromagnetic fields.

So, next we consider the distribution of permittivity $\varepsilon_2(z)$ touches $\varepsilon_2(z)=0$. This problem is difficult to analyze by the MMA.

We consider the following sinusoidal profile② (see Fig.(11))

$$\varepsilon_2(z)/\varepsilon_0 = \varepsilon_A\{0.5-\delta\cos(2\pi z/d) + 0.5\cos(4\pi z/d)\}. \quad (22)$$

It has three zero points at $z_1/d=0.25$, $z_2/d=0.5$,and $z_3/d=0.75$. The definition of ε_A and δ are the same in Eq.(16). The values of parameters chosen are $\varepsilon_1=\varepsilon_3=\varepsilon_0$, $\varepsilon_2(\max)=0.1$ (profile ①), $\varepsilon_2(\max)=0$ (profile ②) , $\varepsilon_2(\min)=-0.1$ and $\sqrt{A}\lambda/d=0.8$.

Figures 12(a) and 12(b) show the normalized magnetic fields $|H_y^{(2)}/H_y^{(i)}|$ and the normalized electric fields $|E_x^{(2)}/E_x^{(i)}|$ for various values of z/d at $\theta_0=30^0$ comparison with the profile ① in Eq.(16) for $N=200$ using the extrapolation method .

From in Fig.(12), we see the following features:

(1)For the $|H_y^{(2)}/H_y^{(i)}|$, the influence of distribution of profiles ① and ② appears over $z/d=0.5$,

(2)The effect of the distribution of permittivity $\varepsilon_2(z)$ which touches $\varepsilon_2(z)=0$ is more significant of the electric fields $|E_x^{(2)}/E_x^{(i)}|$ at $z_2/d=0.5$, and the limiting values are $f_E(z_1)\cong 3.2904$, $f_E(z_2)\cong 0.35798$ and $f_E(z_3)\cong 0.65633$ for the profile ②. In the case of ①,there are

$f_E(z_1)\cong 1.1417$ and $f_E(z_3)\cong 0.77027$.

Finally, we investigate the complex propagation constants in the periodically inhomogeneous layers

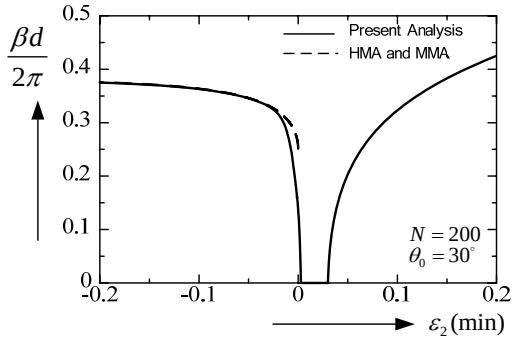

(a) $\beta d/2\pi$

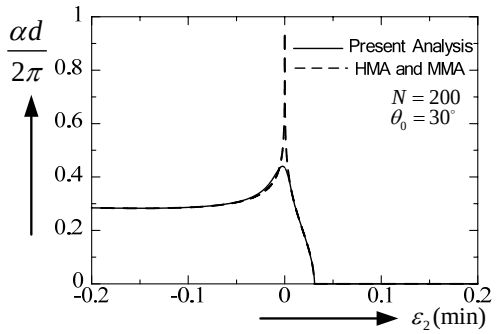

(b) $\alpha d/2\pi$

Fig.13 $\beta d/2\pi$ and $\alpha d/2\pi$ *vs.* $\varepsilon_2(\min)$

changing $\varepsilon_2(\min)/\varepsilon_0$ in the case of fixed $\varepsilon_2(\max)/\varepsilon_0=1.0$ in Eq.(16).

Figures 13(a) and 13(b) show the $\beta d/(2\pi)$ and $\alpha d/(2\pi)$ for various values of $\varepsilon_2(\min)=-0.1\sim 0.1$ at $\theta_0=30^0$ for $N=200$ using the extrapolation method.

In this figure, the dashed line (---) are the results of MMA ($\varepsilon_2(\min)<0$) and HMA ($\varepsilon_2(\min)>0$). Both methods cannot be applied to the $\varepsilon_2(\min)=0$. From in Fig.13, the results of MMA and HMA are not accurate at $\varepsilon_2(\min)=0$,because the normalized attenuation constant $\alpha d/(2\pi)$ in this case appears $\varepsilon_2(\min)/\varepsilon_0 \le 0.0295$.

4 CONCLUSIONS

In this paper, The Fourier series expansion method is applied to the electromagnetic fields with inhomogeneous media mixed the positive and negative regions using the extrapolation method

which obtaines the correct value of the eigenvalue and eigenvectors for the case of TM wave.

Numerical results are given for the power reflection and transmission coefficient, the energy absorption, the electromagnetic fields, and the power flow in the inhomogeneous medium mixed the positive and negative regions including the case of the permittivity profiles touches zero for the case of the TM wave. The results of our method are in good agreement with exact solution which is obtained by MMA.

REFERENCES

Budden K.C., 1961, *Radio Waves in the Ionoshere*, Cambridge Univ., Press, pp.343-347.

Caloz C. , Itoh T.,2004, *Microwave Application of Metamaterial Structures*, IEICE Technical Report. Vol.104, No202, pp135-138.

Casey K.F., Matthes J.R. and Yeh C. ,1969, *Wave Propagation in Sinusoidally Stratified Plasma Media*, J.Math.Phys., Vol.10, no5, pp.891-896.

Casey K.F.,1972, *Application of Hill's Function to problem of propagation in Stratified Media*, IEEE Tran.Antenas Propagt. ,vol.AP-20, 3, p.369-374.

Freidberg J.P., Mitchell R.W., Morse R.L. , *Rudsinski L.I.,1972,Resonant Absorption of Laser Light by Plasma Targets*, Phys. Rev. Lett.,Vol.28,no13.,pp.795-799.

Hosono T.,1973, *Fundation of Electromagnetic Wave Engineering*, p.247, Shioko Publ. Co.(in Japanese) .

Yamaguchi S., Hosono T.,1982, *Some Diffculties in Homogeneous Multilayer Apporoximation Method and Their Remedy*, IEICE Trans.,Vol.J64-B, no10, pp.1115-1122 (in Japanese 1981) [translated Scripta Technica, INC., Vol.65-B, No.5 pp.75-83.

Yamasaki,T ,Hinata T.,Hosono H., 1984, *Analysis of Electrogagnetic Field in inhomogeneous Media by Foirier Series Expansion Methods*, IEICE Trans. Vol.J66-B, no10., pp.1239-1246(in Japanese 1983) [translated Scripta Technica, INC., Vol.67-B, No.6, pp.61-71.

Yamasaki t.,Isono K.,Hinata T., 2004, *Analaysis of Electromagnetic Field in Inhomogeneous media by Fourier Series Expansion Method -The case of a dielectric constant mixed in positive/negative medium* , Part I ,IEE Technical Reports Japan, EMT-04-121, pp.31-36(in Japanese) .

Yamasaki t.,Isono K.,Hinata T., 2005(a), *Analaysis of Electromagnetic Field in Inhomogeneous media by Fourier Series Expansion Method -The case of a dielectric constant mixed in positive/negative medium*, Part II, IEE Technical Reports Japan, EMT-05-7, pp.35-40 (in Japanese) .

Yamasaki T., Isono K., Hinata T., 2005(b), *Analaysis of Electromagnetic Fields in Inhomogeneous media by Fourier Series Expansion Method -The case of a dielectric constant mixed a positive and negative regions*, IEICE Trans. on Electronics, Vol.E88-C, No.12, pp.2216-2222.

Yasuura K., Murayama M., 1986, *Numerical Analysis of Diffraction from a Sinusoidal Metal Grating*, IEICE Trans.,Vol.J69-B, no2, pp.198-205 (in Japanese).

DEVELOPMENT OF MICROWAVE BROADBAND FULL-MIMO CHANNEL SOUNDER

For the Super High Bit-Rate Mobile Communication Systems

Jun-ichi Takada, Minseok Kim, Yuyuan Chang, Yohei Konishi
Graduate School of Science and Engineering, Tokyo Institute of Technology,
Box S6-4, 2-12-1 O-okayama, Meguro-ku, Tokyo 152-8550, Japan
takada@ide.titech.ac.jp, mskim@ide.titech.ac.jp, chang@ap.ide.titech.ac.jp, konishi@ap.ide.titech.ac.jp

Keywords: Full MIMO channel sounder, microwave mobile communication

Abstract: The paper summarizes four year activities and outcomes of development of full MIMO 24x24 channel sounder operating at 11 GHz with the bandwidth of 400 MHz, for the development of microwave frequency for the super high bit-rate mobile communications. The back ground motivation, design criteria, technical challenges and significant results are presented. Since the development of the channel sounder was the project goal, the detailed analyses of the double directional channels are left for future study.

1 INTRODUCTION

The rapid growth of the mobile data traffic demands the super high bit-rate systems in near future, i.e. more than 10 Gb/s/base station (BS). To realize such a high bit-rate transmission, the bandwidth well exceeding 100 MHz is required. Suzuki, Suyama and Fukawa (2010) estimated that 24x24 MIMO transmission with 400 MHz bandwidth can achieve 30 Gb/s/BS by deploying 64QAM and coding rate of 3/4 with overhead efficiency of 70%. Such wide bandwidth is not at all available below 6 GHz, which is believed to be the upper frequency limit for the mobile or personal wireless access. Therefore, the development of higher microwave frequency for the mobile communications is crucial. Such high frequency has been avoided for the mobile communications, because of the strong shadowing and large path loss. However, hybrid spectrum techniques such as carrier aggregation or separation of control and traffic channels have been recognized as promising techniques to resolve the problem. Low frequency narrowband channel is used to keep the link for control and base traffic, while high frequency wideband channel is opportunistically used for high bit-rate traffic.

NTT Docomo, Tohoku University and Tokyo Institute of Technology conducted the research project on super high-bit rate mobile communication systems for 4 years from 2009 until 2013 targetting 30 Gb/s/BS transmission. 11 GHz has been identified due to the availability of the spectrum for the test license with the bandwidth of 400 MHz. In collaboration with the transmission technology team, the authors have developed 24x24 channel sounder with full MIMO software radio architecture.

The paper summarizes the design criteria, technical challenges, and the outcomes in the development of MIMO channel sounder.

2 DESIGN CRITERIA AND TECHNICAL CHALLENGES

Full MIMO architecture is chosen for sharing the limited hardware resources for channel sounding and transmission test. The typical MIMO channel sounders are implemented with SISO RF chain with antenna multiplexers (e.g. MEDAV, n.a.). They have the advantages of the cost and simplicity of calibration. However, full MIMO architecture has an obvious advantage of the flexibility of multilink measurement by introducing the modular architecture. In contrast, simple combination of MIMO channel sounders is not so straightforward for the practical measurements (Kolmonen et al., 2010).

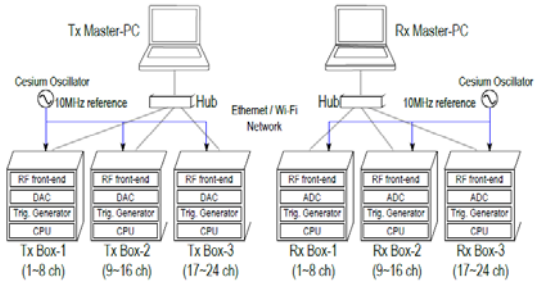

Figure 1: Scalable full MIMO channel sounder architecture.

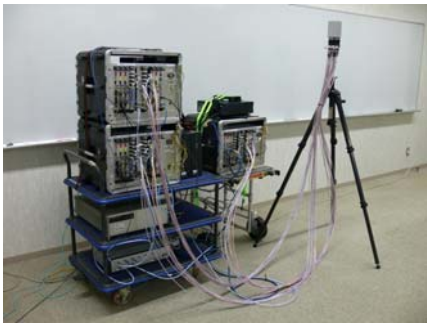

(a) Receiver

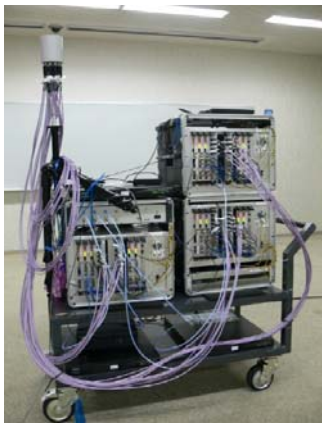

(b) Transmitter

Figure 2: MIMO channel sounder.

2.1 Synchronization

In the developed channel sounder, one transmitter or receiver module consists of 8 RF channels, and three modules can be integrated for directional measurement, or be separated for multilink MIMO measurement. They are synchronized by the common or separated atomic oscillators. It is noted that the absolute synchronization of frequency and phase between transmitters and receivers is a specific requirement for channel sounder, although the hardware architectures are common for sounding and transmission. It is found that rubidium oscillators, which are commonly used as 10 MHz references for synchronization between transmitter and receiver, can not be stable enough when up-converted to 11 GHz. Therefore, the cesium oscillators are used instead. In addition to the frequency synchronization, the clock phase synchronization is necessary. The mechanism is implemented to adjust the clock phases of transmitter and receiver during back-to-back calibration between transmitter and t receiver.

2.2 Signal Format

Due to the simultaneous transmission, multiplexing technology is needed. Although any kind of orthogonal signals can be used for multiplexing, the authors chose unmodulated multitone signals and hybrid FDM-STDM technique suitable for scalable modular structure (Kim, Takada and Konishi, 2012).

Newman phase multitone (Boyd, 1986), which is almost equivalent to chirp signal, has been used as the wideband signal. Multitone signal has the advantage of efficient spectrum usage for high delay resolution. 4 channels are multiplexed in frequency domain (FDM) (Sakaguchi, Takada and Araki, 2002), i.e. 1 module consists of 2 units. 6 units, each of which consists of these 4 channels, are then weighed with orthonormal vectors sequentially to change the spatial pattern of the channel response (STDM). STDM has the obvious advantage over conventional TDM, since all the transmitter ports always transmit the signals to maximize the transmission power by using relatively low power transmitters.

2.3 Antennas

Three types of array antennas are developed.

Directional measurement antenna is a uniform circular array of 12-element dual polarization antennas with 0.44 wavelength spacing. For the high resolution parameter estimation, spherical complex pattern has been measured discretely within the limited range of the scanning, and the continuous patterns for whole sphere are analytically reconstructed by using the spherical wave functions (Miao and Takada, 2013).

Two MIMO capacity measurement antennas are both uniform linear arrays of 12-element dual polarization antennas. Two different types of the antenna elements are used, i.e. omnidirectional and 60 deg sector patterns in horizontal direction.

Antenna spacing can be flexibly controlled, but should be more than one wavelength due to the large size of the horizontal polarization antenna elements.

2.4 Calibration Procedure

To calibrate the whole MIMO system, the following complicated calibration process is needed whenever the units are turned on (Chang, Konishi, Kim and Takada, 2012):

1. Baseband calibration to match all the channels of DACs and ADCs (Pham, Kim and Takada, 2012)
   Following calibration processes are manually conducted by adjusting on-board variable registers of delay chips, as the calibration parameters do not change for long time.
   (a) Phase and DC offsets of DACs are calibrated by connecting DAC to oscilloscope.
   (b) Phase and DC offsets of ADCs are calibrated by connecting ADC to DAC.
2. RF calibration to compensate IQ imbalance and to suppress carrier leakage (Kim, Konishi, Takada and Gao, 2012, Kim, Maruichi and Takada, 2013)
   As PLL synthesizers are reset whenever the power is turned on, the automatic calibration program has been developed.
   (a) Transmitter IQ imbalance and carrier leakage are compensated by digital predistortion.
   (b) They are calibrated by connecting DAC to Tx input and spectrum analyzer to Tx output. IQ imbalance is calibrated first, and carrier leakage next.
   (c) Receiver IQ imbalance and carrier leakage are calibrated in digital domain by connecting whole baseband and RF chain.
3. Back-to-back calibration for transfer function (Chang, Konishi, Kim and Takada, 2012)
   (a) 8x8 calibration circuit has been developed for module-wise back-to-back calibration. 1 out of 8 transmitter ports is selected by RF switch for feeding, while 8-port power divider feed all 8 receiver ports simultaneously. For 24x24 calibration, reference pair of transmitter and receiver modules are selected, and other modules are calibrated against these modules. S-parameters of calibration circuit itself are compensated finally.

3 SPECIFICATION OF CHANNEL SOUNDER

The channel sounder is originally designed to operate in macrocellular and indoor environment (Konishi, Kim, Chang and Takada, 2013).

The channel sounder is operating at the center frequency of 11 GHz with the bandwidth of 400 MHz. Output power of the transmitter is 10 dBm per channel, and the total transmission power is about 24 dBm with 24 transmitter ports.

Special frame format is introduced to transmit the sounding signal and the data stream simultaneously, 4 μs guard interval is inserted into each FDM symbol, which limits the maximum delay spread although 2048 tones are introduced within 400 MHz band. The delay resolution of 2.5 ns is determined from the bandwidth of 400 MHz.

Measurement dynamic range is 55~110 dB in terms of path loss, and the noise floor is dominated by the thermal noise.

Angular resolution of uniform circular array is about 37 degrees. However, ray optical propagation model and maximum likelihood parameter estimation technique (Fleury et al., 1999) are being introduced to de-embed the antenna characteristics from measured propagation channel.

4 FIELD MEASUREMENT CAMPAIGN

Measurement campaign has already been conducted in indoor, microcell and macrocell environments, since the radio license was valid only during the project period.

4.1 Indoor Measurements

Indoor measurements were conducted in the corridor, meeting and lecture rooms, entrance lobby, and hall within the campus of Tokyo Institute of Technology. Point crowds of the interior of the rooms were simultaneously measured by using laser scanner, together with the fish eye images, so that the propagation mechanism can be analyzed in more detail.

Although the detailed data analyses are left for future works, some preliminary works such as multi-link channel characteristics in the hall (Konishi et al., 2012), and path loss and delay spread of corridor-to-room channel (Kim, Konishi, Chang and Takada, 2013) are presented.

4.2 Outdoor Measurements

Outdoor measurements are conducted in macrocell and street microcell environments, within Ishigaki city, Okinawa. Ishigaki city is located in rather remote island, and is populated with about 50,000 people. Measurements were done in urban and residential areas.

Point crowds of the surfaces of the buildings were simultaneously measured by using laser scanner, as well as 3D image (Topcon, n.d.).

Although the detailed analyses are left for future works, some preliminary works such as macrocell line-of-sight path loss (Chang et al., 2013a) and MIMO eigenvalues (Chang et al., 2013b) are presented.

4 CONCLUSIONS

The paper presented the design criteria, technical challenges, and the outcomes in the development of 24x24 full MIMO channel sounder operating at 11 GHz with 400 MHz bandwidth for the development of future super high-bit rate mobile communications. The development of the channel sounder itself was quite successful, while the detailed analysis of the measurement campaigns is still left for the future work.

ACKNOWLEDGEMENTS

This work was supported by “The research and development project for expansion of radio spectrum resources” of The Ministry of Internal Affairs and Communications, Japan.

REFERENCES

Boyd, S. 1986. Multitone signals with low crest factor *IEEE Transactions on Circuits and Systems*, 33, 1018–1022.

Chang, Y., Konishi, Y., Kim, M. and Takada, J. 2012. Calibration Techniques for Fully Parallel 24 X 24 MIMO Sounder. In ISAP 2012, *2012 International Symposium on Antennas and Propagation*.

Chang, Y. et al., 2013a. Analysis of Field Measurement with Wideband MIMO Sounder at 11 GHz Frequency. *IEICE Technical Report*, 112(384), 167-172.

Chang, Y. et al., 2013b Results of Field Measurement with Wideband MIMO Sounder at 11 GHz for Macrocell Environments. *IEICE Technical Report*, 113(8), 7-12.

Fleury, B.H., et al. 1999. Channel Parameter Estimation in Mobile Radio Environments Using the SAGE Algorithm. IEEE Journal of Selected Areas in Communications, 17, 434-450.

Kim, M., Konishi, Y., Chang, Y. and Takada, J. 2013. Characterization and Modeling of Indoor Wideband MIMO Channels At 11 GHz. In EuCAP 2013, *7th European Conference on Antennas and Propagation.*

Kim, M., Konishi, Y., Takada, J. and Gao, B. 2012. Automatic IQ Imbalance Compensation Technique for Quadrature Modulator by Single-Tone Testing. *IEICE Transactions on Communications*, E95-B, 1864-1868.

Kim, M., Maruichi, Y. and Takada, J. 2013. Parametric Method of Frequency-dependent I/Q Imbalance Compensation for Wideband Quadrature Modulator. *IEEE Transactions on Microwave Theory and Techniques*, 61, 270-280.

Kim, M., Takada, J. and Konishi, Y. 2012. A Novel Scalable MIMO Channel Sounding Technique and Measurement Accuracy Evaluation with Transceiver Impairments. *IEEE Transactions on Instrumentation and Measurements*, 61, 3185-3197.

Kolmonen V. et al. 2010, A Dynamic Dual-Link Wideband MIMO Channel Sounder for 5.3 GHz. IEEE Transactions on Instrumentation and Measurements, 59, 873-833.

Konishi, Y. et al. 2012. Multi-link Indoor MIMO Measurements at 11 GHz using Scalable Wideband Channel Sounder. In ISAP 2012, *2012 International Symposium on Antennas and Propagation.*

Konishi, Y., Kim, M., Chang, Y. and Takada, J. 2013, Development of Versatile MIMO Channel Sounder for Double Directional and Multi-link Channel Characterizations at 11 GHz, in preparation to submit to *IEEE Transactions on Instrumentation and Measurements.*

MEDAV (n.a.), Channel Sounder. Retrieved April 27, 2013, from http://www.channelsounder.de/

Pham, V.H., Kim, M. and Takada, J. 2012. Effect of I/Q Skew in Baseband to Wideband Channel Sounder. In MISW 2012, *4th Multidisciplinary International Student Workshop of Tokyo Institute of Technology*.

Sakaguchi, K., Takada, J. and Araki, K. 2002. A novel architecture for MIMO spatio-temporal channel sounder. *IEICE Transactions on Electronics*, 85, 436–441.

Suzuki, H., Suyama, S. and Fukawa, K. 2010. Research Topics for Super High Bit-Rate Mobile Communication Systems (in Japanese). In *Proceedings of IEICE Communication Society Conference*, B-5-51.

Topcon (n.d.). Mobile Mapping System IP-S2 Lite. Retrieved April 27, 2013, from http:// www.topcon.co.jp/en/positioning/products/product/3d scanner/ips2lite.html

Yang, M. and Takada, J. 2013. Antenna Pattern Reconstruction by Spherical Vector Waves for Spherical Antenna Measurement, in EMTS 2013, *2013 URSI International Symposium on Electromagnetic Theory*.

PHOTONIC GENERATION OF TERAHERTZ WAVES FOR COMMUNICATIONS AND SENSING

Tadao Nagatsuma
Graduate School of Engineering Science, Osaka University,
1-3 Machikaneyma, Toyonaka 560-8531, Japan
nagatuma@ee.es.osaka-u.ac.jp

Keywords: Terahertz, Photonics, signal generation, communication, sensing

Abstract: This paper describes how effectively the photonic signal generation schemes are employed to enhance the performance of terahertz-wave systems such as wireless communication, spectroscopy, and tomographic imaging.

1 INTRODUCTION

Research on exploring terahertz (THz) waves, which cover the frequency range from 100 GHz to 10 THz, have lately increased since the nature of these electromagnetic waves is suited to spectroscopic sensing as well as to ultra-broadband wireless communications (Nagatsuma, 2009, 2011). One of the obstacles to developing applications of THz waves is a lack of solid-state signal sources.

For the generation of THz waves, photonic techniques are considered to be superior to conventional techniques based on electronic devices with respect to wide frequency bandwidth, tunability, and stability. Moreover, the use of optical fiber cables enables us to distribute high-frequency (RF) signals over long distances instead of metallic transmission media such as coaxial cables and hollow waveguides.

In this scheme, optical-to-electrical (O-E) converters, or "photodiodes", which operate at long optical wavelengths (1.3-1.55 μm), play a key role, and high output current is required in addition to large bandwidth for practical applications. Recent progress of high-power photodiode technology has accelerated the development of THz-wave system applications (Nagatsuma et al., 2009).

In this paper, we will describe how the photonics technologies are employed in THz-wave systems, showing some of our recent applications, in particular based on based on "continuous wave (CW)" signals, such as wireless communications, spectroscopy and imaging.

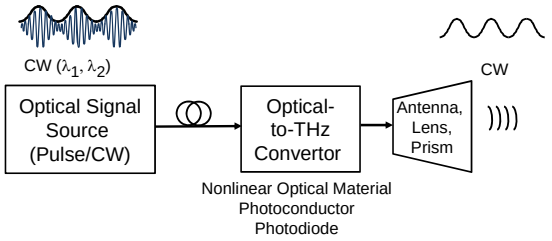

Figure 1: Schematic diagram of photonic continuous-wave THz signal generation.

2 GENERATION AND DETECTION OF CONTINUOUS WAVES

In this section, we briefly review schemes for photonic generation and detection of continuous-wave (CW) THz waves.

2.1 Signal Generation

Figure 1 shows a schematic of CW THz-signal generation based on optical-to-terahertz conversion. First, intensity-modulated optical signals, whose envelope is sinusoidal at a designated THz frequency, are generated with use of light waves at different wavelengths, λ_1 and λ_2. Then, these two-wavelength of lights are injected to conversion media such as nonlinear optical materials (EO), photoconductors (PC), and photodiodes (PD), which

leads to the generation of THz waves at a frequency given by

$$f_{RF} = c\Delta\lambda/\lambda^2 \qquad (1)$$

where $\Delta\lambda$ is a difference in wavelength of lights, and c is a velocity of light. The converted signals are finally radiated into free space by an antenna, a lens, etc.

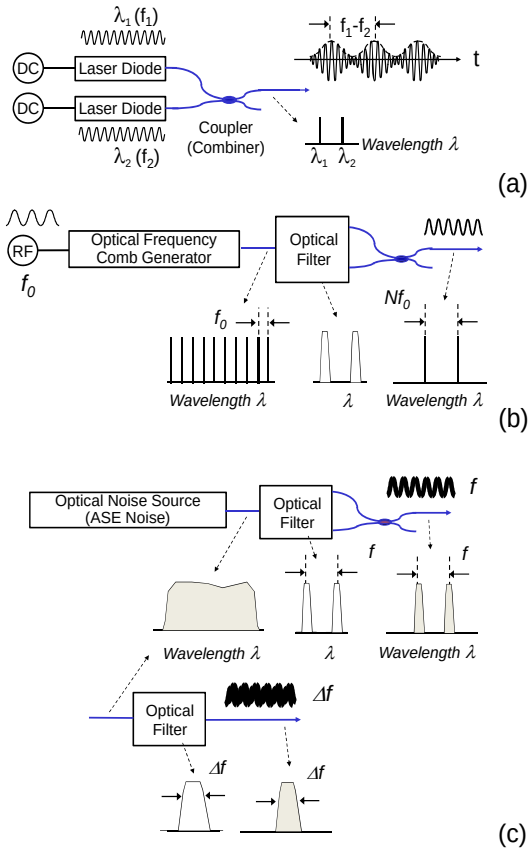

Figure 2: Schematic diagram of optical signal sources.

Typical optical signal sources are depicted in Figs. 2(a) and 2(b); an optical heterodyning technique using two frequency-tunable laser diodes, and using the combination of an optical frequency comb generator and filters, respectively. In the latter case, two wavelength lights are filtered from the optical filters, and this offers us with both wide-band frequency tunability and excellent stability. When so narrow linewidth or frequency resolution in the spectroscopy and/or imaging is not required, we can use two wavelength light filtered from the optical noise source such as ASE noise in optical amplifiers as shown in Fig. 2(c).

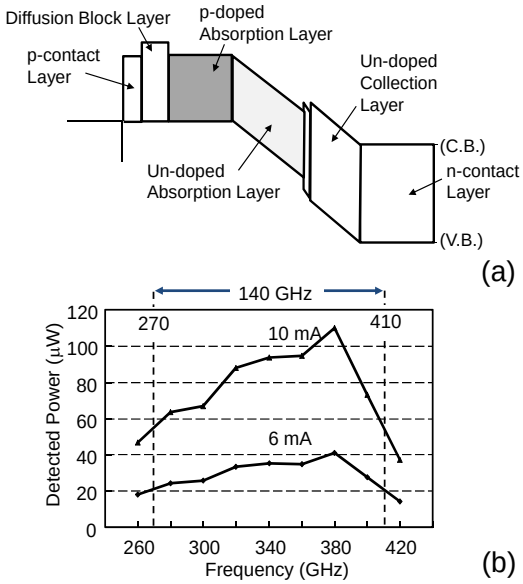

Figure 3: (a) Block diagram of the modified UTC-PD. (b) Output power characteristics.

Among above-memtioned three types of optical-to-electrical conversion media, the photodiode is highly advantageous with respect the conversion efficiency. In addition to the operation at long optical wavelengths (1.3-1.55 μm), large bandwidth and high output current are required for practical applications. Among various types of long-wavelength photodiode technologies, a uni-traveling-carrier photodiode (UTC-PD) and its derivatives have exhibited the highest output powers at frequencies from 100 GHz to 1 THz, with improvement in layer and device structures (Nagatsuma et al., 2009).

Figure 3(a) shows the band diagram of the photodiode optimized for the operation at 300-400 GHz, which is a modification of the UTC-PD. The photodiode chip was packaged into the module with a rectangular waveguide (WR-3) output port (Wakatsuki et al., 2008). Figure 3(b) shows the frequency dependence of the output power generated from the module. The 3-dB bandwidth is 140 GHz (from 270 to 410 GHz), which corresponds to the maximum bit rate of 90 Gbit/s in the case of ASK modulation. The peak output power was 110 μW at 380 GHz for a photocurrent of 10 mA with a bias voltage of 1.1 V. The output power could be further increased to over 500 μW by increasing the photocurrent up to 20 mA with responsivity of 0.22 A/W.

To increase the output power to more than 1 mW, one of the practical approaches is a power-combining technique using an array of photodiodes. With two photodiodes, the output power of >1 mW has been obtained at the photocurrent of 18 mA per photodiode at 300 GHz (Song et al., 2012).

At frequencies of over 300 GHz extending to 1 THz or higher, an antenna-integrated photodiode is more efficient, and semi-spherical silicon lens is often used to collimate a beam radiated from a planar antenna such as bow-tie, log-periodic and dipole antennas (Ito et al., 2005).

2.2 Signal Detection

As for detectors, there are several choices in the THz regions, such as "direct detection" using Schottky barrier diodes (SBDs) or bolometers and "heterodyne detection" by combining mixers and local oscillators (Fig. 4). There are electronic and photonic mixers as well as electronic and photonic local oscillators. We choose the best one depending on required performance in each application.

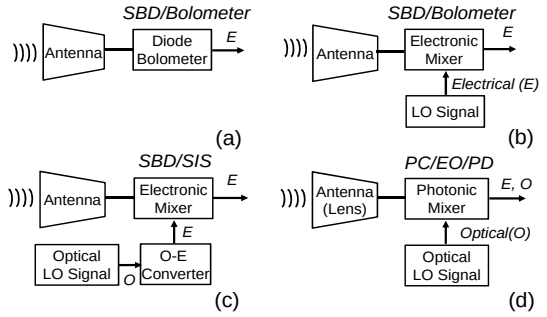

Figure 4: Configurations of THz detection system. O: optical signal, E: electrical signal.

3 APPLICATIONS TO COMMUNICATIONS AND SENSING

In this section, we present our recent applications based on based on CW THz signals, such as wireless communications, spectroscopy and imaging.

3.1 Wireless Communication

Figure 5 illustrates an example of the application schemes with photonics-based approach, showing how the photonic RF signal generation can be employed together with fiber-optic links (Kleine-Ostmann and Nagatsuma, 2011; H.-J. Song and Nagatsuma, 2011). In addition to the wired link using the light wave at a wavelength of λ_1, we can transmit the same data with the wireless link by introducing another wavelength (λ_2) of light wave and mixing the two wavelengths of light in the RF photodiode. The photodiode generates RF signals, whose frequency can be determined the difference in the wavelength of the two light waves, which is given by eq. (1).

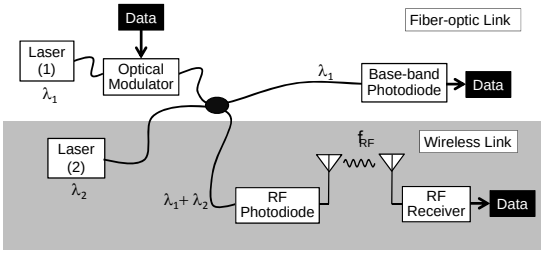

Figure 5: System concept of wired and wireless convergence.

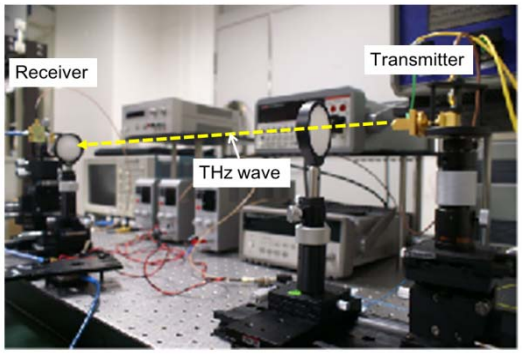

Figure 6: Photo of an experimemtal setup for the wireless link.

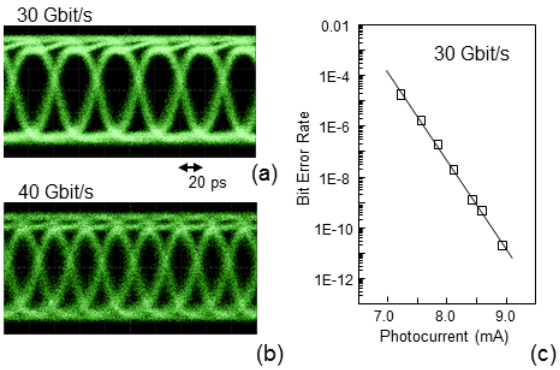

Figure 7: Eye diagrams at 30 Gbit/s and 40 Gbit/s (b), and bit error rate (BER) characteristics at 30 Gbit/s with a carrier frequency of 300 GHz. Photocurrent (horizontal axis of (c)) is proportional to the square root of the transmitted power.

As for the receiver, we can use a simple diode such as a Schottky-barrier diode (SBD) for the demodulation based on the square-law detection in the case of the ASK (OOK) data format. Thus, the receiver becomes more cost-effective and energy-efficient, if we can make use of a wide bandwidth lying over the THz frequency region.

Figure 7 shows transmission characteristics at 300 GHz. For the generation of 300-GHz THz waves, the wavelength difference in two lasers, $\Delta\lambda$, was set to be 2.4 nm, and the optical signal is converted to the RF (THz) signals by the UTC-PD. THz waves are radiated from the horn antenna, and dielectric lenses (2-inch diameter) are used to collimate THz waves for both the transmitter and receiver. The total antenna gain is about 40 dBi. Transmission distance without significant decrease in the received power was typically 0.5 – 1 m.

The performance limitation with respect to the data rate is determined mainly by the bandwidth of the UTC-PD in the transmitter and that of the SBD detector in the receiver. The 3-dB bandwidth of the UTC-PD is 140 GHz (from 270 to 410 GHz), which corresponds to the maximum bit rate of 90 Gbit/s in the case of ASK modulation. While the RF bandwidth of the SBD detector also exceeds 100 GHz, IF (baseband) bandwidth for demodulated signals in the receiver is about 20 GHz, which limits the maximum bit rates. Figures 7(a) and 7(b) shows eye diagrams demodulated by the receiver at 30 Gbit/s and 40 Gbit/s, respectively. From the bit error rate (BER) characteristics, error-free ($BER<10^{-11}$) transmission has been achieved at 30 Gbit/s, which is the highest data rate ever reported for "error-free" wireless links.

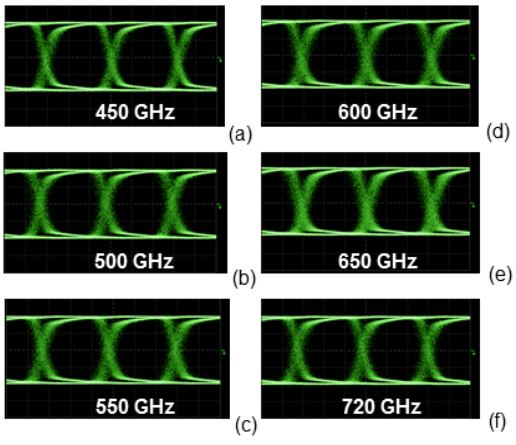

Figure 8: Eye diagrams at the 600-GHz band receiver obtained by changing the carrier frequency or the optical wavelength difference $\Delta\lambda$ from 450 GHz to 720 GHz at a bit rate of 1.6 Gbit/s.

Much larger bandwidth can be ensured when the carrier frequency can be shifted higher. By using antenna-integrated THz UTC-PD module (Ito et al., 2005) together with the 600-GHz band SBD detector (WR-1.5 waveguide), we have increased the available bandwidth of more than 250 GHz with a single transmitter/receiver pair. Figure 8 shows received and demodulated waveforms at carrier frequencies from 450 GHz to 720 GHz. Clear eye diagrams at 1.6 Gbit/s has been obtained, which show error-free transmission over the extremely large bandwidth of 270 GHz.

3.2 Spectroscopy

Recently, THz spectroscopy systems based on CW technology, which use monochromatic sources with an accurate frequency control capability, have attracted great interest (Hisatake et al., 2013). The CW source-based systems, referred to as frequency-domain spectroscopy (FDS), provide a higher signal-to-noise ratio (SNR) and spectral resolution. When the frequency band of interest is targeted for the specific absorption line of the objects being tested, FDS systems with the selected frequency-scan length and resolution are more practical in terms of data acquisition time as well as system cost.

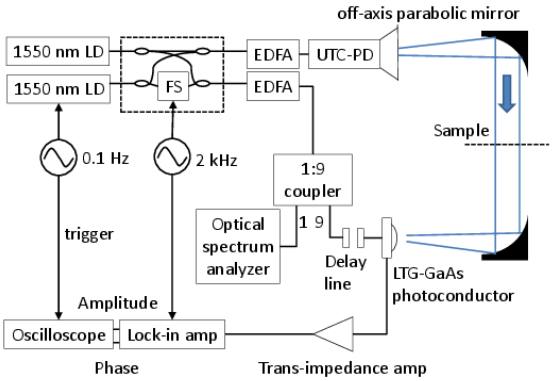

Figure 9: Experimental setup for the frequency-domain spectroscopy. LD: laser diode, EDFA: Erbium-doped fiber amplifier, FS: electro-optic frequency shifter.

THz-FDS system with photonic emitters and detectors is frequently called a homodyne or self-heterodyne system. Figure 9 shows a setup for the THz-FDS system using the UTC-PD for the emitter and a low-temperature-grown (LTG) GaAs photoconductor for the detector. The optical frequency/phase shifter (FS) enables us to accurately measure both the amplitude and phase. Since two

laser diodes (LDs) are free-running, we monitor each wavelength by the optical spectrum analyzer or the wave meter. Figure 10 shows a photo of the experimental setup for the spectroscpoy.

In order to check the frequency accuracy of the system, we measured the absorption line of the water vapor at 557 GHz as shown in Fig. 11. Currently, the experimental standard deviation of the mean for the absorption frequency is about 70 MHz.

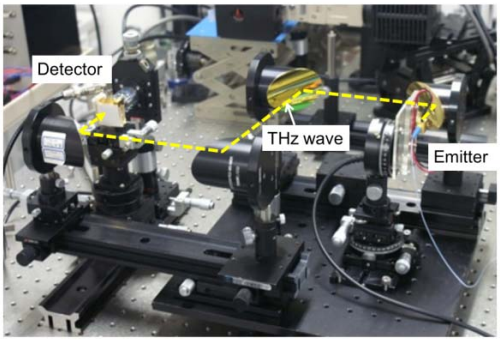

Figure 10: Photo of an experimemtal setup for the spectroscopy.

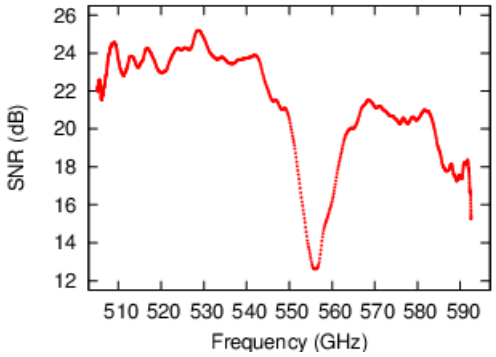

Figure 11: Measured absorption line of the water vapor at 557 GHz.

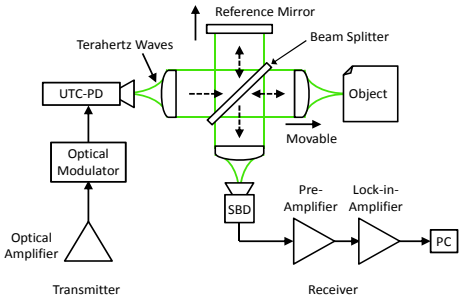

Figure 12: Block diagram of the tomography system using the broadband THz noise signals.

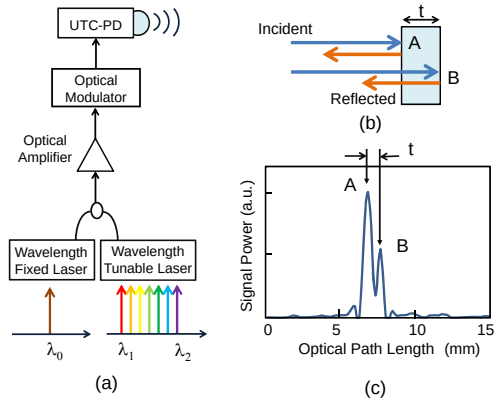

Figure 13: (a) Frequency-swept signal source. (b) Reflection of THz waves at front-side (A) and back-side (B). (c) Point spread function measured with the 600-GHz band system showing the reflection points A and B of a 0.5-mm thick plastic plate.

3.3 Imaging

Figure 12 shows a block diagram of the tomographic imaging system using a broadband terahertz noise (incoherent signal) sources and a Mickelson interferometer (Isogawa et al., 2012). This configuration is similar to that of the optical coherence tomography. The broadband noise signals with sufficient power are generated by feeding the amplified spontaneous emission (ASE) noise from the Er-doped fiber amplifier to the photodiode.

In the setup, first, a THz wave travels to the beam splitter after being collimated by a dielectric lens. The beam splitter divides the THz wave into two directions with a power ratio of 50/50. One goes to the reference mirror and the other to an object after being focused. Both reflected waves travel back to the beam splitter again and go to the SBD as a power detector. Finally, detected signals are amplified by a preamplifier and a lock-in amplifier. A personal computer (PC) controls positions of both the reference mirror and the objective lens. The noise bandwidth of 120 GHz centered at 350 GHz determines the depth resolution of 1.2 mm (Isogawa et al., 2012).

In place of the optical noise sources, the combination of a fixed wavelength laser and a wavelength tunable laser (Fig. 13(a)) enables us to modify the tomography system from time-domain to frequency-domain one (Ikeou et al., 2012). In this scheme, depth-position information can be obtained by Fourier-transforming the frequency-(wavelength-) swept interference signals. Figure

13(c) shows the point spread function, which corresponds to the position of the reflection points at A (front-side) and B (back-side) for a plastic plate with 0.5-mm thickness, when the 600-GHz band system was used.

4 CONCLUSIONS

We have described system applications, which efficiently take advantages of photonics-based ultra-broadband signal generation techniques at over 100-GHz frequencies. Use of optical fiber cables also makes it easy to handle high-frequency signal distribution or cabling in the instrumentation. These features will not be replaced with electronic systems, even though the operation frequency of electronic devices is increasing up to the THz region.

ACKNOWLEDGEMENTS

The author wish to thank Drs H. -J. Song, K. Ajito, N. Kukutsu, S. Kuwano, J. Terada, N. Yoshimoto, and T. Ishibashi with NTT, S. Hisatake, M. Fujita, K. S. Horiguchi, Y. Minamikata, T. Ikeou, H. Nishii with Osaka University for their collaboration and support. This work was supported in part by the JST-ANR WITH program and by the Ministry of Education, Science, Sports and Culture, Grant-in-Aid for Scientific Research (A), 23246067, 2011.

REFERENCES

Hisatake, S., Kitahara, G., Ajito, K., Fukada, Y., Yoshimoto, N., Nagatsuma, T., 2013. *Phase-sensitive terahertz self-heterodyne system based on photodiode and low-temperature-grown GaAs photoconductor at 1.55 μm*. IEEE Sensors Journal, vol. 13, no. 1, pp. 31–36.

Ikeou, T., Isogawa, T., Ajito, K., Kukutsu, N., Nagatsuma, T., 2012. *Terahertz imaging using swept source optical-coherence-tomography techniques.* Tech. Dig. IEEE Intern. Topical Meeting on Microwave Photonics, Session 8, Noordwijk.

Ito, H., Furuta, T., Nakajima, F., Yoshino, K., Ishibashi, T., 2005. *Photonic generation of continuous THz wave using uni-traveling-carrier photodiode.* IEEE J. Lightwave Tech., vol. 23, no. 12, pp. 4016–4021.

Isogawa, T., Kumashiro, T., Song, H.-J., Ajito, K., Kukutsu, N., Iwatsuki, K., Nagatsuma, T., 2012. *Tomographic imaging using photonically generated low-coherence terahertz noise sources.* IEEE Trans. Terahertz Science and Tech., vol. 2, no. 5, pp. 485–492.

Kleine-Ostmann, T., Nagatsuma, T., 2011. *A review on terahertz communications research. J. Infrared Milli. Terhz. Waves*, vol. 32, no. 2, pp. 143–171.

Nagatsuma, T, Ito, H., Ishibashi, T., 2009. *High-power RF photodiodes and their applications.* Laser Photon. Rev., vol. 3, no. 1-2, pp. 123–137.

Nagatsuma, T., 2009. *Generating millimeter and terahertz waves*. IEEE Microwave Magazine, vol. 10, no. 4, pp. 64–74.

Nagatsuma, T., 2011. *Terahertz technologies: present and future,* IEICE Electron. Express, vol. 8, no. 14, pp. 1127–1142.

Song, H.-J., Nagatsuma, T., 2011. *Present and future of terahertz communications.* IEEE Trans. Terahertz Science and Technology, vol.1, no. 1, 256–264.

Song, H.-J., Ajito, K., Muramoto, Y., Wakatsuki, A., Nagatsuma, T., Kukutsu N., 2012. *Uni-travelling-carrier photodiode module generating 300 GHz power greater than 1 mW*. IEEE Microwave and Wireless Components Letters, vol. 22, no. 7, pp. 363–365.

Wakatsuki, A., Furuta, T., Muramoto, Y., Yoshimatsu, T., Ito, H., 2008. *High-power and broadband sub-terahertz wave generation using a J-band photomixer module with rectangular-waveguide output port.* Proc. Int. Conf. on Infrared, Millimeter, and Terahertz Waves, pp. 1999-1–1999-2.

WIRELESS POWER TRANSMISSION IN URSI

Naoki Shinohara[1]
[1]*Research Institute for Sustainable Humanosphere, Kyoto University, Gokasho, Uji, Kyoto, Japan*
shino@rish.kyoto-u.ac.jp

Keywords: Wireless Power Transmission, Energy Harvesting, Rectenna, Beam Forming, Phase Array

Abstract: In URSI, Inter-Commission Working Group on Solar Power Satellites (SPS) was established in 2002 and the URSI Board has been working on writing and reviewing an URSI White Paper on SPS, which was published on June 2007, because the SPS is one of huge application of radio science. One of important application of the radio science on the SPS is a wireless power transmission (WPT) via microwave (microwave power transmission ; MPT). At first, the WPT walked along with the SPS. But now we have some kinds of the WPT and its commercial applications. One of important application of the WPT is an energy harvesting. The other is MPT for the SPS. Some important researches are done as URSI activities in Japan. It is high efficiency rectenna development at low power and at wide band frequency. It is also high efficiency and low cost phased array for the MPT and the SPS. Some of them were published in URSI conference. In this paper, I will show mainly present status of the WPT in Japan and in the world and will also show a relationship between the WPT and the URSI activities.

1 INTRODUCTION

In URSI, Inter-Commission Working Group on Solar Power Satellites (SPS) was established in 2002 and the URSI Board has been working on writing and reviewing an URSI White Paper on SPS because the SPS is one of huge application of radio science. The White Paper on SPS was published on June, 2007(SPS White Paper, 2013). One of important application of the radio science on the SPS is a wireless power transmission (WPT) via microwave (microwave power transmission ; MPT). The MPT researches walked along the SPS researches from the end of 1960s(Brown, 1984)(Matsumoto, 2002). The SPS was one and only application of the MPT because the commercial or industrial MPT system, especially antennas, theoretically become larger than that imagined by users. But in 21st century, some new WPT systems arise to be applied for the commercial or industrial uses(Shinohara, 2011). One is called a resonance coupling WPT which was established by MIT's group in 2006. The other is called an energy harvesting which includes rectifying technologies from weak broadcasting radio waves and power generations from vibration, heat, and light, etc. Technologies for the energy harvesting from radio waves and for the MPT are the same. Difference is only that the energy harvesting is a passive system only with a rectenna, rectifying antenna, against that the WPT is an active system with a power transmitter (Fig.1). The energy harvesting is supported by low power device technologies and is applied for ubiquitous sensor network or simple wireless communications. On contrary, we can transmit power and information simultaneously on the WPT system. The URSI can support to make new theory of the MPT including the energy harvesting and the SPS and can advance its commercialization. In this paper, I will show mainly present status of the WPT in Japan and in the world and will also show a relationship between the WPT and the URSI activities.

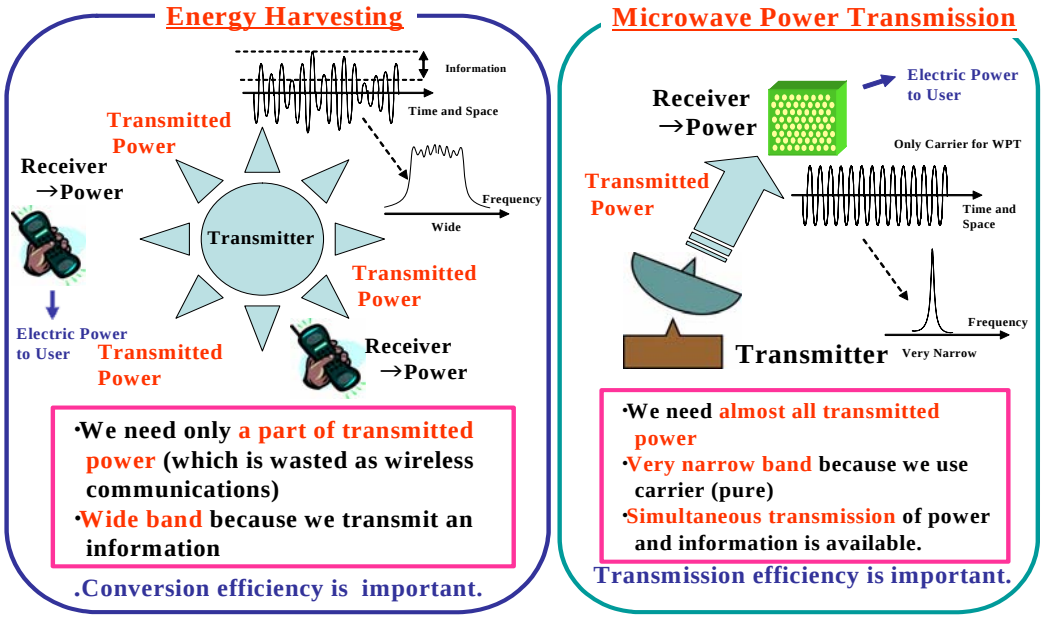

Figure 1 Microwave Power Transmission and Energy Harvesting

2 ENERGY HARVESTING

An energy harvesting is most hopeful wireless power application recently because there have been no allowed frequency for a wireless power transmission in the world. The energy harvesting does not require special frequency because the system is passive and the wireless power is harvested from broadcasting radio waves or waves of wireless communications. There are a lot of researches and developments of the energy harvesting systems in the world(Sample, 2009)(Collado, 2012)(Visser, 2013)(Popovic, 2013). Some of them are researches based on RF-ID technologies and some of them are that based on the energy harvesting from the other power source like vibration or solar.

In Japan, there are also some trials of the energy harvesting from broadcasting waves. One is carried out by ATR (Advanced Telecommunications Research Institute International). They evaluated an energy harvesting system from an 800 MHz cellular BS. For this system, they developed an 800 MHz band twin-loop antenna and an RF-DC conversion circuit. The antenna gain of 5.2 dBi and the RF-DC conversion efficiency of 9 % at -20 dBm input power were obtained. Experimental results showed that a 1.0 F electric double layer capacitor was charged up to 469 mV in 19 hours and drove a low power LCD thermometer for 10 minutes using its stored energy(Kitazawa, 2013).

The other group is Univ. of Tokyo. They developed an energy harvesting system from UHF (at 550MHz) broadcasting wave. They chose charge pump rectifying circuit to charge the tank capacitor to 1.8 and 3.0V are 38 and 70 micro-watts respectively at 550 MHz. At a distance of 6.5km from Tokyo TV tower, the energy harvesting circuit charges up the 100uF charge tank to 2.9V in 3minutes making such a device ideal for battery less operation of wireless sensors for remote monitoring/sensing in most urban areas using just the existing terrestrial TV broadcast infrastructure for power(Vyas, 2012).

Kyoto University's group focuses on development of high efficiency rectenna at low power and at wide band frequency. First of all, we, Kyoto University's group, developed high efficiency rectenna at 5.8GHz with pure spectrum in a MPT system. We proposed a concept of 'Ubiquitous Power Source (UPS)' with the MPT technologies(Shinohara, 2005). In the UPS system, we transmit a microwave power whose microwave is not modulated and pure spectrum and whose power is limited below 1mW/cm^2, safety regulation for human. We chose frequency of 2.45GHz or 5.8 GHz which are on ISM (Industrial, Science, and Medical) band. We developed high efficiency rectenna at low power with expectation of

application for the UPS and the energy harvesting. A picture of the developed rectifying circuit of the rectenna is shown in Fig.2. Target frequency is 5.8GHz continuous wave (CW). The circuit is based on shingle shunt full wave rectifier whose theoretical RF-DC conversion efficiency is 100% with one diode only. As a rectifying theory, line length between a diode and a capacitance (C2) must be λ/4 for 100% efficiency. However, we change the line length between a diode and a capacitance to increase the RF-DC conversion efficiency at 1mW. As a result, we achieved approximately 50% of the RF-DC conversion efficiency at 1mW, 1kΩ in 5.8GHz CW(Fig.3).

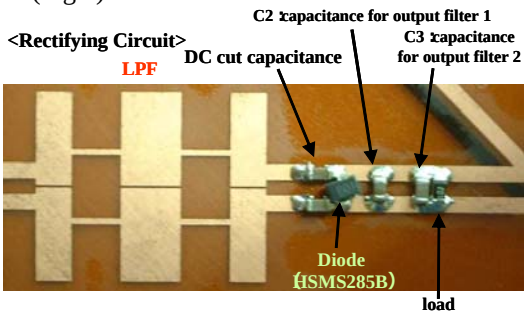

Figure 2 Developed Rectenna for Rectifying of Low Power

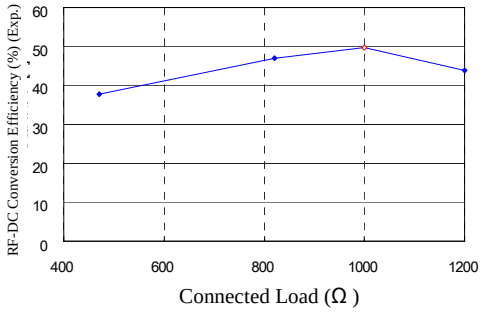

Figure 3: Experimental Result of Load Characteristics of RF-DC Conversion Efficiency at 1mW input microwave power (without Low-Pass Filter)

For 2.45GHz system, we chose the other approach to increase the RF-DC conversion efficiency of the rectenna. Optimization of the line length between a diode and a capacitance was the same. However, we could not increase the efficiency enough with one diode only. Therefore, we increased a number of the diodes and put them like a charge pump rectifier without capacitances (Fig.4). As circuit simulations, we achieved 55.3% at 0.1mW, 8.2kΩ in 2.45GHzCW with type of 6EA (Fig.5). All distributed lines and capacitances are optimized and different in each circuit. Optimum connected loads are also different in each circuit. This was collaborative research with Kyoto University and Mitsubishi Electric Corporation.

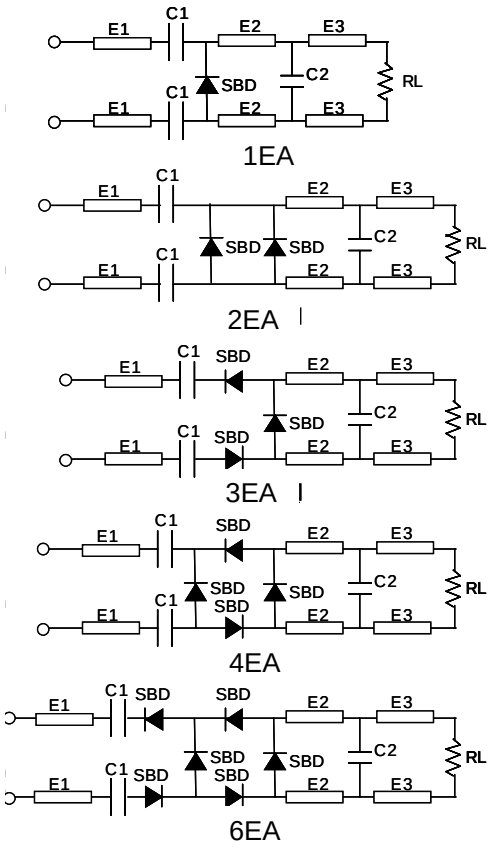

Figure 4 Proposed Rectifying Circuits in 2.45GHzCW (E : Distributed Line, C : Capacitance, SDB : Shottky Barrier Diode)

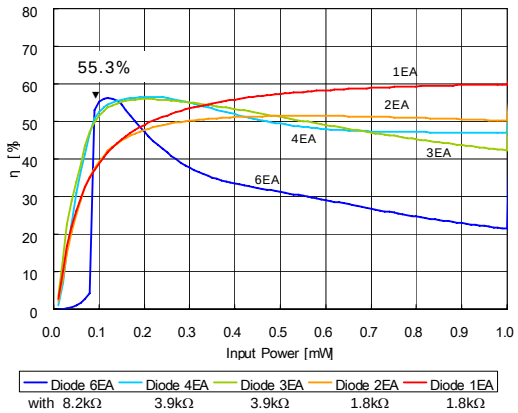

Figure 5 Simulation Results of Proposed Rectifying Circuits in 2.45GHzCW

RF-DC conversion efficiency of these rectennas at low input power is high. However, these are only for continuous waves. We have to develop a rectenna for modulated radio waves whose frequency range is wide. Theoretically, it is difficult to increase RF-DC conversion efficiency by modulated radio waves because some high Q circuits like distributed lines are used to increase the efficiency in a single shunt rectifier. For an energy harvesting with high efficiency, we, Kyoto University and NTT, proposed new rectifying circuit based on the single shunt rectifier in 2013(Shinohara and Hatano, 2013). It is in 24GHz band. The experimental result is shown in Fig.6. We put sector-type open stubs as resonators at higher harmonics instead of a capacitance in a single shunt rectifier. Compared with normal stubs as resonators at higher harmonics, the frequency range is expanded.

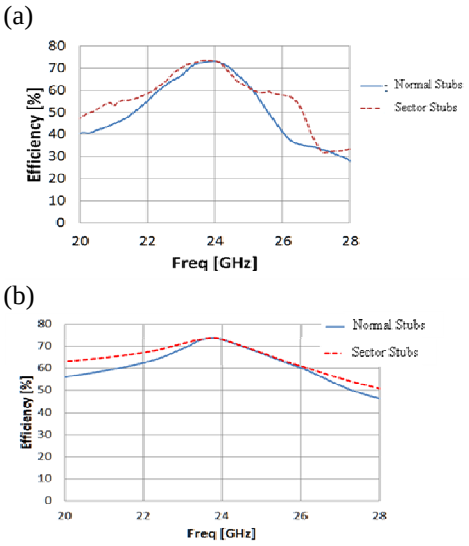

Figure 6 Simulation Result of RF-DC Conversion Efficiency of Class-F Load Rectenna with Sector Stubs(a) with Impedance Matching at 24GHz (b) with Impedance Matching at All Frequencies (Shinohara, 2013)

3 MICROWAVE POWER TRANSMISSION

In URSI activities, we mainly focused on a MPT and a SPS as a MPT application in Japan. Especially, high efficiency beam forming in the MPT and the SPS system is important work. It is not only a new beam forming theoretical algorism but also a beam forming algorism with considering a phased array system.

For the SPS, phased arrays for the MPT were historically developed (Shinohara, 2013). Magnetron phased array developed in Kyoto University is one of hopeful phased array for the SPS. We developed phase controlled magnetron for the SPS. However, one magnetron generates high microwave power, for example, 1kW. For the SPS, the high output power is a weak point because an output power from 1 antenna in the SPS will be less than 1 W. We have to coexistent both beam forming without grating lobes and high efficiency array. In order to coexistent both, we consider two systems. One is a phased array with power divider and sub-phase shifters whose loss are small, between antennas and a magnetron (Shinohara, 2002). We showed that we could keep high beam collection efficiency at wider beam scanning with magnetron phased array with sub-phase shifter, comparing the simple magnetron phased array. Based on the result, we developed magnetron phased array with sub-phase shifters in Kyoto University (Fig.7). The research results were referred in URSI White paper on SPS.

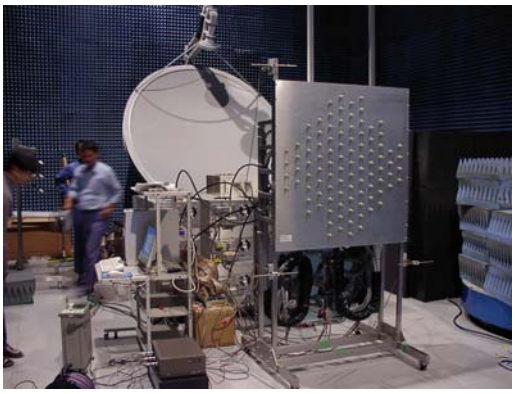

Figure 7 Magnetron Phased Array with Phase Controlled Magnetron through 1-bit sub-phase shifters after 8-way power dividers

The other approach to coexistent both beam forming without grating lobes and high efficiency array, we proposed new random array to suppress grating lobes and to increase beam collection efficiency simultaneously (Shinohara, 2008) (Shishkov, 2009)(Shishkov, 2011). In conventional random array, we can suppress grating lobes with large antenna spacing like a magnetron array. However, energy of the grating lobes merges not to main lobe but to side lobes. As a result, beam collection efficiency of large spacing array with grating lobes and random array without grating lobes

are the same and low. With our new proposed element spacing algorism, grating lobes are suppressed and beam collection efficiency is increased simultaneously (Fig.8).

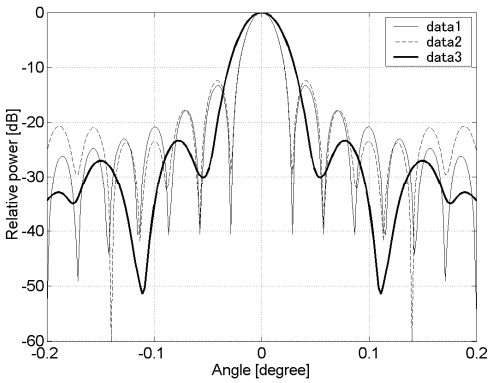

Figure 8 Beam Patterns of data3 (Proposed New Positioning Algorism) and data2 (Conventional Random Array), data1 (Uniform Array) for 1000 elements, average spacing $d_{av} = 2\lambda$ and uniform excitation (Shinohara, 2008)

4 CONCLUSIONS

Radio waves can carry not only information but also energy. A wireless power transmission is one of important new radio scientific and technical region in URSI. In this paper, I only show technical results of the WPT and an energy harvesting. However, propagation, plasma physics, EMC and biomedical of the radio wave are also very important matters to realize commercial WPT and the SPS. I hope fruitful discussions will be in URSI.

REFERENCES

Brown, W. C., 1984. *The history of power transmission by radio waves*, IEEE Trans. Microwave Theory and Techniques, MTT-32, No.9, pp.1230-1242

Collado, A., and A. Georgiadis, 2012. *Improving Wireless Power Transmission Efficiency Using Chaotic Waveforms*, Proc. of IMS2012, TU4F-1, 1849-LL5P2GLnBqBm-2.pdf

Kitazawa, S., M. Hanazawa, S. Ano, H. Kamoda, H. Ban and K. Kobayashi, 2013. *Field Test Results of RF Energy Harvesting from Cellular Base Station*, Proc. of GSMM2013, 1569736061.pdf

Matsumoto, H., Dec. 2002. *Research on Solar Power Station and Microwave Power Transmission in Japan:* Review and Perspectives, IEEE Microwave Magazine, pp.36-45

Popovic, Z., E. Falkenstein, and R. Zane, 2013. *Low-Power Density Wireless Powering for Battery-less Sensors,* Proc. of RWS2013, MO3A, pp.31-33

Sample, A. P. and J.R. Smith, 2009. *Experimental Results with two Wireless Power Transfer Systems*, Proc. of RWS2009, MO2A-5, pp.16-18

Shinohara, N., H. Matsumoto, and K. Hashimoto, 2002. *"Solar Power Station/Satellite (SPS) with Phase Controlled Magnetrons"*, Proc. of 2002 Asia-Pasific Microwave Conference (APMC), pp.2-795-798

Shinohara, N., T. Mitani, and H. Matsumoto, 2005. *Study on Ubiquitous Power Source with Microwave Power Transmission*, Proc. of URSI General Assembly 2005, C07.5(01145).pdf

Shinohara, N., B. Shishkov, H. Matsumoto, K.Hashimoto, and A.K.M. Baki, 2008. *New Stochastic Algorithm for Optimization of Both Side Lobes and Grating Lobes in Large Antenna Arrays for MPT*, IEICE Trans. Communications, Vol.E91-B, No.1, pp.286-296

Shinohara, N., 2011, *Power without Wires*, IEEE Microwave Magazine, Vol.12, No.7, pp.S64-S73

Shinohara, N., K. Hatano, T. Seki, and M. Kawashima, 2013. *Development of Broadband Rectenna at 24GHz"*, Proc. of GSMM2013, 1569734001.pdf

Shinohara, N., 2013. *Beam Control Technologies With a High-Efficiency Phased Array for Microwave Power Transmission in Japan*, Proceeding of IEEE, 10.1109/JPROC.2013.2253062, 0020-SIP-2012-PIEEE

Shishkov, B., K. Hashimoto, H. Matsumoto, N. Shinohara and T. Mitani, 2009. *Direction Finding Estimators of Cyclostationary Signals in Array Processing for Microwave Power Transmission*, Pliska Stud. Math. Bulgar., Vol.19, pp.245-268

Shishkov, B., N. Shinohara, H. Matsumoto, K. Hashimoto, and T. Mitani, 2011. *On the Minimization of Side-Lobes in Large Antenna*, Proc. of URSI General Assembly 2011, CD-ROM CHGBDJK-5.pdf

SPS White Paper, http://www.rish.kyoto-u.ac.jp/SPS/index.html, 2013

Visser, H. J., 2013. *Printed Folded Dipole Antenna Design for Rectenna and RFID Applications*, Proc. of EuCAP2013, pp.2766-2769

Vyas, R. J., H. Nishimoto, M. Tentzeris, Y. Kawahara, T. Asami, 2012. *A Battery-Less, Energy Harvesting Device for Long Range Scavenging of Wireless Power from Terrestrial TV Broadcasts*, Proc. of IMS2012, TU4F-2, 2060-LL6Ai1QvYbBc-2.pdf

Yamamoto, A., H. Okegawa, N. Shinohara, and H. Matsumoto, 2006, *Development of High Efficiency Thin Film Rectenna for Low-Power Input*, Prof. of the 3rd International Symposium on Sustainable Energy System, p.219

EXPERIMENTAL INVESTIGATION ON NONLINEAR CHARACTERISTICS OF A HIGH-TEMPERATURE SUPERCONDUCTING DUAL-BAND BANDPASS FILTER

Shoichi Narahashi[1], Kei Satoh[1], Yasunori Suzuki[1], and Yuta Takagi[1]
[1]*Research Laboratories, NTT DOCOMO, INC., 3-6 Hikari-no-oka, Yokosuka, Kanagawa, Japan*
{narahashi, satokei, suzukiyasu, takagiyu}@nttdocomo.co.jp

Keywords: Dual-band, Bandpass Filter, Superconductor, Intermodulation Distortion, Third-order Intercept Point

Abstract: This paper presents an experimental investigation on the nonlinear characteristics of a high-temperature superconducting (HTS) dual-band bandpass filter (DBPF) that has two passbands and comprises a coplanar-waveguide quarter-wavelength resonator with odd- and even-mode resonant frequencies. An HTS filter is a potential candidate for an RF multi-band bandpass filter (MBPF) that has multiple passbands, which will support broadband transmission in future mobile communication systems. It is, however, indispensable to elucidate the nonlinear characteristics of the HTS-MBPF because the nonlinearity of HTS materials causes intermodulation distortion (IMD). This paper presents the IMD characteristics of a 2.0-/3.5-GHz band HTS-DBPF using a YBCO thin film deposited on a MgO substrate when two tones with a 30-kHz separation are individually and simultaneously input to each passband. Experimental investigations confirm that the HTS-DBPF generates different third-order IMD characteristics depending on how the two tones are input to the HTS-DBPF. This paper also presents a method for estimating the third-order IMD characteristics based on the measurement results.

1 INTRODUCTION

In recent years, Carrier Aggregation (CA) has attracted attention as a technology for improving transmission speeds in future mobile communication systems (Miki, Iwamura, Kishiyama, Anil & Ishii 2010). CA achieves broadband transmission using several fundamental frequency blocks (referred to as component carriers (CCs)) aggregately and simultaneously. An RF filter with multiple passbands, i.e., a multiband bandpass filter (MBPF), is a basic circuit that is expected to achieve broadband transmission such as CA using CCs in different frequency bands.

As a key device for supporting CA, the MBPF is required to have high performance such as sharp-skirt characteristics at the band-edges and a high degree of attenuation in the stopbands with low insertion losses in the passbands, which is remarkable when a wireless system with a high transmitter power is assigned to the frequency band between the two passbands of the MBPF. A high-temperature superconducting (HTS) filter is a potential candidate that satisfies these requirements (Abu-Hudrouss, Jayyousi & Lancaster, 2008).

It is indispensable to investigate the nonlinear characteristics of the HTS filter because intermodulation distortion (IMD) is caused by the nonlinear characteristics of the HTS materials when applying the HTS filter to mobile communication systems. To measure the nonlinear characteristics, there are two common techniques (Wilker, Shen, Pang, Holstein & Face, 1995): one is the IMD measurement method using a signal with two tones and the other is the single tone harmonic generation measurement method. It is desirable to utilize the IMD measurement method using a signal with two closely-spaced tones in evaluating the nonlinear characteristics of the HTS filter since it might attenuate the power level of the harmonic components of the single tone.

The authors have shown the IMD characteristics of the 2.0-/3.5-GHz band HTS-DBPF with a YBCO thin film deposited on a MgO substrate when two signals are individually and simultaneously input to the center of the lower passband and the center of

higher passband as initial research on evaluating the IMD characteristics of an MBPF (Satoh, Takagi, Narahashi & Nojima, 2011; Satoh, Takagi & Narahashi, 2012a; Satoh, Takagi, Narahashi & Nojima, 2012b).

This paper presents an experimental investigation on the IMD of the proposed 2.0-/3.5-GHz band HTS-DBPF. Measurement results show that the third-order IMD (IMD3) characteristics are generated differently depending on how the two-tone signal with a 30-kHz separation is input to the HTS-DBPF. The two ways that the signal is input to the HTS-DBPF are that the two-tone signals are individually input to either the 2.0-GHz band or 3.5-GHz band, or the two tone signals are simultaneously input to both the 2.0-GHz band and 3.5-GHz band. This paper also presents a method for estimating the IMD3 characteristics based on the third-order polynomial approximation of the input-output characteristics of the HTS-DBPF.

2 RESONATOR FOR HTS-DBPF

Figure 1 shows the resonator for the HTS-DBPF that has odd- and even-mode resonant frequencies (Satoh et al., 2011). These two resonant modes have different current flows on the short stub.

This suggests that different current flows allow not only independent configuration of the coupling coefficients for the lower and higher passbands but also suppression of the IMD when a signal is simultaneously input to each passband.

3 IMD MEASUREMENTS

3.1 Measurement System

Figure 2 shows a block diagram of a two-tone IMD measurement system with a fundamental signal cancellation circuit for a single-band bandpass filter (Blount, Olson, Tshudy, Foote & Trantanella, 2004; Futatsumori, Furuno, Hikage, Nojima, Akasegawa, Nakanishi & Yamanaka, 2009). This measurement system enables measurement of the IMD characteristics without the nonlinear effect of the spectrum analyzer because two fundamental signals can be suppressed by more than 60 dB. By using the fundamental signal cancellation circuit, the IMD characteristics could be measured in detail at low power levels.

Figure 3 shows a new block diagram of two kinds of two-tone IMD measurement systems with a fundamental signal cancellation circuit for each

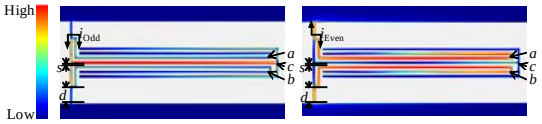

(a) Odd-mode frequency (b) Even-mode frequency

Figure 1: Resonator structure and current density distribution.

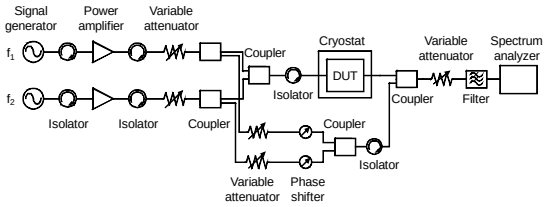

Figure 2: Block diagram for measuring IMD characteristics of single-band bandpass filter.

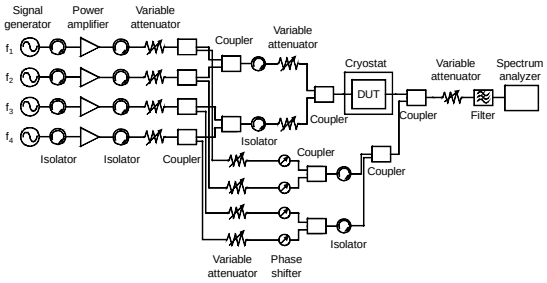

Figure 3: Block diagram for measuring IMD characteristics of dual-band bandpass filter.

passband in order to evaluate nonlinear characteristics when the two kinds of two-tone fundamental signals are input to each passband of the HTS-DBPF.

Figure 4 is a photograph of the configuration for the IMD measurement. This measurement system also enables measurement of the IMD characteristics with a wide dynamic range.

3.2 Measured Results

Figure 5 shows the measured IMD characteristics of the HTS-DBPF together with the ideal IMD3 characteristics. Here, the line with the slope of the third order fitted to the measured results at each passband represent the ideal IMD3 characteristics. In Figure 5(a), blue and red squares represent the third-order IMD (IMD3) characteristics for the 2.0-GHz band and 3.5-GHz band of the HTS-DBPF when a

two-tone fundamental signal with the separation of 30-kHz is input to the 2.0-GHz and 3.5-GHz passbands, respectively. The input and output power per tone are represented on the horizontal and

Figure 4: Experimental configuration for IMD measurement.

vertical axes, respectively. The measured IMD characteristics nearly coincide with the ideal distortion. The third-order input intercept point (IIP3) for the 3.5-GHz passband is +50 dBm at 60 K, while the IIP3 for the 2.0-GHz passband is +43 dBm. If the same IMD is assumed for each passband, the HTS-DBPF can handle an approximately 2.9-times higher input signal power in the 3.5-GHz passband than that in the 2.0-GHz passband at 60 K.

Figure 5(b) shows the measured IMD3 characteristics for both passbands of the HTS-DPBF when two kinds of two-tone fundamental signals (1957.795- and 1957.825-MHz signals for the 2.0-GHz passband, and 3463.515- and 3463.545-MHz signals for the 3.5-GHz passband) are simultaneously input to each passband. The total input power to the HTS-DBPF in Figure 5(b) is 3 dB higher than that in Figure 5(a). The IIP3 for the 3.5-GHz passband is higher than that for the 2.0-GHz passband. Based on Figure 5, the HTS-DBPF has almost the same IIP3 of approximately +43 dBm in the 2.0-GHz passband. If the same IMD is assumed for each passband, the power level of the input signal is defined by the IIP3 for the 2.0-GHz passband.

3.3 IMD3 Estimation

As shown in Figure 5, the IMD3 characteristics are generated differently depending on how the two-tone signal is input to the HTS-DBPF. This section estimates the IMD3 characteristics shown in Figure 5(b) based on the polynomial approximation of the input-output characteristics of the HTS-DBPF.

If a two-tone signal with equal separation is input to each passband of an MBPF that has *n* passbands, the following two combinations represent

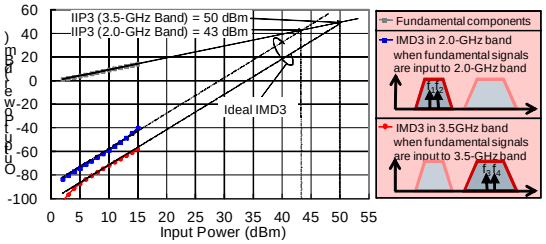

(a) Each passband

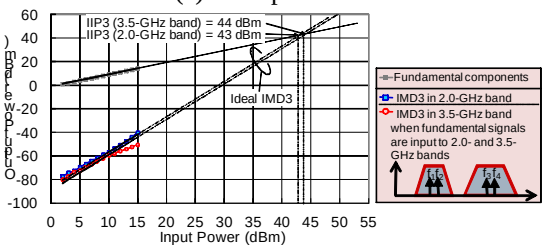

(b) Both passbands

Figure 5: Measured IMD of HTS-DBPF using 30-kHz separated signals at 60 K.

the frequency components of the IMD3 characteristics generated in the vicinity of the two-tone signal at each passband.

$$\begin{aligned} &\text{(i)} \quad 2\omega_{i1}-\omega_{i2}, \quad 2\omega_{i2}-\omega_{i1} \\ &\text{(ii)} \quad \omega_{i1}+\omega_{j1}-\omega_{j2}, \quad \omega_{i2}+\omega_{j2}-\omega_{j1} \\ &\qquad (i,j=1,\cdots,n, \quad i\neq j) \end{aligned} \tag{1}$$

where ω_{i1} and ω_{i2} ($\omega_{i1}<\omega_{i2}$) represent the angular frequencies of the first and second tones at the *i*-th passband, respectively. Here, the input signal, $x_i(t)$, to the *i*-th passband is assumed to be defined as

$$x_i(t)=a_{i1}\cos(\omega_{i1}t+\phi_{i1})+a_{i2}\cos(\omega_{i2}t+\phi_{i2}) \tag{2}$$

where a_{i1} and a_{i2}, and ϕ_{i1} and ϕ_{i2} represent the amplitudes and phases of the two-tone signal, respectively. Assuming that the input-output characteristics of the HTS-MBPF can be expressed by the third-order polynomial approximation, the output signal, $y_i(t)$, of the *i*-th passband of the MBPF is given as

$$y_i(t)=b_{1i}x_i(t)+b_{3i}x_i^3(t) \tag{3}$$

where parameters b_{1i} and b_{3i} are defined as the coefficients of the first-order term and the third-order term of $x_i(t)$ derived from the measured IMD3 characteristics when $x_i(t)$ is input to the i-th passband, respectively. Then, the total output signal, $y(t)$, of the HTS-MBPF can be approximated as

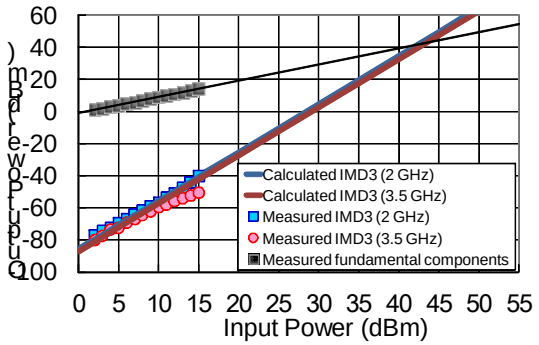

Figure 6: Measured and calculated IMD3 for 2-GHz band and 3.5-GHz band.

$$y(t)=\sum_{i=1}^{n} b_{1i}x_i(t)+\left(\sum_{i=1}^{n} b_{3i}^{1/3}x_i(t)\right)^3. \qquad (4)$$

Figure 6 shows the measured and calculated IMD3 characteristics for each passband as well as the fundamental components of the HTS-DPBF using Equation (4) and parameters b_{1i} and b_{3i} (i = 1, 2). Comparing Figure 5(a) to Figure 5(b) leads to the fact that the IMD3 characteristics are almost the same in the 2-GHz band whereas they are 15.1 dB higher in the 3.5-GHz band at the input power level of 5 dBm. This difference is calculated as 16.6 dB using Eq. (4), which indicates good agreement between the measured and calculated results. The increase in the IMD3 characteristics in the 3.5-GHz band is considered to be due to the following reason. The IMD3 components generated by the combination of angular frequency $\omega_{21}+\omega_{11}-\omega_{12}$ (which depends on parameter b_{31}) appear at the angular frequency of $2\omega_{11}-\omega_{12}$ since parameter b_{31} is 4.9-times (13.7 dB) greater than parameter b_{32}.

4 CONCLUSIONS

This paper presented an experimental investigation on the IMD characteristics of an HTS-DBPF. A new two-tone IMD measurement system enables the evaluation of the IMD characteristics of the HTS-DBPF when the HTS-DBPF simultaneously deals with two kinds of two-tone fundamental signals. This paper also presented a method for estimating the IMD3 characteristics based on the third-order polynomial approximation of the input-output characteristics of the HTS-DBPF.

There still remain technical issues such as clarifying the effective range of the HTS-DBPF using widely-separated signals or a modulated signal, investigating the nonlinearity of the HTS-DBPF when interference signals are input to its passband and when signals are input to its passband edges or stopbands, and confirming whether or not the proposed IMD3 estimation method is available when the two-tone signal employs a frequency separation other than 30 kHz.

REFERENCES

Miki, N., Iwamura, M., Kishiyama, Y., Anil, U., and Ishii, H. 2010. *CA for Bandwidth Extension in LTE-Advanced.* NTT DOCOMO Technical Journal, 12(2), 10-19.

Abu-Hudrouss, A. M., Jayyousi A. B., and Lancaster M. J. 2008. *Triple-Band HTS Filter Using Dual Spiral Resonators with Capacitive-Loading*. IEEE Trans. Appl. Supercond., 18(3), 1728-32.

Wilker, C., Shen, Z., Pang, P., Holstein, W. L., and Face, D. W. 1995. *Nonlinear Effects in High Temperature Superconductors: 3rd Order Intercept from Harmonic Generation*. IEEE Trans. Appl. Supercond., 5(2), 1665-70.

Satoh, K., Takagi, Y., Narahashi, S., and Nojima, T. 2011. *Intermodulation Distortion Characteristics of High-Temperature Superconducting Dual-Band Bandpass Filter*. Proc. of CJMW.

Satoh, K., Takagi, Y., and Narahashi, S. 2012a. *Experimental Investigation of the Intermodulation Distortion Characteristics of High-Temperature Superconducting Dual-Band Bandpass Filter*. Proc. of TJMW, FR4-6.

Satoh, K., Takagi, Y., Narahashi, S., and Nojima, T. 2012b. *Experimental Investigation of the Relationship between Operating Temperature and Power Handling Capability of High-Temperature Superconducting Dual-Band Bandpass Filter*. Physics Procedia, 36, 13-18.

Blount, P., Olson, M., Tshudy, R., Foote, D., and Trantanella, C. 2004. *An Automated Phase Cancellation Method for Measuring Ultra-High Third Order Intercept Points.* IEEE MTT-S Int. Microwave Symp. Dig., 1727-30.

Futatsumori, S., Furuno, M., Hikage, T., Nojima, T., Akasegawa, A., Nakanishi, T., and Yamanaka, K. 2009. *Precise Measurement of IMD Behavior in 5-GHz HTS Resonators and Evaluation of Nonlinear Microwave Characteristics.* IEEE Trans. Appl. Supercond., 19(3), 3595-99.

RF FRONT-END CONSIDERATIONS FOR FUTURE MULTI-BAND MOBILE TERMINALS

Hiroshi Okazaki, Takayuki Furuta, Kunihiro Kawai, Yuta Takagi and Shoichi Narahashi

Research Laboratories, NTT DOCOMO, INC., 3-6, Hikarinooka, Yokosuka, JAPAN
{okazakih, furutat, kawaikun, takagiyu, narahashi}@nttdocomo.co.jp

Keywords: Low noise amplifier, Multi-mode multi-band terminal, Multi-band power amplifier, RF filter, RF front-end.

Abstract: A Radio Frequency (RF) front-end (RF-FE) is one of the keys in multi-mode and multi-band mode mobile terminals. In conventional cellular phones, multiple RF-FEs are installed for multi-band use. There have been a lot of studies of achieving multi-band or broadband circuits that comprise a compact and cost-effective multi-band RF-FE with adequate RF performance. Reconfigurable or tunable RF-FEs are a way to provide multi-band function in future mobile terminals, which takes into consideration the capability to support a large number of wireless systems that use different frequency bands. However, the performance degradation should be considered if adaptive circuits are installed in the RF-FE. This paper presents considerations for the issues that might occur in a multi-band RF-FE for future mobile terminals. As an example, a concept of collaboration between a top RF filter and low-noise amplifier (LNA) is presented.

1 INTRODUCTION

After explosive growth of smart-phones, connecting to the Internet and/or someone else anywhere anytime is becoming necessary in modern lifestyle. To be able to connect from anywhere with adequate bit rate, mobile terminals must have multi-mode and multi-band operation capabilities. In other words, mobile terminals will be expected to function in all the required wireless systems and frequency bands. With regard to frequency bands for cellular systems, some reports indicate that the number of frequency bands required for a global mobile terminal is 3-5 for the third generation (3G) cellular system and it will be increased to 7-9 in the Long Term Evolution (LTE) era. A Radio frequency (RF) front-end (RF-FE) is one of the key components for the global mobile terminal, which should cover a vast number of frequency bands. In this paper, the RF-FE consists of power amplifier(s) (PA(s)), RF filters as a part of duplexers, antenna switches and low noise amplifier(s) (LNA(s)). In conventional cellular phones, multiple PAs, filters, and LNAs are installed for multi-band use, as shown in Figure 1. RFIC generally includes most of RF functions except PA, duplexer, band-pass filter (BPF) and antenna switch, and may have transceivers for wireless local area network (WLAN), Bluetooth and a receiver for the Global Positioning System (GPS).

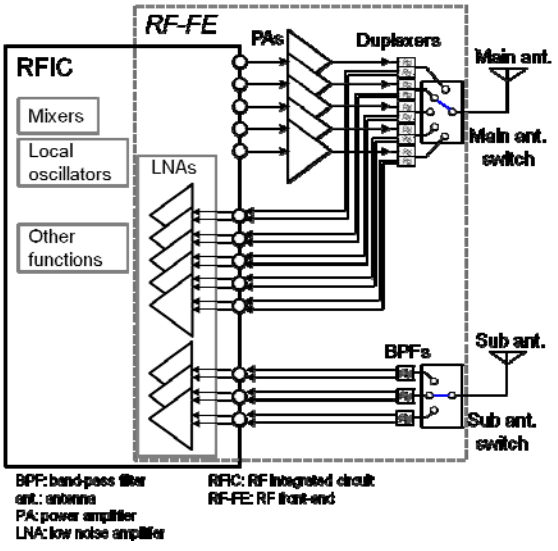

Figure 1: A conventional RF-FE configuration for frequency-division duplexing (FDD) systems.

The RF-FE configuration shown in Figure 1 is based on a conventional scheme, which is selecting the most suitable circuit combination from among several built-in circuits for each frequency band. The RF-FE in the figure can process 5 different frequency bands, and also have a diversity or 2-stream multiple-input and multiple-output (MIMO) receiving capability at 3 out of the 5 bands by using a sub receiver. However, the conventional configuration will reach impasse, and the terminal employing the configuration will be bulky and expensive. This is because the terminal handling *m* bands and *n* spatial streams for MIMO should have ($m \times n$) transceivers in it. Therefore, there have been a lot of studies of achieving multi-band or broadband circuits that comprise a compact and cost-effective multi-band RF-FE with adequate RF performance (Hueber and Staszewski (Ed.), 2011), (Bezooijen, Mahmouji, and Roermund, 2011). A reconfigurable or tunable technique seems to be a way to provide a multi-band RF-FE that supports a large number of frequency bands. An example is shown in Figure 2. However, the performance degradation should be considered if adaptive circuits are installed in the RF-FE. This paper presents considerations for the issues that might occur in a multi-band RF-FE for future mobile terminals. As an example, a concept of collaboration between a top RF BPF and LNA is presented.

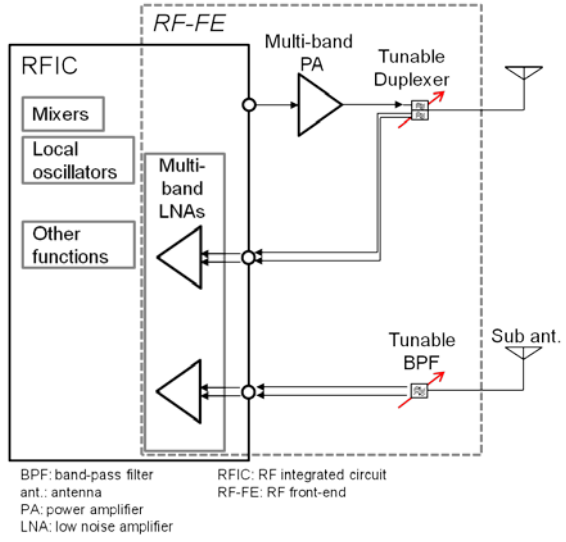

Figure 2: An example of RF-FE configuration employing multi-band circuits for FDD systems.

2 CONSIDERATIONS ON MULTI-BAND CIRCUITS

In this section, some considerations on each component in RF-FE are presented.

2.1 PA

In conventional configuration shown in Figure 1, highly sophisticated PAs are employed. Each of those PA is optimized for a specific frequency band and modulation scheme (mode) operation, thus, it is called as a single-band PA. The main concern of the PA for the mobile terminal is efficiency at required output power levels and spurious specifications at an operating frequency. Generally, efficiency versus frequency characteristics show a peak. That means frequency range where the PA works at high efficiency is limited. There are trade-off relationship between efficiency and frequency range. Figure 3 shows a rough comparison of the efficiency characteristics with PA design schemes.

A single-band PA is usually designed by a narrow-band matching scheme. A multi-band PA based on wide-band matching (wide-band PA) can cover closely-located frequency bands, such as 800, 850 and 900 MHz bands, in compensation for some efficiency degradation from the single-band PA. A wide-band PA is becoming popular because it can merge several PAs which should be required for the conventional RF-FE in a multi-band terminal. However, the wide-band PA is not practical to merge the PAs for widely spread frequency bands, such as 800 and 1900 MHz bands. The PAs based on broadband or distributed matching generally achieve lower efficiency than the wide-band PA, and they are not suitable to use in the mobile terminal.

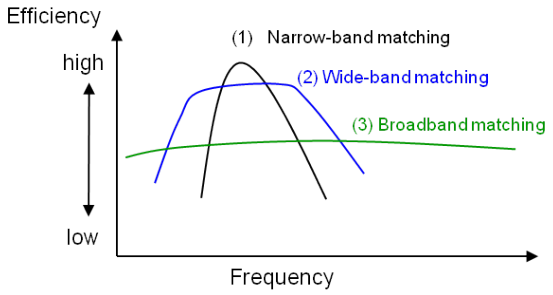

Figure 3: A comparison of design schemes of PA on efficiency versus frequency characteristics.

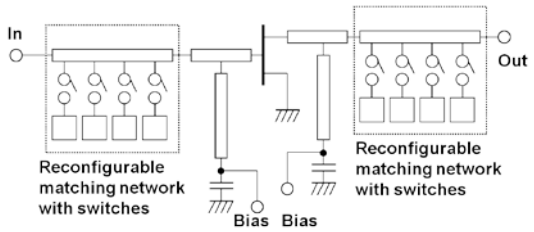

Figure 4: Circuit diagram of reconfigurable amplifier with switches in its matching networks.

On the other hand, a PA with reconfigurable or tunable matching network is expected to achieve high efficiency at each frequency band even if the bands are widely spread. The PAs have variable devices such as switches or varactors in their matching networks to change their operating frequency. Figure 4 shows a circuit diagram example of a reconfigurable amplifier. The status or parameters of the variable devices are set to optimized values for high efficiency based on narrow-band matching at each target frequency. However, efficiency degradation should be considered because the variable components have losses. In the case of the reconfigurable PA with switches, detailed evaluations were presented and it is reported that the degradation can be mitigated (Fukuda, *et al*., 2011).

2.2 Filters and LNAs

Figure 5 shows an example of a receiver RF-FE configuration, which is one generation earlier than that shown in Figure 1. With the progress of CMOS process and efforts on circuit technologies such as "SAW-less" technique (Darabi, 2007), it becomes natural that the LNA is integrated into an RFIC, and the BPF between LNA and RFIC shown in Figure 5 is removed. The main concerns of a LNA for the mobile terminal are sensitivity (gain and noise figure) and linearity, which includes immunity from out-of-band signals. Broadband or wide-band operation of the LNA itself seems to be easier than that of an efficient PA.

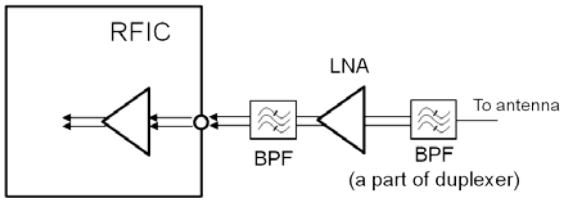

Figure 5: One generation earlier receiver RF-FE configuration example of receiver side.

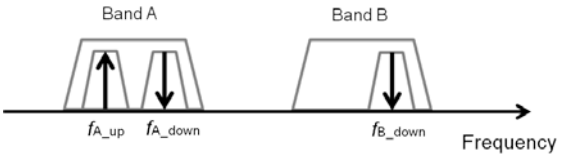

Figure 6: Inter-band CA.

Comparing the receiver configurations shown in Figures 1 and 2, only tunable BPF is required to configure the RF-FE shown in Figure 2. However, it is a considerable challenge to attain a tunable BPF with low-loss at pass-band, high isolation at suppression band, and a wide-tuning frequency range.

Carrier aggregation (CA) technology that employs several bands aggregately and concurrently will be utilized to obtain a wide operating band-width in the LTE-advanced era. Figure 6 shows an example of spectrum usage in inter-band CA. One technical issue for the CA is configuring a duplexer and BPF. Characteristics at the combination band should be considered in the duplexer design in addition to a conventional duplexer design scheme which mainly considers characteristics at an original frequency band for isolation between transmitter and receiver. Because so many combinations of pair-bands are considered for the inter-band CA, a conventional duplexer-bank scheme will make a global terminal more bulky, and using tunable BPFs and tunable band-elimination filers (BEFs) will become more valuable. Otherwise localized mobile terminals for a specific carrier, county, or region will revest.

Considering a tunable filter as a part of the tunable duplexer, one of the serious problems for receiver chain is to generate gain and phase modulation caused by strong out-of-band signals. The LNA will be required to enhance its frequency selectivity in order to prevent the performance degradation from undesired out-of-band signals in a multi-band receiver that yields non-optimum RF filter performance. Frequency response adjustment of the LNA will be a solution.

Figure 7 shows small signal frequency responses of the reconfigurable LNA that has a same circuit topology shown in Figure 4. The responses were obtained in two different switch states (0 and 1) at a class A bias condition. Figure 8 shows the results of the gain suppression measurement at 3.1 GHz with out-of-band signals of 2 GHz. From the results above, the input power of 3.1 GHz for each state is set to -20.3 dBm, which lies in a linear region. In the figure, "gain difference" and "gain diff. at 3.1-GHz," correspond to the difference in gain at 3.1 GHz

between with and without the 2.0-GHz signal input power indicated on the horizontal axis, respectively. The gain of the 2.0-GHz signal without the 3.1-GHz input is also shown for comparison. The gain suppression is observed at a higher level of 2.0-GHz input power, and is mitigated in state 1. Thus, the frequency response adjustment of the LNA is effective in the gain suppression problem caused by out-of-band signals as well as filter response improvement. (Okazaki, *et al*., 2010)

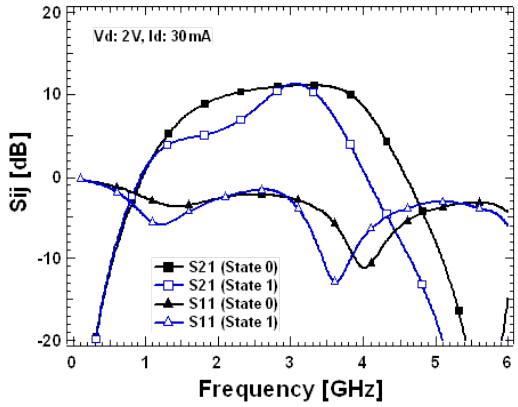

Figure 7: Frequency response of reconfigurable LNA.

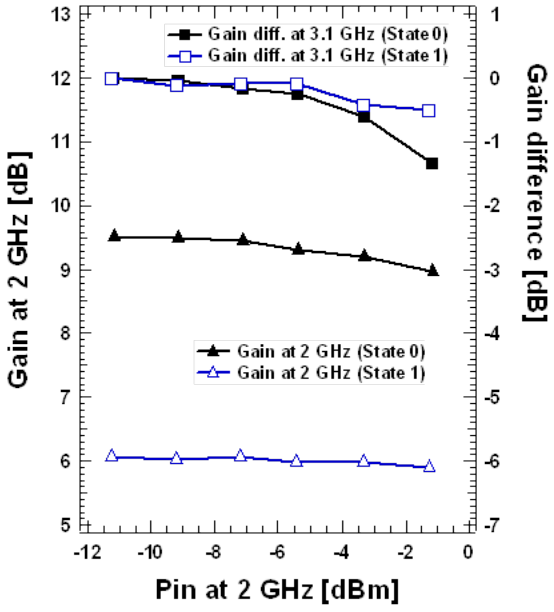

Figure 8: Results of the gain suppression measurement.

3 CONSIDERATIONS ON OVERALL RF-FE

One of the main issues for the overall RF-FE is known collectively as RF coexistence, which is a hot topic (Sahota, 2012). A modern mobile phone has different kind of RF systems such as cellular, WLAN, Bluetooth, GPS, etc., which will be activated at the same time. Each of them may become a source of interference and also a victim of that. Moreover, the MIMO and intra-band CA require also simultaneous operation within multiple transceivers for cellular systems. It seems to be difficult to work all the RF transceivers and receivers installed in a multi-band mobile terminal with expected performance in RF quiet environment.

4 CONCLUSIONS

Several RF-FE considerations for future multi-band mobile terminals are described. Some of them will be solved but others such as ideally tunable filters are remained as issues to be solved and the problems of RF coexistence are still growing. Continuous efforts and innovations are really needed.

REFERENCES

Bezooijen, A., Mahmouji, R., Roermund, A., 2011. *Adaptive RF Front-Ends for Hand-held Applications*, Springer. Dordrecht/Heidelberg/London/New York.

Hueber, G., Staszewski, R.B., (Ed.), 2011. *Multi-Mode/Multi-Band RF Transceivers for Wireless Communications: Advanced Techniques, Architectures, and Trends*, John Wiley & Sons, Inc. Hoboken, New Jersey.

Fukuda, A., Furuta, T., Okazaki, H., Narahashi, S., Nojima, T., 2012. Low-Loss Matching Network Design for Band-Switchable Multi-Band Power Amplifier. *IEICE Transactions on Electronics* E95-C: 1172-1181.

Darabi, H., 2007. A Blocker Filtering Technique for SAW-Less Wireless Receivers. *IEEE Journal of Solid-State Circuits*, 42: 2766-2773.

Okazaki, H., Fukuda, A., Kawai, K., Furuta, T., Narahashi, S., 2010. Reconfigurable amplifier towards enhanced selectivity of future multi-band mobile terminals. In *International Microwave Workshop Series on RF Front-ends for Software Defined and Cognitive Radio Solutions*, IEEE.

Sahota, K., 2012. Coexistence Issues and Mitigation in Multi-Mode Band Cellular Radios, In *International Microwave Symposium*, Workshop WSG, IEEE.

EM WAVE PROPAGATION AND SCATTERING IN SPATIOTEMPORALLY VARYING MOVING MEDIA

The Exponential Model

Dan Censor
Department of Electrical and Computer Engineering, Ben–Gurion University of the Negev, 84105 Beer–Sheva, Israel
censor@ee.bgu.ac.il

Keywords: Electromagnetic Wave Propagation; Electromagnetic Wave Scattering; Special Relativity; Moving Media.

Abstract: An approximate method for analyzing EM wave propagation and scattering in the presence of temporally and spatially varying media is investigated. The method is quasi-relativistic in the sense that for constant velocity it reduces to Einstein's Special Relativity theory to the first order in the normalized speed v/c. The present exponential model was previously used for temporally invariant velocity only. The motion must be irrotational and the characteristic wavelength and period scales of the mechanical motion must be much larger compared to those of the EM field ones. For simple periodic motion it is shown that the EM field is modulated by the motion, and a spectrum of discrete sidebands is created, with frequencies separated by the mechanical frequencies. The results suggest new approaches to the celebrated Fizeau experiment. Rather than using an interferometer setup as in the traditional experiment, the equivalent phase velocity in a periodically moving medium can be deduced from the measured. Simple examples are computed: the effect of the motion on an initially plane harmonic wave, and scattering by perfectly conducting and refractive planes and cylinders.

1 INTRODUCTION AND ABBREVIATIONS

Scattering of EM waves in the presence of moving media and scatterers is of interest for theoretical and engineering applications, see (Van Bladel, 1984) for a comprehensive introduction to the relevant literature. Einstein's SR; Minkowski, 1908; Sommerfeld, 1964; Pauli, 1958) facilitates the analysis for problems involving constant velocities. Historically this is related to the FE and the associated Fresnel drag phenomenon (Einstein, 1905; Pauli, 1958). Heuristic approximations are required for varying velocities, and it stands to reason that they will adequately apply to cases involving the normalized speed v/c to the FO only.

Historically, the present exponential model seems to have originated with Collier and Tai (1965), and later considered for general temporally invariant velocities (Nathan and Censor, 1968; Censor, 1969a, 1972).

1.1 Glossary of Abbreviations

BC=Boundary Condition/s
AKA=Also Known As
BFS= Bessel-Fourier Series
EM=Electromagnetic
EX=Exponential Model/s
FE=Fizeau Experiment/s
FO=First Order in v/c
FT=Field Transformation/s
GT=Galilean Transformation/s
IT=Inverse Transformation/s
LT=Lorentz Transformation/s
MCR= Minkowski Constitutive Relations
ME=Maxwell Equation/s
MM=Mechanical Medium
RE=Relativistic Electrodynamics
RF=Reference Frame/s
SC=Scattering Coefficient/s
SP=Scattering Problem/s
SR=Special Relativity
ZO=Zero Order in v/c

2 FIRST ORDER RELATIVISTIC ELECTRODYNAMICS

Concepts and notation are introduced via a short recapitulation of the FO RE. The source-free ME in a RF $\mathbf{\Gamma}'$ are

$$\begin{aligned}&\partial_{\mathbf{r}'}\times\mathbf{E}'=-\partial_{t'}\mathbf{B}',\ \partial_{\mathbf{r}'}\times\mathbf{H}'=\partial_{t'}\mathbf{D}'\\&\partial_{\mathbf{r}'}\cdot\mathbf{D}'=0,\ \partial_{\mathbf{r}'}\cdot\mathbf{B}'=0\end{aligned}\tag{1}$$

Fields are functions of native coordinates, e.g., $\mathbf{E}'(\mathbf{r}', t')$. According to SR, in an inertial RF $\mathbf{\Gamma}$ we have the form-invariant ME, i.e., (1) without apostrophes

$$\begin{aligned}&\partial_{\mathbf{r}}\times\mathbf{E}=-\partial_{t}\mathbf{B},\ \partial_{\mathbf{r}}\times\mathbf{H}=\partial_{t}\mathbf{D}\\&\partial_{\mathbf{r}}\cdot\mathbf{D}=0,\ \partial_{\mathbf{r}}\cdot\mathbf{B}=0\end{aligned}\tag{2}$$

where the fields are functions of native coordinates, e.g., $\mathbf{E}(\mathbf{r}, t)$.

The FO LT and its IT are given by

$$\mathbf{r}'=\mathbf{r}-\mathbf{v}t,\ t'=t-c^{-2}\mathbf{v}\cdot\mathbf{r}\tag{3}$$

$$\mathbf{r}=\mathbf{r}'+\mathbf{v}t',\ t=t'+c^{-2}\mathbf{v}\cdot\mathbf{r}'\tag{3}$$

respectively. Henceforth the underline notation for IT will be understood even without explicitly writing out the expressions. Formally, all we have to do is exchange primed and unprimed quantities and replace $\mathbf{v}$ by $-\mathbf{v}$. Effecting the limit $c\to\infty$ in (3), (3), yields the GT $t'=t$.

Substituting (3) in the chain rule of calculus

$$\begin{aligned}\partial_{\mathbf{r}}&=(\partial_{\mathbf{r}}\mathbf{r}')\cdot\partial_{\mathbf{r}'}+(\partial_{\mathbf{r}}t')\partial_{t'}\\\partial_{t}&=(\partial_{t}t')\partial_{t'}+(\partial_{t}\mathbf{r}')\cdot\partial_{\mathbf{r}'}\end{aligned}\tag{4}$$

and its IT (4) leads to the FO differential LT and its associated IT

$$\partial_{\mathbf{r}'}=\partial_{\mathbf{r}}+c^{-2}\mathbf{v}\partial_{t},\ \partial_{t'}=\partial_{t}+\mathbf{v}\cdot\partial_{\mathbf{r}}\tag{5}$$

$$\partial_{\mathbf{r}}=\partial_{\mathbf{r}'}-c^{-2}\mathbf{v}\partial_{t'},\ \partial_{t}=\partial_{t'}-\mathbf{v}\cdot\partial_{\mathbf{r}'}\tag{5}$$

respectively. Note that the second formula (5) is in fact the "material derivative" or the "moving derivate" as referred to in continuum mechanics. In the limit $c\to\infty$ the first equations in (5), (5) become the GT $\partial_{\mathbf{r}'}=\partial_{\mathbf{r}}$, as usually used in continuum mechanics.

Substituting (5) into (1) and regrouping terms yields (2), subject to the FO FT

$$\begin{aligned}&\mathbf{E}'=\mathbf{E}+\mathbf{v}\times\mathbf{B},\ \mathbf{B}'=\mathbf{B}-c^{-2}\mathbf{v}\times\mathbf{E}\\&\mathbf{D}'=\mathbf{D}+c^{-2}\mathbf{v}\times\mathbf{H},\ \mathbf{H}'=\mathbf{H}-\mathbf{v}\times\mathbf{D}\end{aligned}\tag{6}$$

and similarly for corresponding IT FT

$$\begin{aligned}&\mathbf{E}=\mathbf{E}'-\mathbf{v}\times\mathbf{B}',\ \mathbf{B}=\mathbf{B}'+c^{-2}\mathbf{v}\times\mathbf{E}'\\&\mathbf{D}=\mathbf{D}'-c^{-2}\mathbf{v}\times\mathbf{H}',\ \mathbf{H}=\mathbf{H}'+\mathbf{v}\times\mathbf{D}'\end{aligned}\tag{6}$$

Assuming in $\mathbf{\Gamma}'$ simple linear constitutive relations

$$\mathbf{D}'=\varepsilon\mathbf{E}',\ \mathbf{B}'=\mu\mathbf{H}'\tag{7}$$

and substituting from (6) into (7) leads to the FO MCR (Minkowski, 1908)

$$\begin{aligned}&\mathbf{D}+\mathbf{v}\times\mathbf{H}/c^{2}=\varepsilon(\mathbf{E}+\mathbf{v}\times\mathbf{B})\\&\mathbf{B}-\mathbf{v}\times\mathbf{E}/c^{2}=\mu(\mathbf{H}-\mathbf{v}\times\mathbf{D})\end{aligned}\tag{8}$$

Although applicable to constant $\mathbf{v}$ only (2), when arbitrarily stipulated to hold for constant local $\mathbf{v}$, it provides the basis for many scattering problems involving rotating spheres and cylinders (see Van Bladel, 1984, pp. 392-3, for relevant articles by D. De Zutter and others).

3 FIRST ORDER RELATIVISTIC ELECTRODYNAMICS, VARYING VELOCITIES

Inasmuch as SR deals with constant $\mathbf{v}$ only, there exists no exact transition to varying velocity. Consequently an heuristically extension of the above FO model must be stipulated, e.g., by generalizing (5), (5) to

$$\partial_{\mathbf{r}'}=\partial_{\mathbf{r}}+c^{-2}\mathbf{v}(\mathbf{r},t)\partial_{t},\ \partial_{t'}=\partial_{t}+\mathbf{v}(\mathbf{r},t)\cdot\partial_{\mathbf{r}}\tag{9}$$

$$\partial_{\mathbf{r}}=\partial_{\mathbf{r}'}-c^{-2}\mathbf{v}(\mathbf{r}',t')\partial_{t'},\ \partial_{t}=\partial_{t'}-\mathbf{v}(\mathbf{r}',t')\cdot\partial_{\mathbf{r}'}\tag{9}$$

The correspondence makes (9), (9), plausible. Note that terms involving the velocity are already of FO, hence ZO coordinates can be dropped or added, e.g., $\mathbf{v}(\mathbf{r}', t')=\mathbf{v}(\mathbf{r}, t)$. Once again note that (9) tallies with the material derivative concept.

It is easily seen that the form invariance of the ME subject to (9), (9) is not preserved here, since by substitution of (9) into the ME (1) we encounter terms like

$$\mathbf{v}\partial_{t'}\times\mathbf{E}=\partial_{t'}(\mathbf{v}\times\mathbf{E})-\partial_{t'}(\mathbf{v})\times\mathbf{E},\ \mathbf{v}=\mathbf{v}(\mathbf{r}',t')\tag{10}$$

where the term $\partial_{t'}((\mathbf{v}(\mathbf{r}', t')\times\mathbf{E})$ obviates the extension of the FT (6) to varying velocity.

However, it is noted that field time derivatives as in $\partial_{t'} \times \mathbf{E}$ involve wave frequencies, say ω, while $\partial_{t'} \mathbf{v}(\mathbf{r}', t')$ involves MM frequencies. Similarly, space derivatives of $\mathbf{v}(\mathbf{r}', t')$, are characterized by a wave number k, while differentiating the velocity involves K, the MM wave number.

We conclude that when the length and time scales characterizing the velocity are larger than the corresponding parameters of the fields, the FT (6), and with them the form invariance of the ME (1), (2), can be assumed. This also implies that the MCR (8) are valid subject to the present restrictions.

4 THE EXPONENTIAL MODEL

Previously the EX (Collier and Tai, 1965; Nathan and Censor, 1968; Censor, 1969a, 1972) was based on the stipulation that (6) remains valid for local time independent $\mathbf{v}$, although $\mathbf{v}(\mathbf{r})$ is spatially varying. Since the MCR (8) are already of ZO, they can be recast in a simplifies form

$$\begin{aligned} &\mathbf{D} = \varepsilon \mathbf{E} + \mathbf{\Lambda} \times \mathbf{H}, \mathbf{B} = \mu \mathbf{H} - \mathbf{\Lambda} \times \mathbf{E} \\ &\mathbf{\Lambda} = \mathbf{v}(\mathbf{r}, t)(C^{-2} - c^{-2}), C = 1/\sqrt{\mu\varepsilon} \end{aligned} \tag{11}$$

Substituting (11) into (2) yields the relevant FO ME for moving media (Tai, 1964; Nathan and Censor, 1968)

$$\begin{aligned} &\partial_{\mathbf{r}} \times \mathbf{E} = \\ &-\mu \partial_t \mathbf{H} + \mathbf{\Lambda} \times \partial_t \mathbf{E}, \varepsilon \partial_{\mathbf{r}} \cdot \mathbf{E} + \partial_{\mathbf{r}} \cdot \mathbf{\Lambda} \times \mathbf{H} = 0 \end{aligned} \tag{12}$$

$$\begin{aligned} &\partial_{\mathbf{r}} \times \mathbf{H} \\ &= \varepsilon \partial_t \mathbf{E} + \mathbf{\Lambda} \times \partial_t \mathbf{H}, \mu \partial_{\mathbf{r}} \cdot \mathbf{H} - \partial_{\mathbf{r}} \cdot \mathbf{\Lambda} \times \mathbf{E} = 0 \end{aligned}$$

Note that by interchanging $\mathbf{H} \leftrightarrow \mathbf{E}, \varepsilon \leftrightarrow -\mu$ in (12), we switch between the two equations. For irrotational $\mathbf{v}(\mathbf{r}, t)$ we have $\partial_{\mathbf{r}} \times \mathbf{\Lambda} = 0$, entailing a conservative field, associated with the scalar potential Φ

$$\mathbf{\Lambda} = \partial_{\mathbf{r}} \Phi, \Phi = \int \mathbf{\Lambda} \cdot d\mathbf{l} \tag{13}$$

therefore the path integral (13) depends on limits only. Accordingly (12) can be recast as

$$\begin{aligned} &\partial_{\mathbf{r}} *\times \mathbf{E} = -\mu \partial_t \mathbf{H}, \partial_{\mathbf{r}} *\times \mathbf{H} = \varepsilon \partial_t \mathbf{E} \\ &\partial_{\mathbf{r}} *\cdot \mathbf{E} = 0, \partial_{\mathbf{r}} * \mathbf{H} = 0, \partial_{\mathbf{r}} * = \partial_{\mathbf{r}} - \partial_t \mathbf{\Lambda} \times \end{aligned} \tag{14}$$

Incorporating the time scales argument as in (10), whereby the velocity's time-derivative is neglected, solutions of (12), (14), can be constructed in the form

$$\begin{aligned} &\mathbf{E} = e^{\Phi \partial_t} \mathbf{E}_1, \mathbf{H} = e^{\Phi \partial_t} \mathbf{H}_1 \\ &\Phi = \int \mathbf{\Lambda} \cdot d\mathbf{l}, \partial_{\mathbf{r}} \times \mathbf{\Lambda} = 0, \mathbf{\Lambda} = \partial_{\mathbf{r}} \Phi \end{aligned} \tag{15}$$

The operator exponential is understood as a symbolic Taylor series $e^{\Phi \partial_t} \equiv 1 + \Phi \partial_t + \ldots$. The ZO fields $\mathbf{E}_1, \mathbf{H}_1$ satisfy the ME

$$\begin{aligned} &\partial_{\mathbf{r}} \times \mathbf{E}_1 = -\mu \partial_t \mathbf{H}_1, \partial_{\mathbf{r}} \times \mathbf{H}_1 = \varepsilon \partial_t \mathbf{E}_1 \\ &\partial_{\mathbf{r}} \cdot \mathbf{E}_1 = 0, \partial_{\mathbf{r}} \cdot \mathbf{H}_1 = 0 \end{aligned} \tag{16}$$

Inasmuch as the operator $e^{\Phi \partial_t}$ acts on the ZO fields, for time harmonic fields possessing the factor $e^{-i\omega_1 t}$ with frequency ω_1, we identify

$$\partial_t \leftrightarrow -i\omega_1, \partial_{\mathbf{r}} * = \partial_{\mathbf{r}} + i\omega_1 \mathbf{\Lambda} \times \tag{17}$$

Thus the EX is a perturbation scheme whereby we start with well-known solutions of the ME in media at rest (16), and with the exponential operator (15) as a factor, a FO solution of the ME in moving media is created. Of course, BC, where applicable, must be taken on the complete fields (15). For simplicity, incompressible media are considered here, therefore Φ satisfies the Laplace equation $\partial_r^2 \Phi = 0$.

Once (11)-(16) are accepted as our working formalism, everything takes place in the "laboratory" unprimed RF.

5 PLANE WAVE PROPAGATION IN OSCILLATING MEDIA

Consider a plane harmonic wave satisfying (16)

$$\mathbf{E}_1 = \hat{\mathbf{E}}_1 E_1 e^{i\theta_1}, \mathbf{H}_1 = \hat{\mathbf{H}}_1 H_1 e^{i\theta_1}, \theta_1 = \mathbf{k}_1 \cdot \mathbf{r} - \omega_1 t \tag{18}$$

with mutually perpendicular $\mathbf{k}_1, \mathbf{E}_1, \mathbf{H}_1$, launched into the moving medium. The medium time-dependent velocity is given according to (11), (13), as

$$\mathbf{\Lambda}(t) = \mathbf{\Lambda}_0 \cos \Omega t, \Phi = \int \mathbf{\Lambda} \cdot d\mathbf{l} = \mathbf{\Lambda} \cdot \mathbf{r} \tag{19}$$

It follows that the solution of the ME (15) is given by

$$\mathbf{E} = \hat{\mathbf{E}}_1 E_1 e^{i\theta},\ \mathbf{H} = \hat{\mathbf{H}}_1 H_1 e^{i\theta}$$
$$\theta = \theta_1 - \omega_1 \boldsymbol{\Lambda}_0 \cdot \mathbf{r} \cos\Omega t = \theta_1 - \omega_1 \Lambda_0 \xi \cos\Omega t \tag{20}$$

where ξ is the coordinate in the direction of $\boldsymbol{\Lambda}$. Note that in (19), (20), $\mathbf{r}$ can assume any value, therefore $\boldsymbol{\Lambda}\cdot\mathbf{r}$ is not necessarily small, in spite of $\boldsymbol{\Lambda}$ being FO. This is a consequence of choosing a time-dependent velocity as in (19) (cf. (23) below). Recasting $e^{i\theta}$ in terms of a BFS (e.g., see Stratton, 1969) yields

$$e^{i\theta} = \Sigma_n F_n e^{i\mathbf{k}_1\cdot\mathbf{r} - i\nu_n t},\ F_n = (-i)^n J_n(\omega_1 \Lambda_0 \xi)$$
$$\nu_n = \omega_1 - n\Omega,\ \Sigma_n = \Sigma_{n=-\infty}^{n=\infty} \tag{21}$$

revealing the spectral structure the plane wave assumes in the moving medium, with the initial carrier frequency ω_1 for $n = 0$ and additional discrete sidebands ν_n for integers n. Throughout J_q denotes the non-singular Bessel function of order q. Thus (20) can be recast as

$$\mathbf{E} = \hat{\mathbf{E}}_1 \Sigma_n E_n e^{i\mathbf{k}_1\cdot\mathbf{r} - i\nu_n t},\ \mathbf{H} = \hat{\mathbf{H}}_1 \Sigma_n H_n e^{i\mathbf{k}_1\cdot\mathbf{r} - i\nu_n t}$$
$$E_n / E_1 = H_n / H_1 = F_n \tag{22}$$

The time periodic velocity (19) can be generalized to a MM space and time harmonic plane velocity wave

$$\boldsymbol{\Lambda}(\mathbf{r}, t) = \boldsymbol{\Lambda}_0 \cos(\mathbf{K}\cdot\mathbf{r} - \Omega t),\ |\mathbf{K}| = 2\pi / \lambda_m \tag{23}$$

with λ_m denoting the MM wavelength. For longitudinal compression waves $\mathbf{K}$, $\boldsymbol{\Lambda}_0$ are parallel, hence we have

$$\partial_{\mathbf{r}} \times \boldsymbol{\Lambda} = \partial_{\mathbf{r}} \times (\boldsymbol{\Lambda}_0 \cos(\mathbf{K}\cdot\mathbf{r} - \Omega t))$$
$$= \boldsymbol{\Lambda}_0 \times \mathbf{K} \sin(\mathbf{K}\cdot\mathbf{r} - \Omega t) = 0 \tag{24}$$

as prescribed for (13). Furthermore (15) prescribes

$$\Phi = \boldsymbol{\Lambda}_0 \int \cos(\mathbf{K}\cdot\mathbf{r} - \Omega t)\cdot d\mathbf{r} =$$
$$\Lambda_0 \int \cos(\mathrm{K}\xi - \Omega t) d\xi = \tag{25}$$
$$= (\Lambda_0 / \mathrm{K}) \sin(\mathrm{K}\xi - \Omega t),\ \mathbf{K} = \mathrm{K}\hat{\boldsymbol{\xi}},\ \boldsymbol{\Lambda}_0 = \Lambda_0 \hat{\boldsymbol{\xi}}$$

with ξ defining the coordinate in the direction of $\mathbf{K}$, $\boldsymbol{\Lambda}_0$. Instead of (20) we now have

$$\mathbf{E} = \hat{\mathbf{E}}_1 E_1 e^{i\theta},\ \mathbf{H} = \hat{\mathbf{H}}_1 H_1 e^{i\theta}$$
$$\theta = \theta_1 - \omega_1 \Phi_\xi,\ \Phi_\xi = (\Lambda_0 / \mathrm{K}) \sin(\mathrm{K}\xi - \Omega t) \tag{26}$$

For $\mathrm{K} \to 0$, i.e., for $\lambda_m \to \infty$, the problem reduces to (19)-(22).

The analog of (21) is now

$$e^{i\theta} = \Sigma_n G_n e^{i\theta_n},$$
$$G_n = J_n(\omega_1 \Lambda_0 / \mathrm{K}),\ \theta_n = \boldsymbol{\kappa}_n \cdot \mathbf{r} - \nu_n t \tag{27}$$
$$\boldsymbol{\kappa}_n = \mathbf{k}_1 - n\mathbf{K} = \mathbf{k}_1 - n\mathrm{K}\hat{\boldsymbol{\xi}},\ \nu_n = \omega_1 - n\Omega$$

It is noted that even though the Bessel functions argument (27) is of FO, it involves the ratio of the MM and EM wavelengths $k_1 / \mathrm{K} = \lambda_m / \lambda_1$, which is not necessarily small and must be assessed for each concrete case. The analog of (22) is now

$$\mathbf{E} = \hat{\mathbf{E}}_1 \Sigma_n E_n e^{i\theta_n},\ \mathbf{H} = \hat{\mathbf{H}}_1 \Sigma_n H_n e^{i\theta_n}$$
$$\theta_n = \boldsymbol{\kappa}_n \cdot \mathbf{r} - \nu_n t,\ E_n / E_1 = H_n / H_1 = G_n \tag{28}$$

In (27), (28), in addition to the temporal spectrum ν_n, we have a discrete spatial spectrum of $\boldsymbol{\kappa}_n$. Due to the vector character of $\boldsymbol{\kappa}_n$, when $\mathbf{k}_1$ is not parallel to $\mathbf{K}$, each spectral component propagates in a slightly different direction, possessing a different phase velocity according to

$$C_n = \nu_n / |\boldsymbol{\kappa}_n| = (\omega_1 - n\Omega) / |\mathbf{k}_1 - n\mathbf{K}| \tag{29}$$

6 IMPORT FOR NEW FIZEAU-TYPE EXPERIMENTS

Doppler Effect frequency shifts are usually associated with moving sources or boundaries. It is therefore of interest to note, as shown in (28) that wave-fronts in moving media can also create a spectrum, without involving moving material boundaries. As far as this author is aware, this phenomenon was not documented before in the present EX context. In a sense, it is akin to some acousto-optics experiments involving interaction of sound and EM waves, but rather than having constitutive parameters modulated by sound, here medium velocity is involved. The present results might suggest new approaches to the celebrated FE.

The classical FE (e.g., Van Bladel, 1984, p. 120ff.) measures the EM wave effective phase velocity C_{eff} in a column of a moving medium (water in the original FE), characterized by C in the rest RF. The results tally with the SR velocity addition formula (Pauli, 1958). Consider (18)-(22), or (23)-(28), with $\mathrm{K} \to 0$, for parallel velocity and propagation directions, and $\Omega = 0$. From θ (20) or (26) we then find effective values

$$k_{eff} = k_1 - \omega_1 \Lambda_0 = \omega_1 / C - \omega_1 \Lambda_0 \tag{30}$$

$$\begin{aligned} C_{eff} &= \omega_1 / k_{eff} = c / n_{eff} = 1/(C^{-1} - \Lambda_0) \\ &\approx C + C^2 \Lambda_0 = C + \mathrm{v}_0 (1 - 1/n^2) \end{aligned} \tag{31}$$

with index of refraction $n = c/C$ in the rest RF. This is the basis for the classical FE. Essentially, with C known, the quest is for the value of Λ_0 in order to compute C_{eff} or vice-versa.

Exploiting the present theory, rather than using an interferometer setup and measuring the displacement of diffraction fringes, as done in the traditional FE, Λ_0 can be found from measurements of spectral components. Thus by measuring the amplitude of waves, and solving for relevant arguments of F_n, G_n in (22), (28), respectively, the value of Λ_0 can be extracted. Using (30), (31), the effective parameters can be computed. One can envision a medium set into periodic motion as in (19) or (23). The EM wave propagated through the medium will display a spectrum of discrete frequencies ν_n, (21), (27). In both cases the cumbersome interferometer setup involving a moving water column is obviated. This also solves the problem of the irregular flow at the source and sink regions where the fluid is injected and drained, as in the classical FE. Better resolution (AKA selectivity) of sidebands can be attained by electronically down-shifting frequencies after detection (AKA mixing, or heterodyning) employed in radio communications techniques.

7 SCATTERING PROBLEMS

SP for the EX with time-independent $\mathbf{v}$ have been discussed before (Collier and Tai, 1965; Censor, 1969; Censor, 1972).

As in the FE and other cases (Censor, 1969b), fluid-dynamics continuity problems of the medium flow in the presence of the scatterer are arbitrarily ignored, assuming that the flow is maintained as if the material scatterer has no effect. Otherwise complicated problems ensue that cannot be tackled with the analytical tools employed here. Realistic flows have been considered in (Censor, 1972).

7.1 Scattering by Plane Interfaces

As the simplest example for a SP consider a perfectly conducting plane at $x = 0$, with a perpendicularly incident wave as in (26) with Φ_x replacing Φ_ξ

$$\begin{aligned} &\mathbf{E}_i = \hat{\mathbf{z}} E_1 e^{i\theta_i}, \mathbf{H}_i = -\hat{\mathbf{y}} H_1 e^{i\theta_i} \\ &\theta_i = k_1 x - \omega_1 t - \omega_1 \Phi_x, E_1 / H_1 = \sqrt{\mu/\varepsilon} = \eta \end{aligned} \tag{32}$$

the ratio η defining the medium impedance in the region $x < 0$.

The reflected wave $\mathbf{E}_r$ must satisfy the BC $\mathbf{E}_r = -\mathbf{E}_i|_{x=0}$. The BC prescribe identical time variation for all waves at the boundary $x = 0$, hence

$$\begin{aligned} &\mathbf{E}_r = \hat{\mathbf{z}} \rho E_1 e^{i\theta_r}, \mathbf{H}_r = \hat{\mathbf{y}} \rho H_1 e^{i\theta_r} \\ &\theta_r = -k_1 x - \omega_1 t - \omega_1 \Phi_x \end{aligned} \tag{33}$$

with $\rho = -1$ denoting the reflection coefficient.

Consider next a refractive medium in the region $x > 0$, with frequency dependent rest RF constitutive parameters $\bar{\mu}(\nu)$, $\bar{\varepsilon}(\nu)$. Correspondingly the RF phase velocity, impedance, are $\bar{C}(\nu) = 1/\sqrt{\bar{\mu}\bar{\varepsilon}}$, $\bar{\eta}(\nu) = \sqrt{\bar{\mu}/\bar{\varepsilon}}$, respectively. In the region $x < 0$ the parameters $\mu(\omega_1)$, $\varepsilon(\omega_1)$, remain dependent on the excitation frequency ω_1 only, in order to satisfy the ME subject to the EX, (15).

The EX solutions (32), (33), are recast in spectral components as in (28)

$$\begin{aligned} &\mathbf{E}_i = \hat{\mathbf{z}} \Sigma_n E_n e^{i\theta_{n,i}}, \mathbf{H}_i = -\hat{\mathbf{y}} \Sigma_n H_n e^{i\theta_{n,i}} \\ &\theta_{n,i} = \kappa_n x - \nu_n t \end{aligned} \tag{34}$$

$$\begin{aligned} &\mathbf{E}_r = \hat{\mathbf{z}} \Sigma_n \rho_n E_n e^{i\theta_{n,r}}, \mathbf{H}_r = \hat{\mathbf{y}} \Sigma_n \rho_n H_n e^{i\theta_{n,r}} \\ &\theta_{n,r} = -\kappa_n x - \nu_n t \end{aligned} \tag{35}$$

and the transmitted wave is given by

$$\begin{aligned} &\mathbf{E}_t = \hat{\mathbf{z}} \Sigma_n \bar{E}_n e^{i\theta_{n,t}}, \mathbf{H}_t = -\hat{\mathbf{y}} \Sigma_n \bar{H}_n e^{i\theta_{n,t}}, \bar{E}_n = \tau_n E_n \\ &\theta_{n,t} = \bar{\kappa}_n x - \nu_n t, \bar{\kappa}_n = \nu_n / \bar{C}_n, \bar{C}_n = \bar{C}(\nu_n) \\ &\bar{E}_n / \bar{H}_n = \bar{\eta}_n, \bar{H}_n = H_n \tau_n \eta / \bar{\eta}_n \\ &\bar{\mu}_n = \bar{\mu}(\nu_n), \tau_n = \tau_n(\nu_n) \end{aligned} \tag{36}$$

The solution for ρ_n, τ_n, are given by the familiar formulas

$$\rho_n = (\bar{\eta}_n - \eta)/(\bar{\eta}_n + \eta), \tau_n = 2\bar{\eta}_n/(\bar{\eta}_n + \eta) \tag{37}$$

7.2 Scattering by Circular Cylinders

For the SP of a perfectly conducting circular cylinder of radius a, the incident excitation plane wave is once again given by (32). Leaving the EX

factor intact and recasting the ZO solution e^{ik_1x} in BFS yields, (15)-(17), in cylindrical coordinates

$$\mathbf{E}_i = e^{-i\omega_1\Phi_x}\mathbf{E}_{i,1} = \hat{\mathbf{z}}E_1 e^{-i\omega_1\Phi_x}\Sigma_m L_m e^{im\psi - i\omega_1 t}$$

$$\begin{aligned}\mathbf{H}_i &= e^{-i\omega_1\Phi_x}\partial_{\mathbf{r}}\times\mathbf{E}_{i,1}/i\omega_1\mu \\ &= i(E_1/\eta)e^{-i\omega_1\Phi_x}\Sigma_m\mathbf{L}_m e^{im\psi - i\omega_1 t}\end{aligned} \tag{38}$$

$$L_m = i^m J_m(k_1 r),\ \mathbf{L}_m = \hat{\mathbf{z}}\times\partial_{k_1\mathbf{r}}L_m$$

Accordingly we construct the scattered wave as

$$\begin{aligned}\mathbf{E}_s &= \hat{\mathbf{z}}E_1 e^{-i\omega_1\Phi_x}\Sigma_m a_m M_m e^{im\psi - i\omega_1 t} \\ \mathbf{H}_s &= i(E_1/\eta)e^{-i\omega_1\Phi_x}\Sigma_m a_m\mathbf{M}_m e^{im\psi - i\omega_1 t} \\ M_m &= i^m H_m^{(1)}(k_1 r),\ \mathbf{M}_m = \hat{\mathbf{z}}\times\partial_{k_1\mathbf{r}}L_m\end{aligned} \tag{39}$$

with $H_m^{(1)}$ denoting the first kind Hankel functions. On application of the BC $\mathbf{E}_r = -\mathbf{E}_i|_{r=a}$, the EX factor cancels and we find

$$a_m = -J_m(k_1 r)/H_m^{(1)}(k_1 r) \tag{40}$$

the familiar SC of the ZO problem.

For a material cylinder we start with (38), (39), and recast $e^{-i\omega_1\Phi_x}$ in BFS

$$\begin{aligned}&e^{-i(\omega_1\Lambda_0/\mathrm{K})\sin(\mathrm{K}x-\Omega t)} = \Sigma_n G_n e^{-in(\mathrm{K}r\cos\psi - \Omega t)} \\ &= \Sigma_{n,p}G_n e^{in\Omega t}P_{n,p}e^{ip\psi},\ P_{n,p} = (-i)^p J_p(n\mathrm{K}r)\end{aligned} \tag{41}$$

Hence

$$\begin{aligned}\mathbf{E}_i &= \hat{\mathbf{z}}E_1\Sigma_{n,p,m}Q_{n,p,m}e^{i(p+m)\psi - i\nu_n t} \\ \mathbf{H}_i &= i(E_1/\eta)\Sigma_{n,p,m}\mathbf{Q}_{n,p,m}e^{i(p+m)\psi - i\nu_n t} \\ Q_{n,p,m} &= G_n P_{n,p}L_m,\ \mathbf{Q}_{n,p,m} = G_n P_{n,p}\mathbf{L}_m\end{aligned} \tag{42}$$

Similarly, (39) becomes

$$\begin{aligned}\mathbf{E}_s &= \hat{\mathbf{z}}E_1\Sigma_{n,p,m}a_{n,p,m}S_{n,p,m}e^{i(p+m)\psi - i\nu_n t} \\ \mathbf{H}_s &= i(E_1/\eta)\Sigma_{n,p,m}a_{n,p,m}\mathbf{S}_{n,p,m}e^{i(p+m)\psi - i\nu_n t} \\ S_{n,p,m} &= G_n P_{n,p}M_m,\ \mathbf{S}_{n,p,m} = G_n P_{n,p}\mathbf{M}_m\end{aligned} \tag{43}$$

In the cylinder's interior $r < a$ fields are obtained as a superposition of regular cylindrical waves of modes u, at frequencies ν_n, satisfying the ME (16) with rest RF parameters $\bar{\mu}(\nu_n), \bar{\varepsilon}(\nu_n)$

$$\begin{aligned}\mathbf{E}_t &= \hat{\mathbf{z}}E_1\Sigma_{n,u}b_{n,u}T_{n,u}e^{iu\psi - i\nu_n t} \\ \mathbf{H}_t &= i(E_1/\bar{\eta})\Sigma_{n,u}b_{n,u}\mathbf{T}_{n,u}e^{iu\psi - i\nu_n t} \\ T_{n,u} &= i^u J_u(\bar{\kappa}_n r),\ \mathbf{T}_{n,u} = \hat{\mathbf{z}}\times\partial_{\bar{\kappa}_n\mathbf{r}}T_{n,u}\end{aligned} \tag{44}$$

On application of BC

$$\mathbf{E}_i + \mathbf{E}_s - \mathbf{E}_t = 0|_{r=a},\ \hat{\boldsymbol{\psi}}\cdot(\mathbf{H}_i + \mathbf{H}_s - \mathbf{H}_t)|_{r=a} \tag{45}$$

prescribing the fields continuity on the interface, the orthogonality of angular modes $e^{iu\psi}$ prescribes nonzero coefficients $b_{n,u} \neq 0$ for $u \neq p+m$. Hence (44) can be recast to include the constraint

$$\begin{aligned}\mathbf{E}_t &= \hat{\mathbf{z}}E_1\Sigma_{n,p,m}\delta(p+m-u)b_{n,u}T_{n,u}e^{iu\psi - i\nu_n t} \\ \mathbf{H}_t &= i(E_1/\bar{\eta})\Sigma_{n,p,m}\delta(p+m-u)b_{n,u}\mathbf{T}_{n,u}e^{iu\psi - i\nu_n t}\end{aligned} \tag{46}$$

where δ denotes the Discrete Kronecker Delta Function. For each spectral component n, and angular mode u the BC lead to an infinite set of equations, which can only solved if properly truncated.

Consider (41)-(46) for the case of a monopole $u = p = m = 0$. This only works for thin cylinders, hence n must be properly truncated, otherwise higher multipole terms must be included. Accordingly

$$\begin{aligned}\mathbf{E}_i &= \hat{\mathbf{z}}E_1\Sigma_n Q_n e^{-i\nu_n t},\ Q_n = Q_{n,0,0} = G_n P_{n,0}L_0 \\ \mathbf{H}_i &= i(E_1/\eta)\Sigma_n\mathbf{Q}_n e^{-i\nu_n t},\ \mathbf{Q}_n = \mathbf{Q}_{n,0,0} = G_n P_{n,0}\mathbf{L}_0\end{aligned} \tag{47}$$

and similarly

$$\begin{aligned}\mathbf{E}_s &= \hat{\mathbf{z}}E_1\Sigma_n a_n S_n e^{-i\nu_n t} \\ \mathbf{H}_s &= i(E_1/\eta)\Sigma_n a_n\mathbf{S}_n e^{-i\nu_n t} \\ S_n &= S_{n,0,0} = G_n P_{n,0}M_0,\ \mathbf{S}_n = \mathbf{S}_{n,0,0} = G_n P_{n,0}\mathbf{M}_0\end{aligned} \tag{48}$$

$$\begin{aligned}\mathbf{E}_t &= \hat{\mathbf{z}}E_1\Sigma_n b_n T_n e^{-i\nu_n t} \\ \mathbf{H}_t &= i(E_1/\bar{\eta})\Sigma_n b_n\mathbf{T}_n e^{-i\nu_n t} \\ T_n &= T_{n,0} = J_0(\bar{\kappa}_n r),\ \mathbf{T}_n = \mathbf{T}_{n,0} = \hat{\mathbf{z}}\times\partial_{\bar{\kappa}_n\mathbf{r}}T_n\end{aligned} \tag{49}$$

From (45) and (47)-(49), we get explicit equations for the SC

$$\begin{aligned}&J_0(k_1 a) + a_n H_0^{(1)}(k_1 a) - \bar{b}_n J_0(\bar{\kappa}_n a) = 0 \\ &J_0'(k_1 a) + a_n H_0'^{(1)}(k_1 a) - \bar{b}_n(\eta/\bar{\eta})J_0'(\bar{\kappa}_n r) = 0 \\ &\bar{b}_n = b_n/[J_n(\omega_1\Lambda_0/\mathrm{K})J_0(n\mathrm{K}a)]\end{aligned} \tag{50}$$

with the prime denoting differentiation with respect to the argument. In form (50) is similar to the classical SP, but including the present velocity effects, therefore solving for the coefficients a_n, b_n is straightforward.

8 SUMMARY AND CONCLUDING REMARKS

The advent of SR (Einstein, 1905) facilitated the analysis of SP involving moving objects and media. However, SR is founded on the concept of inertial RF moving at constant $\mathbf{v}$.

A multitude of scientific and engineering problem involve varying velocities. Heuristic models that in the case of constant $\mathbf{v}$ merge into exact SR are not unique. Presently the Quasi Lorentz Transformation (Censor, 2005, 2010) (9) is employed. Subject to the constraint of MM and EM space and time scaling, the FO ME and FT (1), (2), (6), apply to varying $\mathbf{v}(\mathbf{r}, t)$.

The EX, originating with Collier and Tai (1965) provides FO SR solutions to ME in moving media. The method is generalized here to time-dependent irrotational velocity fields. Previously (Collier and Tai, 1965) only time-independent velocity systems have been considered.

In periodically moving media the solution for the ZO case of plane waves displays discrete sideband spectra. This provides new approaches to the FE. Unlike the original FE, employing interference experiments, the present results suggest measurements based on analysis of the spectra created by periodical mechanical flows or waves.

Canonical SP examples are given for scattering by plane interfaces and by circular cylinders, in the presence of periodically moving embedding media. It is shown that opaque objects, like the perfectly conducting interfaces above, yield the classical SC for media at rest, involving only the excitation frequency ω_1. On the other hand, refractive scatterers are excited by the frequencies created by the MM motion, (37), (43), displaying SC depending on the sideband frequencies.

The results suggest new methods for remote sensing the material parameters of objects that are not directly accessible. To further investigate the present model, more canonical SP will have to be investigated, with various MM motional modes.

REFERENCES

Censor, D., 1969a. Propagation and scattering in radially flowing media, *IEEE Transactions on Microwave Theory and Techniques*, Vol. MTT-17, pp. 374-378.

Censor, D., 1969b. Scattering of a plane wave at a plane interface separating two moving media, *Radio Science*, Vol. 4, pp. 1079-1088.

Censor, D., 1972. Interaction of electromagnetic waves with irrotational fluids, *Journal of the Franklin Institute*, Vol. 293, pp. 117-129.

Censor, D., 2005. Non-relativistic scattering: pulsating interfaces, In *PIER—Progress In Electromagnetic Research*, Vol. *54*, pp. 263-281.

Censor, D., 2010. The need for a first-order Quasi Lorentz Transformation. In *AIP Conference Proceedings*, Vol. 1301, pp. 3-13.

Collier, J. R., Tai C.T., 1965. Guided waves in moving media. *IEEE Transactions on Microwave Theory and Techniques*. Vol. MTT-13, pp. 441-445.

Einstein, A., 1905. Zur Elektrodynamik bewegter Körper. *Ann. Phys. (Lpz.), 17, pp. 891-921*. English translation: On the Electrodynamics of moving bodies. In *The Principle of Relativity*, 1952, Dover.

Minkowski, H., 1908. Die Grundgleichungen für die elektromagnetischen Vorgänge in bewegten Körpern. In *Nachrichten von der Gesellschaft der Wissenschaften zu Göttingen*, pp. 53-116.

Nathan, A., Censor, D., 1968. Extended ∇ relations with reference to EM waves in moving simple media, *IEEE Transactions on Microwave Theory and Techniques*, Vol. MTT-16, pp. 883-884.

Pauli, W., 1958. *Theory of Relativity*, Pergamon.

Sommerfeld, A., 1964. *Electrodynamics*, p. 280ff. Academic Press.

Stratton, J.A., 1941. *Electromagnetic Theory*, McGraw-Hill, 1941.

Tai, C.T., 1964. A study of electrodynamics of moving media, *Proceedings of the IEEE*, Vol. 52, pp. 685-689.

Van Bladel, J., 1984. *Relativity and Engineering*, Springer.

A UCWW CLOUD-BASED SYSTEM FOR INCREASED SERVICE CONTEXTUALIZATION IN FUTURE WIRELESS NETWORKS

Ivan Ganchev[1,2], Máirtín O'Droma[1], Nikola S. Nikolov[3,1], Zhanlin Ji[4,1]
[1]*Telecommunications Research Centre, University of Limerick, Limerick, Ireland*
[2]*Department of Computer Systems, Plovdiv University, Plovdiv, Bulgaria (on leave)*
[3]*Department of Computer Science and Information Systems, University of Limerick, Limerick, Ireland*
[4]*Research Centre for Bioengineering and Sensing Technology, University of Science and Technology Beijing, China*
Ivan.Ganchev@ul.ie, Mairtin.ODroma@ul.ie, Nikola.Nikolov@ul.ie, Zhanlin.Ji@ustb.edu.cn

Keywords: Ubiquitous Consumer Wireless World (UCWW); Future Networks (FN); Cloud-based System; Software Architecture, Middleware, Service Contextualization, Context Awareness.

Abstract: This paper describes the design and development of a novel cloud-based system for increased service contextualization in future wireless networks. The principal objective is the support of mobile users (consumers) in a Ubiquitous Consumer Wireless World (UCWW) seeking to choose and select the 'best' service instance in a UCWW environment matched to their dynamic contextualized and personalized service delivery requirements and expectations, thereby increasing user freedom in where, when and how they access desired services, and increasing user-driven networking. The design challenges to create such a cloud-based system with an ever-enhanced capacity to be attuned to a user-client's dynamic contexts, and do this for all its users, are addressed, and software infrastructural design solutions suggested. The cloud idea proposed here is one which should yield efficiencies and saving for consumers, operate as an additional 'behind-the-scenes' decision support subsystem to make smart decisions based on mining of the most up-to-date data stored in the cloud repositories related to service contexts and personalized profiles. Rather than the use of known efficient heuristic methods employed with large and complex data structures, together with associated algorithms solving the combinatorial optimization problems, an alternative method, proposed here for making predictions, is to discover patterns in the behaviour of the individual client-consumer, to bring into play, in the decision process, patterns and trends of other client-consumers seeking the same or similar services, and also the constant update of the user's wireless environment context through information garnered from other sources, such as wireless access service provider updates, teleservice provider updates, and data sensed by the sensors in the environment. Indentifying and addressing the need as directly as this is a novel approach towards providing context-aware personalized services. It is particularly novel, and desirable, in the UCWW context. Hence, this consumer supportive smart repository solution may appropriately be called a UCWW cloud. The paper sets out an infrastructural design of this cloud, ordered within a conceptual UCWW software architecture, together with its various elements, e.g., decision support subsystem and mobile network environment elements of personalized information retrieval (PIR).

1 INTRODUCTION

The research described in this paper is motivated by the context-awareness and service contextualization problems within the Ubiquitous Consumer Wireless World (UCWW) environment. The UCWW, proposed in (O'Droma, 2007) & (O'Droma, 2010), sets out a generic consumer-centric techno-business model foundation for future generations of wireless communications. The evolution of the UCWW environment represents a shift from the currently dominating subscriber-based access to wireless communication services, towards more consumer-centric one. By utilizing a person-centric IPv6 address scheme, enabling full number portability as well as an access-network-independent third-party

authentication, authorization, and accounting (3P-AAA) service provision, consumers can dynamically select a provider for a service from a list of alternatives. This in turn opens up the opportunity for stronger competition between providers and as such, to an improved level of service for the consumer. Effective exploitation of the attractive benefits of this freedom will need the support of 'smart' software tools. These will dynamically collect and sort through the vast numbers of service options on offer to a consumer at any time and place, which might otherwise be overwhelming, and extract service-type-dependent ranked choice suggestions matched to the consumer's relevant profile.

In support of these tools and of the whole consumer-choice optimization process, we propose here the development of a UCWW cloud-based system to facilitate the delivery of increasingly contextualized services in future wireless networks. Through this user-centric UCWW cloud, mobile users can have access to a more contextualized level of service provision, with a much greater level of choice in terms of service delivery. Moreover, service providers can deliver a much more specialized level of service, to a much larger set of mobile users.

The main goal in our work is to provide the user with a context-aware software tool that can assist the user to choose and select the 'best' service instance in a UCWW environment. Through an appropriate graphical user interface (GUI) the tool may make the service choice easier or may make the choice on behalf of the user when authorized to do so. In both cases, the software tool would benefit greatly from the ability to make accurate predictions of user preferences in particular situations, i.e., making the choice of one particular mobile service instance (provider) when the user desires to use a specific service. This prediction may be the result of solving a combinatorial optimization problem, where the user has specified criteria for making a particular choice. For example, the GUI may allow the user to specify a few parameters such as an upper bound on the price, lower bound on the quality of service (QoS), etc. The difficulty is both computational – often such problems are NP-complete (Garey, 1979) – and related to the limited hardware resources on mobile devices, which may not allow the use of large and complex data structures and algorithms. Therefore, efficient heuristic methods must be used, particularly for the context of solving the combinatorial optimization problems (Wolsey, 1999) & (Cook, 1997) on mobile devices. An alternative method for making predictions is to allow the software to discover patterns in the behaviour of the consumer. In order to achieve this, the user behaviour should be recorded, stored and uploaded as appropriate to a distributed repository. On behalf of individual users, but for many users, this will allow always best connected and best served (ABC&S) applications, within the distributed repository, to carry out effective mining of data (Usama, 1996) & (Mikut, 2011) that may result in more accurate and more beneficial user behaviour predictions (Witten, 2011). Such a repository can be viewed as a *UCWW cloud* that facilitates data storage and offers service predictions based on the patterns discovered within the user data.

For this, foremost cloud computing principles and techniques need to be employed along with effective data collection and data mining techniques to facilitate predictions as to the applicability of services to particular users. The impact of this work will be to provide a more consumer-centric wireless services environment, which can also be commercially attractive to service providers.

The rest of the paper is organized as follows. Section 2 provides an overview of the UCWW. Section 3 presents the UCWW cloud as a context-aware middleware. Section 4 describes the decision support subsystem of the UCWW cloud. Section 5 considers the implementation issues. Finally, section 6 concludes the paper and suggests future research directions.

2 UBIQUITOUS CONSUMER WIRELESS WORLD (UCWW)

Being a wireless communication environment rather than a wireless technology, and while requiring some distinct technological infrastructural modifications and innovations (O'Droma, 2007) & (O'Droma, 2010), UCWW is completely in harmony with, and will benefit fully from, almost all the existing global technological developments and ongoing standardization efforts in wireless communications, e.g., Next Generation Mobile Networks (NGMN) Alliance proposals (Kibria, 2007), 3rd Generation Partnership Project's (3GPP) Long-Term Evolution and System Architecture Evolution (LTESAE) (Ekstrom, 2006), and ITU-T's ongoing work on Next Generation Networks (NGN) (Carugi, 2005). The primary change UCWW brings is that, through it, users become consumers instead of subscribers. The 'in harmony' element of this evolution is emphasized by the fact that UCWW

consumers may opt out (or in) of having such subscriber-like contracts, or may have several simultaneously through a single Consumer Identity Module (CIM) card and without conflict with different access network providers (ANPs). While it is evolutionary, it enables significant and new user-driven wireless communication capabilities and benefits, and converting the wireless environment into a consumer-centric one. True user-driven ABC&S paradigm (Passas, 2004) may be considered to encompass many of these benefits, and more. Most are obviously inherent and distinctively characteristic of UCWW; others are not, e.g., the user-driven integrated heterogeneous networking (IHN) and interworking – a published amendment to an existing ITU-T recommendation standard for the latter is shown in (O'Droma, 2010). In this, UCWW marks a seismic shift from the network-centric, subscriber-based techno-business model (SBM) of today, with its long-term lock-in type contract between the subscriber and the ANP, with all its constraints, to a new consumer-centric techno-business model (CBM).

Figure 1 portrays schematic representations of both techno-business models (SBM & CBM), illustrating the main mobile service paths and business agreement relationships. Transition to the UCWW, where the new CBM environment may co-exist side-by-side with the SBM environment, is shown as a passage through a global standardization frontier.

In SBM, the subscriber primarily gets wireless services through his/her 'home' (cellular) ANP or from visited-ANPs, if roaming agreements are in place. WiFi hotspots, Femto-cells and the like, when they offer services using the AAA infrastructure of a user's home-ANP, come under the visited-ANP umbrella. Teleservice providers (TSPs) and value-added service providers (VASPs) can also offer their own services through access networks under respective bilateral business agreements.

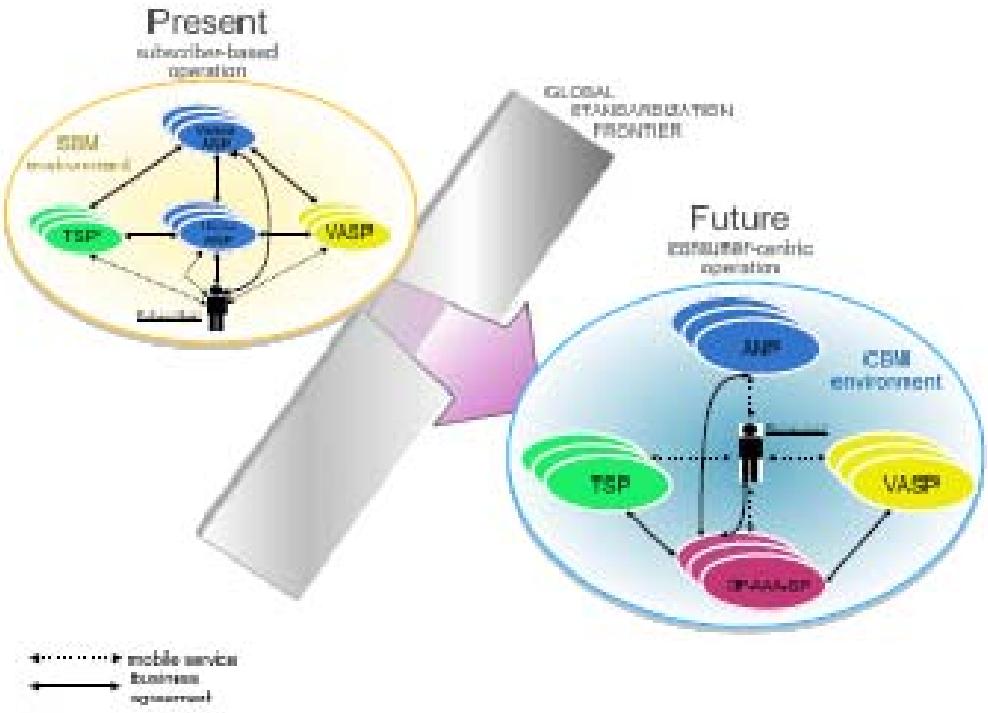

Figure 1: Subscriber-based (SBM) and consumer-centric (CBM) techno-business models.

The main downsides of SBM, mainly linked to the 'lock-in' constraint of the (long-term) subscriber contract with a home-ANP, include: roaming charges which are often perceived as non-cost based, domination of ANP marketplace by a few large operators, poor market openness for new or niche ANPs due to prohibitive start-up costs, limited 'number portability & mobility' among ANPs. In regard to the latter, subscribers who desire to move ANP, rather than porting their number, tend to the

easier solution of buying a new (U)SIM card with another phone number in the other network. *Spinning* is another popular approach whereby subscribers, using multiple-(U)SIM-card phones, can choose to operate on any one of ANPs at any time. However, this is still quite far removed from the full 'number portability & mobility' within the CBM, where consumers will be allowed always to use the 'best' ANP for each particular service instance.

Transition to UCWW and enabling the growth of CBM open opportunities to address these issues. The two principles underpinning this new CBM environment are: (i) the decoupling and separation of the administration and management of users' AAA activity from the supply of a wireless access (transport) service and its devolution to new non-ANP trusted 3P-AAA entities, and (ii) the full consumer ownership and portability of their globally significant address.

Besides a range of new benefits for the consumer, UCWW has the clear potential to stimulate the creation of a number of new interesting business opportunities and to create a more liberal, more open and fairer wireless marketplace for existing and new ANPs. The primary ANP business success indicator will shift from subscriber numbers to the volume of consumer transactions – a radical change. This will increase the range of competitive price/performance and price/QoS offerings, specialist and niche access-network service offerings, and so forth, all of which will drive forward innovation in the mobile services market.

The preliminary blue-skies research work on crystallizing and defining the UCWW concepts and its key infrastructural pillars has been done already, e.g., (O'Droma, 2007) & (O'Droma, 2010). In-depth research, elaboration, design and implementation of these novel infrastructural components along with their integration into a pilot system prototype are the next phase of this project. The main goals are the following:

- Research, innovate, derive, design, implement, field-trial, validate and evaluate the performance of:
  - A feasible UCWW software architecture, operating within OSGi (Alliance, 2007) and cloud environments.
  - New UCWW infrastructural protocol interfaces and functionalities, especially for those on the 3P-AAA (Ganchev, 2006) and the third-party charging and billing (3P-C&B) (Jakab, 2011) service provision infrastructural elements, which satisfy and respect the network-independent, autonomous, trusted, and pervasive requirements and criteria of the service providers entities;
  - A prototype of the new universal CIM card employing the new 'personal IPv6' identity, (Ganchev, 2007) & (Ganchev, 2009).
- Design and establish the technological dimensions of the first scalable UCWW cloud-based system and provide a field-trial demonstration of its operation.
- On the back-end, design an UCWW cloud to facilitate the storage of user data harvested via mobile devices, and based on the analysis of this data, to offer predictions as to the applicability of services to particular users, and enable ever-enhanced contextualization and personalization functionalities and services. By monitoring this information, the system should accurately predict the types of services most applicable to individuals, and in turn, recommend these to the users. Furthermore, efficient heuristic algorithms must be designed to facilitate service utilization predictions locally on the mobile devices or as part of the UCWW cloud as an alternative to mining the stored data.
- Within the client devices, facilitate the effective functional design of the user profiles and GUI templates, targeted at the major smartphone platforms (Android, iOS, Windows Mobile), with each variation interoperating with the UCWW back-end cloud.
- Finally, making this UCWW cloud-based system commercially viable will be investigated. Clearly legacy mobile operators are likely to be reluctant to open their own customer profile database to competitors in whatever way that might happen; or not happen, as it is not in anyway essential to the proposal. UCWW cloud providers will market their services directly to consumers. In such a market, legacy providers would already be in prime position – to manage and market their own UCWW cloud services. Hence, the proposals in this paper could make the shift to UCWW more attractive for these operators. With such realization potency in mind, the deployment of service contextualization mechanisms will be investigated from an operator's point of view.

3 THE UCWW CLOUD AS A CONTEXT-AWARE MIDDLEWARE

From one point of view, the UCWW cloud that we envision can operate as a middleware of a context-aware system. In its traditional sense, a context-aware system is a distributed system, which consists of hardware devices (sensors) to sense or collect context data, applications which make use of this data, and middleware that manages the flow of context data from the points of collection to the applications. In our case mobile devices such as smartphones and tablet computers play the role both of the sensors of context data and the platform that runs applications which use this data. Besides the context that relates to the mobile *services* available and on offer, the context data may relate to the *user* (e.g., the user location, local time, current battery charge and other operational characteristics of the user's mobile device, etc.), and/or relate to the constraints of the wireless access *network* currently utilized by the user (e.g., QoS level and pricing scheme,), Figure 2.

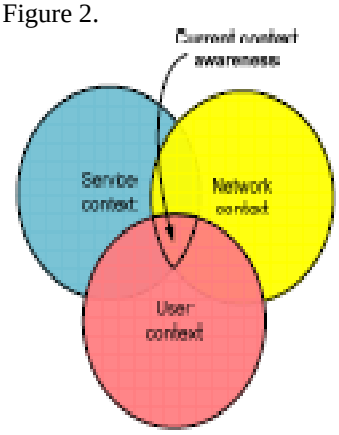

Figure 2: Context types and context awareness in UCWW.

According to the characterization of context-aware systems proposed in (Henricksen, 2005), the various functions and components of such systems can be organized into a five-layer architectural model, with layers (each providing services for the layer above it) as follows:

- *Layer 4*: Application components.
- *Layer 3*: Decision support tools/subsystem.
- *Layer 2*: Context repositories.
- *Layer 1*: Context processing components.
- *Layer 0*: Context sensors.

At the lowest layer, the mobile devices collect context data from the environment, and at the highest layer applications, which run on those mobile devices, make use of this data. Layers 1-3 form the middleware of the system, which can be entirely or partially implemented as cloud services. In particular, we propose layers 2 and 3 to be entirely implemented within the cloud, while layer 1 can be partially implemented at the mobile devices for increasing the overall efficiency of the system.

Surveys of context-aware middleware, (Henricksen, 2005) & (Romero, 2008), summarize the functional and non-functional requirements for a context-aware middleware. Besides the functions, already listed above (i.e., processing of context data, storing context data in repositories, and providing decision support tools), a context-aware middleware may also be expected to address the following issues:

- *Heterogeneity*: In our particular case, this means to support a variety of mobile devices and operating systems.
- *Adaptation*: In order to adapt to the user's habits, the system needs to perceive the context of the environment (via sensors) and quickly react and adapt to changes in the context. This is particularly important for our system because we expect frequent and constant changes in the context due to the mobile nature of the user devices (sensors).
- *Scalability*: The performance of the system when interacting with a large number of users should be on the same scale as when interacting with a small number of users. In a typical scenario, there could be a few thousands of sensors at a site (e.g., a large airport) and potentially millions of users at various sites who simultaneously query the decision support subsystem (c.f. the query configuration in Figure 3).
- *Privacy*: The privacy of the users' data must be maintained according to their preferences. Levels of confidentiality, options in regard to this, and distribution of responsibility are challenging issues in this context.
- *Traceability and control*: Users should be able to control any automatic functions of the system and the systems should provide means of making those decisions transparent to users.
- *Application building support*: It is also essential for our system to provide application programming interfaces (APIs), which enable software developers to build a variety of smartphone applications which interact with the context-aware middleware.
- *Easy deployment and configuration.*
- *Tolerance to component faults.*

There have been a few generic context-aware middleware solutions proposed in the research literature, including Gaia (Román, 2002), Reconfigurable Context-Sensitive Middleware (RCSM) (Yau, 2002), PACE (Henricksen, 2005), CARISMA (Capra, 2003). While using these as a base for comparison, we propose to design a cloud which provides the features expected from a context-aware middleware and at the same time is highly specialized for the particular nature of the UCWW.

Furthermore, we consider a concept of context which allows the decision support subsystem to make smart decisions based on mining of data stored in the cloud repositories. We propose the context to include both the data sensed by the sensors in the environment (as in a typical context-aware system), and the history of the user and the collective history of users who have used the system in the same environment. To the best of our knowledge, this is a novel approach in providing context-aware services with elements of personalized information retrieval (PIR) in a mobile network environment.

Extension of the UCWW cloud's functionality is also envisaged which will open opportunities for trusted third-party communication service providers (Toseef, 2011). These will negotiate with providers on behalf of users for their service requests and they may assist in handling seamless handovers to ensure uninterrupted service delivery to users.

4. DECISION SUPPORT SUBSYSTEM

Figure 3 summarizes the flow of context data between a smart mobile device and the UCWW cloud as well as the mechanism of sending requests and receiving responses from the decision support subsystem. The role of the decision support subsystem is to provide ratings (ranking) of the service providers available for particular type of service requested by the user. In order to make accurate predictions, the decision support system makes use of additional context data, which may include any of the following:

- User-specified parameters such as the upper bound on the price, lower bound on QoS, etc.;
- Current user location, current time, battery charge and potentially other parameters of the environment;
- The request and decision history of the user who is requesting the decision;
- The request and decision history of users who have requested the same service in the same or similar context.
- 'User-unaware' context autonomous cloud functionality, including new wireless services of which a user(s) may be totally unaware but may likely prefer as a replacement for existing services. An example could be the vast array of government services coming down the line, e.g., G-Cloud in the UK (c.f. gcloud.civilservice.gov.uk).

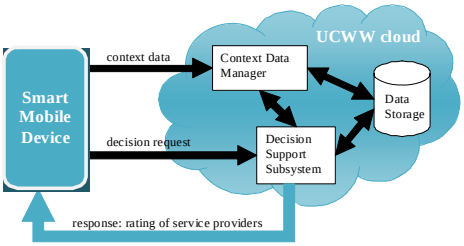

Figure 3: Communication between a smart mobile device and the UCWW cloud.

Context data can be sent from the mobile device to the cloud either together with the request for decision or asynchronously when changes in the context occur. Any context data gets processed by the context data manager which prepares the data for storage and makes changes to the data storage. When a request for a decision arrives, it is accepted by the decision support subsystem, which in turn requests the current context from the context data manager before making a decision. After a decision is made, the decision support subsystem notifies the context data manager so that the decision can be stored in the data storage. In accordance with the requirements listed in the previous section, the decision support subsystem may also accept requests to explain its decision. In satisfying such requests, it is assisted by the context data manager, which can provide the correct historic information that was used in making the decision. Such mechanisms would also serve service auditing processes, service level agreements, etc.

Systems which retrieve information that is both relevant to the submitted queries and personalized for the user are known as PIR systems. They have been the subject of extensive research in the last couple of decades with a major application in web search as well as in other areas such as eLearning and news dissemination (Ghorab, 2012). A community-based PIR (Teevan, 2009) & (Sugiyama, 2004) would suit our needs best because ideally we would like to offer personalized results to the user

based on their previous behaviour and experience but also based on the experience of other users who have used the service in a similar context. An early research action is to decide what information about users should be tracked, how this information will be gathered and stored in a user model and then how user models will be used for retrieving personalized results.

In summary, we propose to build the data repository according to existing models employed for community-based PIR. The decision support subsystem will be tuned by experimenting with a variety of data mining algorithms (Witten, 2011) and finding an acceptable compromise between speed and accuracy of the predicted rating of providers. Once the decision support subsystem's software tool can make accurate predictions – whether by running heuristic algorithms for solving optimization problems (Papadimitriou, 1998) locally on the smart mobile device or by using a service provided by the cloud, or a combination of both –, these predictions can be delivered to the application level and incorporated into the client's GUI, aiding the user in making a choice for a particular service or, where the user so desires, configuring the system to make automatic choices.

5 IMPLEMENTATION ISSUES

While UCWW is a completely distributed wireless communications environment as described earlier, one could conceptually consider the software underpinning its various infrastructural elements within a conceptual software architectural model. This may help facilitate comprehensive, systematic, organized and managed software designs and solutions, with a view also towards increasing software re-use. Hence below a speculative 3-tier architecture model is suggested (Figure 4).

5.1 UCWW software architecture model

The 3-tier UCWW software architecture model typically would include, at the application tier level, such key elements as the 3P-AAA/3P-C&B applications, the CIM card, a multi-agent platform, and a Hadoop cloud environment (Borthakur, 2007).

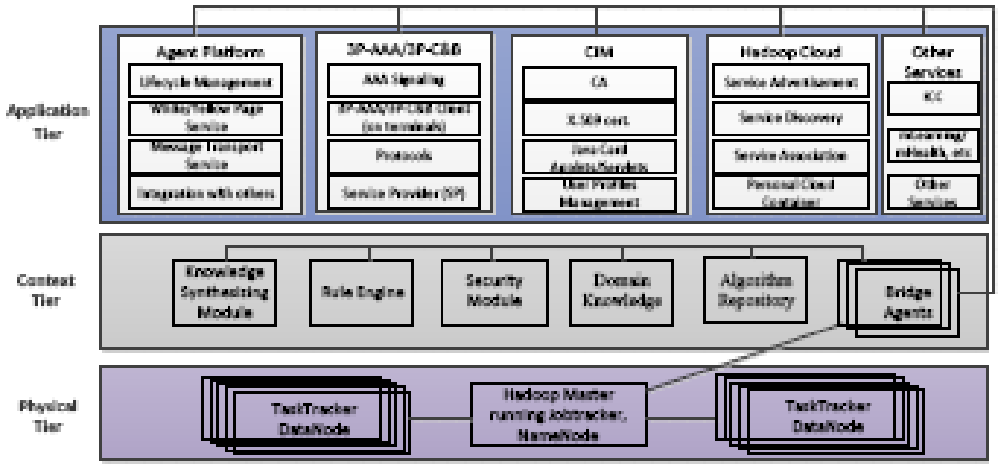

Figure 4: The UCWW software architecture model.

The UCWW middleware is being developed with three clusters, namely Kafka (kafka.apache.org), Storm (storm-project.net), and Hadoop HDFS (Figures 5 & 6). Kafka is a high-throughput distributed messaging system, used as a load balancing cluster for parallel data loading into Hadoop. The data output from Kafka is sent to the Storm cluster for real-time processing. Then the useful dataset is serialized to HBase in the Hadoop cluster. The Hive (hive.apache.org), Cloudera Impala (ccp.cloudera.com), and Flume (flume.apache.org) will be used for data mining.

5.2 3P-AAA/3P-C&B

Based on the 3P-AAA/3P-C&B infrastructure, an amendment to ITU-T's SBM authentication architecture for interworking in NGN is being designed, developed and implemented (O'Droma, 2008), based on the ITU-T Draft Rec. Q.3202.1

(ITU-T, 2008) SBM 3P-AAA model. A JDiameter (JDiameter, 2013) based 3P-AAA framework is being realized. The 3P-AAA/3P-C&B platform will be realized in a lab environment with corresponding mix of client applications for smartphones.

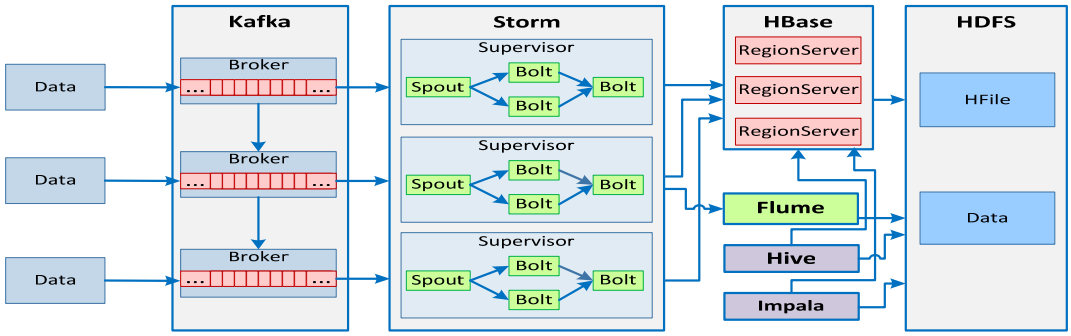

Figure 5: The UCWW middleware.

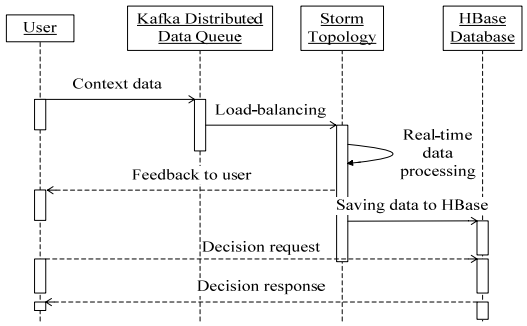

Figure 6: Context data processing in the UCWW middleware.

5.3 CIM

The universal CIM card acts as a user data server in the UCWW system. A number of security applications run on a single virtual machine to maintain the user profiles, associated credit-card information, user's personal IPv6 address, 3P-AAA/3P-C&B related data, X.509 certification, personal cloud container, etc., and ROM and EEPROM on the CIM card. These applications will communicate with each other using shared interface objects (SIO), (Avvenuti, 2012). A firewall is defined by each application to provide application-level security.

A personal cloud container is being designed to include a UCWW personal cloud identifier, personal data category, session ID, cookies, etc. The client application is being developed to work within a Google Android (Fledel, 2012) environment (Figure 7). A SIMAlliance Open Mobile API specification (SIMAlliance, 2013) will be integrated into the Android platform to enable user devices to communicate with secure elements of the CIM.

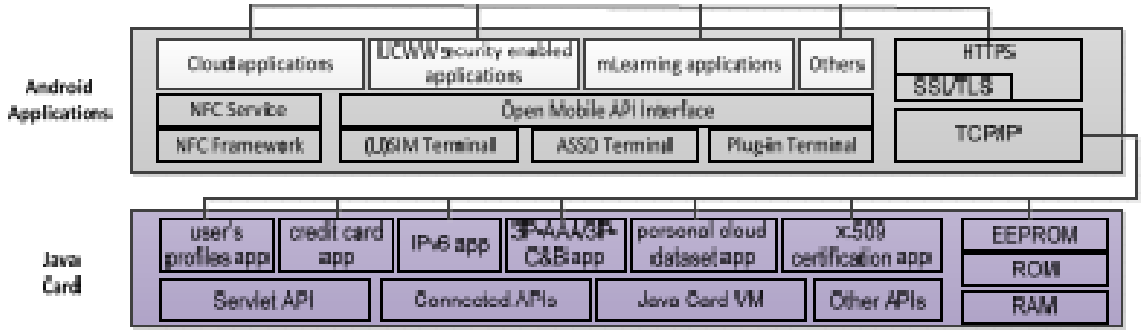

Figure 7. The CIM module on Android.

6 CONCLUSIONS AND FUTURE WORK

The UCWW infrastructural entities and protocols are all novel. Hence also all of the work on this project is innovative and advancing knowledge in the area. Our work will show that this completely original way of organizing the global mobile telecoms business is feasible. The innovative infrastructural and technological changes to be realized in the pilot field trial will demonstrate how UCWW will enable greater service choice, contextualization and management capabilities for consumers, much more openness in the wireless access market for the supply of mobile services, and a technologically friendly environment for the incorporation of new and revolutionary ideas in wireless communications. It will demonstrate for instance, the inherent full number-portability and the disappearance of roaming charges. The work will yield foundational contributions to global NGN standardization work within ITU-T's Future Networks workgroup.

The UCWW is a big undertaking with huge and complex international socio-economic implications for the wireless communications business, and encompassing the present and future rapid growth of wireless communications and cloud-based computing technologies. Our aim is to design a context-aware middleware for the UCWW by having most of its functions offered as cloud services and the rest running locally on mobile devices. In addition, we plan to create a set of sample GUIs, which possess the necessary intelligence to harvest the requisite information to facilitate service predictions (Raskin, 2000). The design and development of an efficient context-aware middleware for the UCWW cloud requires taking into account a number of aspects:

- On the back-end, the designed UCWW cloud must facilitate the storage of data harvested via mobile devices, and based on the analysis of this data, offer predictions as to the applicability and ABC&S suitability of services to particular users. Over time the data collected relating to particular users can give an accurate view of particular cohorts, based on common interests, repetitive access of particular services, etc. By monitoring this information, the system can accurately predict the types of services most applicable to individuals, and in turn, recommend these to the users. Furthermore, efficient heuristic algorithms must be investigated to facilitate service utilization predictions locally on the mobile devices or as part of the UCWW cloud as an alternative to mining the stored data.
- The option of this UCWW cloud collaboration with wireless billboard channel (WBC) service providers (Flynn, 2006) holds potential. Through it, consumers may have their UCWW cloud distilled information, relevant to their particular (or upcoming) location and time, delivered to them in a personalized frame through an appropriate WBC.
- Within the client devices, an effective functional design of the GUI must be facilitated. With this in mind, different mobile platforms will be targeted, particularly in the case of the smartphones market, where Android-based devices, iPhones, Windows phones etc. each have a market share.

ACKNOWLEDGEMENTS

The authors wish to acknowledge the support of the Telecommunications Research Centre (TRC), UL, Ireland and the NPD of the Plovdiv University under Grant No. NI11-FMI-004.

REFERENCES

Alliance, O., 2007. *OSGi service platform, core specification, release 4, version 4.1*, OSGi Specification.

Avvenuti, M., Bernardeschi, C., Francesco, N. D., Masci, P., 2012. *JCSI: A tool for checking secure information flow in Java Card applications*, In Journal of Systems and Software.

Borthakur, D., 2007. *The Hadoop distributed file system: Architecture and design*. In Hadoop Project Website, vol. 11.

Capra, L., Emmerich, W., Mascolo, C. Carisma, 2003. *Context-aware reflective middleware system for mobile applications.* In IEEE Transactions on Software Engineering, 29 (10).

Carugi, M., Hirschman, B., et al., 2005. *Introduction to the ITU-T NGN focus group release 1: target environment, services, and capabilities*. In IEEE Communications Magazine. 43(10).

Cook, W., Cunningham, W., Pulleyblank, W., Schrijver, A., 1997. *Combinatorial Optimization*. John Wiley & Sons. 1st edition.

Ekstrom, H., Furuskar, A., et al., 2006. *Technical solutions for the 3G long-term evolution. In IEEE Communications Magazine, 44(3).*

Fledel, Y., Shabtai, A., Potashnik, D., Elovici, Y., 2012. *Google Android: An Updated Security Review*. In Mobile Computing, Applications, and Services.

Flynn, P., Ganchev, I., O'Droma, M., 2006. *Wireless Billboard Channels: Vehicle and Infrastructural Support for Advertisement, Discovery, and Association of UCWW Services*, In: Annual Review of Communications, Vol. 59 (Chicago, Ill.: International Engineering Consortium).

Ganchev, I., O'Droma, M., Siebert, M., Bader, F., Chaouchi, H., et al., 2006. *A 4G Generic ANWIRE System and Service Integration Architecture.* In ACM SIGMOBILE Mobile Computing and Communications Review, 10(1).

Ganchev, I., O'Droma, M., 2007. *New personal IPv6 address scheme and universal CIM card for UCWW*. In ITST'07, 7th International Conference on Intelligent Transport Systems Telecommunications.

Ganchev, I., O'Droma, M., Wang, N., 2009. *Consumer-Oriented Incoming Call Connection Service for UCWW*. In Springer Wireless Personal Communications, 50(1).

Garey, M., Johnson, D., 1979. *Computers and Intractability: A Guide to the Theory of NP-Completeness*, W. H. Freeman. USA.

Ghorab, M. R., Zhou, D., O'Connor, A., Wade, V., 2012. *Personalised Information Retrieval: survey and classification.* In User Modeling and User-Adapted Interaction, Springer. Netherlands.

Henricksen, K., Indulska, J., McFadden, T., Sasitharan Balasubramaniam, S., 2005. *Middleware for Distributed Context-Aware Systems*. In OTM'05, On the Move to Meaningful Internet Systems. LNCS 3760, Springer.

ITU-T Draft Rec. Q.3202.1 (Q.nacf.auth1), 2008. *Authentication Protocols based on EAP-AKA for Interworking among 3GPP, WiMax, and WLAN* in NGN.

Jakab, J., Ganchev, I., O'Droma, M., 2011. *Third-Party Charging and Billing for the Ubiquitous Consumer Wireless World.* In International Journal on Communications, Antenna and Propagation, 1(2).

JDiameter Project, URL (2013) http://code.google.com/p/jdiameter/.

Kibria, M. R., Jamalipour, A., 2007. *On designing issues of the next generation mobile network.* In IEEE Network. 21(1).

Mikut, R., Reischl, M., 2011. *Data mining tools*. In Wiley Interdisciplinary Reviews: Data Mining and Knowledge Discovery, 1.

O'Droma, M., Ganchev, I., 2007. *Toward a ubiquitous consumer wireless world*, In IEEE Wireless Communications, 14 (1).

O'Droma, M., Ganchev, I., 2008. *Strategic Innovations through NGN Standardization for a Ubiquitous Consumer Wireless World.* In 1st ITU-T Kaleidoscope Academic Conference "Innovations in NGN".

O'Droma M., Ganchev, I., 2010. *The Creation of a Ubiquitous Consumer Wireless World through Strategic ITU-T Standardization.* In IEEE Communications Magazine, 48 (10).

Papadimitriou, C., Steiglitz, K., 1998. *Combinatorial optimization: algorithms and complexity*. Dover. 2nd edition.

Passas, N., Paskalis, S., Kaloxylos, A., et al., 2004. *Enabling technologies for the 'always best connected' concept.* In Wiley Wireless Communications and Mobile Computing, 6(4).

Raskin, J., 2000. *The humane interface - New directions for designing interactive systems*. Addison Wesley. Reading, MA, USA.

Román, M., Hess, C.K., Cerqueira, R., Ranganathan, A., Campbell, R.H., Nahrstedt, K., 2002. *Gaia: A Middleware Infrastructure to Enable Active Spaces.* In IEEE Pervasive Computing.

Romero, D, 2008. *Context-Aware Middleware: An overview.* Paradigma.

SIMAlliance, Open Mobile API: An Introduction. URL(2013) http://www.simalliance.org/.

Sugiyama, K., Hatano, K., Yoshikawa, M., 2004. *Adaptive Web search based on user profile constructed without any effort from users.* In WWW '04, 13th International Conference on World Wide Web.

Teevan, J., Morris, M.R., Bush, S., 2009. *Discovering and using groups to improve personalized search.* In WSDM 2009, 2nd ACM International Conference on Web Search and Data Mining.

Toseef, U., Khan, M.A., Gorg, C., Timm-Giel, A., 2011. *User satisfaction based resource allocation in future heterogeneous wireless networks,* In CNSR 2011, 9th Annual Communication Networks and Services Research Conference.

Usama, F., Piatetsky-Shapiro, G., Smyth, P., 1996. *From Data Mining to Knowledge Discovery in Databases.* In AI Magazine, 17.

Witten, I, Frank, E., Hall, M, 2011. *Data Mining: Practical Machine Learning Tools and Techniques.* Elsevier. 3rd edition.

Wolsey, L., Nemhauser, G., 1999. *Integer and Combinatorial Optimization*. Wiley-Interscience. New York, NY, USA.

Yau, S.S., Karim, F., Wang, Y., Wang, B., Gupta, S.K.S., 2002. *Reconfigurable context-sensitive middleware for pervasive computing.* In IEEE Pervasive Computing, 1(3).

ANALYTICAL DESCRIPTION OF THE PRODUCTION OF FORMATS IN HUMAN SPEECH

Damyan Damyanov
Technical University of Sofia, Faculty of Automation, Department for Industrial Automation,
Bulgaria, Sofia, Darvenitsa 1756,Bul. Kliment Ohridksi 8, block 9,room 9420
damyan_damyanov@tu-sofia.bg

Keywords: model of speech production, man-machine systems.

Abstract: For the purposes. of speech synthesis, biometrics , medical and psychological diagnosis, the functioning of the glottis during phonation has been studied many times. At present, a relatively trivial solution proposed by Fant has established itself, regardless of the actual purpose of the system, using the "pusle source - filter" model. The model of Fant allows the linear prediction method to perform reconstruction of the current form of the vocal tract and the excitation of glottal volume velocity. But the practice shows that the fluctuations of the speech tract due to psycho-physiological effect on the functioning of the facial muscles in most cases are negligible. Thus, they are below the accuracy, which the linear model allows, using approximation with a cascade of coaxial cylindrical sections of equal length and constant cross-section. This requires more complex algorithms, and thus additional information is extracted from the pattern of air volume velocity after glottis. In this study, it is to be shown, that the model of Fant actually allows depiction of the psycho-physiological changes in the spectral features of the speech signal without the use of additional models. For this purpose it is sufficient to analyze the relationships of the main parameters of the excitation pulse of the source with the frequency response of the filter. In the current practice, these correlations are not considered and the source and the filter are examined separately.

1 INTRODUCTION

Phonation is a process which takes place in the middle part of the larynx and sets up vibrations to the exhaled airstream. As a consequence of this process the air volume velocity after the glottis immediately shows vibrational patterns (Figure 1), which determines the pitch frequency of the speech signal (Тилков, Д., Бояджиев., Т 1990). Changing the tension of the vocal folds and the pressure during the speech production process, one gets the desired pitch frequency, needed for phonation of vowels and voiced consonants. In the formation of non-voiced consonants the vocal folds do not come near each other and their constellation is like at physiological breathing (Pickett J.M, 1982). In this case, the incoming air pressure from the lungs is modulated by the formation of turbulence and closure of the vocal tract. The spectra of the resulting sound sources are modified by resonances, the frequency of which depends on the time-varying shape of the throat and mouth, the location of the tongue and many more.

Modern study of acoustic phenomena in the oral-pharyngeal tract began in 1941 with the work of Chiba and Kajiyama (Chiba, T., Kajiyama M., 1941). The fundament of the present theory and practice is shaped in 1960 by Fant (Fant, G., 1960), and others. The systems for processing, transmitting and storing of speech signals use various methods and techniques, but they are all based on a model of the functioning of articulatory tract and the air volume velocity after the glottis. The purpose of the modelling process of speech production is not only to study its properties and specifics, but also to solve problems for its effective coding and transmission ,

the automatic synthesis of speech and speech recognition, for biometrical applications and others.

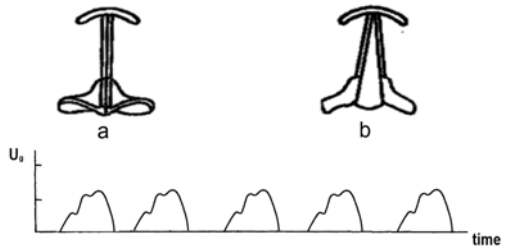

Figure 1: Air volume velocity immediately after the glottis for vowels and voiced consonants. Position of the vocal folds: a - phonation of vowels and voiced consonants, b - physiological breathing.

In every such model (Proakis, J.,2000), in one degree of another, the main components of articulatory tract in terms of the laws of acoustics are reflected (Figure 2)

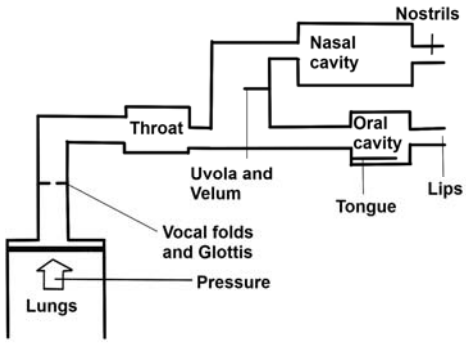

Figure 2: Main components of the acoustic articulatory tract.

These components include the excitation of the vocal cords, the time-varying shape of the vocal tract, radiation from the lips etc. Resonant phenomena in the speech production process are actually affected by losses in the walls of the tract, depending on the thermal conductivity, elasticity and friction. Significant influence is done by the nasal cavity with the absorption of certain frequency components of the spectrum (antiresonant phenomena). This complex nature of the process allows the development of many models, differing in structure and degree of relevance. Interestingly, despite the apparent complexity of the problem, it found a relatively trivial solution proposed by Fant (Fant, G., 1960), which has established itself in practice regardless of the actual purpose of the system.

The classical model of Fant separates the excitation from the shaping of individual sound components of speech, allowing approximately treatment of speech sounds as a linear system. Lungs, which provide air volume velocity, are presented as direct current power source. Their output is divided, corresponding respectively to the voiced and unvoiced parts of the signal. The pulse generator modulates the air volume velocity from periodical excitation of the vocal folds, and the noise generator models the formation of turbulence in the places, where the vocal tract changes its cross-section. The final speech signal is obtained after the components are added together and passed through a filter with linear transfer function, which models the articulatory tract.

In modern systems, this model has found its discrete implementation (Figure 3).

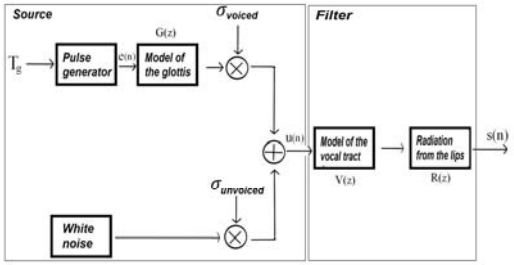

Figure 3: Digitalized model of Fant.

Generating a voiced speech segment after the z-transform of a sampled speech signal is described by the equation:

$$S(z) = U_g(z)V(z)L(z) \tag{1}$$

$$U_g(z) = \sum_{n=0}^{\infty}(z^{-K})^n G(z)\sigma_{son} = \frac{\sigma_{son}}{1-z^{-K}}G(z) \tag{2}$$

It is assumed, that the sampling period is T=1, and the period of the pitch frequency is a multiple of it Tp = KT (Damyanov, D., Galabov, V., 2012a). The transfer function of the model of the glottis, the model of the vocal tract and the lips radiation can be combined in a common transfer function:

$$H(z) = G(z)V(z)L(z) \tag{3}$$

And the speech production process can be written as

$$S(z) = E(z)H(z) \tag{4}$$

$$S(z) = Z\{s(nT)\}, \quad s(nT) = s(t)\big|_{t=nT} \tag{5}$$

Where E(z) is the z-transformed pulse excitation of the glottis. Adoption of certain hypothesis about the spectral properties of the glottis, of the vocal tract and the lips radiation (Fant, G., 1960) allows the use of an all-pole filter:

$$H(z) = \frac{1}{1 + \sum_{i=1}^{M} a_i z^{-i}} \tag{6}$$

Finding the coefficients of this filter is a task, successfully solved in theory and practice. (Proakis, J.,2000, Trashlieva, V., Puleva, T., 2011)

2 MOTIVATION

Using a process of speech production of type source-filter, based on the model of Fant, many of the tasks, associated with the processing of speech signals are successfully solved. In this study, it is to be shown, that despite their simplicity, these models are able to explain some phenomena of the speech production, observed in the changes of current psycho-physiological state of humans. These include changed rations of the amplitudes of formant frequencies (less harsh or ringing voice), impaired understandability, etc. For their description and analysis of the functioning of the glottis during phonation has been studied many times, in order to create relevant model, especially for the purposes of speech synthesis, medical and psychological diagnosis, and biometrics. Much of the testing methods are borrowed from medicine in order to achieve greater accuracy, or to make measuring easier. All of the above methods do not work directly with the desired variable, but with some other, depending on the desired one. Given the complexity of making laryngoscopic and laryngoendoscopic studies, and especially the need for medical intervention, and because of the significant impact of these methods on the overall process of speech production, a great number of indirect methods have been developed. These include methods, base on electromyography - registering the signals of muscle activity in the throat while speaking, glottography - working with the impedance of the neck in the plane of the glottis, which largely depends on the cross-section of the air volume velocity after the glottis. Despite numerous studies, currently there is no unified theory that explains the process of these changes in the spectral characteristics of the speech signal. Most authors seek the cause of these phenomena in the psycho-physiological change in current form of the articulatory tract. The model of Fant allows the linear prediction method to perform reconstruction (with some degree of approximation) of the current form of the tract and the excitation of acoustic volume velocity after the glottis. It is expected, that the modelling of the speech tract provides conditions for obtaining relevant information about the functioning of the facial muscles and the corresponding parts of the nervous system, which are extremely sensitive to current psycho-physiological state of the individual (Ekman, P, Friesen, W., 1978). But the practice shows, that the fluctuations of the speech tract due to psycho-physiological effect on the functioning of the facial muscles in most cases are too small . Thus they are below the accuracy, which the linear model allows, using approximation with a cascade of coaxial cylindrical sections of equal length and constant cross-section (Pfister, B., Kaufmann, T., 2008).

This requires more complex algorithms and thus additional information is extracted from the pattern of air volume velocity after glottis. The air volume velocity gives information about the current psycho-physiological condition in two ways - first, through the entire process of speech production, concerning the higher nervous activity, and the second by the functional state of the autonomic nervous system, including the overall muscular tonus (Reuter-Lorenz, Patricia A., et.al., 2010, Kalat, James W. 2012). For the extraction of this information, the use of relatively complex models is required, describing the tension on the vocal folds, the mechanism of stretching and vibrating, the pressure of the incoming air flow from the lungs, etc. In this study, it is to be shown, that the model of Fant actually allows depiction of the psycho-physiological changes in the spectral features of the speech signal without the use of additional models. For this purpose, it is sufficient to analyze the relationships of the main parameters of the excitation pulse of the source with the frequency response of the filter. In the current practice, these correlations are not considered and the source and the filter are examined separately. For readability purposes, the following simplifications will be made that do not change the generality of the study:

- The influence of the transfer function of the glottis and the lips radiation will be neglected, since they don't affect the

formant frequencies, but only their decay ;

- The excitation of the source will be considered as a sequence of rectangular pulses;
- The attenuation of formant frequencies will be ignored, i.e. poles of the filter of the vocal tract will lie of the unit circle;

3 PRODUCTION OF FORMANTS IN HUMAN SPEECH

In this study, it is assumed, that the model of the vocal tract is of second order:

$$H(s) = \frac{k_1 \omega_1^2}{s^2 + \omega_1^2} \tag{7}$$

i.e. the signal will contain only one formant with circular frequency ω_1 . The excitation pulses are of type (Damyanov, D., Galabov, V., 2012b):

$$e(t) = \begin{cases} 1, & (m-1)T_g \le t < t_{open\_glottis} + (m-1)T_g \\ 0, & t_{open\_glottis} + (m-1)T_g \le t < mT_g \end{cases} \tag{8}$$
$$m = \overline{1, N_{imp} - 1}$$

where T_g is the period of the pitch frequency , and $t_{open\_glottis}$ is the duration of the phase of open glottis. The output signal for the period of the pitch frequency (m=1) is:

$$s^{1F}_{open\_glottis}(t) = AO^{1F}_{open\_glottis} - A^{1F}_{open\_glottis} \sin(\omega_1 t + \varphi^{1F}_{open\_glottis}) \tag{9}$$

for $t_{open\_glottis}$, i.e. in the phase of open glottis, and:

$$s^{1F}_{closed\_glottis}(t) = \\ = A^{1F}_{closed\_glottis} \sin(\omega_1 t + \phi^{1F}_{closed\_glottis}) \tag{10}$$

for $t \ge t_{open\_glottis}$, i.e. in the phase of closed glottis, where:

$AO^{1F}_{open\_glottis} = k_1$ is the DC component of the signal in the phase of open glottis

$A^{1F}_{open\_glottis} = k_1$ and

$A^{1F}_{closed\_glottis} = 2k_1 \sin(\frac{\omega_1 t_{open\_glottis}}{2})$ are the amplitudes of the signal in the phases of open and closed glottis

$\varphi^{1F}_{open\_glottis} = \frac{\pi}{2}$ and

$\varphi^{1F}_{closed\_glottis} = 2\pi - \frac{\omega_1 t_{open\_glottis}}{2}$ are the angular phases of the signal in the phases of open and closed glottis

$\omega_1 = 2\pi f_1$ are the circular frequency, which corresponds to the formant frequency f_1 .

We can observe the following important features:

- In the two phases - of open and closed glottis - the formant frequency is determined only on the coefficient of plain gain of the filter
- The amplitude of the signal in the phase of closed glottis depends again on this coefficient, but also in a complicated way on the ratio of duration of the preceding phase of open glottis to the period of the formant frequency.
- The phase shift of the signal depends in a similar way on the above stated variables.

Practically, this means that without changes in the filter parameters, i.e. the geometry of the vocal tract, changes in length of the phase of open glottis can increase or decrease the formant frequencies of the speech signal (Damyanov, D., Galabov, V., 2012a). For better understanding of the paradigm, a dimensionless coefficient is introduced, which is proportional to the duration of the phase of open glottis to the period of the formant frequency:

$$r_{\omega_1 t_{open\_glottis}} = \omega_1 t_{open\_glottis} \tag{11}$$

In terms of amplitude of the signal before and after closure of the glottis the coefficient can be defined:

$$r_{A^{1F}_{open\_glottis} A^{1F}_{closed\_glottis}} = \frac{A^{1F}_{open\_glottis}}{A^{1F}_{closed\_glottis}} \tag{12}$$

where the $t_{closed\_glottis} = T_g - t_{open\_glottis}$ is the duration of the phase of closed glottis during the period of the pitch frequency (Damyanov, D., Galabov, V., 2012b). The functional relationship between these two coefficients is:

$$r_{A^{1F}_{open\_glottis}A^{1F}_{closed\_glottis}} = f\left(r_{\omega_1 t_{open\_glottis}}\right) = \left|2\sin(\frac{\omega_1 t_{open\_glottis}}{2})\right| \quad (13)$$

It can be seen, that varying the duration of the phase of open glottis, without changing the filter parameters, i.e. the geometry of the vocal tract, for a given amplitude of the generated signal in the phase of closed glottis can take any value from zero to two times the amplitude in the phase of open glottis (Damyanov, D., Galabov, V., 2012c).

This effect becomes more interesting, if the speech segment contains several periods of the pitch frequency. Then, besides the coefficient $r_{\omega_1 t_{open\_glottis}} = \omega_1 t_{open\_glottis}$, the ratio of the amplitudes will be affected by the ratio of the length phase of closed glottis during the period of pitch frequency:

$$k_{full\_imp} = \frac{t_{open\_glottis}}{T_g} \quad (14)$$

In this case one can obtain relatively complex analytical dependencies. For example the relationship of the amplitudes of the signal in the phase of closed glottis to the phase of open glottis in the second period of the pitch frequency is given by

$$r_{A^{1F}_{open\_glottis}A^{1F}_{closed\_glottis}} = f(r_{\omega_1 t_{open\_glottis}}) = \left[4k_1 \sin(\frac{r_{\omega_1 t_{open\_glottis}}}{2})\cos(\frac{r_{\omega_1 t_{open\_glottis}}}{2k_{full\_imp}})\right] \quad (15)$$
$$\left[\left(k_1 \sin(r_{\omega_1 t_{open\_glottis}}) + k_1 \sin(2\pi - \frac{r_{\omega_1 t_{open\_glottis}}}{k_{full\_imp}})\right)^2 + \left(-2k_1 \sin^2(\frac{r_{\omega_1 t_{open\_glottis}}}{2}) + k_1 \sin(\frac{r_{\omega_1 t_{open\_glottis}}}{k_{full\_imp}} - \frac{\pi}{2})\right)^2\right]^{-\frac{1}{2}}$$

If we assume that:

$$numbits = total\ number\ of\ bits\ from\ the\ binary\ presentati\ on\ of\ N \quad (16)$$

Then, for the N-th period of the pitch frequency the dependencies are as follows:

$$A^{1F}_{closed\_glottis} = 2k_1' \sin(\frac{\omega_1 t_{open\_glottis}}{2})$$
$$\left\{\begin{array}{l} \sin(\omega_1 t - \frac{\omega_1 t_{open\_glottis}}{2})(1 + \frac{1}{k_{full\_imp}} \\ \sum_{sab=2}^{numbits-1} 2^{numbits} + 2^2 BSB)) BFB \\ + \sum_{sab=2}^{numbits} (\prod_{ampl=2}^{sab} 2\cos(\frac{\omega_1 t_{open\_glottis}}{k_{full\_imp}} 2^{(ampl-3)})) \\ + \sin(\omega_1 t - \frac{\omega_1 t_{open\_glottis}}{2})(1 + (2^{sab-1} - 2^0 + 2^{sab+1} \\ (\sum_{\substack{sub=sab+1 \\ sab+1<numbits}}^{numbits} BBS))) BSB \end{array}\right\} \quad (17)$$

where

$$BSB = \begin{cases} 0, if\ the\ sab-th\ significan\ t\ bit\ from\ the\ binary\ presentati\ on\ of\ N\ is\ equal\ 0 \\ 1, else \end{cases} \quad (18)$$

$$BFB = \begin{cases} 0, if\ the\ first\ bit\ from\ the\ binary\ presentati\ on\ of\ N\ is\ equal\ 0 \\ 1, else \end{cases} \quad (19)$$

$$BSS = \begin{cases} 0, f\ the\ sub-significan\ t\ bit\ from\ the\ binary\ presentati\ on\ of\ N\ is\ equal\ 0 \\ 1, else \end{cases} \quad (20)$$

$$BBS = \begin{cases} BSS, if\ sab = numbits \\ BSB + numbits - sab - 1, else \end{cases} \quad (21)$$

and

$$A^{1F}_{open\_glottis} = k_1' + A^{1F}_{closed\_glottis}((N-1)T_g) - \sin(\omega_1 t - \frac{\omega_1 t_{open\_glottis} N}{k_{full\_imp}} + \frac{\pi}{2}) \quad (22)$$

One can make the following conclusion:

By changing the ratio of the duration of the phase of close glottis to the length of the pitch frequency and without changing the geometry of the vocal tract, one can generate speech segments, in which the formant amplitude for each subsequent period increases, decreases, or does not change much. This can be seen in the two parts of figure 4. In the figure, a speech signal, generated with the model of Fant is resented. It contains one formant, which has frequency 420 Hz. The pitch is 199 Hz, and the plot contains 9 pitch periods. The signal in the first part has

$$t_{open\_glottis} = 39\ ms\ ,$$

and the second part has

$$t_{open\_glottis} = 25\ ms\ .$$

4 CONCLUSIONS

The study shows that the model of Fant adequately describes many phenomena of the speech production process, that are known form theory and practice. The reason for this probably lies in the genesis of the model. A "pulse source-filter" model is created for simplification of the process of analysis and parameterization of a specific implementation. This is accomplished, with the assumption, that the filter is practically independent of the source of excitation. This allows the implementation of effective methods and techniques for the evaluation of the filter. This approach gives excellent results in most cases - mainly in speech analysis, synthesis, coding and transmission. When the speech signals are used for medical, psycho-physiological, biometrical purposes however, it is customary to consider that the model of Fant is not sufficiently relevant. This requires the use of much more complex models and additional information sources. Recently, the problem becomes even more acute with the ever increasing demands on quality of processing and transmission of speech signals and their use in mobile devices. This paper shows, that the model can be made much more efficient without further complication. This is achieved, using the cumulative effect of some of the processes, that can be found in source and in the filter.

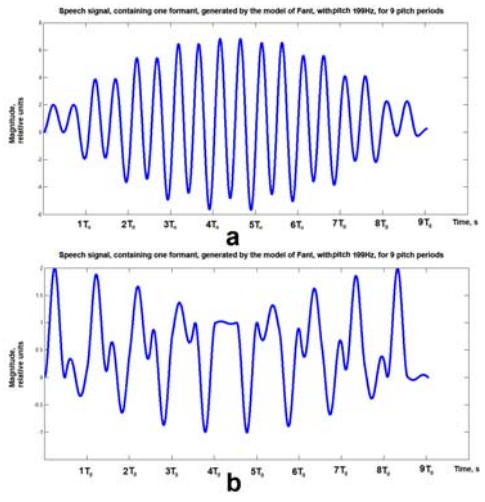

Figure 4: Speech signal, generated with the model of Fant, containing one formant, with pitch 199 Hz, 9 pitch periods, with formant frequency 420 Hz, and duration of the phase of open glottis 39 ms for a) and 25 ms for b).

REFERENCES

Chiba, T., Kajiyama, M.1995,*The vowel, Its Nature and Structure*. Tokyo-Kaiseikan, Tokyo 1995

Damyanov, D., Galabov, V., 2012a, *Characteristics of the model of Fant of second order on speech production*, Proceedings of the Technical University - Sofia, Volume 62, Issue 2, pp. 181-188, ISSN 1311-0829 , Sofia, 2012,

Damyanov, D., Galabov, V., 2012b, *On the Impact of duration of the phase of open glottis on the spectral characteristics of the phonation process*, Proceedings of the Technical University - Sofia, Volume 62, Issue 2, pp. 173-180, ISSN 1311-0829 , Sofia, 2012,

Damyanov, D., Galabov, V., 2012c, *Some effects of the assumption of an all-pole filter, used to describe processes of type "pulse source*, 1-st International Conference on Telecommunications and Remote Sensing, August, 29-30, pp. 139-145, ISBN 978-989-8565-28-0 , Sofia, 2012,

Ekman, P., Friesen W., 1978, *The Facial Action Coding System*, Consulting Psychologist Press, San Francisco. CA, 1978

Fant, G., 1990, *Acoustic Theory of Speech Production*, Mouton&Co, Hauge

Flannagan, J., 1992, *Speech analysis, Synthesis and Perception*, Springer, Berlin, 1992

Hayes, M., 1999, Schaum's Outline of Theory and Problems of Digital Signal Processing, Singapore, McGraw-Hill, 1999

Kalat, James W. 2012, *Biological Psychology*, Wadswoth. Cengage Learning, 10-th edition, Belmont, 2009

Pfister, B., Kaufmann, T., 2008, *Sprachverarbeitung - Grundlagen und Methoden der Sprachsynthese und Spracherkennung*, Springer Verlag, Heidelberg, 2008

Pickett, J.M. 1982, *The sounds of speech communication* , Univercity Park Press, Baltimore, 1982

Proakis, J.,2000, *Discrete Time Processing of Speech Signals*, New Jersey, JohnWiley&Sons, IEEE Press, 2000

Rabiner, L., Schafer R. 1992, *Digital processing of speech signals*, Prentice-Hall Inc, Engelwood Cliffs, New Jersey, 1992

Reuter-Lorenz, Patricia A., et.al., 2010, *The Cognitive neuroscience of mind: A tribute to Michael S. Gazzaniga*, MIT Press, April, London, 2010

Trashlieva, V., Puleva, T., 2011, *Model building for optimal administrative process management*, International Conference Automatics and Informatics'11, Bulgaria, 3-7.10.2011, pp B-263-B-266, ISSN 1313-1850, Sofia, 2011

Тилков, Д., Бояджиев., Т 1990, *Българска Фонетика*, Наука и изкуство София 1990

SOUND SOURCE LOCALIZATION IN A SECURITY SYSTEM USING A MICROPHONE ARRAY

Vera Behar[1], Hristo Kabakchiev[2] and Ivan Garvanov[3]
[1]*Institute of Information & Communication Technologie, BAS, 25-A Acad. G.Bonchev Str., Sofia, Bulgaria*
[2]*Faculty of Mathematics & Informatics,Sofia University, 15 Tsar Osvoboditel Blvd., Sofia, Bulgaria*
[3]*University of Library Studies & Information Technologies, Sofia, Bulgaria*
behar@bas.bg, ckabakchiev@yahoo.com, igarvanov@yahoo.com

Keywords: Adaptive array processing, microphone arrays, sound signal processing, DOA estimation

Abstract: A possible algorithm for sound source localization in a security system that is based on beamforming of a microphone array is described in this paper. It is shown that the adaptive beamforming algorithm, Minimum Variance Distortionless Response (MVDR), can be a part of the signal processing implemented in a security system. This signal processing includes the following stages: sound source localization, signal parameter estimation, signal priority analysis and, finally, control of protective and warning means (for example, video camera). The adaptive beamforming method MVDR is used for estimating the direction-of arrival (DOA) of signals generated by different sound sources, which arrive at the microphone array from different directions of the protected area. The scenario, in which four sound sources located at different points of the protected area generate different sound signals (warning, alarm, emergency and natural noise), is simulated in order to verify the algorithm for DOA estimation. The simulation results show that an adaptive microphone array can be successfully used for accurate localization of all sound sources in the observation area. The parallel version of the described algorithm is tested in Blue Gene environment using the interface MPI.

1 INTRODUCTION

The security system is a standard part of any building in the city. In most sensors used by a security system for protection of a limited space (home, parking) are mounted sound sirens that are activated in the event of an adverse situation in the protected space. Usually, in case of such a situation (fire, smoke, vibration, and breakage of glass or opening the car) the sirens of sensors give a loud beep for a few minutes. The assessment of the direction and parameters of the incoming sound signals can be used to control the movement of a video camera that records the situation in the most dangerous direction and submits the data to the management centre.

The novelty of this paper is to use the adaptive beamforming algorithm in order to locate, using a microphone array, the direction of sound signals coming from sensors or other sound sources. Microphones arrays represent a set of microphones arranged in some geometric configuration. They can be realized as linear microphone arrays, where the microphones are positioned in a straight line, or as circular microphone arrays, where the microphones are placed in a circle, or as rectangular microphone arrays, where the microphones are arranged in the shape of a rectangle plate (Benesty, 2008). Microphone arrays have many advantages. Firstly, the beamforming can be done digitally so as to control all dangerous directions (door, windows, cars) using only a single microphone array. Otherwise, when using directional microphones of other types, for example, parabolic microphones, a lot of such microphones are required, because each microphone can control only one direction. Secondly, all noise signals coming from other uncontrolled directions (speaking of people, banging on the walls, etc.) are adaptively rejected by a microphone array, which increases the detectability of signals from sensors and improves the security of the protected area. For comparison, when using a

directional parabolic microphone, noise signals are not removed and they interfere with the detection of the signal. In third, a microphone array can simultaneously generate several independent beam patterns and collect the information from multiple sound sources. In the fourth, the signal power at the output of a microphone array is increased M times (M - is the number of array microphones), which allows to substantially increase the security of the protected area. Moreover, a three-dimensional area can be controlled using the rectangular or circular microphone arrays, and, finally, microphone arrays can be easy adapted to detect acoustic signals with different frequency characteristics by change of the distance between microphones in the array.

In this paper, we propose to use the Minimum Variance Distortionless Response (MVDR) beamforming algorithm for DOA estimation of signals arrived from different sound sources at a microphone array (Godara, 1997; Trees, 2002; Vouras, 1996; Moelker, 1996). We consider the case, when each sound source is located in the array's far-field, and the sounds generated by sound sources propagate through the air. The DOA is proposed to be estimated as a direction, in which the signal power at the output of a microphone array exceeds a previously predetermined threshold. The paper is structured as follows. In the next second section, the expressions for calculation of array response vectors are derived for three types of microphone arrays. The model of signals arrived at a microphone array in a security system is described in the third section. The MVDR algorithm for DOA estimation is mathematically described in the forth section.

The parallel version of the MVDR algorithm tested in Blue Gene environment using the interface MPI is described in the fifth section. The simulation scenario, in which four sound sources located at different points of the protected area generate different sound signals (warning, alarm, emergency and natural noise), is described in the sixth section. The simulation scenario is used in order to verify the algorithm for DOA estimation. The results obtained show that the MVDR beamforming algorithm applied to a microphone array can be successfully used for accurate localization of all sound sources in the observation area. The parallel version of the described algorithm is tested in Blue Gene environment using the interface MPI.

2 MICROPHONE ARRAYS

Microphone arrays are composed of many microphones working jointly to establish a unique beam pattern in the desire direction. The array microphones are put together in a known geometry, which is usually uniform - Uniform Linear Arrays (ULA), Uniform Rectangular Arrays (URA) or Uniform Circular Arrays (UCA) (Ioannidis, 2005). Since the ULA beam pattern can be controlled only in one dimension (azimuth), so in various sound applications, URA and UCA configurations with the elements extended in two dimensions must be used in order to control the beam pattern in two dimensions (azimuth and elevation).

2.1 URA Configuration

In a URA array, all elements are extended in the x-y plane. There are M_X elements in the x-direction and M_Y elements in the y-direction creating an array of (M_X x M_Y) elements. All elements are uniformly spaced d apart in both directions. Such a rectangular array can be viewed as M_Y uniform linear arrays of M_X elements or M_X uniform linear arrays of M_Y elements. Usually, the first array element is considered as the origin of Cartesian coordinates as shown in Fig.1.

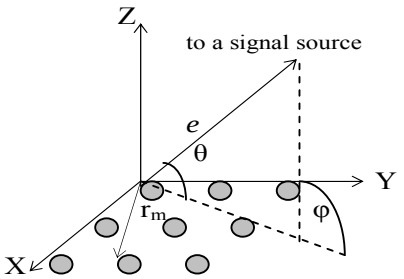

Figure 1: URA configuration

The direction of a signal arriving from azimuth φ and elevation θ can be described with a unit vector e in Cartesian coordinates as:

$$e(\varphi,\theta) = (e_X, e_Y, e_Z) = \\ = (\cos\theta\sin\varphi, \cos\theta\cos\varphi, \sin\theta) \quad (1)$$

The vector r_m in the direction of the $m(i,k)$ element can be described in Cartesian coordinates as:

$$r_{m(i,k)} = (d(i-1), d(k-1), 0) \quad (2)$$

In (2), *i* and *k* denote the element position along the *y*- and the *x*-axis, respectively. The sequential element number *m(i,k)* is defined as:

$$m(i,k) = (i-1)M_x + k \qquad i = 1 \div M_Y, k = 1 \div M_X \tag{3}$$

If the first element in the rectangular array is a reference element, the path-length difference $d_{m(i,k)}$ for a signal incident at element *m(i,k)* can be defined as the projection of the vector $r_{m(i,k)}$ on the signal direction vector *e*:

$$d_{m(i,k)} = e^{\mathrm{T}} r_{m(i,k)} \tag{4}$$

Therefore, the URA array response vector a_c takes the form:

$$a_c(\varphi,\theta) = \left[1, \exp\left(\frac{j2\pi d_2}{\lambda}\right), ..., , ..., \exp\left(\frac{j2\pi d_{m(i,k)}}{\lambda}\right), ..., \exp\left(\frac{j2\pi d_M}{\lambda}\right)\right] \tag{5}$$

In (5), the total number of elements in the microphone array is:

$$M = M_X M_Y \tag{6}$$

2.2 ULA Configuration

The ULA array response vector a_c is calculated by (5) where M_X=1.

2.3 UCA Configuration

In a UCA array, all elements are arranged along the ring of radius *r* (Fig.2).

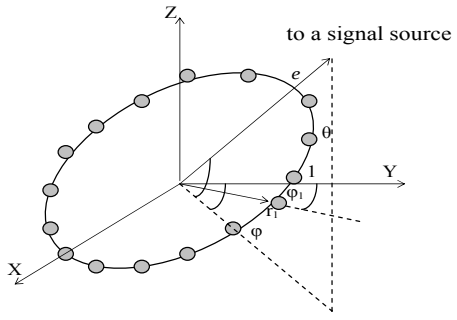

Figure 2: UCA configuration

The ring contains *M* array elements. Since these elements are uniformly spaced within the ring, so they have an interelement angular spacing $\Delta\varphi = 2\pi/M$ and a linear interelement spacing $d = 2r\pi/M$. It is usually assumed that the first antenna element is located at the *y*-axis, and the ring center is the origin of Cartesian coordinates. The vector in the direction of the *m*-th array element can be written in Cartesian coordinates as:

$$r_m = \left(r\sin\varphi_m, r\cos\left(\varphi_m, 0\right)\right) \tag{7}$$

In (7), the angle φ_m is calculated as:

$$\varphi_m = \frac{2\pi(m-1)}{M} \tag{8}$$

The unit vector $e(\varphi,\theta)$ in the direction of a signal source is given by (1). If the ring center serves as a reference point, the propagation path-length difference d_m for a signal incident at element *m* can be defined as the projection of the vector r_m on the direction vector *e*:

$$d_m = e^{\mathrm{T}} r_m = d\cos\theta\cos(\varphi - \varphi_m), \qquad m = 1 \div M \tag{9}$$

Therefore, the UCA array response vector a_c takes the form:

$$a_c(\varphi,\theta) = \left[\exp\left(\frac{j2\pi d_1}{\lambda}\right), ..., \exp\left(\frac{j2\pi d_M}{\lambda}\right)\right] \tag{10}$$

where d_m is calculated by (9) for *m=1,2,..,M*.

3 SIGNAL MODEL

The signal model is based on the scenario, according to which one or several (*L*) sensor signals combined with some sound noise arrive at the microphone array with *M* microphones. The output signal of each microphone is a sum of sound-source-generated signals and thermal noise. The vector of complex samples of the output signal of a microphone array at time instant *k* can be mathematically described as:

$$x(k) = \sum_{i=1}^{L} b_l s_l(k) + n(k) \tag{11}$$

In (1), *x(k)* is the (*M* x 1) complex data vector, $s_l(k)$ is the complex signal generated by the *l*th sound source, b_l is the (*M* x 1) microphone array response vector generated in the direction of the *l*th sound source, *n(k)* is the (*M* x 1) complex noise vector and *L* is the number of sound sources. The signal received from the sound source *l* is given by:

$$s_l(k) = \sqrt{P_l} A_l(k) \cos(2\pi f_0 t + \varphi) \qquad (12)$$

In (12), P_l is the received signal power, $A_l(k)$ is the modulating function, different for each sound source and f_0 is the sound carrier frequency. The microphone noise $n(k)$ occupies the entire frequency bandwidth of a microphone and can be represented mathematically as band-limited white additive Gaussian noise (AWGN).

4 SIGNAL PROCESSING

Many sensors for fire detection or building surveillance are equipped with sound alarm devices. In case of alarm event (smoke, flame, intrusion, glass breaking, and unauthorized car opening) the alarm device generates powerful sound signal with certain parameters and duration. For the sake of simplicity, let's assume that a set of sensors and one microphone array are installed for the object protection in the observation area and a video camera is located above a microphone array as shown in Fig.3.

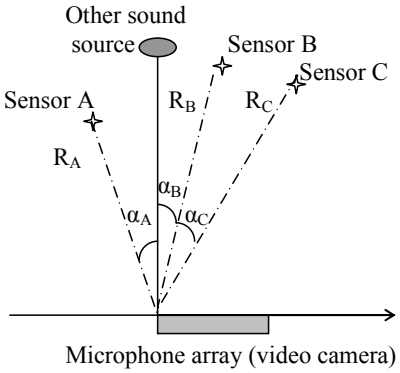

Figure 3: The security system topology

In a security system, the sound source localization could be used for pointing the additional video surveillance devices (video cameras) in the needed directions, which record the additional information and send it to control center of a security system. The priority direction for pointing of a video camera is determined by analysis and identification of signals received from the detected sound sources. The analyzed signal parameters used for signal identification are duration, frequency, modulation, type (continuous, intermittent), and power. The general block-scheme of a possible signal processing in a security system is shown in Fig.4.

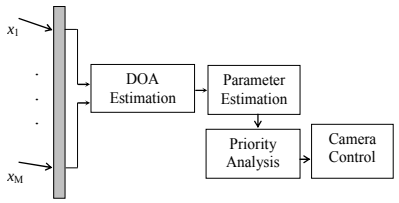

Figure 4: Signal processing in a security system

We assume that the direction of-arrival (DOA) of sound signals is referred to a Cartesian coordinate system, the origin of which coincides with the first element of a microphone array. In a security system, in which each sensor is equipped with a sound generator, a microphone array scans the protected area of observation in an electronic way (Fig.5). In the process of scanning, a microphone array with a predetermined angular step directs its main beam in a certain direction.

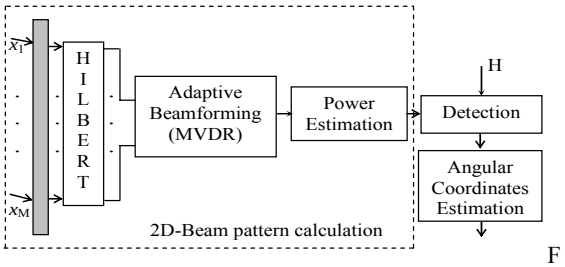

Figure 5: The block-scheme of DOA estimation

At the output of a microphone array, the signal power received from any direction is estimated as:

$$P(\varphi,\theta) = \left| y(\varphi,\theta) \right|^2 \qquad (13)$$

In (13), y and P are the output signal and the output power of a microphone array steered in the (β,θ)-direction (β - azimuth and θ - elevation). The output of a microphone array with M elements is formed as:

$$y(k) = W^H x(k) \qquad (14)$$

where k is the time instant, and $x(k)$ is the complex vector of array observations, $W=[w_1,w_2,\ldots w_M]^T$ is the complex vector of the beamformer weights, T and H denote transpose and conjugate transpose, respectively. The conventional (delay-and-sum) beamformer is the simplest, with all its weights of equal magnitudes and the phases that are selected to steer the array in particular direction, i.e. the complex vector of weights W is equal to the array response vector a_c, which is defined by the array configuration. The conventional non-adaptive beamformer has unity response in each look direction, that is, the mean output power of the beamformer in the look direction is the same as the

received source power. In conditions of no directional interferences, this beamformer provides maximum SNR but it is not effective in the presence of the other directional signals, intentional or unintentional. The others beamformers such as a Minimum Variance Distortionless Response beamformer can overcome this problem by suppressing unwanted signals from off-axis directions (Tummonery, 1994; Vouras, 2008). To suppress unwanted signals, this beamformer does not require the a priori information about them. It requires only the information for the direction-of-arrival of expected signals. In this paper we propose to form the signal y according to the adaptive MVDR method. The MVDR-beamformer adaptively calculates the vector of weights (W) providing the maximum gain in the desired direction while minimizing the power in the other directions. According to this method, the optimal weight vector (W) is chosen to maximize the signal to interference plus noise ratio (SINR) in a certain direction:

$$SINR = \frac{\sigma_S^2}{W^H K W}\left|W^H a_c\right|^2 \qquad (15)$$

In (15), K is the "interference + noise" covariance matrix of size (M x M), σS2 is the signal power, and ac is the array response vector in the (□, θ) direction determined by an array configuration. The solution is found by linear constrained optimization. The criterion of optimization is formulated as:

$$\min_W W^H K W \text{ subject to } W^H a_c = 1 \qquad (16)$$

The solution of (16) gives the following weights:

$$W_{MVDR} = \frac{K^{-1} a_c}{a_c^H K^{-1} a_c} \qquad (17)$$

Many practical applications of MVDR-beamformers require online calculation of the weights according to (17), and it means that the covariance matrix K should be estimated and inverted online. However, this operation is very computationally expensive and it may be difficult to estimate the sample covariance matrix in real time if the number of samples is large. Furthermore, the numerical calculation of the weights WMVDR using the expression (17) may be very unstable if the sample covariance matrix is ill-conditioned. A numerical stable and computationally efficient algorithm can be obtained by using QR decomposition of the incoming signal matrix. This matrix is decomposed as X=QR, where Q is the unitary matrix and R is the upper triangular matrix. Hence the QR-based algorithm for calculation of beamformer weights includes the following three stages:

The linear equation system $R^H z_1 = a_c$ is solved for z_1 , and the solution is $z_1^* = (R^H)^{-1} a_c$

The linear equation system $Rz_2 = z_1^*$ is solved for z_2 , and the solution is $z_2^* = R^{-1} z_1^*$

The weight vector $\widehat{W}$ is obtained as $\widehat{W} = z_2^* / (a_c^H z_2^*)$

In the process of scanning of the observation area, the microphone array is digitally steered in each angular direction (□,θ). After adaptive beamforming of a microphone array in the direction (□,θ), the signal power at the output of a microphone array is stored, forming in this way the beam pattern of a microphone array i.e. P(φ,θ). Next, firstly the local maximums of the obtained beam pattern must be found and after that they are compared with a fixed predetermined threshold H. If some local maximum of the beam pattern, i.e. Pmax,i(φ*,θ*), corresponding to some angular direction (φ *,θ*) exceeds the threshold H, then this angular direction (φ *,θ*) is the estimate of the $\min_W W^H$ DOA.

5 PARALLEL ALGORITHM

5.1 Algorithm Description

Parallel version of the algorithm for DOA estimation is implemented as a program in Blue Gene environment using the interface MPI. The parallel program calculates the signal power at the output of a microphone array simultaneously for all directions of observation (Fig.5). The structure of the parallel program uses the fact that the server loads one the same copy of the program on all processors from 0 to (NumProc - 1) where NumProc is the number of processors allocated to the program. The program uses the current processor number iD, which is defined by MPI-subroutine MPI_COMM_RANK, in order to determine which of the two processes to be performed (depending on that whether the processor is a master processor, i.e. iD = 0 or slave processor, i.e. iD> 0). The master processor (iD = 0) performs initialization of parameters and prepares the data for all processors. This processor performs simulation

of signals (or, in practice, reading the signals from the buffer), in result of which the signal matrix X is formed. Moreover, for each slave processor, the main processor calculates the angular direction (FFI), for which the slave processor (iD = 1 ... NumProc -1) calculates the signal power at the output of an adaptive microphone array. The angular direction (FFI), in which the microphone array is steered, is sent from the master processor to each slave processor using the loop organized by the MPI-subroutine MPI_Send. The main processor also prepares its data portion (FFI = -90 º and an array FFI (i), i = 1 ... NumProc, which contains all angular directions). Then all processors perform identical calculations - each of them determines the signal power at the output of a microphone array for angular direction FFI, using the subroutine DIAG_AZ_PAR. Once calculating the signal power at the output of a microphone array, each slave processor sends the resulting value to the master processor via the MPI-subroutine MPI_Send.

The master processor via the MPI-function MPI_Recv accepts the results from all slave processors and forms the beam pattern of the microphone array. After that the subroutine FIND_AZIMUTH finds the angular positions of all local maximums of the beam pattern, which exceed the predetermined threshold H. The angular positions of local maximums are the directions of arrival of sound of signals. The number of processors NumProc is equal to the number of (□,θ)- directions used in calculation of the beam pattern of a microphone array. At step 2º, the number of processors is equal to NumProc = (180º /2º +1) = 91.

5.2 Create and Run the Executable File

Firstly, in Blue Gene environment with the interface MPI, the executable file, for example, SOUND_F_PAR.exe, is created using the pre-created file makesound_F_PAR.txt, which is started with the command make:

> make-f makesound_F_PAR.txt

With this command all program modules of the program package are translated and, as a result, the executable file SOUND_F_PAR.exe is created. The executable file SOUND_F_PAR.exe is run using the control file SOUND_F_PAR.jcf (Job Control File) with the following command:

> llsubmit SOUND_F_PAR.jcf

After the execution the system responds with a message like:

llsubmit:

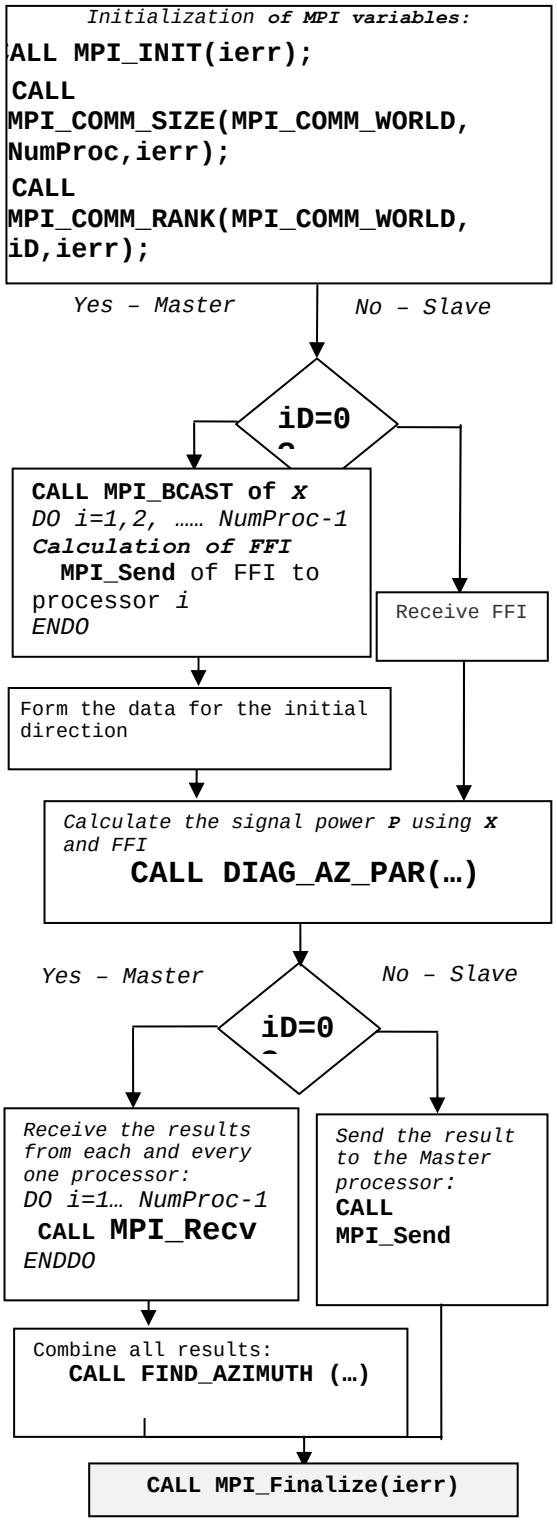

Figure 6: Parallel version of the algorithm

The job "bgpfen.daits.government.bg. < task number>" has been submitted.

The content of the control file SOUND_F_PAR.jcf can be like that:

```
# @ job_name = SoundDetect
# @ comment = "SoundDetect :BlueGene"
# @ error = $(jobid).err
# @ output = $(jobid).out
# @ environment = COPY_ALL;
# @ wall_clock_limit = 01:00:00
# @ notification = error
# @ notify_user = never
# @ job_type = bluegene
# @ bg_size = 128
# @ class = n0128
# @ queue
/bgsys/drivers/ppcfloor/bin/mpirun
 -exe SOUND_F_PAR.exe -verbose 1
-mode VN -np 91
```

The number of processors np in the file SOUND_F_PAR.jcf given above, equals to the number of angular (for example, azimuthal) directions, which were used in the formation of the beam pattern of a microphone array. At step 2º, the number of processors is equal to np = 91.

6 SIMULATION RESULTS

The computer simulation is performed to verify the described algorithm for sound source localization. As shown in Fig.3, the scenario of simulation includes three sensors (A, B and C) located respectively at 50m, 60m and 70m away from the microphone array. In order to evaluate the performance of the algorithm for DOA estimation when using different types of sensors, the parameters of the sensors produced by three well-known companies (SONITRON, E2S and SYSTEM SENSOR) are used in simulation.

Depending of the company of production, the sirens of sensors generate sound signals at frequency f0 with the power LW in range from 96dB to 103 dB (Table 1). In simulation we assume that all sensors in the protected area are produced by the same company.

According to the simulation scenario, the source of natural noise is a car located in the perpendicular direction relative to the microphone array.

The horn of this car generates a sound, whose power is 110dB (Fig.3). The distance to the car is 90m.

Table 1: Sensor parameters

Company	Signal power LW [dB]	Sound frequency [Hz]
SONITRON	96	2500
E2S	100	1000
SYSTEM SENSOR	103	2400

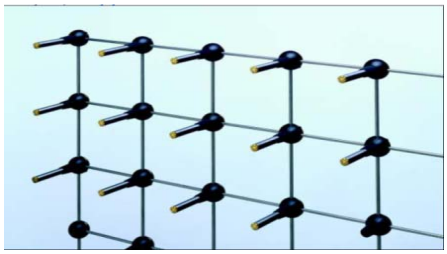

Figure 7: Microphone array WA 0807

Two microphone array configurations, the uniform linear array (ULA) and the uniform rectangular array (URA), are simulated for each sensor type. The topology of a microphone array WA 0807 of the company Brüel & Kjær is used in simulation (Fig.7).

- The Brüel&Kjær microphone array parameters are:
- Frequency, at which the controlled sensors generate the sound (Hz);
- Array configuration (linear, rectangular, square);
- Distance between array microphones (d), which can be changed for each type of sensors;
- Total number of microphones in the microphone array.

The parameters of microphones of the type 4935 according to the catalogue of the company Brüel & Kjær are used in simulation of the microphone array (Fig.8).

Figure 8: Microphone 4935 (Brüel & Kjær)

The noise level of such a microphone is 35dB in the frequency range [100 - 5000] Hz. It is assumed that all simulated microphone arrays (ULA and URA) have the same overall dimension of 0.5m. The interelement spacing of each microphone array and as a consequence the corresponding number of elements are determined according to the carrier frequency of a signal generated by the sound source.

For each type of sensors, the interelement distance in a microphone array is calculated as $d = \lambda / 2$, where λ is the wavelength of the sound generated by a sensor. The sound wavelength depends on the frequency of the generated sound, i.e. $\lambda = c/f0$, where $c = 344$ m/s is the propagation velocity of sound in air, and f0 is the frequency of the acoustic signal (Table 1). The signal amplitude (A) at the output of each microphone of a microphone array is calculated as a function of the sound pressure LP:

$$A = 0.00002 \cdot 10^{\frac{L_p}{20}} \tag{18}$$

In (18), the sound pressure LP (in dB) depends on the power of the sound LW, which is different for each sensor (Table 1) and also depends on the distance R to the sound source:

$$L_p = LW - 11 - 20 \log R \tag{19}$$

The real and estimated values of the DOA are presented in Table 2 for each type of a microphone array. The beam patterns of the microphone arrays are presented respectively in Fig.9 … Fig.14.

Table 2: True and estimated azimuthal directions

SENSOR TYPE	Array Type	Source Azimuth [°]	Estimated Azimuth [°]
SONITRON	ULA (11x1)	-14;0;14;28	-14; 0;14; 28
	URA (11x4)	-14;0;14;28	-14; 0; 14; 28
E2S	ULA (4x1)	-26; 0; 26	-26; 0; 26
	URA (4x4)	-26;0;26;52	-26; 0; 26; 52
SYSTEM SENSOR	ULA (8x1)	-14;0;14;28	-14; 0;14; 28
	URA (8x4)	-14;0;14;28	-14; 0;14; 28

The number of directions, for example, in azimuth (NAZ), controlled by a microphone array depends on the angular resolution of the microphone array ($\Delta\square$), which in its turn is determined by the geometrical configuration of the microphone array and the number of its elements:

$$N_{AZ} = 180^0 \frac{\square}{\Delta\varphi} \tag{20}$$

The angular resolution $\Delta\varphi$ is determined as the width of the main lobe of the beam pattern created by a microphone array. Comparing the plotted beam pattern presented on Fig.9…Fig.14, it can be seen that the best angular resolution in azimuth is provided by using the microphone array ULA-11 (with 11 microphones) and opposite, the worst angular resolution is provided by using the microphone array ULA-4 (with 4 microphones). Therefore, the ability of a microphone array to separate the signals from different sound sources is improved with increasing the number of microphones in the array.

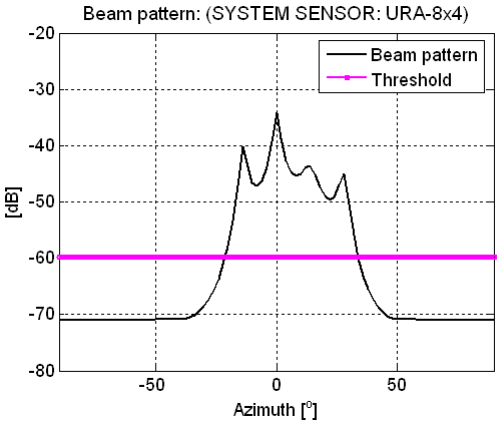

Figure 9: Beam pattern of the URA-8x4 (Sensor Type –SYSTEM SENSOR)

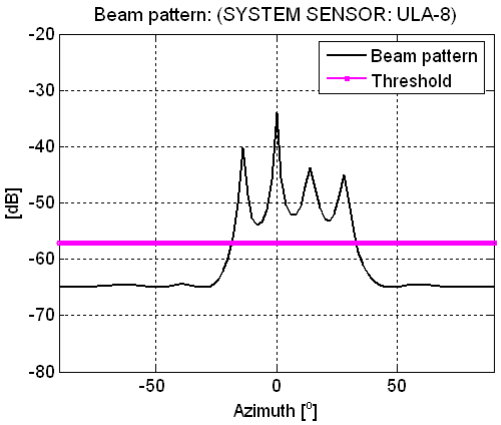

Figure 10: Beam pattern of the ULA-8x4 (Sensor Type – SYSTEM SENSOR)

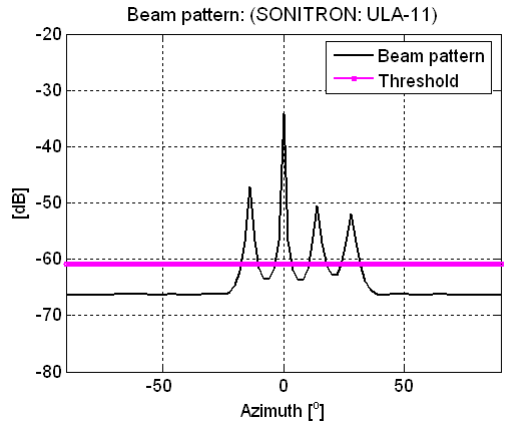

Figure 11: Beam pattern of the ULA-11 (Sensor Type –SONITRON)

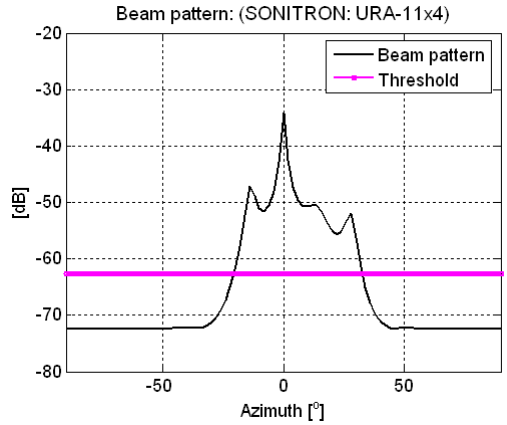

Figure 12: Beam pattern of the URA-11x4 (Sensor Type –SONITRON)

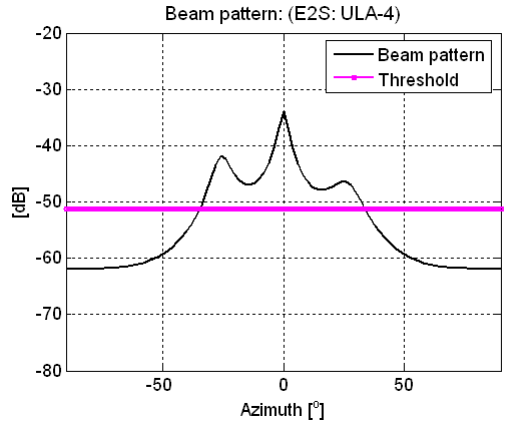

Figure 13: Beam pattern of the ULA- 4x1 (Sensor Type –E2S)

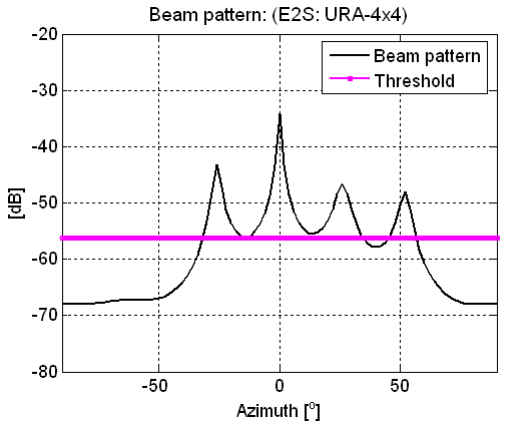

Figure 14: Beam pattern of the URA- 4x4 (Sensor Type –E2S)

It is well known that the maximal number of signals arrived from different directions, which can be separated by a microphone array, equals (M-1), where M is the number of array elements. Therefore, the beam pattern plotted in Fig. 13 shows that the microphone array ULA-4 can separate only 3 sound signals received from different directions and generated by 3 E2S sensors. The graphical results also show that linear microphone arrays (ULA) should be used in cases where it is important to control the movement of the video camera only in azimuthal direction. However, when it is important to control the movement of the video camera in 2D space (azimuth and elevation), you must use rectangular microphone arrays (URA). Comparison analysis of the beam patterns plotted in Fig. 11 (for ULA-11, SONITRON) and Fig.12 (for URA-11x4, SONITRON) shows, that the use of a rectangular microphone reduces the angular resolution in azimuth.

7 CONCLUSIONS

The results obtained show that the accurate DOA estimates can be obtained using a microphone array if the adaptive MVDR-algorithm is used for beamforming. It is also shown that the maximal number of separated signals and also the effectiveness of microphone arrays depend on the number of array elements. Finally, the results obtained can be successfully used for solving different problems associated with noise source localization and identification.

ACKNOWLEDGEMENTS

The research work reported in the paper is partly supported by the project AComIn "Advanced Computing for Innovation", grant 316087, funded by the FP7 Capacity Programme (Research Potential of Convergence Regions).

REFERENCES

Benesty, J., Chen, J., Huang, Y., 2008. *Microphone array signal processing*, Springer.

Godara, L., 1997. *Application of antenna arrays to mobile communications, part II: beam-forming and direction-of-arrival considerations*. In Proc. of the IEEE, vol.85, No 8, pp.1195-1245.

Ioannides, P., Balanis, C., 2005. *Uniform circular and rectangular arrays for adaptive beamforming applications.* IEEE Trans. on Antenna. Wireless Propagation. Letters, vol.4., pp. 351-354.

Trees, H., Van, L., 2002. *Optimum Array Processing. Part IV. Detection, Estimation, and Modulation Theory.* New York, JohnWiley and Sons, Inc..

Tummonery, L., Proudler, I., Farina, A., McWhirter, J., 1994. *QRD-based MVDR algorithm for adaptive multi-pulse antenna array signal processing.* In Proc. Radar, Sonar, Navigation, vol.141, No 2, pp. 93-102.

Vouras, P., Freburger, B., 2008. *Application of adaptive beamforming techniques to HF radar*. In Proc. IEEE conf. RADAR'08, May, pp. 6.

Moelker, D.,VandePol, E., 1996. *Adaptive Antenna Arrays for Interference Cancellation in GPS and GLONASS Receivers.* In Proc. of the IEEE symp. on Position Location and Navigation, April, pp.191-196.

http://sonitron.be/site/index.php,\

http://www.e2s.com/

http://www.systemsensor.com/

PZT AND PNZT-BASED THIN FILM CAPACITORS AND TRANSMISSION LINES FOR MICROWAVE INTEGRATED CIRCUIT APPLICATIONS

Zaiki Awang and Suhana Sulaimanand
Microwave Technology Centre, University Technology MARA, 40450 Shah Alam, Malaysia
zaiki.awang@gmail.com, anisafiq2@yahoo.com

Keywords: Thin film capacitor, co-planar waveguide transmission line, PZT, PNZT, thin dielectric films, monolithic microwave integrated circuits.

Abstract: Ferroelectric materials have superior dielectric properties but the processing conditions of thin ferroelectric films influence their dielectric properties and thus affect the performance of devices which employ them. A detailed characterization is carried out for lead zirconate titanate (PZT) and lead niobate zirconate titanate (PNZT) thin films in this work by employing planar-circuit structures. The films were applied to built microwave capacitors and co-planar waveguide transmission lines. S-parameter measurements were performed from 40 MHz to 20 GHz using wafer probes in conjunction with a vector network analyzer. The results show the loss tangent and relative permittivity of the films vary with frequency, with typical permittivity values of the order of 110 to 350 and 200 to 780 for PZT and PNZT, respectively, over the said frequency range. The investigation revealed the effect of dielectric polarization of the films over the broad frequency range. The transmission lines showed acceptable insertion losses of the order of 17 dB from 5 to 20 GHz for lines of length 100 μm and width 5 μm fabricated on PNZT films 1 μm thick. These figures demonstrate the feasibility of using thin ferroelectric films as a new substrate material for monolithic microwave integrated circuits (MMIC).

1 INTRODUCTION

Ferroelectric materials are popular due to their superior dielectric properties characterized by their high dielectric constant and polarization values. The review made by (Setter *et. al.*, 2006) discussed their dielectric properties and represented the state of the art development of the material - the domain structure and their effects on relative permittivity and loss, and their implication in micro-systems and high frequency device applications .

Lead zirconate titanate (PZT) and lead niobate zirconate titanate (PNZT) belong to the family of ferroelectric materials. Both are known for their high dielectric constant as well as their superior perovskite characteristics useful for high capacitor density applications (Dimos and Mueller, 1998, Riemens *et. al*. 2003 and Haccart *et. al*., 2006). With the addition of a dopant such as Nb, the PZT can demonstrate higher dielectric constant and promote larger perovskite crystals, as well as increased film resistivity (Souza *et.al.,* 2004). The addition of Nb also influences the film characteristics such as microstructure, as well as the electrical properties. Also, there is correlation between internal electric field and 'self polarization' of the films that increases with Nb concentration.

Souza *et.al.,* 2004 found that the enhancement of the piezoelectric and ferroelectric properties of PNZT is possible with careful control of the crystallographic orientation of the polycrystalline films or growing the epitaxial films with preferred orientation. Their study also investigated the film thickness effects on the ferroelectric and piezoelectric properties of PNZT thin films.

In our work, PZT and PNZT thin films prepared differently were utilized to explore their microwave

properties. The films were studied over two types of applications – as thin film metal-insulator-metal (MIM) capacitors, and as a new substrate material for the construction of co-planar waveguides. The principal motivation of this work was to exploit the high dielectric constant of these films to reduce the size of capacitors and transmission lines, two components which traditionally take up large area of MMIC. Thus using these ferroelectric films offer the potential of reducing the size of MMICs, leading to wireless systems having more efficient power consumption.

Two capacitor test structures of 2500 μm^2 area were fabricated on the films and measured by employing the planar circuit technique. The measurement was performed using *Cascade Microtech* wafer probes and a vector network analyzer with short-open-load (SOL) calibration technique. The measurements were carried out over a wide frequency range of 40 MHz to 20 GHz which are suitable for MMIC applications. The capacitance, loss tangent and relative permittivity of the films were then extracted from the experimental data. From the analysis, behavior of dielectric polarization of PNZT and PZT over a broad frequency range was deduced.

Various transmission lines were then constructed in co-planar form with both films acting as the substrate. The novelty of this work is to show the feasibility of using ferroelectric materials as the substrate for MMIC. This paper reports results of further investigations of our previous work, which has been extended to include tests on the various transmission line structures.

2 METHODOLOGY

The films were prepared using standard methods compatible with MMIC processing. The objectives of the experimental work made were to two-fold: to analyze the capacitance, loss tangent and their relative permittivity at microwave frequencies, and to measure the insertion loss of the films by analyzing the transmission lines constructed out of these films.

2.1 Sample Preparation

The PZT and PNZT samples were categorized based on the method of deposition, doping, dielectric thickness, orientation, crystallinity and grain size obtained from the X-ray diffraction (XRD). The PNZT films were grown using metal organic deposition to give films of 1 μm thick, while the PZT was prepared with RF sputtering with thicknesses of the order of 0.5 μm. The PNZT films were tetragonal (20/80) and doped with 4 % Nb, while the PZT films were (50/50) cubic. The top metallization layers of the capacitor structures were Ti, while Pt was used as bottom electrodes.

2.2 Device Fabrication

The fabrication processes used are compatible with semiconductor processing, details of which are reported earlier (Bakar *et. al*., 2008). The fabrication for PNZT sample was modified slightly due to the Pt etchant which attacked the PMMA photoresist used. For this sample, the capacitor test structures were delineated after the Pt layer was removed. Figure 1 shows the capacitor prototype with area 50 μm × 50 μm.

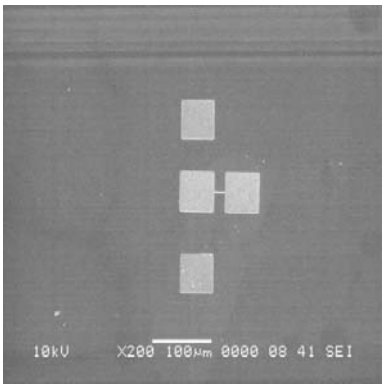

Figure 1: A typical thin film capacitor test structure constructed in this work, with ground-signal-ground (GSG) pads on the left for wafer probing.

2.3 Measurement

High frequency measurements were carried out on the capacitor using on-wafer probe and vector network analyzer (VNA). The SOL one-port calibration technique was performed for the capacitance measurements, while SOLT was employed to calibrate the two-port transmission line structures to minimize measurement errors due to parasitics (WinCal 3.2 User Guide, 2000). The Open standard in SOL was obtained by lifting the probe at least 0.25 mm in air, while the Short and 50 Ω standards were provided by the manufacturer impedance standard substrate (ISS). The probe tip placements were ensured to be consistent to achieve repeatable measurements and calibrations. The short standard defines a zero-length reference plane. The reflection coefficient, S_{11} of the test structure is obtained after the probe calibration is completed.

3 RESULTS AND DISCUSSION

3.1 Capacitors

The S-parameter data obtained from the measurement consist of real and imaginary parts of the input impedance of the test structures. The complex permittivity of a dielectric is written as (Al-Omari and Lear, 2005);

$$\varepsilon^* = \varepsilon' - j\varepsilon'' \tag{1}$$

where the ε' is the real part that represents the relative dielectric constant which characterizes a material's ability to store charges. On the other hand, ε'' is the imaginary part that describes the dielectric loss which is a measure of the dispersion in the material. The data is then used to extract the capacitance, relative permittivity and loss tangent of the films.

The impedance equation is shown in equation (2); where ε_0 is the free space permittivity, A is the capacitor area which is 2500μm^2, d is the dielectric thickness and ω is the angular frequency.

$$Z = \frac{d}{j\omega\varepsilon_0\varepsilon^* A} \tag{2}$$

The capacitance is calculated from S_{11} using :

$$\frac{d}{j\omega\varepsilon_0\left(\varepsilon' - j\varepsilon''\right)A} = Z_0\left(\frac{1+S_{11meas}}{1-S_{11meas}}\right) \tag{3}$$

where S_{11meas} is the measured S_{11}. Using (3) the real and imaginary parts of $\varepsilon' - j\varepsilon''$ give the following expressions (Park *et. al*., 2002):

$$\varepsilon'(\omega) = \left(\frac{d}{\omega\varepsilon_0 A}\right)\frac{1}{Z_0}\,\mathrm{Im}\left(\frac{1-S_{11meas}}{1+S_{11meas}}\right) \tag{4}$$

$$\varepsilon''(\omega) = \left(\frac{d}{\omega\varepsilon_0 A}\right)\frac{1}{Z_0}\,\mathrm{Re}\left(\frac{1-S_{11meas}}{1+S_{11meas}}\right) \tag{5}$$

Both equations yield the frequency dependence of ε' and ε''. Subsequently, these equations are made use to evaluate the capacitance, the relative permittivity as well as the loss tangent. The capacitance of the structure is obtained by relating the imaginary part of the impedance;

$$X_c = \frac{1}{j\omega C} \tag{6}$$

From the measured S_{11}, the impedance is calculated as in (4) using the equation:

$$Z = 50\left(\frac{1+S_{11meas}}{1+S_{11meas}}\right) \tag{7}$$

The capacitance is extracted using the following equation:

$$C = \frac{1}{\omega\times 50\times \mathrm{Im}\left(\frac{1+S_{11meas}}{1-S_{11meas}}\right)} \tag{8}$$

The loss tangent is determined from the ratio of the imaginary and the real parts of (4) and (5) respectively;

$$\tan|\delta| = \frac{\varepsilon''}{\varepsilon'} \tag{9}$$

Details of our work have been reported elsewhere (Sulaiman *et. al*., 2011), and hence only the main findings relevant to the discussion of our new results are repeated here. Figures 2 and 3 below show typical response of the dielectric properties over the frequency range mentioned. The PNZT films exhibited higher permittivity compared to PZT, this is expected due to the Nb doping. Both films showed decreasing trends of ε_r as the frequency is increased, again this is expected as the films get more lossy with frequency due to polarization.

As expected, the decrease in ε_r was accompanied by an increase in loss tan for both samples (Sulaiman *et. al*., 2011). The values of tan δ for the PZT film were in the range of 0.04 to 0.18, while similar behavior were seen for PNZT. This response can be explained by the presence of the relaxation phenomena where as the frequency of electric field is increased, there is a point where the permanent electric dipoles of the material can no longer rotate fast enough to remain in phase with the field. Hence, these mechanisms reduce the polarization and

subsequently reduce the permittivity, while the loss tangent increases (Al-Omari and Lear, 2005).

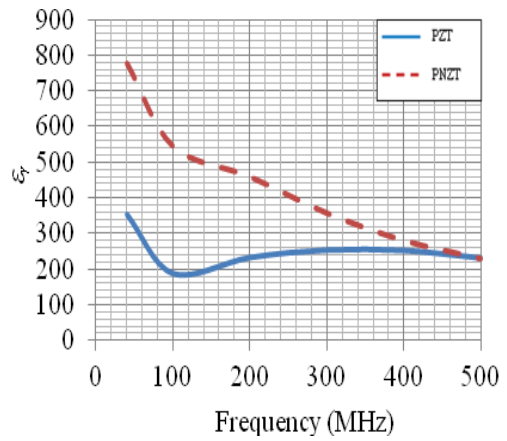

Figure 2: Permittivity versus frequency between 40 to 500 MHz.

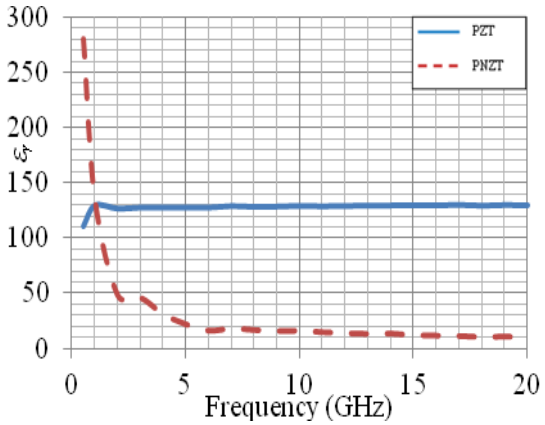

Figure 3: Permittivity versus frequency between 0.5 to 20 GHz

From the results we could see the effect of doping to PZT has significant impact on the capacitor performance. Nb^{5+} is a donor dopant which replaces the Zr^{4+}/Ti^{4+} ions in the B-site of PZT - this compensates the positive charge introduced (Riemens *et. al*., 2003). Also, there is correlation between the grain size and ε_r with Nb concentration. Riemens *et. al*, 2003, Haccart *et. al.* 2003 and Souza *et.al.,* 2004 reported enhancement to ε_r with Nb doping. However, the increase of ε_r is also influenced by composition as well as Nb concentration. The work by Souza *et.al* 2004 showed that PNZT with high ε_r has higher tan δ ompared to PZT. Similar lossy behavior of PNZT in our samples is seen in Figures 2 and 3.

The drastic decrease of ε_r with frequency for PNZT may be attributed to grain size as proposed by (Chikuvula, 2000). The degradation of ε_r can be caused by several factors such as dielectric relaxation and microstructure defects (Dimos and Mueller, 1998; and Elisalde and Ravez, 2001). In addition, different types of polarizations (which are classified according to dipole type) can give rise to several dispersion regions over the broad frequency range. With the decreasing permittivity, therefore, the loss is expected to increase with frequency. This behavior was indeed observed for both our films over the two frequency ranges. Many factors contribute to dissipation in a ferroelectric material - among them is the effect of oxygen and lead vacancies (Park *et. al*., 2002; Chang and Anderson, 1997 and Zhu *et. al*., 2006), ferroelectric domain wall motion, as well as film composition and microstructure (Park, *et. al*., 2002; and Elissalde and Ravez, 2001).

Table 1 summarizes the dielectric properties of our films from 40 MHz to 20 GHz, and compares with those of (Vilarinho, *et. al*., 2005). Though the loss tangent in this work was higher, the permittivity values were in the expected range for both thin films.

Table 1: Comparison of material properties.

	ε_r	**tan д**
PZT (this work)	110 - 353	0.04 – 0.1
PNZT (this work)	11 - 778	0.15 – 1.18
Vilarinho *et. al.* 2005	200- 1000	0.01 - 0.07

3.2 Transmission Lines

To demonstrate the feasibility of using these films in MMIC, several transmission lines were constructed on them. The lines were designed in both microstrip and co-planar waveguide (CPW) form. The co-planar waveguide format is preferred for high frequency on-wafer probing due to the co-planar arrangement of the *Cascade* probes used in this work. The CPW is also preferred over microstrip in MMIC applications since the former eliminates the need to use via holes, which is difficult to realize, and model, in MMIC. An example of the co-planar waveguide line structure used in our work is shown in Figure 4.

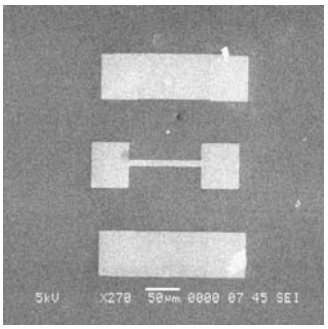

Figure 4: The test structure showing co-planar waveguide transmission line fabricated on PNZT film.

3.2.1 Simulation Results

a) Effect of ε_r

The transmission lines were also simulated to predict their behavior. The *CST Microwave Studio* electromagnetic simulator was employed for this purpose. In the simulation, ε_r values between 200 to 1000 were used to replicate the high-*k* properties of the films. Figure 5 depicts the simulated insertion loss values of CPW lines for different ε_r. The line length and width were set to 100 µm and 5 µm respectively. The CPW structure was treated as a symmetrical configuration, (Kuang *et. al.*, 2010; Pozar, 2005 and Kitzawa and Itoh, 1991) with the gap between the ground pad and the center conductor set to 50 µm apart to comply with the GSG probe pitch limitation. The tan δ value was fixed to 1 as ceramic materials are normally lossy (Pozar, 2005; and Mirshekar-Syahkal, 1983). The results show that as ε_r increases; the insertion loss increases with frequency. These results indicate that for a given frequency; as the relative permittivity is increased, the insertion loss is degraded. This is because more rf energy is lost in the dielectric as ε_r is increased.

b) Effect of line geometry

The CPW was treated as symmetrical configuration throughout the simulation. The gap *s* was set to 50 µm to comply with the probe pitch, while the centre strip line width *w* was varied. However, the minimum *w* is limited by the fabrication process. In this simulation the insertion loss was computed when *w* was varied over two sets of values - from 1 to 5 µm, and from 5 to 50 µm. The results of these two sets of simulations are shown in Figures 6 and 7 respectively. ε_r for both simulations were set at 200, and the line length was 100 µm with loss tangent of 1. The electrode thickness was fixed at 0.26 µm. The results in Figures 6 and 7 illustrate that S_{21} did not show a significant dependency on the line width. Both sets of results exhibit the same trend and comparable insertion loss values.

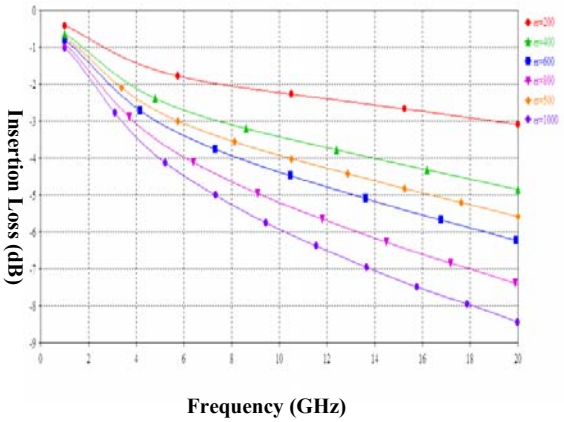

Figure 5: Variation of insertion loss of CPW lines with frequency for different ε_r values: 200 (●), 400 (▲), 500 (♦), 600 (■), 800 (▼) and 1000 (♦).

Now, if the insertion losses are calculated with different

$$\frac{W}{W+2s}$$

ratios at a fixed frequency of 10 GHz, the response obtained is shown in Figure 8 when *w* was varied from 5 to 50 µm. It can be seen that the insertion loss remain almost unchanged when *w* was varied.

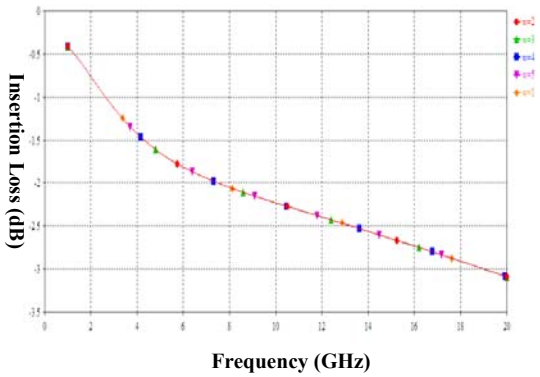

Figure 6: Variation of insertion loss with frequency for different line widths: 1 µm (♦), 2 µm (●), 3 µm (▲), 4 µm (■) and 5 µm (▼).

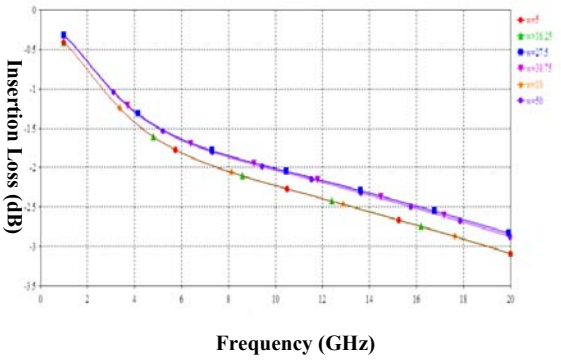

Figure 7: Variation of insertion loss with frequency for different line widths: 5 µm (●), 10 µm (♦), 16.25 µm (▲), 27.5 µm (■), 38.75 µm (▼) and 50 µm (●).

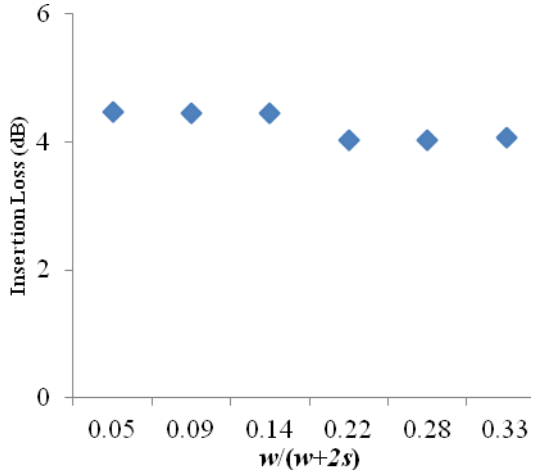

Figure 8: Insertion loss versus $w/w+2s$ for w = 5 to 50 µm at 10 GHz.

Using the electromagnetic simulator the current density distribution over the conducting strip was examined. These are shown in Figures 9 and 10 for cases where the width is decreased gradually from 50 µm to 16.25 µm. It can be seen that when the width of the conducting strip is equal to those of the ground planes the currents are equally distributed (Figure 9), and as the width was reduced the current density in the center conductor decreased as well – this is expected since the line impedances are now higher.

Current crowding at the conductor edges may also affect the performance of a CPW besides conductor surface roughness (Wen, 1969 and Jackson, 1986). Using an electromagnetic simulator this current can be examined quite conveniently as shown in Figure 9. In this figure current crowding at the conductor edge is revealed by plotting the current density across the width of the conductor. The current density values at the edge was about 5.13×10^7 A/m^2, the arrows are more densely located at the conductor edges, indicating current crowding. As the metal thickness was set to be 0.26 µm, which is less than the skin depth of Au at 10 GHz (0.8 µm); this implies that the rf current flow is concentrated at the edge of the lines in the slot region. In contrast, when the width-gap ratio decreases, as expected the current distribution in the center conductor decreases too (Riaziat, 1990), as shown in the plot of current density in Figure 10.

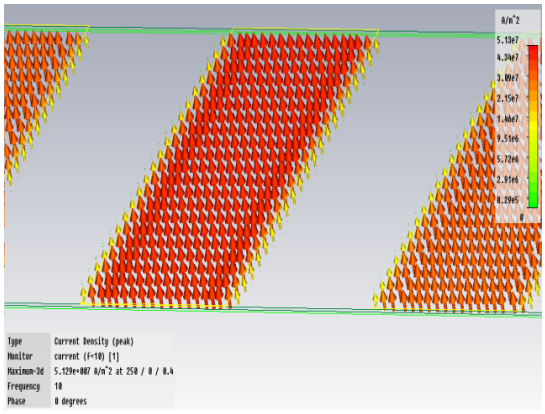

Figure 9: Current density of CPW for w = 50 µm.

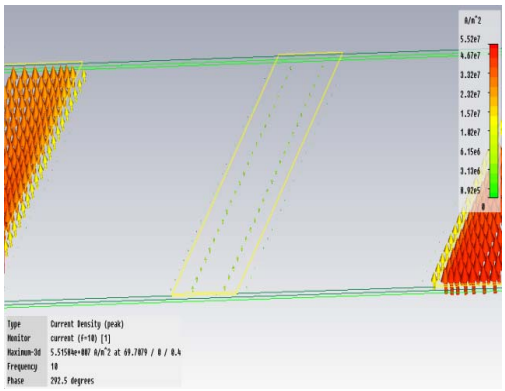

Figure 10: Current density of CPW for w = 16.25 µm.

c) Effect of Film Thickness

As mentioned previously, the thicknesses of PZT and PNZT films were 0.5 µm and 1.0 µm respectively. In the simulation however, the film thicknesses were varied to investigate the CPW performance. The values of ε_r and tan δ were obtained from the capacitance measurement: for

PZT they were 110 and 0.2, and for PNZT they were 280 and 1.

Figure11 shows the result of this simulation for PNZT, where plots of $|S_{21}|$ with PNZT film thicknesses varying from 1 to 5 µm. Two things are clear from the figure: firstly we see that the as the film gets thicker, $|S_{21}|$ decreases, implying a reduction in the insertion loss. This behavior is expected because as the film gets thicker, its physical properties will be more uniform and approach those of bulk samples. This is supported by evidences reported in the literature (Zhi-Xiang *et. al*., 2008, Haccart *et. al*., 2003 and Riemens *et. al*., 2003) whereby bulk samples show better performance than thin films. Secondly, $|S_{21}|$ also decreases with frequency, suggesting that the films get more lossy with frequency. This is due to the fact that at elevated frequencies the charges in the films are unable to switch to the higher frequency electric field. From the graphs it is important to note that for practical integration circuit applications, it is advisable not to use films thinner than 1 µm since the losses degraded quickly after that. In this work, the films used were 1 µm thick since it is quite difficult to get thicker films using metal organic deposition.

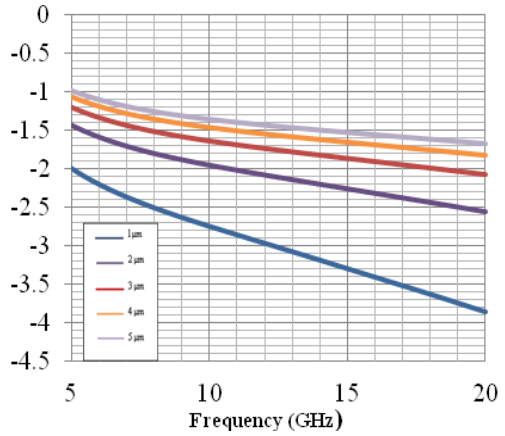

Figure 11: $|S_{21}|$ versus frequency for PNZT films of varying thicknesses.

3.2.2 Measurement Results

Test structures in the form of planar circuits such as stripline, microstrip and co-planar waveguide are commonly used for material property characterization at microwave frequencies. These test structures consist of dielectric substrates and conductors that act as conducting strips and grounding conductors. Microwave measurements are made to examine the effect of substrate property and conductor geometry so that microwave properties of the circuit can be analyzed (Chen *et. al*. 2004).

In this work, experimental investigations of the microwave behavior of both PZT and PNZT thin films were performed using microstrip and co-planar waveguide structures. In each structure, the PZT and PNZT films which acted as a dielectric supported by the silicon substrates.

The fabrication of the co-planar waveguide and microstrip transmission lines was identical for both films. The width and length of the lines are 5 µm and 100 µm respectively. The structures were measured with wafer probes in conjunction with a vector network analyzer for high frequency characterization. Measurement calibrations were performed using the SOLT technique, aided by the ISS impedance standard supplied by the probe manufacturer. Two-port measurements were carried out to evaluate the insertion loss of the films over a frequency range of 5 GHz to 20 GHz.

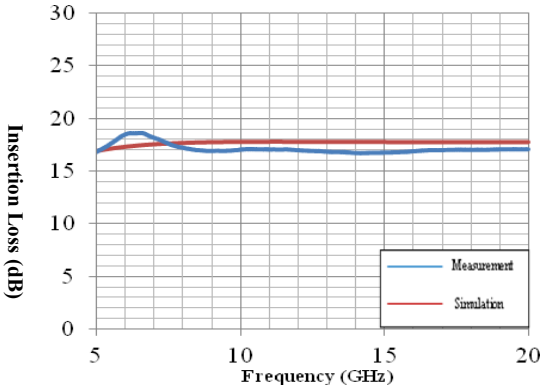

Figure 12: Comparison of simulated and measured insertion loss values of PNZT-based CPW.

Figure 12 shows the plot of one such result for PNZT-based CPW, shown together with the computer simulation for comparison. Both traces show the same trend, and the agreement is quite good, although the simulated values were slightly higher. The results are the evidence that PNZT can be used as a dielectric material in a CPW. The slight discrepancies between the two results were probably due to the mismatch loss that occurred in PNZT films and to factors other than substrate properties – this may include errors in the calibration and device fabrication, and the electrode behaviour at high

frequency. The mismatch happened due to the fact the transmission lines were not exactly 50 Ω – with the high dielectric constants exhibited by the films, the line width required to give 50 Ω was too small to be realized with our fabrication facilities. The difference in the impedance of the line and that of the probes would have given rise to reflections at the input port, and this resulted in mismatch loss. In addition, the loss of the PNZT-based CPW might not only be due to the properties of the thin films themselves, but to the geometrical aspects of the transmission lines as well.

In the course of our work we found better agreements with simulation were observed for PNZT samples. We also found the PZT samples exhibited higher insertion losses compared to PNZT of the same line dimensions and film thickness. PNZT-based CPW as a whole generally showed better all round performance in our work.

In order to determine the film properties, as well as to investigate the effect of microwave frequency on PNZT as a high-*k* material; a parametric study was carried out by varying the film parameters, to fit the simulation results with measurements. The line dimensions were actual ones used in the fabrication, while the film parameters such as ε_r and tan δ were varied. The effects of these variations on the insertion loss are shown in Figures 13 and 14 respectively.

Figure 13 a) shows that as the loss tangent is increased, the fit is better. This is expected from theory since in a transmission line, the insertion loss is mainly due to energy dissipation in the substrate (in this case the ceramic film) – a material with high loss tangent implies significant energy loss in the material, and this leads to high insertion loss. Ceramic materials in thin film form are known to be quite lossy, and our results seem to concur with this. In this example, a good fit between measurement and simulation is obtained for $\varepsilon_r = 200$ and tan $\delta = 1$ as shown in Figures 13 a) and b) respectively. Nevertheless our work has demonstrated that it is possible to implement PNZT and PZT thin films for use in MMIC.

4 CONCLUSIONS

PZT-based and PNZT-based thin film capacitors have been fabricated and their performance compared to investigate the effect of polarization at high frequencies. The high frequency measurement is divided into two frequency ranges; 40 MHz to 500 MHz and 500 MHz to 20 GHz. The results reveal that Nb doping affect the relative permittivity of the films, but the losses increased at high frequencies. The relative permittivity values were higher for PNZT films as expected due to doping.

The insertion loss characteristics of the films were studied by implementing co-planar waveguide transmission lines on PNZT. The films showed acceptable performance and proved the feasibility of using the films as a new substrate material for microwave integrated circuits. Our future work will include the use of these materials in the design of passive MMIC devices such as filters and phase shifters.

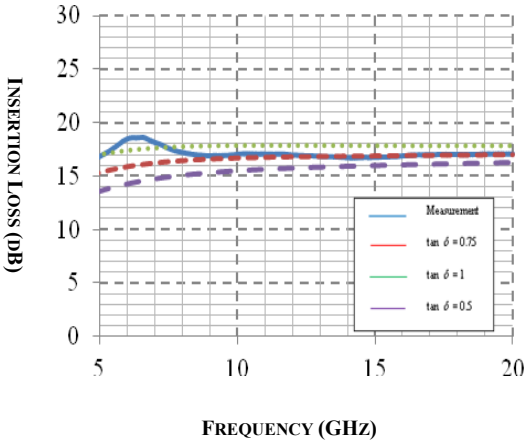

a)

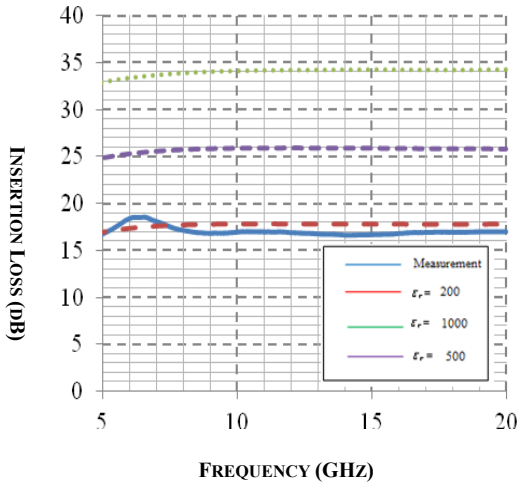

b)

Figure 13: Comparison between simulated and measured results of PNZT-based CPW transmission lines; with adjusted a) tan δ and b) ε_r.

ACKNOWLEDGEMENTS

The authors would like to thank Prof. Dr. Mohamad Rusop and his team from the Nanotechnology Research Group of University Technology MARA for the assistance given in the fabrication. We are also grateful to Dr. Sukreen Hana Herman for the PZT thin film samples used in this work.

REFERENCES

Al-Omari A. N. and Lear K. L. 2005. *Dielectric Characteristics of Spin-Coated Dielectric Films using On-wafer Parallel-Plate Capacitors at Microwave Frequencies.* IEEE Trans. on Electrical Insulation, 12, 1151-1161.

Bakar R. A. et. al. 2008. *Optimized Fabrication Process of PZT Thin Film Capacitor for MMIC Applications, Proc. Int. Conf. on Nanosc. and Nanotech.,* Shah Alam, Malaysia, Nov 18 – 21.

Chang L. H. and Anderson W. A. 1997. *Single and Multilayer Ferroelectric PZT on $BaTiO_3$.* Thin Solid Films, 303, 94-100.

Chen L. F. et. al, 2004. *Microwave Electronics: Measurement and Material Characterization*. New York: John Wiley & Sons, Ltd., 382.

Chikuvula, V. et. al. 2000. *Ferroelectric Dielectric for Integrated* Ciruit Applications at Microwave Frequencies, US Patent 6146905.

Dimos D. and Mueller C. H., 1998. *Perovskite Thin Films for High-Frequency Capacitor Applications 1*, Annual Reviews in Materials Science, 28, 397-419.

Elissalde C. and Ravez J. 2001. *Ferroelectric Ceramics: Defects and Dielectric Relaxations", J. of Mat.* Chem., 11, 1957-1967.

Haccart T. et. al, 2003. *Substitution of Nb Doping on the Structural, Microstructural and Electrical Properties in PZT Films*", Thin Solid Films, 423, 235-242.

Jackson R. W. 1986. *Considerations in the Use of Coplanar Waveguide for Millimeter-Wave Integrated Circuits,* IEEE Trans. on Microwave Theory and Tech., 34 (12), pp. 1450-1456.

Kitzawa T. and Itoh T. 1991, *Propagation Characteristics of Coplanar Type Transmission Line with Lossy Media,* IEEE Trans. on Microwave Theory and Technique , 39 (10), 1694-1700.

Kuang, K. et. al. (eds). 2010. *RF and Microwave Microelectronics Packaging. Netherlands:* Springer Science + Business Media.

Mirshekar-Syahkal, D. 1983, *An Accurate Determination of Dielectric Loss Effect in Monolithic Microwave Integrated Circuits Including Microstrip and Coupled Microstrip Lines*, IEEE Trans. on Microwave Theory and Tech., 31(11), 950-953.

Park Y. et. al. 2002. *Effect of Excess Pb on Fatigue Properties of PZT Thin Films Prepared by Rf-Magnetron Sputtering*. Mat. Lett., 56, 481-285.

Pozar, D. M. 2005, *Microwave Engineering*, 3rd ed. New York: John Wiley & Sons Inc.

Riaziat M. *et. al*,. 1990. *Propagation Modes and Dispersion Characteristics of Coplanar Waveguide*," IEEE Trans. on Microwave Theory and Tech., 38 (3), pp. 245-251.

Riemens D. et. al, 2003. *Piezoelectric Properties of Sputtered PZT Films: Influence of Structure, Microstructure, Film Thickness (Zr,Ti) Ratio and Nb Substitution*, Materials Science in Semiconductor Processing, 5, 123-127.

Setter N. et. al,. 2006. *Ferroelectric Thin Films: Review of Materials, Properties and Applications*, J. App. Phys, 100, 510-606.

Souza, E. C. F. et.al. 2004. *The Effect of Nb Doping on Ferroelectric properties of PZT Thin Films Prepared from Polymeric Precursors*, Materials Chemistry and Physics, 88, 155-159.

Sulaiman, S., Nadzar H. M. and Awang, Z. 2011, *Characterization of PZT and PNZT thin films for monolithic microwave integrated circuit applications,* Proc. 2011 IEEE Region 10 Conf. (TENCON2011), pg. 1264 – 1268, Nov. 22 – 24, Bali, Indonesia.

Vilarinho, P. M. et al. (eds.). 2005. *Scanning Probe Microscopy: Characterization, Nanofabrication, and Device Application of Functional* Materials. Netherlands: Kluwer Academic Publishers, 3-33.

Wen C. P. 1969. *Coplanar Waveguide: A Surface Strip Transmission Line Suitable for Non-reciprocal Gyromagnetic Device Applications.* IEEE Trans. on Microwave Theory and Tech., 77 (12), pp. 1087-1090.

WinCal 3.2 User Guide. 2000, Cascade Microtech, Inc.

Zhi-Xiang *et. al*. 2008. *Thickness and Nb-Doping Effects on Ferro and Piezoelectric Properties Highly a-axis Oriented Nb-doped $Pb(Zr_{0.3}Ti_{0.7})O_3$ Films*. J.of App. Phys., 140, pp. 2003-2007, 2008.

Zhu C. et. al. 2006. T*he Effects of the PbO Content and Seeding Layers upon the Microstructure and Orientation of Sol-gel Derived PZT Films*. J. Mat. Sc.: Materials in Electronics, 17, 51-55.

DETECTION IMPROVEMENT OF HIDDEN HUMAN'S RESPIRATORY USING REMOTE MEASUREMENT METHODS WITH UWB RADAR

Saeid Karamzadeh, Mesut Kartal
Informatics Institute, Department of Advanced Technology, Satellite Communication & Remote Sensing Program Istanbul Technical Universitym Maslak, 34469, Istanbul, TURKEY
{ Karamzadehsaeid, kartalme}@ itu.edu.tr

Keywords: Gaussian signal, wavelet transforms.

Abstract: Sensing vital parameters especially respiration, is important in many application fields, such as military services, medical activities, and rescue missions. Because of high resolution and appropriate penetrating factors, ultra wide band (UWB) radars have got more attention in these applications. In this study, we use UWB radar to detect respiratory signal of hidden human behind a wall. Acquiring the optimal transmitted signal, to obtain the best detection result in receiver's output is the novelty and the aim of our proposed work. For this purpose, we test Gaussian signal and some derivatives of this signal as transmitted signal and compare the receiver output results. To extract the required information about the target from receiving signal and subtract the background noise, the wavelet transforms are the adequate methods and are used in this work. At the signal processing part, different wavelet transforms will be considered, depending on some parameters such as the distance between the radar and the target or the wall's substance. With choosing the appropriate wavelet transform we can detect accurate human breathing signal affected by background noise that will be shown in the obtained results.

1 INTRODUCTION

One of the most important challenges about using UWB signals is to eliminate environmental noises from the desired signal.

In spite of many advantages, UWB signals are always exposure to noise because of operated frequency domain. Also in human respiration detection with UWB radars, background subtraction is always considered, because of the sensitivity of respiration signal and its enormous influence ability by environmental noises.

Different methods have been used for this application. Using matched filters in receiver is one of these methods, which is most often used to obtain human respiration signal in absence of barriers like a wall (Goswami et al., 2012).

The most common application of this method is taking care of patients and elderly exposure to cardiac arrest at hospital and at home.

In second method, averaging and Hilbert's transform are used in signal processing section to obtain respiration signal from received signal (Zhao et al., 2010).

Also other methods like using wavelet transform for extracting respiration signal in signal processing section are appropriate for complex environments with barriers like a wall. In this paper, different wavelets for extracting the optimized detection results from received signal are analyzed and compared.

This method can be applied in different fields like detecting location of criminals hidden inside of the apartments by police forces, or finding wounded people buried under debris of disasters like earthquake or avalanches.

2 GENERAL FORM OF SYSYEM

Figure 1, shows the signal changing during the scattering state that can be expressed as in (Eq. 1).

$$S_2(t)=\frac{dS_1(t)}{dt}, S_3(t)=\frac{dS_1(t+\tau)}{dt}, \quad S_4(t)=\int\frac{dS_1(t+\tau)}{dt}\times h(t-\tau)dt \tag{1}$$

In this figure $S_1(t)$ is the transmitted signal, τ is the time delay and h is the channel function indicating the reflection model of the target.
The signal released from transmitter antenna changes according to the antenna characteristics. Then it hits different layers of barriers and target with different dielectric constants and signal changes accordingly. At last, after time delay and assembling with channel noise, the signal reaches to receiver.

Choosing an appropriate antenna for better radiation and also choosing a suitable signal in transmitter can improve the results of target detection accuracy. To extract more complete information about the target, an appropriate signal processing method can be used.

In the next section, the appropriate antenna types and the transmitter signal have been discussed. Finally, obtained results have been presented after applying the proposed signal processing method. It is worth noting that in this work, CST microwave studio (computer simulation technology) software is used to simulation the antenna-target model and obtain the received signal

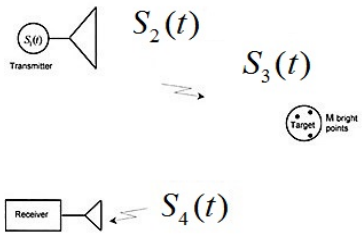

Figure 1: Signal changes during forward and backward path to radar

2.1 Antenna

The most proper antennas used in UWB radars are Horn and Vivaldi antennas which in most of the published papers. These antennas have been used as both the transmitter and the receiver antenna.

Vivaldi antenna gets to use because of its wide bandwidth and high gain and simple shape. Another advantage of this antenna is, easy fabrication for PCB (Printed Circuit Board) products. Horn antenna also has high gain and because of ability of decreasing the operating frequency to pass from barriers with high dielectric constants is more adequate. In this work, the horn antennas result has been discussed

Figure 2 shows a man behind a wall with real dimensions in the presence of horn antenna. Figure 3 shows the used CST human model in simulations which is a complete model of human presence considering all organs to obtain real results.

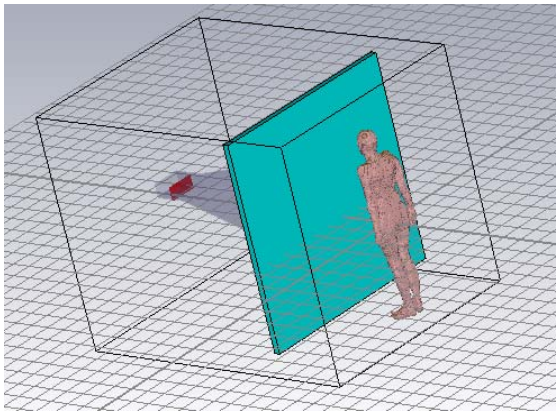

Figure.2: Using horn antenna for human detection

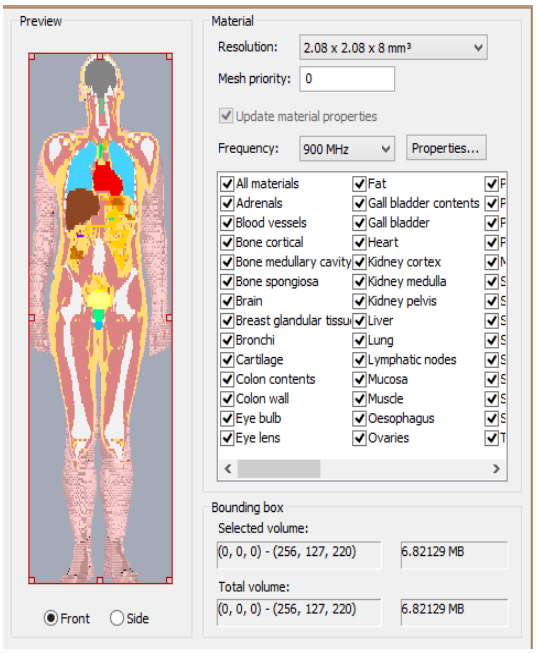

Figure 3: The model of human body that used in simulation

2.2 Signals

The most commonly used signal in UWBs is Gaussian signal and some of its derivatives. The most important advantage of this signal is its localization in both time and frequency domains.

In this paper, Gaussian signal, sinusoidal Gaussian and seven derivative of Gaussian signal is used as transmitted signal from antenna (transmitter) and the obtained results from these signals are analyzed individually in the receiver.

Figure 4 shows Gaussian signal and some of its derivatives used in this work.

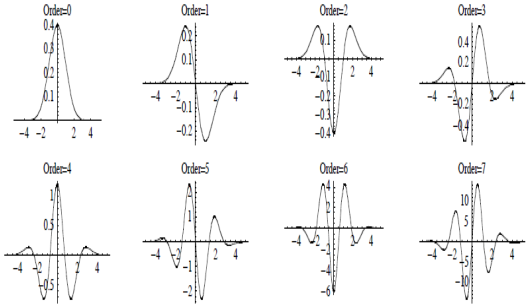

Figure 4: Gaussian signal and some of its derivatives

2.3 Wavelet transform

Wavelet transform can work with non-stationary signals. And therefore in this paper it is preferred to the others like Fourier transform.

Wavelet transform also provides multi resolution analysis with dilated windows which makes it possible to check different resolutions in various frequencies. So, wavelet transform would be a good choice for processing the received signals that change during passing different layers like air and wall.

In this paper, different wavelets transforms for extracting the optimized results from received signal are used. Some of them are: Daubechies, Symlets, Coiflets, Meyer, Gaussian, Mexican hat and Morlet wavelet. For the received signal f(t), its wavelet transform is given by,

$$W_f(a,\tau) = \frac{1}{\sqrt{a}} \int f(t) h^*\left(\frac{t-\tau}{a}\right) dt \qquad (2)$$

(h is the mother wavelet)

3 RESULTS AND DISCUSSION

In this study, 9 different types of signals containing Gaussian and sinusoidal Gaussian and seven derivatives of Gaussian signal are used as transmitted signal. Figure 5 shows the sample of these signals. The returned signal from target is received by the receiver antenna and to extract target information, proposed signal processing method is used to analyze. Figure 6 shows some examples of received signals. (In all figures the horizontal axis is time and the vertical axis is amplitude)

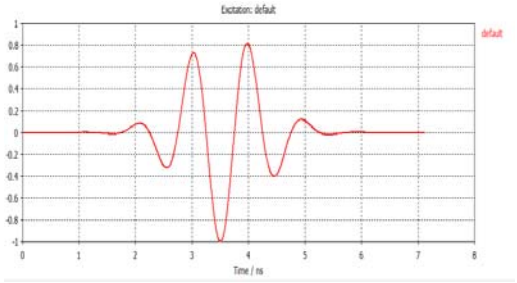

Figure 5a: Gaussian signal using as transmitted signal.

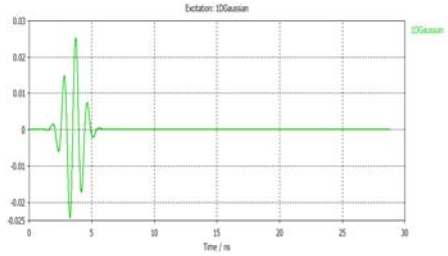

Figure 5b: First derivatives of Gaussian signal using as transmitted signal

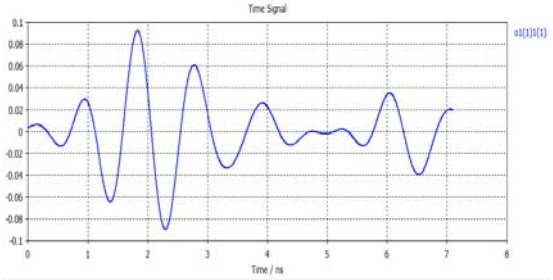

Figure 6a: The received signal when Gaussian signal used as transmitted signal

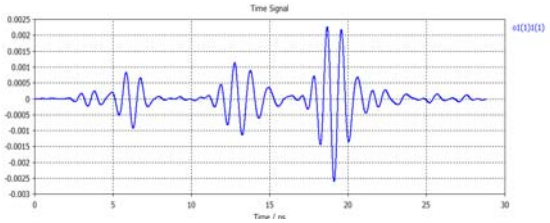

Figure 6b: The received signal when first derivatives of Gaussian signal used as transmitted signal

3.1 Signal processing

As explained in the first section, the shape and bandwidth of transmitted signal changes during passing the wall, hitting the target and returning to the receiver antenna. Wall thickness and its substance and distance between the human and antenna also affect the received signal.

By using appropriate signal in transmitter, the received signal can be predicted. As derivative of transmitted signal, the bandwidth of the signal changes and appears in receiver. Using wavelet transform, because of predicting the occurred changes like waveform and received signal bandwidth, is helpful in background subtraction and results appropriate output signal. Figure 7 shows diagrams of final data resulted from signal processing part which is human respiration periodic signal.

The obtained results show that, Mayer and Morlet wavelets give the best results by sending first derivative of Gaussian signal in transmitter. Also between these two wavelets, Mayer is closer to received signal and has better results. In these results, the background noise is completely omitted and respiration signal with acceptable amplitude can be observed (Figure 7a).

By sending the second derivative of Gaussian signal, Mexican hat wavelet gives better and acceptable output. By the way, Mayer wavelet would be more suitable as the transmitted signal in sending the second derivative of Gaussian signal (Figure 7.b).

During simulation process, it could be understood that the forth derivative of Gaussian signal in transmitter would have the best results using Morlet. For other derivatives (5, 6, 7), using Coiflets, Symlets and Daubechies wavelets would have better results which among them. Symlets would be more appropriate for fifth derivative and Daubechies would be more appropriate for sixth derivative of Gaussian signal.

It can be concluded from the results that the transmitted signal is formed by the transmitting antenna and then it can be interpreted as the second derivative of the transmitted signal at the receiver. Considering this, the best results for the target can be obtained by choosing appropriate wavelet.

In forward, after different simulations, it could be observed that second derivative of Gaussian signal would be the best choice for similar environments. Also, if the distance between human and antenna increase, using Daubechies wavelet would be a better choice for extracting desired target specifications. About walls with higher dielectric constant, using second derivative of Gaussian signal with Morlet wavelet would give the best results for target specifications.

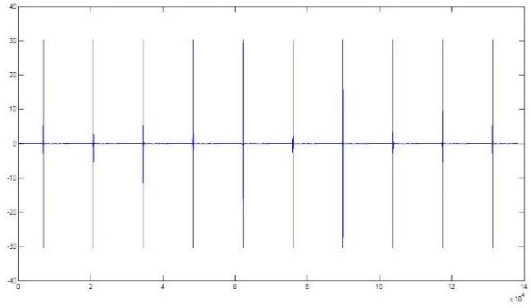

Figure 7a: the result of Meyer wavelet when first derivatives of Gaussian signal used as transmitted signal

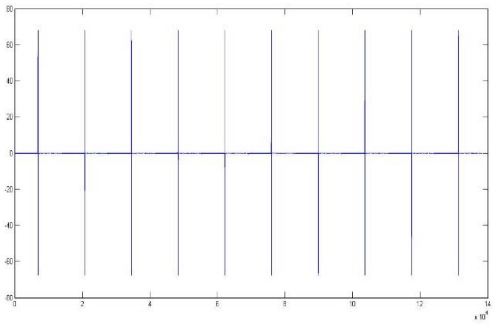

Figure 7b: the result of Mexican hat wavelet when second derivatives of Gaussian signal used as transmitted signal

(Vertical axis show the amplitude of breathing signal and the horizontal axis show the repeat of this signal)

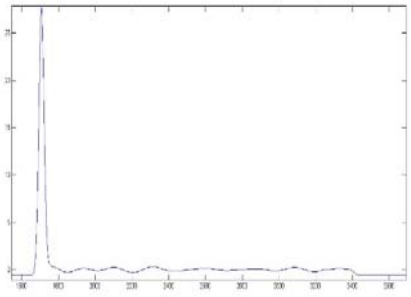

Figure 7c: one pulse of received signal after using wavelet methods

4 CONCLUSION

In this paper, human respiration detecting is considered. At first, the general UWB system used in detection is discussed. Then the choice of the antennas used in this work is presented. According to the importance of the transmitted signal form, appropriate transmitting signal for improving detection and obtaining better results are introduced. Finally, the wavelet transform method as the best method for background subtraction is used and simulation results are presented. It is concluded that for different system geometries, appropriate derivative of the transmitted signal and the mother wavelet selection give the best result. Additionally the respiratory signal of more than one hidden humans and moving humans could be consider in next work.

ACKNOWLEDGMENT

I would like to thank CST team for providing me CST software and voxel data for simulation part of this work.

REFERENCES

Goswami, D., Borkotoky, S. S., Mahanta, A., Sarma, K. C., 2012. *A Matched Filtering Technique for Noninvasive Monitoring of Human Respiration Using IR-UWB Radar, International Journal of Advanced Technology & Engineering Research (IJATER), 2 (4), 2250-3536*

Zhao, X., Gaugue, A., Liebe, C., Khamlichi, J., Menard, M., 2010. *Through the Wall Detection and Localization of a Moving Target with a Bistatic UWB Radar System*, Proceedings of the 7th European Radar Conference, 978-2-87487-019-4, Paris, France

Immoreev, I., Tao, T.H., 2008. *UWB Radar for Patient Monitoring*, IEEE A&E Systems Magazine

Staderini, M.E., 2002. *UWB Radars in Medicine, University of Rome ''Tor Vergata*", IEEE AESS Systems Magazine

Immoreev, Y.I., Samkov, S., Tao, T.H., 2005. *Short - Distance Ultrawideband Radars*, IEEE A&E Systems Magazine

Poularikas, A.D. (*Editor-in-Chief*), Sheng, Y., 2010. *Transforms and Applications Handbook*, Ch. 10 Wavelet Transforms, CRS Press, 3rd Edition

http://www.cst.com/

VALIDATION OF TWO NEW EMPIRICAL IONOSPHERIC MODELS IRI-PLAS AND NGM DESCRIBING CONDITIONS OF RADIO WAVE PROPAGATION IN SPACE

Maltseva Olga, Mozhaeva Natalia, Vinnik Elena
Institute of Physics Southern Federal University, Stachki, 194, Rostov-on-Don, Russia
mal@ip.rsu.ru, mozh_75@mail.ru

Keywords: GPS. Total electron content. Ionospheric model. Radio wave propagation. Geomagnetic disturbances. CHAMP. DMSP

Abstract: An empirical modeling of the behavior of ionospheric parameters is an important goal. The most complicated it is for the total electron content (TEC). The article focuses on two approaches: 1) the integration of N(h)-profiles using empirical parameters foF2 and hmF2, 2) the use of experimental values of the TEC. In recent years, two new models were developed: 1) IRI-Plas as a representative of the first approach, and 2) the Neustrelitz Global Model (NGM) as a representative of the second approach. Both models have their advantages over previous models. Any new model needs to be tested to get a quantitative estimate of proximity between the model and experiment, but both models have not been tested yet by anyone other than the authors of models. This article is dedicated to such testing. Besides the traditional comparison of model parameters foF2 and TEC with experimental data, in the paper the testing of additional parameters was performed with the help of independent experiments. For the IRI-Plas model, these are N(h)-profiles, data of incoherent scatter radars, and plasma frequency, measured at a height of satellites. For the NGM model, this is the equivalent slab thickness of the ionosphere τ. For the European region, it is shown that in most cases, the IRI-Plas model may be preferred to determine the parameters foF2 and TEC. For the parameter τ(NGM), there are conditions under which τ(NGM) provides better results than τ(IRI).

1 INTRODUCTION

Ionospheric models play an important role in determining wave propagation conditions of different frequency ranges in the nearest Earth space. The main parameters are the critical frequency foF2, the maximum height hmF2, the total electron content TEC. The most important parameter to operate navigation and communication systems is the TEC (e.g. Goodman, 2005). Positioning accuracy is directly proportional to the TEC. It can also be used to determine foF2 (Maltseva et al., 2012a). The article focuses on two approaches: 1) the integration of N(h)-profiles using empirical parameters foF2 and hmF2, 2) the use of experimental values of the TEC. The disadvantage of the first approach is the large discrepancy between model and experimental values of the TEC (Maltseva, Zhbankov, Nikitenko, 2011). In the second approach, there was no global empirical model of the TEC, and the existing regional models provide a large range of values TEC (up to an order of magnitude) (e.g. Arican, Erol, Arican, 2003). In recent years, two new models were developed: 1) the IRI-Plas model (Gulyaeva, 2011) and 2) the Neustrelitz Global Model (Jakowski, Hoque, Mayer, 2011). In this paper, it is abbreviated by NGM. The IRI-Plas model refers to the first approach, the NGM model - to the second one. Both models have their advantages. The IRI-Plas model introduces the topside basis scale height Hsc, which improves the shape of the N(h)-profile, and takes into account a plasmaspheric part of the profile. As for the NGM model, according to (Jakowski et al., 2011) this empirical model can be operated autonomously without any ionospheric measurements. To characterize the solar activity dependency, the 10.7-cm flux of the Sun is used as a proxy for the ionizing extreme ultraviolet radiation. The model is easy to handle and can efficiently be used in single frequency GNSS and radar systems for estimating

range error or ionosphere related polarization changes by the Faraday effect. (p. 966).

Both models need to be tested, since no one other, than the authors themselves, did test these models. In this paper, testing will be conducted as to the common parameters (foF2 and TEC), allowing us to compare the results of both models to each other, and to the parameters that the authors did not test, but which are of great practical importance. In the first case, these are N(h)-profiles. They are tested by data of incoherent scatter radars and plasma frequency, measured at a height of satellites. In the second case, the model allows to determine the equivalent slab thickness of the ionosphere τ(NGM) = TEC(NGM) / NmF2(NGM). This parameter also needs an empirical model but doesn't have it. The relevant test is to show whether can τ(NGM) be an empirical model of the equivalent slab thickness of the ionosphere.

2 DATA AND MODELS USED

Experimental data of TEC values are used from the global maps of JPL, CODE, UPC, ESA, which are calculated from IONEX files (ftp://cddis.gsfc.nasa.gov/pub/gps/products/ionex/) for given coordinates and time points. Values of other parameters of the ionosphere were taken from the SPIDR database (http://spidr.ngdc.nasa.gov/ spidr/index.jsp). Of the model, as indicated in the Introduction, there are two ones: IRI-Plas and NGM. The IRI model is well known and widely used. It is presented in some detail in the work (Maltseva, Mozhaeva, Zhbankov, 2012, below paper1) and in many others. Since the NGM model is completely new, it is necessary to give its brief description. A global model of the TEC(NGM) is given by product of five multipliers:

$$TEC(NGM) = F1 * F2 * F3 * F4 * F5.$$

It is based on data of the global CODE map. Each multiplier reflects the dependence of TEC on certain physical factors and is calculated using 2 to 6 coefficients CI. Coefficients are determined by the least-squares procedure superimposed on experimental data for several years. Coefficient F1 describes the dependence of TEC on the local time LT, i.e. on a solar zenith angle, and includes daily, half-day, 8-hour variations. It is calculated using 5 coefficients (C1-C5). Maximum of daily variations is shifted to LT = 14. Coefficient F2 describes annual and semi-annual variations, using coefficients C6-C7. Coefficient C8 is included in the F3 multiplier describing the dependence of the TEC on the geomagnetic latitude. Coefficients C9 and C10 correspond to accounting equatorial anomalies in the latitude dependence of the TEC (factor F4). Coefficients C11 and C12 describe the dependence of the TEC on the index F10.7: F5= C11+C12*F10.7. A model for NmF2 (Hoque and Jakowski, 2011) is built on the same principle, but has 13 coefficients, since in this case the factor F1 of daily course includes 6 coefficients. Maximum of daily variation is also shifted to LT = 14. A model of hmF2 (Hoque and Jakowski, 2012) includes 4 multipliers: hmF2=F1*F2*F3*F4, because there is no special factor of the equatorial anomaly. F10.7 values are tied to the number of days of a year. Dependence on F10.7 is described by the factor F4. Below we give a comparison of parameters of the two models with experimental data and with each other. Results are represented using data of the Juliusruh station (in the main), located in the central part of Europe.

3 TESTING MODELS BY IS RADARS

As noted, because a value of TEC of the IRI model is calculated by integrating N(h)-profiles, it is important to test the profile shape with the help of independent experiments. One of them is incoherent scatter radars (ISR). Paper1 (Section 3) represented results of testing IRI-Plas according to three radars on the borders of the European zone near the maximum of solar activity. In recent years, much attention was paid to peculiarities of simulation results of ionospheric parameters and N(h)-profiles during periods of low activity (Cander and Haralambous, 2011; Liu et al., 2011; Zakharenkova et al., 2013; Cherniak et al., 2012; Maltseva, Mozhaeva, Nikitenko, Thinh Quang, 2012). This is all the more relevant as the forecast of maximum of the 24 cycle will be less than the maximum of the 23 cycle, and the 25 cycle will be even less powerful, as can be seen from Fig. 1 (from http://solarscience.msfc.nasa.gov/predict.shtml).

Data of the Kharkov radar (49.6°N, 39.6°E), located in the central part of Europe, allow to fulfill an additional test for the conditions of the minimum activity.

According to data for two years (2007-2008), the authors (Cherniak,Zakharenkova, Dzyubanov, 2013) were able to select only the two days: 25 September 2007 and 29 October 2008. Both days are

characterized by quiet geomagnetic conditions. Authors (Cherniak et al., 2013) compared critical frequencies foF2 of ISR with results of the Juliusruh station (54.6°N, 13.38°E).

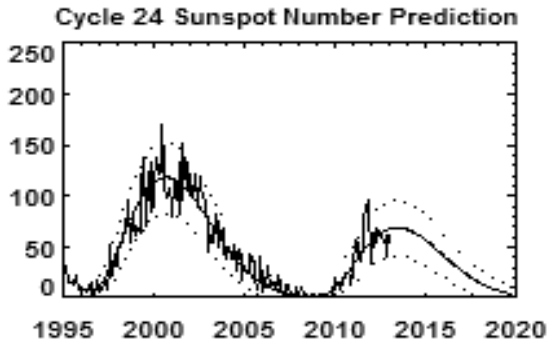

Figure 1. Solar number prediction for the 24 cycle

We compared them with results of the Průhonice station (50°N, 14.5°E), which is closer to the Kharkov radar than the Juliusruh station. Fig. 2 shows the daily run of foF2 for the following cases: 1) monthly median of foF2 (icon "med"), 2) the experimental value ("obs)", 3) data of ISR, 4) values of foF2(rec), calculated using τ(med) of the JPL map (Paper1), 5) the value of the original IRI model, which is the median, 6) the value of the NGM model. Unlike the IRI model, which uses moving 12-month indices RZ12, the NGM model formally defines not only the median (they just still need to be calculated from the values for the daily F10.7), but also the value for a particular day. The left panel refers to 29/10/2008, right – to 25/09/2007. In Fig. 3, these dependences are shown for the Juliusruh station.

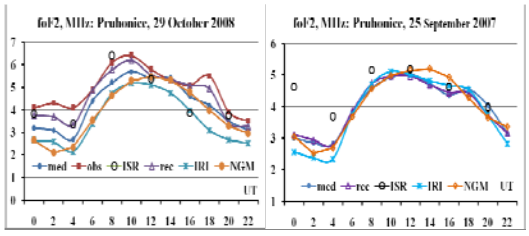

Figure 2. Comparison of various options of the foF2 determination (selected days, the Pruhonice station)

In Fig. 3, these dependences are shown for the Juliusruh station.

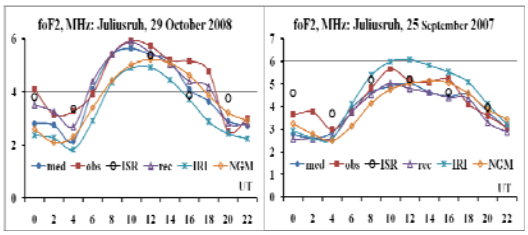

Figure 3. Comparison of various options of the foF2 determination (selected days, the Juliusruh station)

For completeness, the results are given for the Rostov station closest to the radar (data of this station were not available for October 2007), and Chilton at 09/25/2007 (fig. 4).

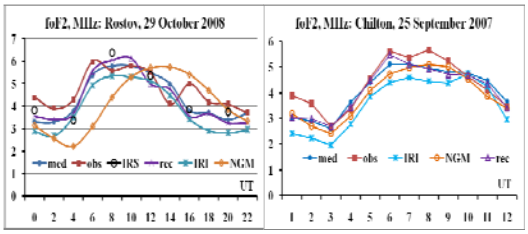

Figure 4. Comparison of various options of the foF2 determination (two stations)

Even these few graphs allow us to make some conclusions: with two exceptions of September 25, 2007 (2UT and 4UT), values for both models are fairly well with the experiment as medians and foF2 values on specific days. Quantitative deviations |ΔfoF2| are minimal for foF2(rec) and maximum for foF2(IRI) or foF2(NGM). It is difficult to give preference to one of the models. For all 12 cases of ISR data, N(h)-profiles were calculated for the original model, and for adaptation of the model to the experimental values of various parameters, separately for cases of foF2, TEC and their joint use. Unlike paper1, an additional adjustment to the TEC(NGM) was added. The whole set of values of the TEC is shown in Fig. 5.

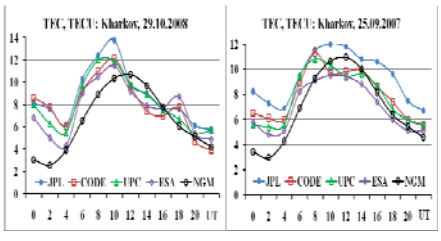

Figure 5. Comparison of various options of the TEC determination for the two days of Kharkov ISR measurements

Examples comparing N(h)-profiles with ISR profiles for the various options are shown in Fig. 6 for night (0 UT) and day (16 UT) conditions. This comparison has several objectives: a) to determine the map the N(h)-profile of which is the closest to the ISR profile, b) to determine the N(h)-profile for TEC(NGM).

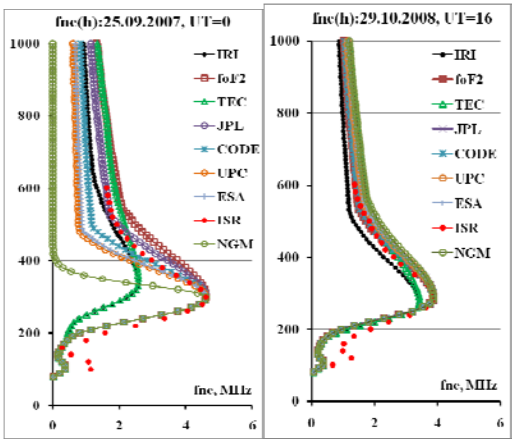

Figure 6. Comparison of N(h)-profiles calculated with N(h)-profiles of the Kharkov ISR

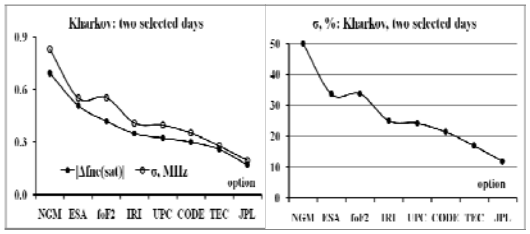

Figure 7. Comparison of model results with ones of global maps

It can be seen that the correspondence of N(h)-profiles are very different in day and night conditions. Daily profiles for all TEC options including TEC(NGM) are very close to the ISR profile. At night, only the N(h)-profile of the JPL map is close to the ISR profile. It is necessary to note that the JPL map gives the highest values of TEC. Profile for the NGM model shows virtually no ionization in the upper ionosphere, it is hard to imagine even in period of the minimum activity. A more complete picture is given by the analysis of all 12 cases. Fig. 7 (the left panel) shows the absolute deviations of the plasma frequency fne(600) and their dispersion (in MHz). They were obtained as the average for all days. The right panel displays the dispersion in %. This dispersion is important when comparing the results for different conditions of solar activity, because the relative dispersion is less dependent on RZ12, than absolute. The values are sorted from maximum to minimum to highlight an option with the maximum and minimum deviation. We see that in this case, the maximum deviations correspond to the NGM model, minimum – to the JPL map. Fig. 8 shows the values of fne(h = 600) for the profiles of ISR, NGM and JPL (the left panel). The right side shows their deviation. The abscissa is date of the measurement for the two selected days.

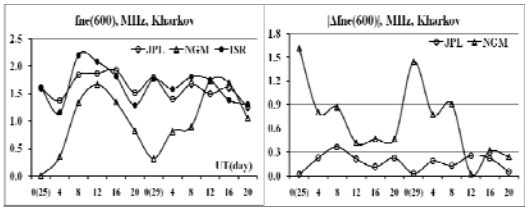

Figure 8. Comparison of plasma frequencies and their deviations for the two selected days and the two models

4 COMPARING THE CONFORMITY OF IONOSPHERIC PARAMETERS

Fig. 6 of the previous Section shows that the deviation of the JPL map does not exceed a certain value, and the NGM model is characterized by large deviations at night. This Section provides an illustration of conformity of ionospheric parameters of the two models to the experimental data for the conditions of varying solar activity..

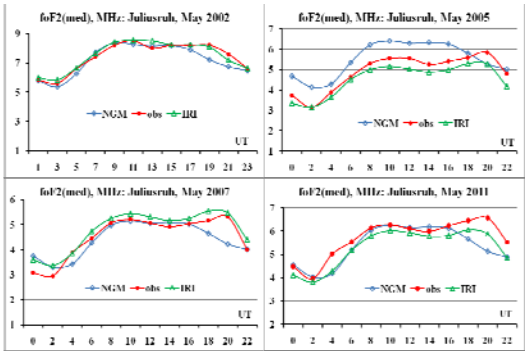

Figure 9. Examples of appropriate foF2 for different levels of solar activity (May, various years)

Comparison was made for medians of the corresponding parameters. Fig. 9 shows a comparison of foF2(med) for May. Fig. 10 represents results for December

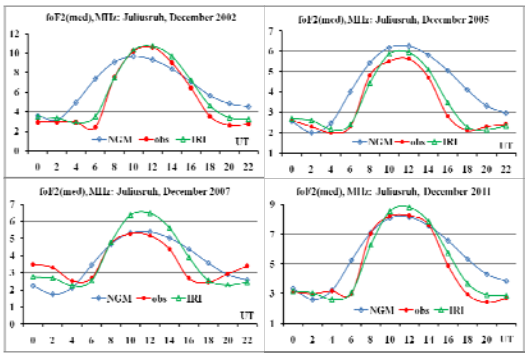

Figure 10. Examples of appropriate foF2 for different levels of solar activity (December, various years)

It is seen that in May and December the NGM model does not reflect the characteristics of diurnal values of foF2 (med). Examples of seasonal differences are shown in Fig. 11.

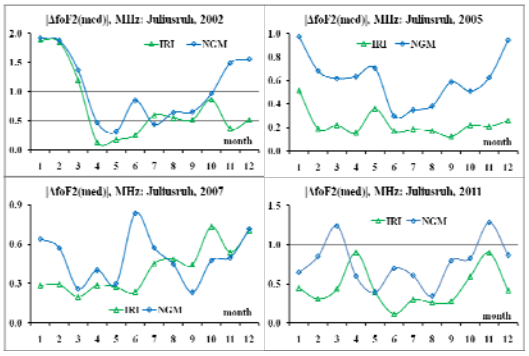

Figure 11. Examples of seasonal conformity foF2 for different levels of solar activity

Figures 12-14 represent similar results for the TEC. Here are experimental values of TEC(CODE). Additionally results of the JPL map are given, because its values are most commonly used in applications. For the IRI model, results are reported for 2 versions: IRI-Plas and IRI2001 (Bilitza, 2001).

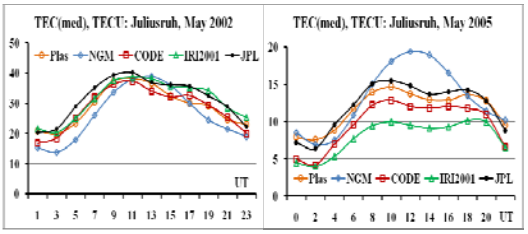

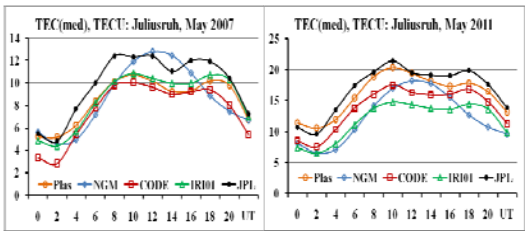

Figure 12. Examples of relevant TEC for different levels of solar activity (May, various years)

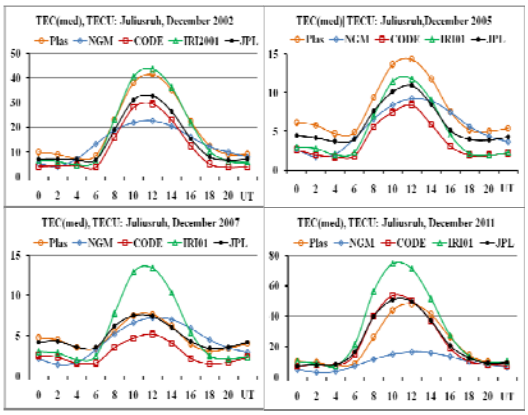

Figure 13. Examples of relevant TEC for different levels of solar activity (December, various years)

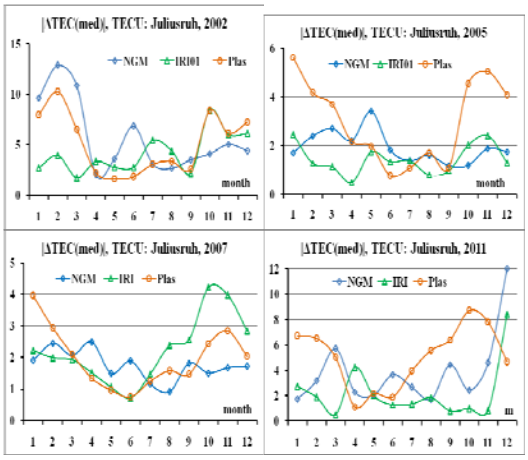

Figure 14. Examples of seasonal conformity of TEC for different levels of solar activity

As can be seen from Fig. 14, the value of this particular version is closest to the experimental TEC.

As for the two models, the IRI-Plas model often overestimates the value of TEC (compared with CODE), and hence gives greater deviations than NGM. Relative deviations in % are given in Table 1.

Table 1. Comparison of relative deviations for the two parameters of the ionosphere for the Juliusruh station

	y(foF2),%		y(TEC),%		
	NGM	IRI	NGM	IRI	Plas
2002	18.3	11.8	30.8	25.5	29.1
2005	17.7	6.5	34.3	29.7	56.0
2007	15.3	12.0	44.8	69.2	51.2
2008	19.0	20.0	96.3	57.0	125.
2011	18.1	10.3	40.7	27.8	62.7

As for the parameter hmF2, then it is more difficult to make the test for it, because experimental data are very limited. Fig. 15 shows the curves for maximum activity (May 2002, the Athens station) and for minimum (October 2008, the Juliusruh station).

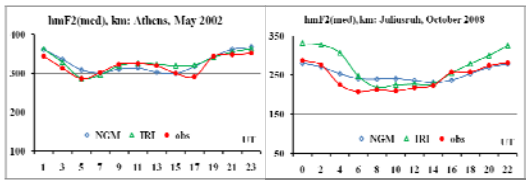

Figure 15. Examples of compliance of hmF2

On the one hand, there is a tendency inherent in the first two parameters: the deviation is less for both models in near maximum solar conditions, on the other hand, in both cases, the NGM model provides results that are 2 times better than the IRI (relative deviations are 5 and 10% in the first case and 8 and 15% in the second one.)

5 COMPARISON OF RESULTS FOR THE MEDIAN OF THE EQUIVALENT SLAB THICKNESS OF THE IONOSPHERE τ(MED)

Parameter τ (= TEC/NmF2) may play a role in assessing the state of the ionosphere. In (Gulyaeva, 2011), a formula between parameters Hsc (the topside basis scale height) and foF2 was obtained, allowing (maybe) to predict the behavior of this parameter during disturbances. Since there is a relationship between τ and Hsc (Hsc is a part of τ), it is possible, apparently, to get a connection for τ. But in this work, as in the paper1, we focus on assessing the possibility of determination of foF2 from experimental TEC with τ(med). Traditional methods are based on the use of τ(IRI) (McNamara, 1985; Houminer and Soicher, 1996; Gulyaeva, 2003), i.e. NmF2(rec) = TEC(obs)/τ(IRI). Frequency foF2(rec) is proportional to the square root of NmF2(rec). Naturally, the calculated values NmF2(rec) will be the closer to the experimental NmF2(obs), the closer τ(IRI) to τ(obs).

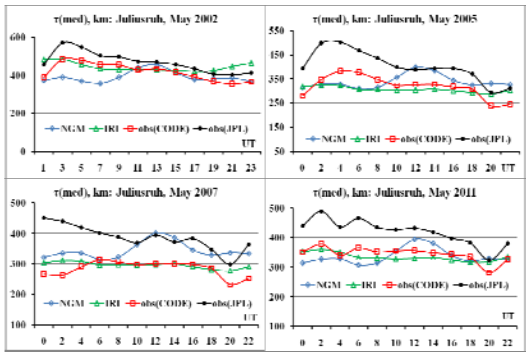

Figure 16. Examples of appropriate τ(med) for different levels of solar activity (May, various years)

In this section, these values are determined for the NGM model, to compare the experimental values (defined from the CODE map) with τ(IRI) and τ(NGM). Additionally they show τ(JPL), since in most cases this map gives the best fit to the experimental data of foF2. The corresponding results are shown in Fig. 16-17, which are obtained using curves of Figs 9-10, 12-13.

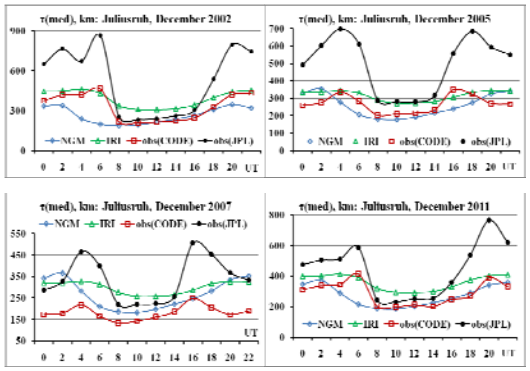

Figure 17. Examples of appropriate τ(med) for different levels of solar activity (December, various years)

These large differences between τ(CODE) and τ(JPL) should not be discouraged, because they are obtained from different TEC (TEC(CODE) and

TEC(JPL)). Authors (Jakowski et al., 2011) selected the CODE map. If they chose the JPL map, the results would have been closer to τ(JPL). As can be seen from these Figures, almost all the values of τ(NGM) are closer to the experimental τ(CODE), than τ(IRI), therefore, foF2(rec) for τ(NGM) should be closer to the foF2(obs) than foF2(IRI). To confirm this important fact and assess the possible use of τ(NGM) for the determination of foF2, calculations were fulfilled for IRI, NGM, and different maps (Fig. 18).

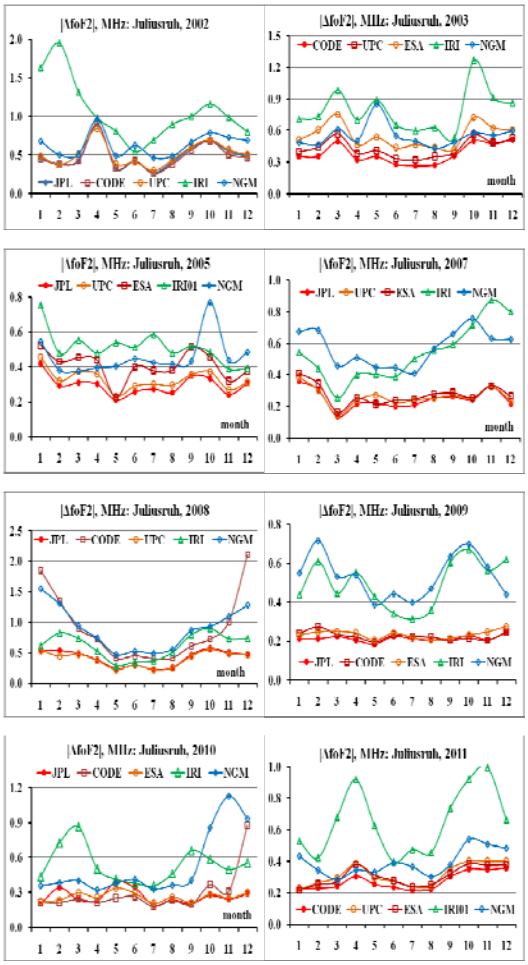

Figure 18. The absolute difference between experimental frequencies foF2 and frequencies calculated using the values of medians of τ for global maps of JPL, CODE, UPC, ESA and empirical models IRI and NGM

It turned out that the results depend on the level of solar activity, so we have provided detailed graphs for several years to illustrate what the conditions are most favorable for τ(NGM). Each graph shows the absolute difference between experimental values foF2(obs) and values foF2(rec), recovered using appropriate TEC. The general trend is to ensure that, in determining foF2(rec) from the TEC best results are obtained for the JPL map. The "second" place belongs to the CODE map. As for NGM, then its deviations |ΔfoF2| are much smaller than these for the model IRI under the conditions of high solar activity though they are larger in magnitude than deviations for global maps. As already noted, the simulation results in low solar activity is of great interest because of the evidence found that the model IRI is worse working in these conditions (2007-2009) (Zakharenkova et al., 2011; Maltseva et al., 2012a). Fig. 18 shows that the NGM model does not improve results compared with the IRI model. In addition, results for 2008 (the year with the lowest activity) show that the determination of the TEC from the CODE map reveals a significant effect of measurement error on the values themselves (apparently, the value of error is much greater than the TEC for this map)

6 TESTING MODELS USING PLASMA FREQUENCIES MEASURED BY SATELLITES

Paper1 has attempted to test the IRI model by data of CHAMP (h ~ 400 km) and DMSP (h ~ 860 km) satellites. It has been shown that in most cases N(h)-profiles corresponding to various maps do not provide an exact match of the plasma frequency fne(sat) at the height of the satellite, but one can choose a profile that passes through the foF2(obs) and plasma frequency of one or two satellites. This yields a value of TEC, other than the maps. In most cases, these values fall in the range of maps and form there an own subset. We use the fne(sat) to evaluate the situation for the NGM model. The results are shown in Fig. 19 for stations Juliusruh and Chilton and the various levels of solar activity. The red circles show the values of TEC(fne) for N(h)-profiles passing through fne(sat) of the DMSP satellite. The remaining values correspond to global maps (no values of the UPC map, because they are very close to the values of CODE). Values of TEC are ordered from maximum to minimum for each hour of UT, shown on the horizontal axis.

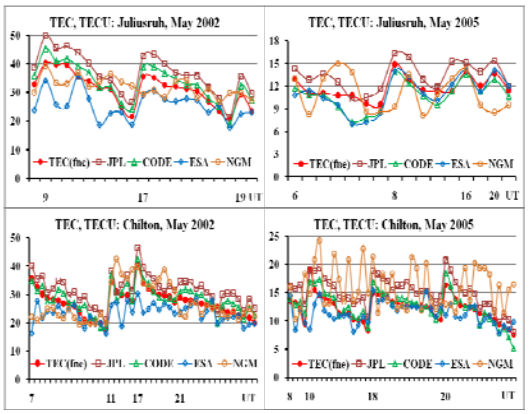

Figure 19. A comparison of different sets of TEC

Fig19 shows: a) the range of possible values for each of the experimental hour is large, b) TEC is experiencing great changes for various days and one hour, but changes are sufficiently synchronized for all maps. NGM model values, in-first, go far beyond the experimental range, to-second, within the hour have large random variation in various days.

7 EXAMPLES OF THE DISTURBED BEHAVIOR OF N(h)-PROFILES

Examples of the disturbed behavior of N(h)-profiles are represented in Fig. 20 during the last disturbance of May 2005. The strongest phase of this disturbance falls on 30 May. One can see response of various parts of N(h)-profiles on this disturbance in different latitudes. The top panel concerns to the Juliusruh station. The middle panel displays results for the Sofia station. The part of them was given from paper1 (fig. 10) to compare with new results. The bottom panel concerns to the Athens station. All profiles are close to model ones in 4UT (near quiet conditions). In the next moments 10-14UT, the positive disturbance over the Juliusruh station is developed covering only topside profiles. N(h)-profiles over the Sofia station show redistribution of ionization, i.e. its increase near hmF2 due to depletion of the higher part. Conditions over the Athens station are characterized by input of ionization from the magnetosphere (10UT), two-fold increased ionization of the whole profile (12UT). Phase of recovering (31 May) is faster in the topside part than in the bottom of the F2 layer, where the negative disturbance continues during all day. It shows that N(h)-profiles of the IRI-Plas model can be used not only in technical applications but to solve some problems of physics of the ionosphere.

8 CONCLUSION

The paper discusses two new models that give average values of ionospheric parameters: the critical frequency foF2, the maximum height hmF2, the total electron content TEC. One of them is the IRI-Plas model, which is a new option of the IRI model, the best known and most widely used, which is constantly updated. Its additional testing was held according to the Kharkov IS radar and the satellite data in a period of low solar activity. The second one is the new NGM model (the Neustrelitz Global Model), which is extremely simple: each parameter is the product of no more than 5 factors: P = F1*F2*F3*F4*F5 with clear physical binding of each factor. Another feature of the model is the dependence of each parameter on the number of days in the year and the corresponding index F10.7. To build the model TEC, its authors selected the global CODE map. Results obtained confirm the findings of the paper1 concerning to the high efficiency of adaptation of the IRI-Plas model to the experimental values of foF2, hmF2, and TEC. Further adaptation to the plasma frequency fne, measured by satellite DMSP, leads to new values of TEC(fne), which fall in the range of experimental values of global maps and can be considered as an independent estimate of the TEC. As regards the NGM model, for the purposes of its authors, i.e. in single frequency GNSS and radar systems, it is possible that the simplicity of the model plays a crucial role and the model will be used with success. In principle, the average foF2 and TEC values are predicted well, and in some cases the NGM model can give better results than IRI. But for the purposes of the wave propagation this is not enough, because the NGM model does not reflect daily variations of foF2 and TEC, and the discrepancy with the experimental data and with the IRI model may be 1.5-3 times.

It should be noted that in some cases the best results for the TEC are provided by the IRI2001 model, whose ceiling of N(h)-profile is 2000 km. This is due to the fact that the IRI2001 model strongly overestimates the concentration in the upper ionosphere (up to 1000 times) and this compensates for the lack of the plasmaspheric part of the N(h)-profile. Apparently, the fact that the new IRI-Plas option also overestimates TEC in some cases, suggests that the real Hsc of the new profile is

smaller than the model Hsc. As for the median equivalent thickness of the ionosphere τ(med), then there are conditions of solar activity, when the NGM model gives results better than the IRI model. Such a conclusion cannot be generalized to other regions without additional testing because of a strong dependence of the results on the location of the observation point and the solar activity. We can note also that previous versions of the IRI model (IRI2001 (Bilitza, 2001) and IRI2007 (Bilitza and Reinisch, 2008)) were validating during tens of years and this validation is continued. Validation of the IRI-Plas model and the NGM model began just now.

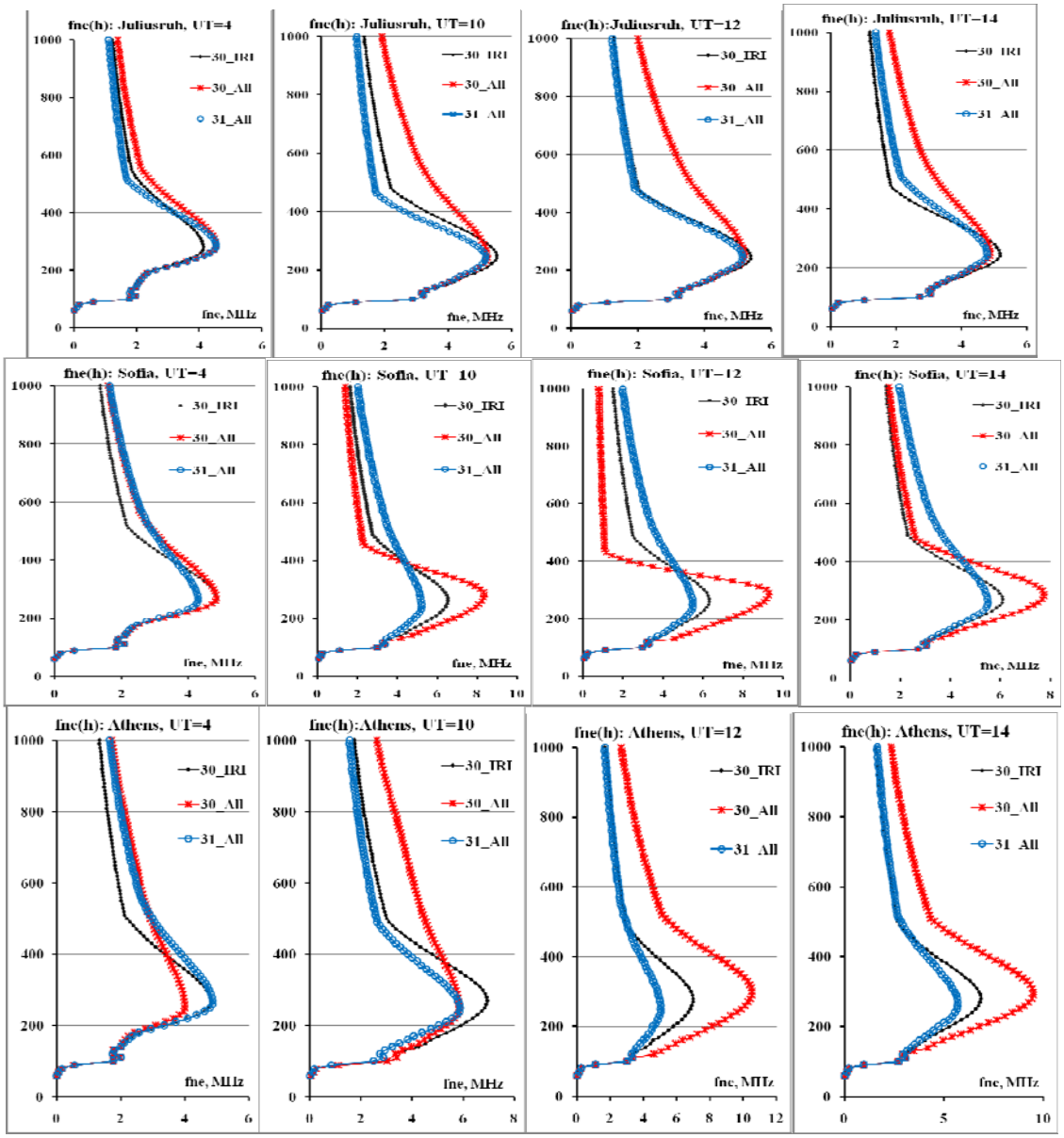

Figure 20. Development of disturbance of 30-31 May 2005 in N(h)-profiles on different latitudes

ACKNOWLEDGEMENTS

Authors thank organizations and scientists who are developing the IRI model, providing data of SPIDR, JPL, CODE, UPC, ESA, Dr M. Hoque for detailed comments on the NGM model, two reviewers for useful comments.

REFERENCES

Arikan, F., Erol, C. B., Arikan, O. (2003). *Regularized estimation of vertical total electron content from Global Positioning System data*. Journal of Geophysical Research, 108(A12), 1469, doi:10.1029/2002JA009605.

Bilitza, D. (2001). *International Reference Ionosphere*. Radio Science, 36(2), 261-275.

Bilitza D., Reinisch, B.W. (2008). *International Reference Ionosphere 2007: Improvements and New Parameters*. Advances in Space Research, 42, 599-609.

Cander, L.R., Haralambous, H. (2011). *On the importance of TEC enhancements during the extreme solar minimum.* Advances in Space Research, 47, 304-311.

Cherniak, Iu.V., Zakharenkova, I.E., Dzyubanov, D.A. (2013a). *Accuracy of IRI profiles of ionospheric density and temperature derived from comparisons to Kharkov incoherent scatter radar measurements*. Advances in Space Research, 51(4), 639-646.

Cherniak, Iu.V., Zakharenkova, I.E., Krankowski, A., Shagimuratov, I.I. (2012b). *Plasmaspheric electron content from GPS TEC and FORMOSAT-3/COSMIC measurements: solar minimum conditions*. Advances in Space Research, 50(4), 427-440.

Goodman, J.M. (2005). *Operational communication systems and relationships to the ionosphere and space weather.* Advances in Space Research, 36, 2241–2252.

Gulyaeva, T.L. (2003). *International standard model of the Earth's ionosphere and plasmasphere*. Astronomical and Astrophysical Transaction, 22(4), 639-643.

Gulyaeva, T.L. (2011). *Storm time behavior of topside scale height inferred from the ionosphere-plasmosphere model driven by the F2 layer peak and GPS-TEC observations*. Advances in Space Research, 47, 913-920.

Hoque, M.M., Jakowski, N. (2011). *A new global empirical NmF2 model for operational use in radio systems*. Radio Science, 46, RS6015, 1-13.

Hoque, M.M., Jakowski, N. (2012). *A new global model for the ionospheric F2 peak height for radio wave propagation*. Annales Geophysicae, 30, 797-809.

Houminer, Z., Soicher, H. (1996). *Improved short –term predictions of foF2 using GPS time delay measurements*. Radio Science, 31(5), 1099-1108.

Jakowski, N., Hoque, M.M., Mayer, C. (2011). *A new global TEC model for estimating transionospheric radio wave propagation errors*. Journal of Geodesy, 85(12), 965-974.

Liu, L., Chen, Y., Le, H., Kurkin, V.I., Polekh, N.M., Lee, C.-C. (2011). *The ionosphere under extremely prolonged low solar activity*. Journal of Geophysical Research, 116, A04320, doi:10.1029/2010JA016296.

Maltseva, O., Mozhaeva, N.S., Nikitenko, T.V., Thinh Quang T. (2012a). *HF radio wave propagation in conditions of prolonged low solar activity*, Proceedings of IRST2012, York, P07, 1-5.

Maltseva, O.A., Mozhaeva, N.S., Poltavsky, O.S., Zhbakov, G.A. (2012b). *Use of TEC global maps and the IRI model to study ionospheric response to geomagnetic disturbances*. Advances in Space Research, 49, 1076-1087.

Maltseva, O., Mozhaeva, N., Zhbankov, G. (2012c). *A new model of the International Reference Ionosphere IRI for Telecommunication and Navigation Systems*. Proceedings of the First International Conference on Telecommunication and Remote Sensing, 129-138.

Maltseva, O.A., Zhbankov, G.A., Nikitenko, T.V. (2011). *Effectiveness of Using Correcting Multipliers in Calculations of the Total Electron Content according to the IRI2007 Model*. Geomagnetism and Aeronomie, 51(4), 492–500.

McNamara, L.F. (1985). *The use of total electron density measurements to validate empirical models of the ionosphere.* Advances in Space Research, 5(7), 81-90.

Zakharenkova, I.E., Krankowski, A., Bilitza, D., Cherniak, Yu.V., Shagimuratov, I.I., Sieradzki, R. (2013). *Comparative study of foF2 measurements with IRI-2007 model predictions during extended solar minimum*. Advances in Space Research, 51(4), 620-629.

OPTIMIZATION OF BEAMFORMING TECHNOLOGY FOR COGNITIVE SPATIAL ACCESS IN MILLIMETRE WAVE

Femi-Jemilohun O.J, Walker S.D
School of Computer and Electronic Engineering, University of Essex, Wivenhoe Park, CO4 3SQ, United Kingdom
{ojfemi, stuwal}essex.ac.uk

Keywords: Phase shift beamformer, Minimum Variance Distortion less Response

Abstract: The allocation of 60GHz spectrum for WLAN has made the quests for gigabit data rates delivery to the end users possible in the wireless communication domain. The peculiar propagation characteristics in the millimetre wave can be exploited for improved system capacity. In optimizing beamforming techniques, a weight vector that minimizes a cost function is determined. The most commonly used optimally beamforming techniques or performance measures (cost function) are Minimum Mean Square Error (MMSE), Maximum Signal-to-Noise ratio (MSNR), and Minimum (noise) Variance (MV). A matlab based MVDR (Minimum Variance Distortion Response) and Phase-Shift Beamforming algorithms are proposed in this paper as means for cognitive spatial access in the millimetre wave band to enhance the signal of interest (SOI), with the suppression of interferences. Simulation results reveal that MVDR outperforms the Phase-Shifts in interference limited spatial multiple access (SMA) systems.

1 INTRODUCTION

The formidable growth rate in the wireless technology in the recent times has resulted in new and improved application services at lower cost. Invariably, the increased in demand for airtime by numerous subscribers has led to shortage in the limited frequency spectrum. The most readily practical solution to this problem will be in spatial processing. According to Andrew Viterbi, "Spatial processing remains as the most promising, if not the last frontier, in the evolution of multiple access systems''(Balanis 2005).The wider range and high quality of service required for effective wireless communication by the users that daily increase in exponential rate, can only be realized through the smart antenna technology, and spatial processing is pivotal to this technology. The exponential increase rate of subscribers coupled with limited frequency allocation by FCC, compel wireless system capacity availability a corresponding growth, this has been a huge problem to cope with in communication industry, hence cellular radio system has evolved several techniques through the years. Smart antenna technology among other techniques, with its quality of high interference rejection, will lower the BER thereby providing a substantial system capacity improvement.

The frequency spectrum in the Millimetre wave band has been proven to be the only candidate capable of gigabit throughput delivery required in the multimedia applications. This has received great attentions in research arena for developing ultra-high speed gigabit wireless communication systems for both short ranges such as WPAN as well as WLAN. (Wu, Chiu et al. 2008; Lin, Peng et al. 2011). Nevertheless, the capability of multi-gigabit data rate at 60GHz is faced with a very challenging power budget, this in collision with the propagation conditions of the channel, especially the path loss(Herrero and Schoebel 2010). The major technical challenge of the limited link budget due to high path loss, reflection loss are intended to be optimized for spatial reuse for improved wireless system capacity and quality of service. This was achieved by engaging high gain and high directivity antennas to compensate for the path loss in 60GHz transmission. The short wavelength of 60GHz radio signal necessitates the use of large number of tiny antennas, makes it an ideal wireless interface to support spatial reuse while on the other hand beamforming has emerged as an important

technology to support high directivity in 60GHz radio transmission to provide high data rates for local users under severe penetration and path loss(Yin, Chiu et al. 2011). The large number of antenna available in 60GHz will be used to serve multiple users while the received SNR to a single user is increased. It is obvious that as spatial reuse in dense environment will lead to CCI among the co-located radio links.

In this work, Optimal Adaptive Beamforming Algorithms (OABA) for cognitive spatial access was used to mitigate the collocated radio links interferences. This was implemented in the digital domain with phased antenna array antenna. A multiple effective antenna is employed to enhance reception to users in the SDMA system, where different users will have different permissible operating regions in order to maintain the SINRs for all users in the SDMA system.

1.1 Related Work

Quite a few number of works have been done on millimetre wave band beamforming using phased array antenna.(Lin, Peng et al. 2011) proposed a MMSE based switched beamforming code selection algorithm for mixed analog/digital beamforming structure to enhance interference mitigation and spatial reuse capability in the presence of CCI. The disadvantage of Switched Beam(SB) is that the fixed beam required the user to be in the centre of the beam for the placement of the desired signal at the maximum of the main lobe; otherwise, an interferer can be enhanced instead. Also SB is unable to fully reject the interferers. Hence we chose to use adaptive array system to customise an appropriate radiation pattern for individual user in simulated wireless system in our work.(Liu 2007) Used NLMS algorithm with the replacement of the delay-lines (TDLs) in the traditional broadband beamforming by sensor delay-lines to determine the effectiveness of the adaptive broadband beamforming with spatial only information. Beamforming algorithm with the suppression of interference was proposed by (alias Jeyanthi and Kabilan 2009) using matrix Inversion-Normalised Least Mean Square adaptive beamforming with minimum Bit Error Rate (BER). NLMS is characterised by computational complexity and low convergence, It also requires a reference signal.

In this paper, An empirical analysis of a typical wireless network deployed in millimetre wave band was conducted to determine the QoS and reliability of the channels in a spatial multiple access (SMA) system. We adopted Phase Shift and MVDR adaptive beamforming techniques algorithms in a digital domain transmission. A matlab based simulation was implemented for digital beamforming structure to achieve an optimal adaptive beamforming (OAB) for an enhanced signal of interest (SOI) and suppression of non-signal of interest (NSOI) to improve system capacity in a dense spatial reuse environment. Moreover, a comparison of the two beamforming algorithms was done for better and effective performance. Our simulation results showed that the proposed algorithms are able to provide interference mitigation while the beamforming capability in the millimetre wave is optimized in the dense spatial reuse scenario with multiple service users for effective utilization of frequency spectrum. The rest of this paper is organised as follows: section two discussed the Array Signal Processing and adaptive beamforming, while section three discussed the challenges in the millimetre wave frequency band, with empirical analysis in a real world scenario. Section four proposed and implemented the beamforming algorithms targeting at the optimization of cognitive spatial access system for improved system capacity. The results of the simulations and discussions were presented in section five. The conclusion was presented in section six.

2 ARRAY SIGNAL PROCESSING

This is one of the major areas of signal processing with wide applications in radar, sonar, communications e.t.c. The technology involves multiple sensors at different locations in space to process received signals arriving at different directions. (Matsuo, Ito et al. 2011). The three major areas of ASP are: Detecting the presence of an imping signal and determine the signal number, finding the direction of arrival angles of the impinging signals, and enhancing the signal of interest from known/unknown directions and suppress the interfering signals(Liu and Weiss 2010).This work is based on the third category: we developed an algorithm using the ASP technique to mitigate co-location interference in wireless access network for the improvement of the communication network system.

2.1 Adaptive Beamforming

This is a technique geared towards forming a multiple beams towards desired users while nulling

the interferers at the same time through the adjustment of the beamformer's weight vectors. It is the process of altering the complex weight on-the-fly to maximize the quality of the communication channel. Smart Antenna which is pivotal in adaptive beamforming is a system of antenna with smart signal processing algorithms. These algorithms are used to identify the spatial signature like direction of arrival (DOA) of the signal as well as to determine the beamforming vectors, which is used to track and locate the antenna beam on the mobile terminal (Park 2011). The figure 1 below depicts the process involved in adaptive beamforming

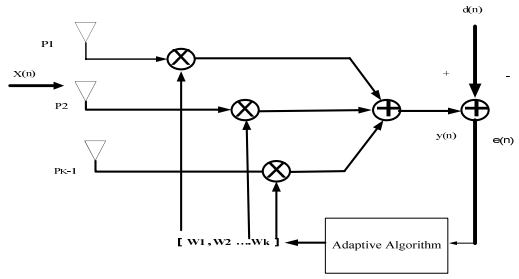

Figure 1: .Block diagram of Adaptive beamforming

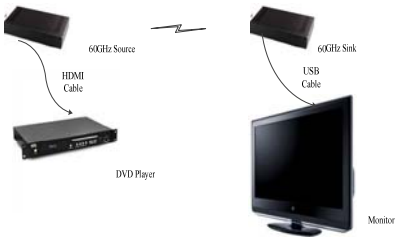

Figure 2: 60GHz Transmission Measurement set up

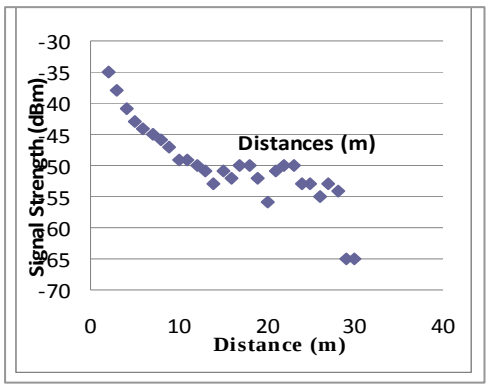

Figure 3: 60GHz Transmission at MSc Lab Beam Steering.

3 CHALLENGES IN 60GHz BAND

The peculiar characteristics of the millimetre wave such as limited emitted power, high temperature noise, and high oxygen absorption has confined its propagation to within the rooms or open areas in the

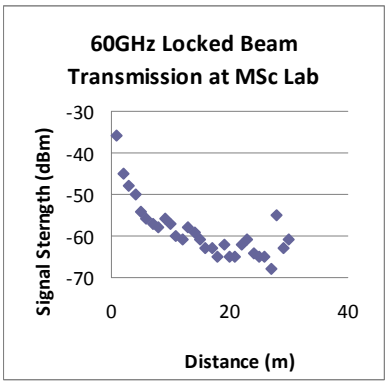

Figure 4: 60GHz Transmission at MSc Lab Locked Beam

close proximity of the antennas. There is unacceptable strong interference occurrence in these scenarios as a result of reuse of resources which attracts broadband mobile telecommunication. It was shown by (Flament 1999; Flament 1999) that the Signal-to- Interference ratio can drop from 15dB to 0dB within a few centimetres. .Likewise, a human influence on the path of transmission can attenuate the signal by 15dB or more, hence complete breakage of link.(Yang and Park 2009). The importance of antenna design in an indoor environment at 60GHz cannot be overlooked, since each room/small coverage area is a single cell with its own antenna, full coverage as well as lack of signal spill across rooms must be guaranteed. In case of coverage areas overlap results in co-channel interference(Voigt, Hubner et al. 1999; Xia, Qin et al. 2007). Adaptive Beamforming is method where antenna array are used to improve system capacity through interference reduction and also mitigates multipath fading. This was demonstrated in this work through matlab simulations and the results are depicted in the graphs.

3.1 Empirical Measurements Setup of Millimetre Wave Access Networks

The setup for source and sink transceivers for the radiation pattern measurements of 60GHz is shown in figure 2. The SiBeam P5 HDMI reference kits contain two host MCUs. One host is on the SK9200DB debug board and the other host is on the

module board. The SBAM2 (SiBeam Applications Manager) software is installed on a PC with XP operating system to monitor status, set configuration and control other parameters of the WiHD transceiver modules. The SK9200DB Boards (Source and Sink) are connected to the PC through the USB cable, the source is connected to the DVD player via an HDMI cable, both source and sink are connected to monitors separately for monitoring signal transmitted and received.

3.2 Data Acquisition and Processing

The transmission measurement was carried out at the MSc laboratory of the University of Essex, Colchester campus. The total distance 30m was covered at a step distance of 10m.The recorded received signals at different locations were processed through the excel software to generate the graphs 3 and 4 above.

4 BEAMFORMING ALGORITHMS FOR OPTIMIZATION OF COGNITIVE SPATIAL ACCESS SYSTEM

The Normalized Least Mean Square (NLMS) and Recursive Least Square (RLS) are the classes of adaptive algorithms and cost functions used for wideband beamforming when a reference signal is available and are characterised with computational complexity. Linearly constrained Minimum Variance Beamforming and Minimum Variance Distortion less Response (LCMV and MVDR) beamforming can be better options when a reference signal is not available but the DOA angle of the signal of interest and the range of their bandwidth is known. Some constraints can be imposed on the array coefficients to adaptively minimize the variance or power of the beamformer output such that the SOI impinging on the array from specific directions are preserved by a specified gain and phase response while all other contributions from NSOI from other directions are suppressed.(Liu and Weiss 2010).Taken a transmitted signal with a frequency of ω and DOA angle of θ, then the beamformer's response can be expressed as follows:

$$P(\theta,\omega) = W^H d(\theta,\omega) \quad (1)$$

Where $d(\theta,\omega)$ is the steering vector for wideband Beamformer with corresponding elements of complex exponentials expressed as:

$$d(\theta,\omega) = \begin{bmatrix} e^{-j\omega\tau_0} & \dots & e^{-j\omega\tau_{M-1}} e^{-j\omega(\tau_0+\mathrm{T}_S)} \\ & \dots & e^{j\omega\tau_{M-1}+\mathrm{T}_S} \\ & \dots & e^{j\omega(\tau_0+(j-1)\mathrm{T}_S)} \\ & \dots & e^{j\omega(\tau_{M-1}+(j-1)\mathrm{T}_S)} \end{bmatrix}^{\tau} \quad (2)$$

For any signal with frequency ω_0 and DOA angle θ_0 to pass through the beamformer, with a specified response, a Constraint is set as follows:

$$W^H d(\theta,\omega) = G_0 \quad (3)$$

The power output is given by:

$$E\left\{\left| y[n] \right|^2\right\} = W^H R_{xx} \quad (4)$$

$$R_{xx} = E\left\{XX^H\right\} \quad (5)$$

The LCMV beamforming problem follows equation Below:

$$W = \arg\min W^H R_{XX} W \quad (6)$$

These constrains determines the response of the beamformer to signal coming from specified direction and at specified frequencies. The resultant beamformer is called the minimum variance distortion less response (MVDR) beamformer.

Table 1: Simulations Parameters.

SOI angle	35
Interfering signals angles	45 and 55
SNR 1	4dB
SNR 2	40dB
Element number	10
Carrier Frequency	60GHz
Element spacing	lambda/2

5 SIMULATION RESULTS AND DISCUSSION

In this part we provided simulation results of the proposed algorithms. There are 10 sensors aiming at enhancing SOI at 35dgrees and adaptively suppress two wideband interfering signals arriving at 45 and 55 degrees respectively. SNR is 4dB and 40dB.A set of 500 channel iterations was generated using 60GHz NLOS multipath channel model.

Figure five is the magnitude plots of two antennas out of the array of ten to depict the transmission of the SOI and some thermal noise modelled as complex Gaussian distributed random numbers. Figure six depicts the output of a phase shift beamformer used to suppress signals from all directions other than the desired signal direction. The SOI becomes stronger than the noise as a result of the 10-array multiplicative power to give a gain of 10. The output response of this beamformer is shown in figure seven, where the mainlobe of the beamformer is pointing to the SOI direction (35degrees) as desired. A challenging scenario for the phase shift beamformer is depicted in figure eight. Interference signal from neighbouring transmitter masked antenna array and the SOI fell to the side lobe, therefore an adaptive MVDR Beamformer was used for the suppression of the interference at 45 and 55 degrees. This is depicted in figure nine; the output response of these beamformer for comparison is depicted in figure ten. The two nulls in the graph shows the suppression of interfering signals. It also shows the outperformance of the MVDR Beamformer over the phase shift beamformer for optimization of beamforming technology in spatial access system.

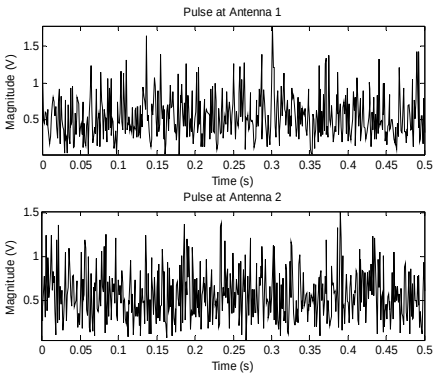

Figure 5: Magnitude plots of the first two channels.

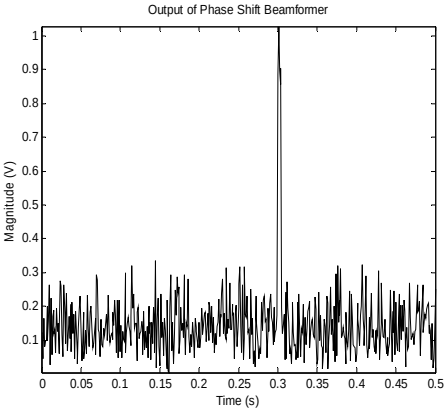

Figure 6: Output of the phase shift beamformer.

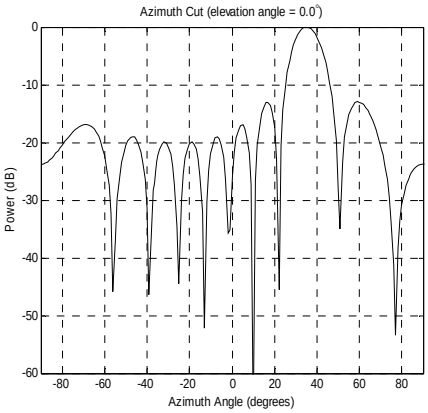

Figure 7: Beam pattern response of the beamformer.

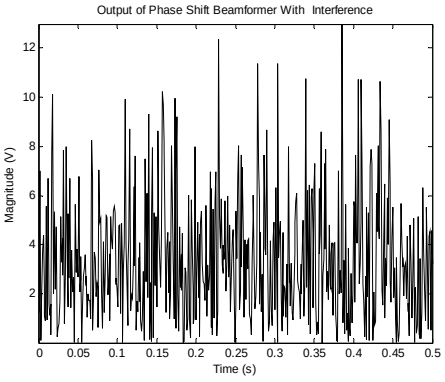

Figure 8: Response of the Phase shift beamformer with interference.

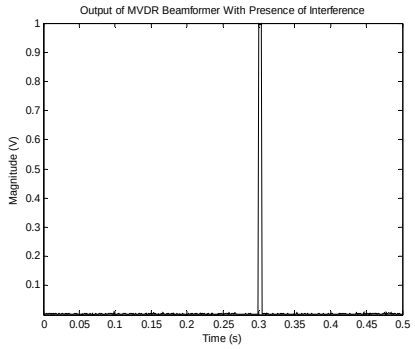

Figure 9: Response of the MVDR beamformer in the presence of interference.

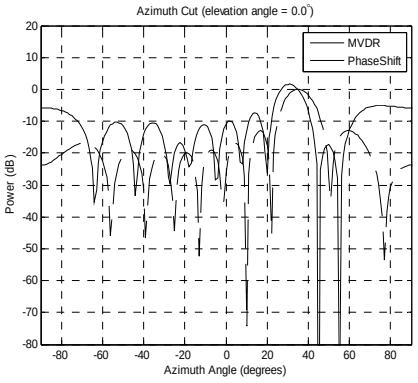

Figure 10: Beam pattern response of the beamformers.

5.1 Discussion

Fig 6 shows the desired signal is stronger than the noise. The SNR here is 10 better than for the single antenna shown in fig 5. Fig 7 shows the beam pattern response of the beamformer with the applied weights. The main beam of the beamformer is pointing to the set desired direction for the received signal (35). While fig8 shows the response of the beamformer when interference was introduced. The SNR is increased to 40dB to reflect the presence of interference. The interring signals are set to arrive at angles 45 and 55 degrees. It is obvious that phase shift beamformer cannot handle the challenge of interference; hence another beamformer called MVDR was used to retrieve the desired signal in this condition as depicted in fig 9. Fig. 10 shows the beam pattern response of the beamformers. While the phase shift fails to null the interferences; the MVDR does totally suppress the interferences and enhances the signal of interest.

6 CONCLUSION

Considering the effects of oxygen absorption and related technical challenges in 60GHz, it is obvious that the availability of large chunk of spectrum in it may not satiate the quest for high throughput as well as quality of service with high reliability required in the wireless network and multimedia applications. The confinement of transmission to a small area requires many access points to reasonably provide a wider coverage for users in the SMA systems, and consequently, a co-located interference is inevitable. An MVDR and Phase Shift beamforming algorithms are proposed to achieve improved system capacity and quality of service through interference suppression and enhanced SOI in a spatially dense transmission scenario. The simulation results demonstrated effective gigabits throughputs in the MMW band.

REFERENCES

alias Jeyanthi, K. M. and A. Kabilan 200). *"A Simple Adaptive Beamforming Algorithm with interference suppression.*" International Journal of Engineering and Technology **1**(1): 1793-8236.

Balanis, C. A. 2005. *Antenna Theory*. Analysis and Design. New Jersey, John Wiley & Sons, INC, Publication.

Flament, M. (999. *Propagation and Interference Issues in a 60 GHz Mobile Network.* Proc. of the 2nd Personal Computing and Communications Workshop, Citeseer.

Herrero, P. and J. Schoebel 2010. *Planar antennas and beamforming devices for a multi gigabit 60 GHz demonstrator with Quality of Service.* Antennas and Propagation (EuCAP), 2010 Proceedings of the Fourth European Conference on, IEEE.

Lin, Z., X. Peng, et al. 2011. *Enhanced beamforming for 60GHz OFDM system with co-channel interference mitigation.* Ultra-Wideband (ICUWB), 2011 IEEE International Conference on, IEEE.

Liu, W. 2007. *Adaptive broadband beamforming with spatial-only information.* Digital Signal Processing, 2007 15th International Conference on, IEEE.

Liu, W. and S. Weiss 2010. *Wideband beamforming: concepts and techniques*, Wiley.

Matsuo, M., R. Ito, et al. 2011. *Wireless transmission of JPEG 2000 compressed video*, IEEE.

Park, M. 2011. IEEE 802.11 ac: Dynamic Bandwidth Channel Access, IEEE.

Voigt, J., J. Hubner, et al. 1999. *Design pattern for a single frequency TDMA-system in a typical office environment at 60 GHz*, IEEE.

Wu, S. H., L. K. Chiu, et al. 2008. *Planar arrays hybrid beamforming for SDMA in millimeter wave applications.* Personal, Indoor and Mobile Radio Communications, 2008. PIMRC 2008. IEEE 19th International Symposium on, IEEE.

Xia, P., X. Qin, et al. 2007. *Short range gigabit wireless communications systems: potentials, challenges and techniques*, IEEE.

Yang, L. L. and M. Park 2009. *"Multi-band Gigabit Mesh Networks: Opportunities and Challenges."* International Journal On Advances in Networks and Services **2**(1): 88-99.

Yin, Y. S., L. K. Chiu, et al. 2011. *A space-time precoded hybrid beamforming architecture for broadband transmissions in 60GHz radio*. Personal Indoor and Mobile Radio Communications (PIMRC), 2011 IEEE 22nd International Symposium on, IEEE.

NON-UNIFORM SAMPLING FOR SPECTRAL ANALYSIS OF MULTI-BAND SIGNALS

Samba Traorè, Babar Aziz, Daniel Le Guennec and Jacques Palicot
IETR / SUPELEC, Campus de Rennes Avenue de la Boulaie - CS 47601, F-35576 Cesson-Sevigne cedex, Francey
fsamba.traore, babar.aziz, daniel.leguennec, jacques.palicotg@supelec.fr

Keywords: Non-Uniform Periodic Sampling, Non-Uniform Spectral Analysis, Cognitive radio.

Abstract: Recently, sub-Nyquist sampling of wideband signals has gained much attention in wireless communications. One of the main reasons for this popularity is the reduction in energy consumption in the ADCs. In this paper, we present an overview of the best known non-uniform sub-Nyquist sampling techniques and the associated spectral analysis. Spectral analysis using sub-Nyquist samples can be done in two ways. We can reconstruct the original Nyquist samples from the sub-Nyquist samples and then by using Fourier transform we can obtain the estimated power spectral density using classical methods like Welch method. We can also obtain the power spectral estimate directly from the sub-Nyquist samples without reconstructing the Nyquist samples. Both approaches can be used based on the application.

1 INTRODUCTION

In recent years, spectral estimation has attracted more and more interest due to its importance in the field of cognitive radio, where secondary users (unlicensed) can opportunistically use the frequency spectrum unused (holes) by primary users (licensed). For this purpose, the secondary user is forced to scan the radio environment of broadband in order to detect the holes. In [Zhang, 2010] authors use Filters Banks in order to share the wide band spectrum in many narrow bands and to comput in each narrowband in parallel the PSD. In [Tian and Giannakis, 2006] author apply wavelet transform in order to detect transitions between different subband of the wide band signal. But this type of wideband analysis involves a very high sampling rate and consequently a large energy consumption. This situation encouraged the researchers to examine the exploitable characteristics of the spectrum for a reduction of the requirements of the ADCs. A lot of papers propose to use the spectrum sparsity property to reduce the sampling rate [Bourdoux A. and der Perre L., 2011] [Miar et al., 2012]. Multi- Coset sampling studied in [Rashidi Avendi, 2010] [Venkataramani and Bresler, 2000] [Venkataramani and Bresler, 2001] is an effective way to reduce the frequency sampling for multi-band signals whose frequency support is a finite union of intervals. Similarly, [Mishali and Eldar, 2010] evaluates the subnyquist sampling for multi-band analog signals using a sparse ModulatedWideband Converter (MWC), consisting of several branches, each of which uses a different mixing function followed by a low-pass filtering and a low rate uniform sampling. Both the above approaches can be combined with compressive sampling. The reconstruction process can be carried out using methods such as sparse recovery algorithm LASSO (Least Absolute Shrinkage and Selection Operator) [Tibshirani, 1996] or even using traditional methods such as MUSIC (MUltiple Signal Classification) [Bresler, 2008]. The methods described in [Mishali and Eldar, 2010] [Rashidi Avendi, 2010] are known as blind spectral sampling methods, whose objective is to sample the signal at a minimum rate and reconstruct the unknown spectrum from these samples, while considering the spectrum is sparse. It was found in this work that for most signals, the minimum sampling frequency is given by the average lower limit of Landau (as studied in [Feng and Bresler,1996] [Landau, 1967]), which is equal to the Nyquist frequency divided by the spectrum occupancy. But for optimal reconstruction, all these meth

ods assume that the number of bands and the maximum bandwidth, a band can have, is known.

The methods presented before, assume that the signal to be analyzed is sparce in the frequency domain. There are other non-uniform sampling methods which do not make this assumption like Additive Random Sampling (ARS), Jittered Random Sampling (JRS). These methods are alias-free therefore we can sample at sub-nyquist rates. But we will show later that their performance is not good in terms of spectral analysis. In [Traoré et al., 2013], we proposed a new sampler based on Multi-Coset (MC) sampling scheme, which adjusts its sampling rate according to the changes in the frequency spectrum of the input signal. That is, if the signal is sparse in the frequency domain, it samples at sub-nyquist rate, else it samples at nyquist rate.

In this paper, we present an overview of the best known techniques of non-uniform sampling and the associated spectral analysis. This article is organized as follows. In Section 2, we present two non-uniform sampling techniques (Jittered Random Sampling and Additive Ransom Sampling) and the associated spectral estimation. In Section 3, we present a well known non-uniform sampling technique (Multi-Coset Sampling) and its limitations. In Section 4, we present an adaptative Multi-Coset Sampling technique. Numerical results are presented in Section 5 followed by the conclusion in Section 6.

2 NON-UNIFORM SAMPLING

—Uniform Sampling (US) consists in representing a signal $x(t)$ with the values $x(k)$ at time instants which are integer multiples of T, called sampling period. In the case of non-uniform sampling, all $\{t_k\}_{k\in\mathbb{Z}}$, sampling instants, must be different from the set of instants $\{kT\}_{k\in\mathbb{Z}}$, for a sampling period T. The non-uniformly sampled digital signal obtained is given by:

$$x_s(t) = \sum_{k=-\infty}^{+\infty} x(t)\delta(t-t_k) \tag{1}$$

The estimate of the Fourier transform of the signal randomly sampled at the instants $\{t_k\}_{k\in\mathbb{Z}}$ consists only of the Fourier transform of continuous time $x(t)$ denoted $X(f)$ such that :

$$\hat{X}_s(f) = E\left[\sum_{k=-\infty}^{+\infty} x(t_k)e^{-j2\pi f t_k}\right] = \frac{1}{T}X(f) \tag{2}$$

Next we presente an overview of the well know non-uniform sampling techniques.

2.1 Jittered Random Sampling

In JRS Sampling, at the uniformly distributed sampling instants, a deliberate error obeying a statistical law of distribution defined on an interval $[-0.5T, 0.5T]$ is added. The n sampling instants by JRS mode are described by [Wojtiuk, 2000] [Ben Romdhane, 2009]:

$$t_k = kT + \tau_k, \quad 1 \le k \le n \tag{3}$$

with $E[t_k] = kT$, $Var[t_k] = \sigma^2$ and T is the average sampling period. For $n \ge 1$, $\{\tau_k\}_{k=1}^{n}$ is a set of random variables independent and identically distributed with probability distribution $p_1(\tau)$, with zero mean and variance σ^2. The probability density of the k^{th} sampling instant is given by:

$$p_k(t) = p_1(t-kT), \quad 2 \le k \le n \tag{4}$$

The digital signal obtained is given by :

$$x_s(t) = \sum_{k=-\infty}^{+\infty} x(t)\delta(t-kT-\tau_k) \tag{5}$$

There are several formulations of the Power Spectral Density (PSD) for random sampling using JRS mode [Wojtiuk, 2000] [Shapiro and Silverman, 1960]. However, the most exhaustive formulation which is based on justified hypotheses is that of Wojtiuk [Wojtiuk, 2000]. Wojtiuk demonstrated that in the case of JRS mode, the PSD of a randomly sampled signal is given by (6) :

$$P_{xJRS}(f) = P_x(f) \otimes \{\frac{1}{T^2}\sum_{n=-\infty}^{+\infty} |\Phi_1(\frac{n}{T})|^2\delta(f-\frac{n}{T}) + \frac{1}{T}\left[1-|\Phi_1(f)|^2\right]\} \tag{6}$$

where $P_x(f)$ is the PSD of the signal $x(t)$, $\otimes$ is the convolution operation, $\frac{1}{T}$ is the mean sampling rate and $\Phi_1(f)$ is the characteristic function of the distribution $p_1(\tau)$. The discrete term in (6) represents the aliasing operation and the continous term represents a wide band noise (Fig. 3). It was also verified that, for a uniform distribution, we improve the elimination of aliasing when we increase the average sampling rate and the standard deviation of the distribution (Fig. 4).

For the Gaussian distribution we have a very strong reduction for $\frac{\sigma}{T} = 0.2887$. The complete elimination of spectral aliasing achieved for uniform and poisson distribution (Fig. 5).

2.2 Additive Random Sampling

When the time interval between two successive sampling instants follow a statistical law of distribution defined on an interval $[0.5T, 1.5T]$, the sampling

is said random cumulative (ARS, Additive Random Sampling). The n sampling instants by ARS mode are described by [Wojtiuk, 2000] [Ben Romdhane, 2009]:

$$t_k = t_{k-1} + \tau_k = t_0 + \sum_{i=1}^{+\infty} \tau_i, \quad 1 \leq k \leq n \qquad (7)$$

where $E[t_k] = kT$ and $Var[t_k] = k\sigma^2$

For $n \geq 1$, $\{\tau_k\}_{k=1}^{n}$ is a set of random variables independent and identically distributed of probability distribution $p_1(\tau)$, with zero mean and variance σ^2. For $k = 0$, $p_0(t) = \delta(t)$. The probability density of the k^{th} sampling instant is given by:

$$p_k(t) = \otimes_{i=1}^{k} p_1(t) \qquad (8)$$

The digital signal obtained is given by :

$$x_s(t) = \sum_{k=-\infty}^{+\infty} x(kT + \tau_k)\delta(t - kT - \tau_k) \qquad (9)$$

The estimate of the Fourier transform of the randomly sampled signal is given by [Wojtiuk, 2000] (10):

$$P_{xARS}(f) = P_x(f) \otimes \{\frac{1}{T^2}\delta(f) + \frac{1}{T}\Re[\frac{1+\Phi_1(f)}{1-\Phi_1(f)}]\} \qquad (10)$$

From (10), the PSD of a randomly sampled signal according to the ARS mode is different from that of the JRS mode, because there is no sum of discrete components. Furthermore, the elimination of aliasing is better when we increase the ratio $\frac{\sigma}{T}$ (Fig. 6). For example, for gaussian distribution with $\frac{\sigma}{T} = 0.2887$, aliasing is completely eliminated (Fig. 7).

3 MULTI-COSET SAMPLING

In this section, we give an overview of the sampler based on Multi-Coset (MC) sampling [Mishali and Eldar, 2010, Rashidi Avendi, 2010] and discuss its limitations. MC sampling is a periodic non-uniform sampling technique which samples the signal $x(t)$ at a rate lower than the Nyquist rate, thereby capturing only the amount of information required for an accurate reconstruction of the signal. MC sampling starts by first choosing an appropriate sampling period T, less than or equal to the Nyquist period associated to $x(t)$. Two parameters L and p are selected such that $L \geq p > 0$. Then the input signal $x(t)$ is non-uniformly sampled at $t_i(n) = (nL + c_i)T$, where $1 \leq i \leq p$ and $n \in \mathbb{Z}$ [Mishali and Eldar, 2010] . The set $\mathcal{C} = \{c_i\}$ contains p distinct integers from $\mathbb{L} = \{0, 1, , L-1\}$ and is termed as the *sampling pattern*. In short, the process of MC sampling can be viewed as first sampling the input signal at a uniform rate with period T and then selecting only p non-uniform samples from L equidistant uniform samples. The process is repeated for consecutive segments of L uniform samples such that the p selected samples have a sampling period L. The set $\mathcal{C}$ specifies the p samples that are retained in each segment of length L such that $0 \leq c_1 < c_2 < ... < c_p \leq L-1$.

MC sampler is usually implemented by placing p ADCs in parallel as shown in Fig.1. Each ADC operates uniformly at a period $T_s = LT$. The $\Delta_i = c_i T$ represent the time shifts in sampling instants introduced in each branch. Thus we have

$$t_i(n) = (nL + c_i)T = (n + \frac{c_i}{L})T_s$$

where $1 \leq i \leq p$. It should be noted that MC sampling is highly sensitive to even small errors [Mishali and Eldar, 2010]. Because of this sensitivity, an apparently possible perfect reconstruction is not achievable and the signal easily becomes corrupted and unrecognizable in certain practical conditions. A good choice of the sampling pattern $\mathcal{C}$ reduces the margin of error due to spectral aliasing and sensitivity to noise in the reconstruction process [Rashidi Avendi, 2010]. It is

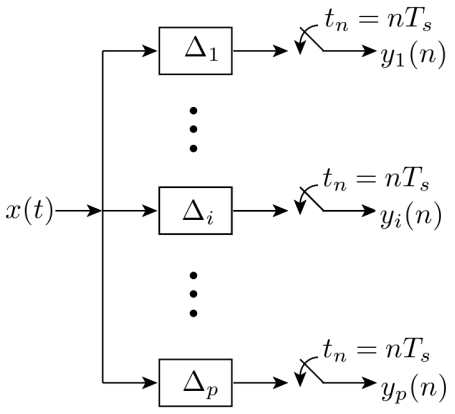

Figure 1: Multi-Coset (MC) sampler implemented as a multi-channel system.

quite evident from Fig.1 that once the sampling parameters (such as p) are selected, architecture of the MC sampler will remain unchanged irrespective of the input signal characteristics modifications. In other words, once designed, the sampler in Fig.1 cannot be changed because of hardware limitations. If the input signal changes, the MC sampler does not adapt, which results in sub-optimal sampling of the signal.

This motivated the author of [Traoré et al., 2013] to look for an optimal system which conforms with

the spectrum of the input signal. In the next section, we explain the functioning of this new sampling scheme and show that it is more flexible compared to the MC sampler in Fig.1.

4 DYNAMIC SINGLE BRANCH MULTI-COSET SAMPLER

With the exponential growth in the means of communications, modifying radio devices easily and cost-effectively has become business critical. Software radio (SW) technology brings the flexibility, cost efficiency and power to drive communications forward, with wide-reaching benefits realized by service providers and product developers through to end users [Palicot and al, 2010]. One of the main objectives of SW is to propose new technologies to design radio terminals and wireless infrastructure able to support hardware-independent, multi-service operations and are remotely reconfigurable. Furthermore,

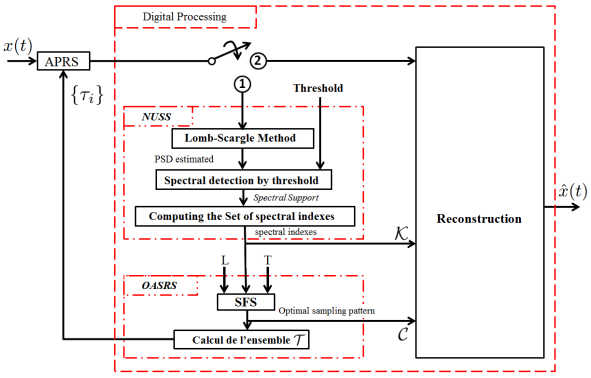

Figure 2: Dynamic Single Branch Non-Uniform Sampler

Cognitive radio continues to gain popularity as it adapts intelligently to the radio environment, there by dynamically managing the spectrum [Palicot and al, 2010]. As a result, the spectrum changes continously and rarely remains constant. Keeping the aspects of Software radio and Cognitive radio in mind, authors in [Traoré et al., 2013] present a sampler, that not only adapts to the changes in the input signal but is also remotely reconfigurable and is, therefore, not constrained by the inflexibility of hardwired circuitry. [Traoré et al., 2013] proposed non-uniform sampler is shown in Fig. 2. They call it the *Dynamic Single Branch Non-Uniform Sampler* (DSB-NUS) or simply the DSB sampler. It operates in blind mode, without any knowledge of the input signal's spectral support and the number of bands. The DSB-NUS works in two phases:

1. Adaptation phase: When the switch is in position 1, the system has no information about $x(t)$ (number of bands N, bands location, set $\mathcal{K}$ of spetral indices, maximum bandwidth B_{max}. It performs a spectral analysis using block NUSS (Non Uniform Spectrum Sensing) (estimate the Spectral support of the signal and $\mathcal{K}$, using Lomb-Scargle Method Fig. 8). In the Optimal Average Sampling Rate Search block (OASRS), according to (L, T, $\mathcal{K}$), used the Sequential Forward Selection (SFS) algorithm to find the optimal sampling pattern $\mathcal{C}$ and then the optimal set of sampling instants $\{\tau_i\}$.
2. Reconstruction Phase: When the switch is in position 2, the DSB-NUS sampler performs multi-coset reconstruction.

5 NUMERICAL RESULTS

For simulations, we consider a multi-band signal with 6 bands, each with a maximum bandwidth of $80MHz$. $16-QAM$ modulation symbols are used that are corrupted by the additive white Gaussian noise with $\frac{E_b}{N_0} = 50dB$. The wideband of interest is in the range of $\mathcal{B} = [-1.0, 1.0]GHz$ i.e. $f_{nyq} = 2GHz$.

Figures 3-4-5 show the PSD of the non-uniform samples obtained using JRS method, for different values of the average sampling rate i.e. at Nyquist, $\frac{4}{5}$ of Nyquist and $\frac{3}{5}$ of Nyquist. Spectral analysis was performed using Welch method with 50% overlap. Missing samples were all replaced with zeros.

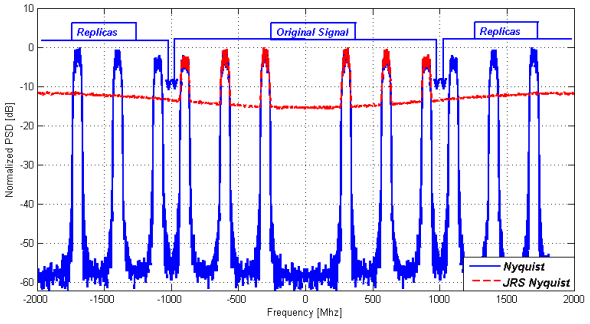

Figure 3: JRS presented free-aliasing property

We clearly see in Figure 3 that the curves obtained from JRS non-uniform samples are alias free. The curve obtained from uniform Nyquist samples present spectral replicas at multiples of the Nyquist rate.

In Figure 4, we show that the quality of the estimated PSD increases with increase in the average sampling rate of JRS technique. It can be seen that the wideband noise level increases and decreases in direct relation with the average sampling rate of the JRS

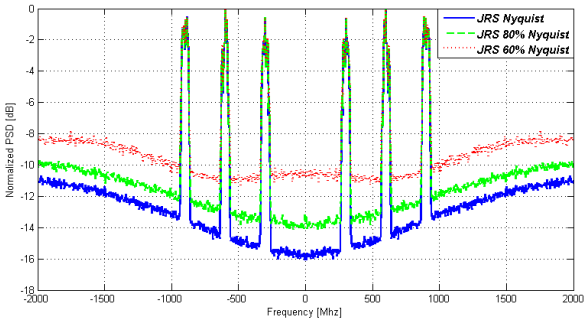

Figure 4: JRS with Uniform distribution and different average sampling rates

mode. For average sampling rate of 60% of Nyquist rate, the noise level is very high compared to the average sampling rate of 80% of Nyquist rate. However, this improvement in quality of the estimated PSD comes at the expense of more samples. Moreover, it should be noted that the results presented in Figure 4 are averaged over 100 iterations.

Next, in Figure 5, we present the effect of distributions of sampling instances, used for JRS sampling, on the estimated PSD. We compare three distributions, namely, Gaussian, Poisson and Uniform. We can see that when Gaussian distribution is used, spectral replicas appear, however, there amplitude is small. When Poisson distribution is used, no spectral replicas are observed, however the noise level has increased compared to the Gaussian distribution. Finally we present the estimated PSD obtained using uniform distribution and it can be seen that there are no spectral replicas. Furthermore, with unifrom distribution the noise level remains approximately the same as obtained with Gaussian distribution.

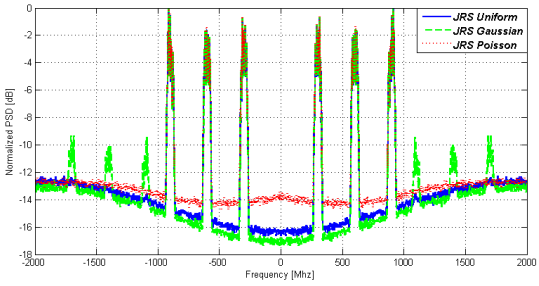

Figure 5: JRS with Uniform, Gaussian($\frac{\sigma}{T} = 0.2887$) and poisson distribution

The results presented in Figures6-7, are for ARS sampling. In Figure 6, the effect of the average sampling frequency of ARS is shown on the estimated PSD. It can be seen clearly, just as was observed in the case of JRS sampling that with increase in sampling rate the PSD estimates improve. Another important point to note is that the noise in the estimated PSD for ARS sampling is less than that of JRS sampling.

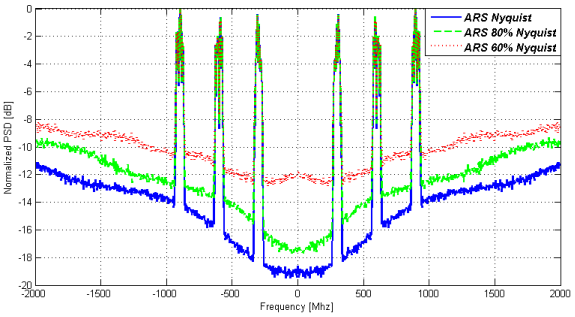

Figure 6: ARS with Uniform distribution and different average sampling rates

In Figure 7, the estimated PSD obtained with ARS sampling is plotted for three different distributions of the sampling instances. Again results are presented for Gaussian, Poisson and Uniform distributions. For Poisson distribution we have a high noise level. An interesting result to note is that, contrary to the JRS case, no spectral replicas are observed for the Gaussian distribution and furthermore, its performance is better compared to the uniform distribution.

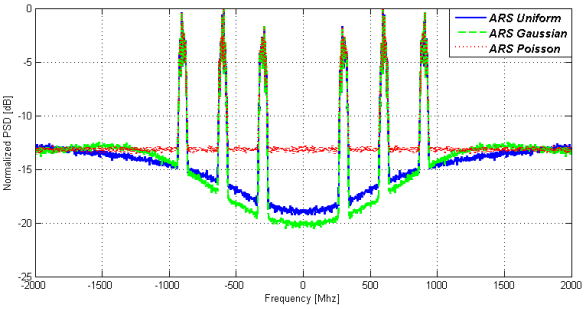

Figure 7: ARS with Uniform, Gaussian($\frac{\sigma}{T} = 0.2887$) and poisson distribution

Next in Figure 8, the estimated PSD obtained from DSB samples, is presented. The results are compared with the Welch method which uses uniform Nyquist samples. It must be noted that for the DSB sampler, no prior knowledge of the spectral support of the signal is available. The spectral support is computed in the adaptation phase using Lomb-Scargle method []. Note that while operating in adaptation phase $L = 128, p = 90$. The interesting aspect of the DSB sampler is that it will adjust p for the reconstruction phase, based on the information obtained in the adaptation phase. Therefore, the DSB sampler adjusts the sampling rate based on the spectral support of the

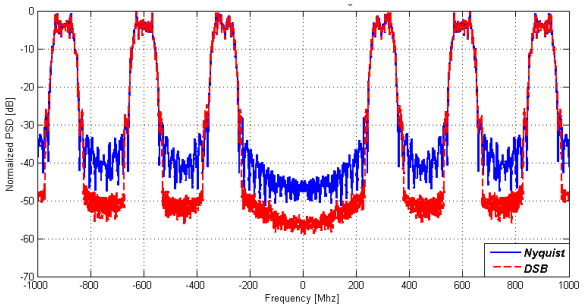

Figure 8: PSD with Lomb-Scargle method

input signal. From Figure 8, it can be seen that the results obtained using DSB sampler are quite good.

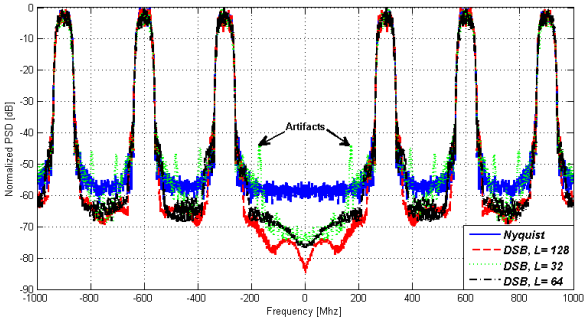

Figure 9: Influence of the parameter L in the variation of the PSD after DSB

Figure 9 shows the effect of the parameter L on the estimated PSD from DSB samples. For $L = 32$, spectral artifacts are observed in the estimated PSD, as shown in Figure 9. But as L is increased these artifacts are eliminated. Therefore, it is clear that the reconstructed spectrum is better when L increases.

6 CONCLUSIONS

In this paper we have presented some best known non-uniform sampling techniques. JRS and ARS mode gives approximately the same PSD without spectral replicas but with a much smaller dynamic than Uniform samples PSD. These two techniques can be used for spectrum sensing, condition not having a large difference in power between the bands. We dissassed about a new sampler based on Multi-Coset sampling scheme, which adjusts its sampling rate according to the changes in the frequency spectrum of the input signal. That is, if the signal is sparse in the frequency domain, it samples at sub-nyquist rate, else it samples at nyquist rate. We also saw the effect of the parameter L on the estimated PSD from DSB samples.

ACKNOWLEDGEMENTS

This work is supported by the French “Region Bretagne” for the projects “FUI AMBRUN” and “PME SoftRF”.

REFERENCES

Ben Romdhane, M. (2009). *chantillonnage non uniforme appliqu la numrisation des signaux radio multistandard*. PhD thesis.

Bourdoux A., Pollin S., D. A. and der Perre L., V. (2011). Sparse signal sensing with non-uniform undersampling and frequency excision. pages 246–250.

Bresler, Y. (2008). Spectrum-blind sampling and compressive sensing for continuous-index signals. *Information Theory and Applications Workshop, 2008*, page 547554.

Feng, P. and Bresler, Y. (1996). Spectrum-blind minimum-rate sampling and reconstruction of multiband signals. *ICASSP*, 3:16881691.

Landau, H. (1967). Necessary density conditions for sampling and interpolation of certain entire functions. *Acta Mathematica*, 117(1):37–52.

Miar, Y., D’Amours, C., and Aboulnasr, T. (2012). A novel reduced power compressive sensing technique for wideband cognitive radio. *EURASIP J. Wireless Comm. and Networking*, page 281.

Mishali, M. and Eldar, Y. C. (2010). From theory to practice: Sub-nyquist sampling of sparse wideband analog signals. *Selected Topics in Signal Processing, IEEE Journal of*, 4(2):375–391.

Palicot, J. and al (June 2010). *Radio Engineering: from Software Radio to Cognitive Radio*. John Wiley and Sons.

Rashidi Avendi, M. (2010). Non-uniform sampling and reconstruction of multi-band signals and its application in wideband spectrum sensing of cognitive radio.

Shapiro, H. S. and Silverman, R. A. (1960). Alias-free sampling of random noise. *Journal of the Society for Industrial & Applied Mathematics*, 8(2):225–248.

Tian, Z. and Giannakis, G. (2006). A wavelet approach to wideband spectrum sensing for cognitive radios.

Tibshirani, R. (1996). Regression shrinkage and selection via the lasso. *Journal of the Royal Statistical Society. Series B (Methodological)*, page 267288.

Traoré, S., Aziz, B., and Guennec, D. L. (2013). Dynamic single branch non-uniform sampler. *DSP, Santoriri, Greece, International Conference on Digital Signal Processing*.

Venkataramani, R. and Bresler, Y. (2000). Perfect reconstruction formulas and bounds on aliasing error in sub-nyquist nonuniform sampling of multiband signals. *Information Theory, IEEE Transactions on*, 46(6):21732183.

Venkataramani, R. and Bresler, Y. (2001). Optimal sub-nyquist nonuniform sampling and reconstruction for multiband signals. *Signal Processing, IEEE Transactions on*, 49(10):23012313.

Wojtiuk, J. J. (2000). *Randomised sampling for radio design*. PhD thesis, Citeseer.

Zhang, H. (2010). Filter bank multicarrier (fbmc) for cognitive radio systems. *These de doctorat, Conservatoire National des Arts et Metiers et Wuhan Universite*.

SHORT PAPERS

SCATTERING OF ELECTROMAGNETIC WAVE BY OFFSET SPHERICAL PARTICLES

Felix O. Ngobigha and David H. O. Bebbington
School of Computer Science and Electronic Engineering, University of Essex,
Wivenhoe Park, Colchester CO4 3SQ, United Kingdom
{ fngobi, david } @essex.ac.uk

Keywords: Offset spherical particle, T-matrix method, electromagnetic waves scattering.

Abstract: The Lorentz–Mie theory is applicable to calculating scattering characteristics of spherical shaped particles. It is often applied to slightly non-spherical particles where its range of validity is uncertain. This paper defines the range of validity of the T-matrix technique of Barber and Hill as applied to homogeneous spherical and non-spherical particles. Scattering calculations are made for a set of non-absorbing homogeneous spherical particles with the origin of the particle offset over a certain range. The numerical results show that even for small offset value with the same input parameters, the phase function, extinction and scattering cross sections differ quite significantly compared to the generalized Lorentz–Mie technique known to give accurate scattering characteristics for spherical particle.

1 INTRODUCTION

The scattering of electromagnetic waves by spherical object is a problem that has received increased attention in past and recent years. Knowledge of the scattered field is required in many areas of science and engineering applications. The idea was first developed by Gustav Mie in 1908 in order to understand the colours that resulted from light scattering of gold particles suspended in water. Applications of Mie solution has been extended from one end of the electromagnetic spectrum to the other, from Ultraviolent solar radiation backscattered by stratospheric aerosols to satellites, through visible and Infrared radiation scattered by clouds and aerosols, to microwaves and radar scattered from large hydrometeors. An excellent introduction to the theory is reported in (Kerker 1969; van de Hulst 1981; Mishchenko, Travis et al. 2002; Bohren and Huffman 2008). Although, the Mie-theory it is exact, but with the emergence of computing it has become practical to calculate various scattering characteristics (Wiscombe 1980). The Mie-theory has limitation of being restricted to spherical particles. However, it has served as a reference for validation of other techniques for evaluating scattering properties from scatterers, and implementation of this theory with slightly non-spherical particles has yielded similar results.

This paper deals with the range of validity of T-matrix method reported in (Barber and Hill 1990) as applied to a lossless dielectric spherical particle with the origin moved of centre over a certain range. Our aim is show the uncertainty with reference to particle shape when calculating scattering cross sections in which the origin is displaced from the centre of the spherical object as previously reported (Waterman 1965; Barber and Yeh 1975; Barber and Hill 1990) by adopting and implementing the code in (Barber and Hill 1990) and not the theoretical analysis as numerous papers have already addressed this aspect. Nevertheless, the results in the cited references differ with ours. Clearly, the final results given in this paper are not new. Rather, our contribution is based on offset range validity at various frequency bands with the goal of providing a consistent result regardless of the mathematics that led to their derivation.

2 RELATED WORK

The approach adopted in this paper was originally introduced by P C Waterman (Waterman 1965) as a technique for computing electromagnetic scattering by a smooth, perfectly conducting, homogeneous, arbitrarily shaped particle illuminated by an incident plane electromagnetic wave. This technique is also known as null field method (Zheng 1988) or extended boundary condition method (EBCM) (Barber and Wang 1978), and is developed further by (Barber and Yeh 1975), (Mishchenko and Travis 1994; Mishchenko, Travis et al. 1996; Mishchenko and Travis 1998; Mishchenko, Hovenier et al. 1999). The technique has also gained wide acceptance in the field of electromagnetic waves scattering due to its capability to calculate the scattering properties of arbitrarily shaped scatterers. The approach of the T-matrix formulation utilizes vector spherical harmonic function expansions of the incident and scattered fields in conjunction with boundary conditions at the surface of the scattering particles to obtain a system of linear equations relating the unknown expansion coefficients of the scattered field to the known coefficients of the incident field. The most attractive feature of T-matrix technique starts as Lorenz-Mie theory when the scattering particle is homogeneous or layered sphere composed of isotropic materials.

Given a specific scattering object, first step is to select an internal origin on the scattering particle and surround the object with imaginary sphere of radius *r* large enough to circumscribe the scatterer (Barber and Hill 1990; Mishchenko, Travis et al. 2002), and numerically perform the surface integrations over the scatterer which are required to fill the coefficient matrix. The next step is to carry out matrix operation to obtain the scattered field coefficients f_ν and θ_ν . The final step then is to substitute the scattered field coefficients into (1) to yeild the scttered field and other desire characteristics.

$$E^s\left(kr\right) = E_0 \sum_{\nu=1}^{\infty} D_\nu \times \left[f_\nu M_\nu^\lambda \left(kr\right) + g_\nu N_\nu^\lambda \left(kr\right) \right] \quad (1)$$

where M and N are the vector spherical harmonic functions and the superscript 3 on M and N indicates that these functions are of the type suitable for radiation or outgoing fields (Hankel function), ν represents the spherical harmonic triple index σ (even or odd), m, n. The argument of the vector spherical wave functions *kr* **,** where k=2π/λ denotes wave number in the surrounding medium, λ is the incident wavelength, and *r* is the position vector which defines a point in three-dimensional space. The E_0 is the amplitude of the incident electric field, and D_ν denotes normalization constant.

The important formulas for Mie scattering are well defined (Kerker 1969). The quantities required at this level are summarized. The amplitude matrix S for spherical object is a diagonal matrix; due to symmetry it takes the form:

$$E_s = \begin{pmatrix} E_\perp^s \\ E_\parallel^s \end{pmatrix} = \frac{e^{ikr}}{r} \begin{pmatrix} S_{hh} & 0 \\ 0 & S_{vv} \end{pmatrix} \begin{pmatrix} E_\perp^i \\ E_\parallel^i \end{pmatrix} \quad (2)$$

where

$$S_{vv}\left(\Theta\right) = \sum_{n=1}^{\infty} \frac{2_n+1}{n\left(n+1\right)} \left[a_n \pi_n \left(\cos\theta\right) + b_n \tau_n \left(\cos\theta\right) \right] \quad (3)$$

$$S_{hh}\left(\Theta\right) = \sum_{n=1}^{\infty} \frac{2_n+1}{n\left(n+1\right)} \left[b_n \pi_n \left(\cos\theta\right) + a_n \tau_n \left(\cos\theta\right) \right] \quad (4)$$

which are respectively, scattered electric field and complex scattering amplitude for the two orthogonal directions of incident polarization.

$$\left|S_{vv}\right|^2 \text{ and } \left|S_{hh}\right|^2$$

are the scattered intensities, π and τ are the angular function, a_n and b_n are Mie expansion coefficients in terms of the vector spherical harmonic, depend on the size parameter and on the complex refractive index. They are also expressed in terms of spherical Bessel functions.

3 SIMULATION RESULTS

An incident plane polarized wave propagating in the $+z$ direction is assumed, with the origin of the scatterer coincides with the spherical coordinate system for the calculation of differential scattering cross section of spherical, and slightly non-spherical

particles. Some of the input parameters such as size parameter

$$\left(x = 1 = 2\pi r / \lambda\right)$$

and refractive index

$$\left(m = 2.0 + i0.0\right)$$

are chosen to compare results (van de Hulst 1981). For a sphere, r is the radius of the scattering object but for non-spherical particles (oblate or prolate spheroid), the choice of r gives users the option of defining r as the radius of a sphere of either equal volume, or equal surface area to that of the scattering object while for offset spherical particle, it is the distance from the origin of the spherical coordinate system to the surface of offset spherical scatterer calculated by applying Pythagoras or Cosine rule.

Numerical illustrations confirm that the results for spherical bodies are identical at different frequencies compared to those obtained by the Mie theory. The check was extended to slightly non-spherical particles (oblate and prolate spheroids); a similar agreement is generally observed for both particles. The vertical and horizontal polarizations are denoted VV and HH respectively.

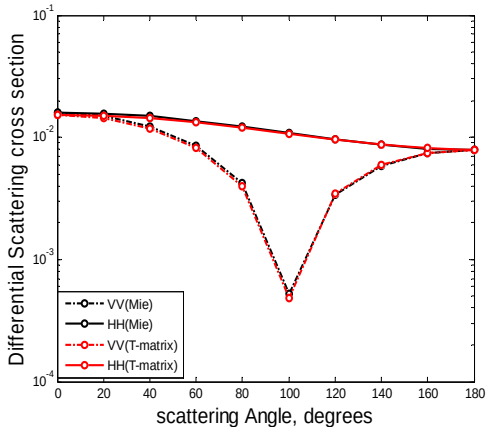

Figure 1: Comparison of Mie-theory and T-Matrix method for differential scattering cross sections of non-absorbing spherical and offset spherical particles at 220 GHz.

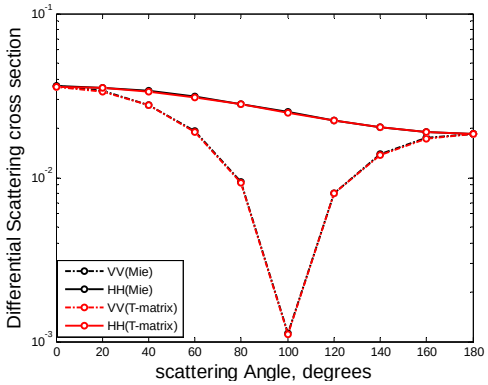

Figure 2: Comparison of Mie-theory and T-Matrix method for differential scattering cross sections of non-absorbing oblate spheroid at 94 GHz.

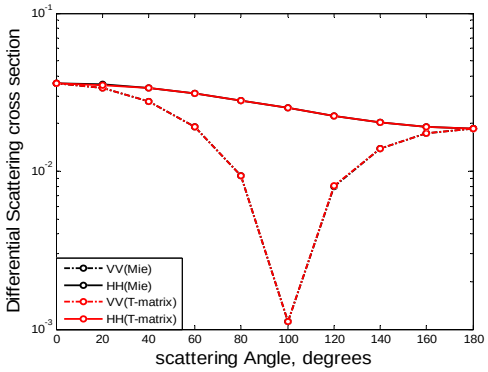

Figure 3: Comparison of Mie-theory and T-Matrix method for differential scattering cross sections of non-absorbing prolate spheroid at 94 GHz.

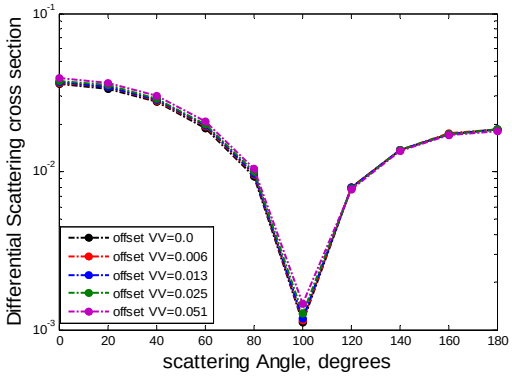

Figure 4: Comparison of Mie-theory and T-Matrix method for non-absorbing spherical and offset spherical particles at 94 GHz.

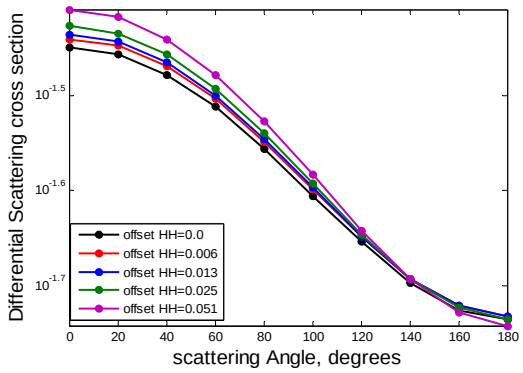

Figure 5: Comparison of Mie-theory and T-Matrix method non-absorbing spherical and offset spherical particles at 94 GHz.

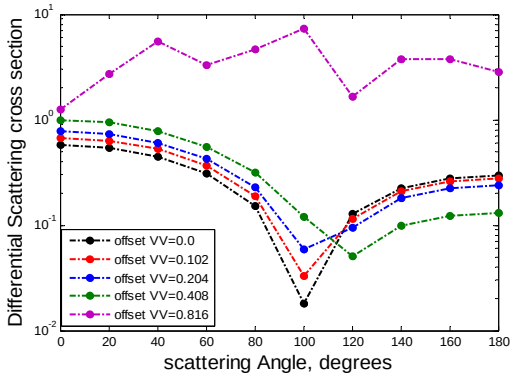

Figure 6: Comparison of Mie-theory and T-Matrix method for non-absorbing spherical and offset spherical particles at 5.8 GHz.

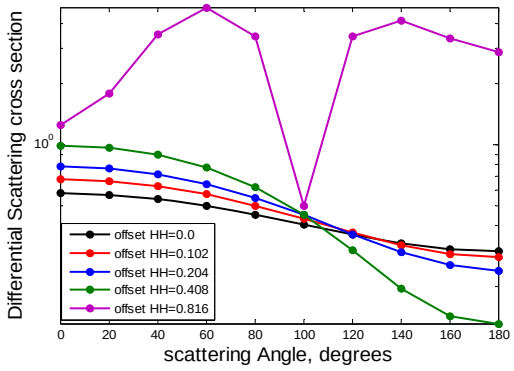

Figure 6: Comparison of Mie-theory and T-Matrix method for non-absorbing spherical and offset spherical particles at 5.8 GHz.

It is evident from Figure 1 that our results for both approach show good agreement with (Barber and Yeh 1975; Barber and Hill 1990) and (Waterman 1965) regardless of the scatterer (i.e. spherical or offset spherical particles) at 220 GHz. This is also observed in Figure 2 and 3 comparing Mie-theory and T-Matrix method for differential scattering cross sections of non-absorbing spheroid at 94 GHz.

Evaluation of results from Mie-theory and T-Matrix method for non-absorbing spherical and with the spherical particle origin moved over a range at 94 GHz for vertical polarization still show reasonable agreement, but with horizontal polarization in Figure 5, it is obvious that the differential scattering cross-sections increases as the offset range increases, this effect is least noticed with increase in scattering angle. This shows that at higher operating frequencies the effect is insignificant; however, Figure 6 and 7 results show that even for small offset value with the same input parameters, the phase function, extinction and scattering cross sections differ quite significantly at 5.8 GHz compared to the generalized Lorentz–Mie technique.

4 CONCLUSIONS

We have demonstrated in our results that the effect of offset values relative to the frequency bands and how the scattering calculation in terms of geometric properties of the particles; (shapes and size parameter) for spherical and slightly non-spherical particles adopting Mie theory and T-matrix techniques are similar with previous works at higher frequency bands. Furthermore, the same trends of results are observed in terms of vertical polarization for non-absorbing offset spherical scatterer at 94 GHz. On the other hand, scattering characteristics for horizontal polarization at 94 GHz, and at lower frequency bands (i.e. 5.8 GHz) differs quite significantly with the same input parameters. Hence, scattering calculation from non-absorbing homogeneous spherical particles with the origin of the particle moved over a certain range should be used with caution depending on the wave frequency. This is particularly important due to previous concept that the same scattered cross section is obtained with the origin of the spherical scatterer at the centre. Obviously, the difference in our results with the former at lower frequency (i.e. 5.8 GHz) would lead to erroneous values being generated as the offset value increases and tends toward the

radius of scattering object, and inaccurate prediction of hydrometeor shapes are likely if the previous concept is applied in radar and remote sensing applications.

ACKNOWLEDGEMENT

This work was supported by Petroleum Technology Development Fund (PTDF) under scholarship number PTDF/E/OSS/PHD/NF/355/11.

REFERENCES

Barber, P. and C. Yeh (1975). *"Scattering of electromagnetic waves by arbitrarily shaped dielectric bodies."* Applied optics **14**(12): 2864-2872.

Barber, P. W. and S. C. Hill (1990). *Light scattering by particles: computational methods*, World Scientific Publishing Company Incorporated.

Barber, P. W. and D. S. Wang (1978). *"Rayleigh-Gans-Debye applicability to scattering by nonspherical particles."* Applied optics 17(5): 797-803.

Bohren, C. F. and D. R. Huffman (2008). *Absorption and scattering of light by small particles*, Wiley-Vch.

Kerker, M. (1969). *"The scattering of light, and other electromagnetic radiation."*

Mishchenko, M. I., J. W. Hovenier, et al. (1999). *Light scattering by nonspherical particles: theory, measurements, and applications*, Academic Press.

Mishchenko, M. I. and L. D. Travis (1994). *"T-matrix computations of light scattering by large spheroidal particles."* Optics communications **109**(1): 16-21.

Mishchenko, M. I. and L. D. Travis (1998). *"Capabilities and limitations of a current FORTRAN implementation of the< i> T</i>-matrix method for randomly oriented, rotationally symmetric scatterers."* Journal of Quantitative Spectroscopy and Radiative Transfer **60**(3): 309-324.

Mishchenko, M. I., L. D. Travis, et al. (2002). *Scattering, absorption, and emission of light by small particles*, Cambridge university press.

Mishchenko, M. I., L. D. Travis, et al. (1996). *"< i> T</i>-matrix computations of light scattering by nonspherical particles: A review."* Journal of Quantitative Spectroscopy and Radiative Transfer **55**(5): 535-575.

van de Hulst, H. C. (1981). *Light scattering by small particles*, Dover publications.

Waterman, P. (1965). *"Matrix formulation of electromagnetic scattering."* Proceedings of the IEEE **53**(8): 805-812.

Wiscombe, W. J. (1980). "*Improved Mie scattering algorithms."* Applied optics **19**(9): 1505-1509.

Zheng, W. (1988). *"The null field approach to electromagnetic scattering from composite objects: The case with three or more constituents."* Antennas and Propagation, IEEE Transactions on **36**(10): 1396-1400.

SOUND PARAMETER ESTIMATION IN A SECURITY SYSTEM

Ivan Garvanov, Hristo Kabakchiev
University of Library Studies & Information Technologies, Sofia, Bulgaria
Faculty of Mathematics & Informatics,Sofia University, 15 Tsar Osvoboditel Blvd., Sofia, Bulgaria
igarvanov@yahoo.com, ckabakchiev@yahoo.com

Vera Behar
Institute of Information & Communication Technologie, BAS, 25-A Acad. G.Bonchev Str., Sofia, Bulgaria
behar@bas.bg

Keywords: Adaptive signal processing, microphone arrays, sound parameter estimation

Abstract: In this paper, the signal processing approach is applied to the sound parameter estimation using adaptive microphone arrays. The simulation scenario describes a situation where three sensors generate three different sound signals (warning, alarm and emergency) and a car is the source of natural noise. The results obtained demonstrate that the parameter estimation can be used for recognition of the type of abnormal situations arisen in the area of observation in order to be taken the corresponding solutions for control of the security system.

1 INTRODUCTION

The sensors used for protection are activated in the event of an adverse situation in the protected space. In case of fire, smoke, vibration, and breakage of glass or opening the car the sirens of sensors give a loud beep for a few minutes. The assessment of the direction and parameters of the incoming sound signals can be used to guide the camera that records the situation in the most dangerous direction. The algorithm described in (Benesty, 2008; Godara, 1997; Trees, 2002; Vouras, 1996; Moelker, 1996; Behar,2010) is intended to locate the direction of sound signals coming from sensors or other sources of sound using microphone arrays. Microphone arrays represent a set of microphones arranged in a geometric configuration. In fact, they can be realized or linear microphone arrays, where the microphones are positioned in a straight line or circular microphone arrays, where the microphones are placed in a circle or rectangular microphone arrays, where the microphones are arranged in the shape of a rectangle plate.

After the analysis of parameters of such sound signals that arrived from the detected directions the video cameras are directed in such directions, from where have been arrived the signals having the most important priority (emergency, alarm and warning). In modern security and surveillance systems, the operational control of protective and warning means is based on the analysis of alarms received from different sensors installed in the observation area. In this paper we consider a situation where the operational control of a video camera is based on sound parameter estimation.

The simulation scenario includes three sensors, which generate three types of signals (warning, alarm and emergency), and one source of natural noise (car). The parameters of three sound generators produced by three well-known companies SoniTron, E2s and Sensor Systems are used in simulation. The results obtained demonstrate that the sound parameter estimates are very close to real sensors parameters. The paper evaluates both the duration of the sound pulse and the signal frequency spectrum by using the FFT.

In this paper, a possible signal processing algorithm is proposed for sound parameter estimation. We consider the case, when the sound source is located in the array's far-field, and the sounds generated by sound sources propagate through the air. After analysis of parameters of all signals received from the detected directions, a

video camera is directed in such a direction, from where has been arrived the signal having the most important priority (emergency, alarm and warning).

2 SENSORS AND SIGNALS

In this work are tested the signal generated by sensors of several companies SONITRON, E2S and SYSTEM SENSOR (Behar, 2010). Two main signal parameters of such sensors are the sound power and the sound frequency (Table 1).

Table 1: Sensors parameters

Company	**Sound power [dB]**	**Sound frequency [Hz]**
SONITRON	96	2500
E2S	100	1000
SYSTEM SENSOR	103	2400

Depending on the non-normal situation the sensors emit different sound signals (continuous, intermittent) with the parameters given in Table2.

Table 2: Signal parameters

Sensor signals		
Continuous (warning)	Intermittent-I (alarm)	Intermittent-II (emergency)
$f_{int} = 0$ Hz $T_{sig} = 10$ s	$f_{int} = 5$ Hz $T_{sig} = 30$ s	$f_{int} = 1$ Hz $T_{sig} = 60$ s

The security sensors, using the mounted sirens, that generate special beeps, warn on abnormal situations that arise in the protected space, “warning”, “alarm” and “danger”. The sound signal “Warning” is a continuous harmonic sound signal with duration of 10s. The signal “Alarm” is an intermittent signal with the frequency of interruption of 5 Hz and duration of 30s (type-I). The different devices generate various sound signals of type “alarms”. In figures 1-3 (on the left), are shown the sound signals of type “warning”, “alarm” and “danger”. On the same figures (on the right) are presented their frequency spectra. The plotted sound signals are generated by the sensors of the well-known companies SONITRON, E2S and SYSTEM SENSOR.

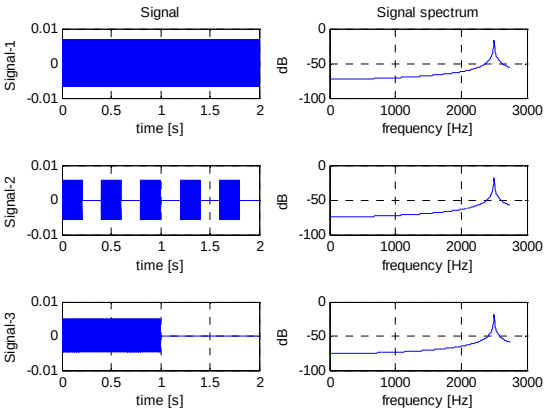

Figure 1: SoniTron signals and spectrums

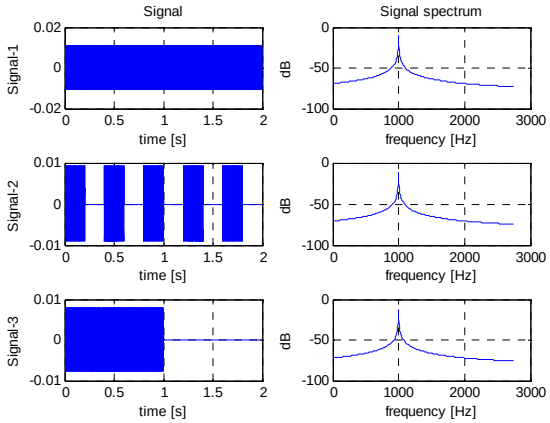

Figure 2: E2S signals and spectrums

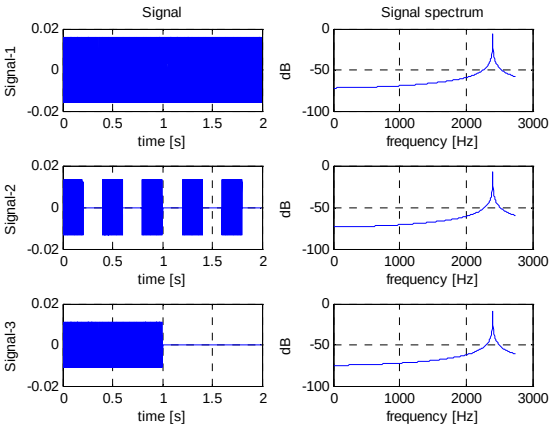

Figure 3: System signals and spectrums

3 SIGNAL PROCESSING

Many sensors for fire detection or building surveillance are equipped with sound alarm devices. In case of alarm event (smoke, flame, intrusion, glass breaking, and unauthorized car opening) the alarm device emits powerful sound signal with various duration. For the sake of simplicity, let's assume that a set of sensors and one microphone array are installed for the object protection in the observation area and a video camera can be located above a microphone array (Fig.4).

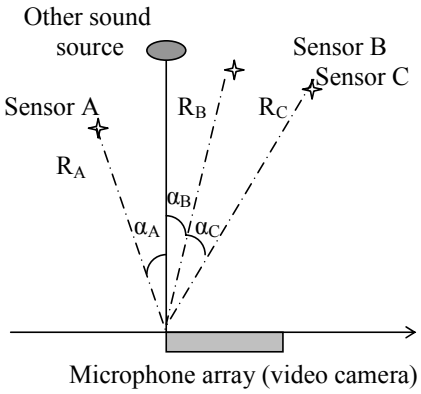

Figure 4: The security system topology

In a security system, the sound direction localization could be used for pointing the additional video surveillance devices (video cameras), which record the additional information and send it to control center of a security system. The priority direction for pointing of a video camera is estimated on the base of a parameter analysis of the signals received from the detected sound sources. The general block-scheme of signal processing in a security system is shown in Fig.5.

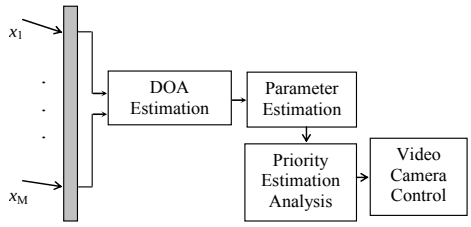

Figure 5: Signal processing in a security system

We assume that the adaptive beam pattern thresholding (CFAR) is performed and, finally, the direction of-arrival (DOA) estimates are found as directions where the local maximum exceeds an adaptive threshold.

The block-scheme for sound parameters estimation is shown on Fig. 6. The duration of the sound pulse is obtained after comparing the envelope of the signal with a threshold that is 80% of the average envelope. The estimation of the carrier frequency of the sound signal is received again compared with a threshold value of -10 dB (Fig. 6).

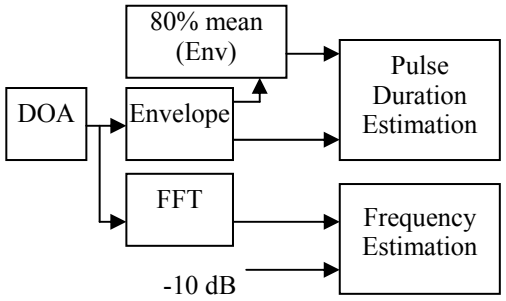

Figure 6: The block-scheme of sound parameters estimation

4 SIMULATION RESULTS

The computer simulation is performed in order to demonstrate the capability of the presented algorithm to estimate sound parameters. The scenario of simulation includes three sensors (A, B and C) located respectively at a distance of 50m, 60m and 70m from the microphone array (Fig. 4). The bandwidth of the used microphones is [100 - 5000] Hz. During the experiment, we simulated the sound of a car, which is a broadband noise signal, filling the entire bandwidth of the microphones. Power of the sound signal generated by a car is 110dB. In the scenario of simulation, the azimuth of a car is zero relative to the microphone array and the car is located at 90 m from the microphone array (Fig.4).

In Fig. 7, 9 and 11 are shown the sound signals of type "warning", "alarm" and "danger" together with the corresponding thresholds of detection. These signals are generated by sensors manufactured by the well-known companies SONITRON, E2S and SYSTEM SENSOR.

In Fig 8, 10 and 12 are presented the corresponding frequency spectra of these signals.

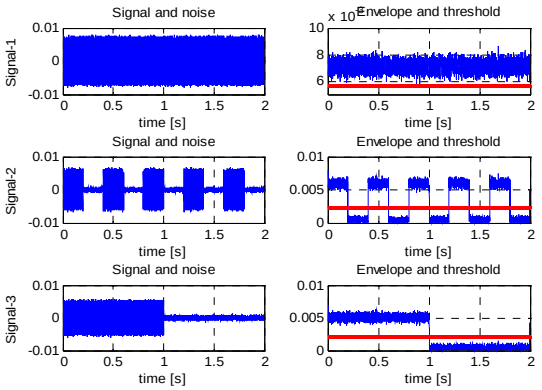

Figure 7: SoniTron signals and threshold

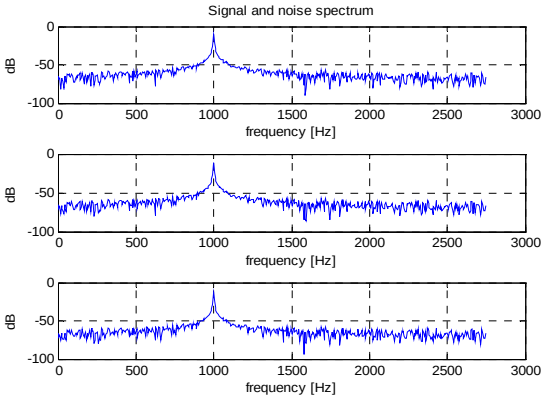

Figure 10: E2S signals spectrum

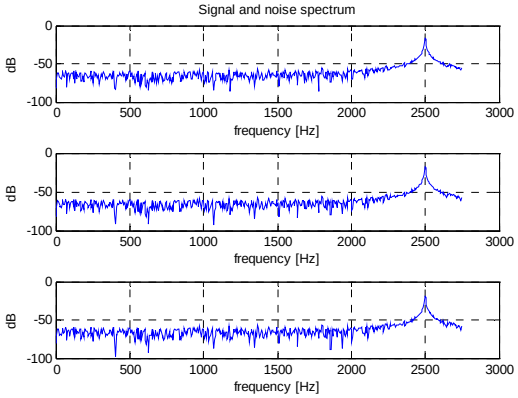

Figure 8: SoniTron signals spectrum

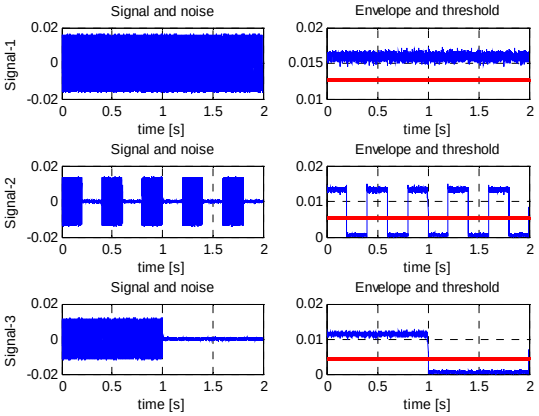

Figure 11: System Sensor signals and threshold

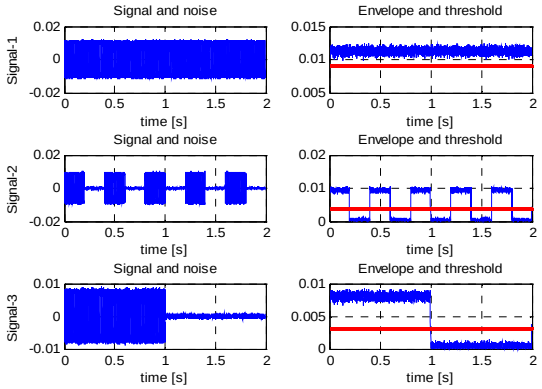

Figure 9: E2S signals and threshold

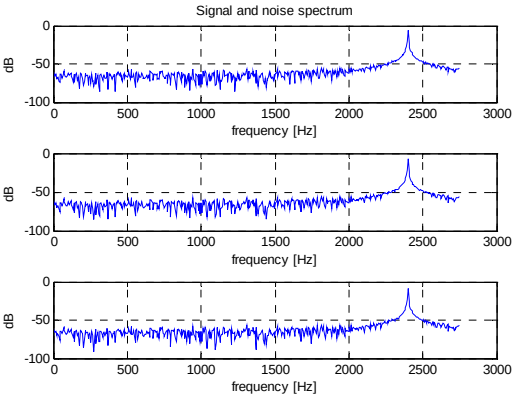

Figure 12: System Sensor signals spectrum

In Fig.13 are shown the broadband interference signal generated by a car and the internal noise of a microphone noise of the microphone array. In Fig.14 are presented the corresponding frequency spectra of these signals.

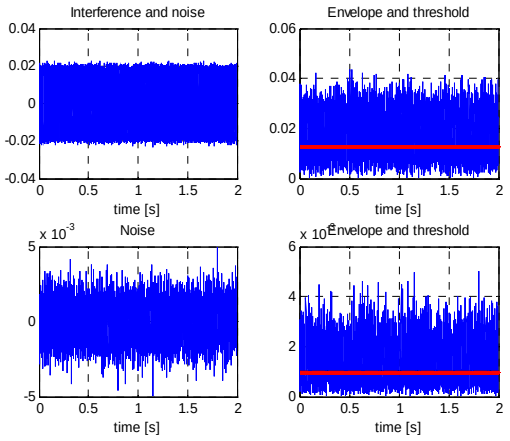

Figure 13: Interference and noise

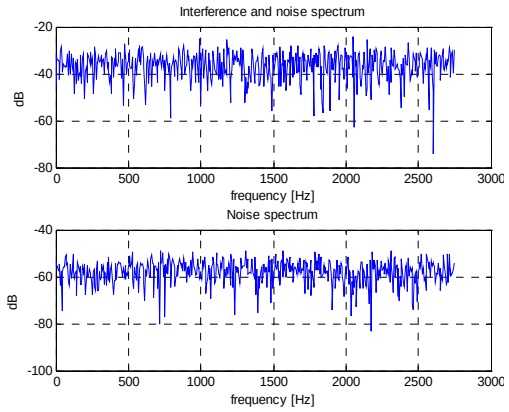

Figure 14: Interference and noise spectrum

The results obtained demonstrate that the signals from different sensors can be estimated and there parameters are equal to real sensors parameters. The presence of interference and noise does not affect significantly the estimation of signal parameters.

5 CONCLUSIONS

It is shown that the obtained estimates of the sound signal parameters are close to the actual parameters of the signals. The algorithm presented enables to recognize the type of abnormal situations arisen in the area of observation in order to be taken the corresponding solutions for control of the security system. Thanks to the adaptive microphone array processing, the presence of interference signals does not influence significantly the determination of the signal parameter estimates.

ACKNOWLEDGEMENTS

The research work reported in the paper is partly supported by the project AComIn "Advanced Computing for Innovation", grant 316087, funded by the FP7 Capacity Programme (Research Potential of Convergence Regions).

REFERENCES

Benesty, J., Chen, J., Huang, Y., 2008. Microphone array signal processing, Springer.

Godara, L., 1997. Application of antenna arrays to mobile communications, part II: beam-forming and direction-of-arrival considerations. In *Proc. of the IEEE*, vol.85, No 8, pp.1195-1245.

Ioannides, P., Balanis, C., 2005. Uniform circular and rectangular arrays for adaptive beamforming applications. *IEEE Trans. on Antenna. Wireless Propagation. Letters*, vol.4., pp. 351-354.

Trees, H., Van, L., 2002. Optimum Array Processing. Part IV. Detection, Estimation, and Modulation Theory. New York, JohnWiley and Sons, Inc..

Tummonery, L., Proudler, I., Farina, A., McWhirter, J., 1994. QRD-based MVDR algorithm for adaptive multi-pulse antenna array signal processing. In *Proc. Radar, Sonar, Navigation,* vol.141, No 2, pp. 93-102.

Vouras, P., Freburger, B., 2008. Application of adaptive beamforming techniques to HF radar. In *Proc. IEEE conf. RADAR'08*, May, pp. 6.

Behar V., Kabakchiev, Chr, Kyovtorov, V., 2010. STAP Approach for DOA Estimation using Microphone Arrays, *Signal Processing Workshop, SPW-2010*, 14-15 June 2010, Vilnius, Lithuania, SPIE Proceedings, vol. 7745, 77451J

FSR MARINE TARGET CLASSIFICATION WITH DATA MINING APPROACH

Dorina Kabakchieva
University of National and World Economy, Sofia, Bulgaria
dkabakchieva@unwe.bg

Hristo Kabakchiev
Faculty of Mathematics and Informatics, Sofia University St. Kliment Ohridski, Sofia, Bulgaria
ckabakchiev@fmi.uni-sofia.bg

Vera Behar
Institute of Information and Communication Technologies, Bulgarian Academy of Sciences, Sofia, Bulgaria
behar@bas.bg

Ivan Garvanov
University of Library Studies and Information Technologies, Sofia, Bulgaria
igarvanov@yahoo.com

Keywords: Radar target classification, Data mining

Abstract: The purpose of this paper is to present the research results from a study focused on the possibilities for implementing data mining approach for classification of radar detected marine targets. The study is based on experimental data collected by researchers from Birmingham University with Bistatic Forward Scattering Radar. The data is further processed by using a CA CFAR approach for radar detection and target specific estimation, proposed by Sofia University team. Rough estimation of the target parameters in time domain in implemented, based on the hypothesis that the number of detected samples received from the target defines the target projection (length) and the energy reflected from the target. The classification models for predicting the class of the detected marine targets, achieved with selected algorithms in data mining software WEKA, for two values of the predicted variable (the marine target class), are described in the paper. The results from the evaluation of the models are compared with the results received in our previous paper, concerning classifiers achieved for predicted target variable with three values. The proposed hypothesis that the decreased number of values for the predicted variable will lead to achieving classifiers with better quality is validated.

1 INTRODUCTION

Forward scattering radar (FSR) is a special type of bistatic radars that operate in the narrow area of the forward scattering effect where the bistatic angle β is close to 180^0. FSR has some fundamental limitations: the absence of range resolution; operation within narrow angles ($\pm 10^0$). Due to the forward scattering effect (diffraction), the Radar Cross Section of a target extremely increases (by 2-3 orders) and mainly depends on the target's physical cross section and is independent of the target's surface shape and the absorbing coating on the surface. Forward Scattering Radar is effective for detection of "stealth" targets. The Doppler shift (radial velocity) of the target reduces when the target

moves from the boundary of the forward scattering zone to the baseline "transmitter-receiver", equals zero when the target crosses the baseline and increases again as the target approaches the zone (see Fig.1 and Fig.2).

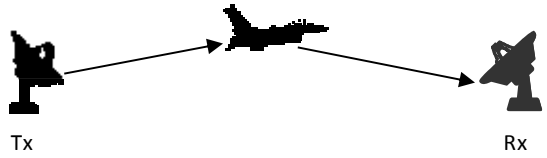

Figure 1: FSR system topology.

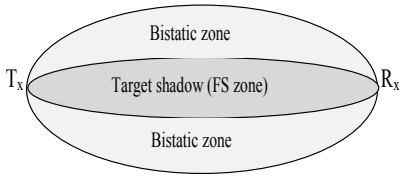

Figure 2: Coverage of BS and FS radar systems.

A team from Birmingham University has been working on these issues and considers different structures and algorithms for detection, estimation and classification of ground and marine targets in a Forward Scatter Radar (FSR) system in many published papers. They propose equations for calculating marine target parameters, i.e. velocity and length, on the basis of the estimated signal parameters (Cherniakov, Gashinova et al., 2007, Cherniakov, Raja, et al., 2005, Rashid, et al., 2008, Raja, 2005). One of these equations shows that the linear size of the target is proportional to the speed of movement of the target and inversely proportional to the first spectrum minimum. The time duration of the target signal is related in the FSR zone to the approximate profile of the object. Then, the precision estimation of the time duration of the Doppler signal is very important because it guarantees the quality of estimates of the frequency calculated on the first minimum and the maximum of the Power Spectrum Density. In our previous papers (Kabakchiev, et al., IRS, 2011, Kabakchiev, et al., SPS, 2011) we have considered a rough approach in time domain for calculating the length (time duration) and energy (FSR Radar Cross Section) of marine targets in a Forward Scatter Radar (FSR) system. The error of estimation of the target length is about 15-20% which is within the engineering accuracy.

The purpose of this paper is to present the research results from a study focused on the possibilities for implementing data mining approach for classification of radar detected marine targets. The study is based on experimental data collected by researchers from Birmingham University with the constructed by them Bistatic Forward Scattering Radar, as described in (Cherniakov, Gashinova et al., 2007). The collected data is further processed, by using the CA CFAR approach presented in (Kabakchiev et al., IRS, 2011, Kabakchiev et al., SPS, 2011), for achieving radar detection and target specific estimation development from Sofia University team. They use rough estimation of the target parameters in time domain, based on the hypothesis that the number of detected samples in the signal received from the target defines the target projection (length) and the energy reflected from the target. In our previous paper (Kabakchiev, Kabakchieva et al., 2011), the targets were distributed in three classes corresponding to three variants of detected marine objects (water-jets, boats, ships) that are crossing a maritime electronic fence (Cherniakov, Gashinova et al., 2007). The classification models for predicting the detected target class were based on the received and pre-processed target data and were built by applying different data mining methods. The WEKA software (Witten, 2005) was used for the Data Mining analysis. The achieved results from the classification, for the three classes of marine targets (MISL Boat, Average Boat, Big Boat) in time domain, were similar to the results achieved by Birmingham University team for speed and length estimates of ground targets in frequency domain.

The thorough analysis of the achieved results revealed that the trained classifiers for predicting the class of the detected marine targets based on the available signal data did not perform with high accuracy for all the three classes (Kabakchiev, Kabakchieva et al., 2011). The classifiers worked best for the MISL Boat class which was most represented in the available data, and much worse for the other two classes which were less represented in the data.

The purpose of this paper is to find an approach for increasing the classifiers' accuracy of prediction of the marine target class for the same dataset. Our hypothesis is that the accuracy of prediction will increase if the number of classes is decreased, i.e. by combining the marine targets from the two less represented classes into a single class. The classification models for predicting two classes of marine targets are described in the paper, using popular evaluation criteria for estimating the classifiers' quality. A comparison is also made between the classifiers achieved for the two variants of the predicted target variable – with three and two classes. The received results confirm the validity of the proposed hypothesis, showing that the decreased

number of classes of the predicted variable lead to achieving classifiers with better quality. These results are comparable to the results achieved by the researchers from Birmingham University for classification based on the Doppler velocity (Cherniakov, Raja et al., 2005, Rashid et al., 2008, Raja, 2005, Ibrahim, 2009).

2 DATA COLLECTION AND MARINE TARGET ATTRIBUTE EXTRACTION

2.1 Data Collection

The experimental data is collected by the team from Birmingham University in February and March 2010. The experiment site and the MISL Boat used for the experiments are presented on Fig.3 and Fig.4.

Figure 3: The Experiment Site.

Figure 4: The MISL Boat used for the Experiments.

The signal detection and data processing are based on the experimental records provided by the team from Birmingham University.

2.2 Marine Target Attribute Extraction

Several target attributes are extracted from the experimental data, including target time duration (length or sample number), reflected energy (power) from the target, signal-to-clutter ratio, the level of correlation before and after pulse cancellation, etc. They are calculated at the output of an original structure of an MTI CA CFAR K/M-L processor in time domain (Kabakchiev, Kabakchieva et al., 2011).

Moving Target Indicator is a method to reject the radar clutter. If one pulse is subtracted from the previous pulse, clutter echoes will cancel and will not be detected. Moving targets change in amplitude from one pulse to the next because of their Doppler frequency shift. If one pulse is subtracted from the other, the result will be not enough non-cancelled residue power after cancellation. In our previous papers (Kabakchiev et al., SPS, 2011, Kabakchiev et al., IRS, 2011) we used a two-pulse MTI technique for removing of correlated sea clutter, because implementation of three pulse MTI algorithm further reduced the correlation, but the improvement is not as great.

After the MTI processing, an original *CA CFAR processor* is used. The original CA CFAR processor differs from the standard CA CFAR because it uses bigger distance between the test cell and the two reference windows (equal to the half cells of the biggest target).

Then a *K/M-L test* is implemented. When the time duration of the target (corresponding to the signal sample size) is unknown, the approach for automatic batch detection of binary samples is usually used - determining the beginning and the end of the target plot and then estimating the plot length. Two nonparametric tests are used – a K/M test for determining the beginning of the target plot and a nonparametric L test for determining the target plot end based on the number of detected zero values. The aim is to use this approach for estimation of the unknown length of the samples of marine targets.

The calculation of the number of samples corresponding to the detected target at the output of the K/M-L detector is performed with a standard mathematical operator in Matlab. The time duration of the Doppler signal is calculated by multiplying the number of samples by the value of the Pulse Repetition Time. The time duration of the target signal is equivalent in FSR to the approximate profile/length of the target.

The average Doppler target power estimate is formed as square of the average difference between the amplitude of the extracted Doppler target signal and the CFAR detection threshold. The average energy of the Doppler target is formed as a product of the time duration and the average power. A standard statistical average procedure in Matlab is used to calculate roughly the average estimation of the target energy or power.

Table 1: Dataset used for the Data Mining Analysis.

No	Variable Name	Variable Type	Values	Missing Values
1	Trial Date	Nominal	17/02/10 (43), 18/02/10 (10), 21/03/10 (14), 23/03/10 (13)	0 (0%)
2	Distance Between Radars	Numeric	Min=300m, Max=500m, Mean=330.6m, StdDev=57.22 (300m, 316m, 500m)	0 (0%)
3	Antenna	Nominal	A1/2/V/A2/1/V; A1/3/H/A2/1/H	0 (0%)
4	Weather	Nominal	Sunny (56), Gloomy (11), Raining (13)	0 (0%)
5	Wind Speed	Numeric	1 - 5.1 m/s	2 (3%)
6	Wind Direction	Nominal	SE (42), S (22), NW (1), SW (10), W (3)	2 (3%)
7	Boat Direction	Nominal	South (11), North (12)	57 (71%)
8	S/N Ratio Before PC	Numeric	0 – 93.04, Mean=37.246, StdDev=26.207	12 (15%)
9	S/N Ratio After PC	Numeric	0 – 65.59, Mean=17.937, StdDev=22.605	14 (18%)
10	Number of Pulses Before PC	Numeric	0 – 2557, Mean=1148.892, StdDev=720.049	15 (19%)
11	Number of Pulses After PC	Numeric	0 – 4361, Mean=863.424, StdDev=1113.801	14 (18%)
12	Correlation Before PC	Numeric	0.62 – 1, Mean=0.954, StdDev=0.099	17 (21%)
13	Correlation After PC	Numeric	0.008 – 0.982, Mean=0.676, StdDev=0.322	18 (23%)
14	Energy Before PC	Numeric	0 – 2.939, Mean=0.599, StdDev=0.712	14 (18%)
15	Energy After PC	Numeric	0 – 0.499, Mean=0.024, StdDev=0.067	13 (16%)
16	Target Variant 1 – 3 Classes Variant 2 – 2 Classes	Nominal	 BigBoat (11), MISL_Boat (62), AverageBoat (6) MISL_Boat (62), OtherBoat (17)	1 (1%)

For investigating the robustness of the MTI CA GFAR K/M-L detector in different marine situations, we use estimation on other parameters in the time domain. These are estimates at the output of the K/M-L detector including correlation coefficient and signal-to-clutter ratio. The correlation coefficient and the SNR parameter are calculated as a ratio between the two standard deviations of the detected package pulses after the CA CFAR filtering and the clutter from the tested window, with standard functions in Matlab.

3 DESCRIPTION OF THE DATA USED IN THE DATA MINING RESEARCH

The data received at the output of the MTI CA CFAR K/M-L processor is used for the data mining analysis. It is currently organized in a simple excel file, because the originally collected data to this moment is actually very limited. However, if the radar system is put into operation, it is assumed that large volumes of data will be collected and processed, and they should be arranged in a database or a data warehouse in order to be in a format that is suitable for further analysis.

The currently analyzed data contains 80 instances described by 16 features (see Table 1), including the target variable. It contains nominal and numeric variables, describing various aspects, including the distance between the radars used in the experiment, the antenna parameters, the weather conditions including the wind speed and direction, and the evaluated target parameters.

As it is shown in Table 1, there are a lot of missing values for some of the data features. This is either due to missing information from the trials data, or to difficulties in measuring those parameters.

The Target Variable is the detected radar target that has to be classified in order to identify it. The original trial data contains 14 different targets that have been recorded. However, since the available data for the analysis is very limited (80 instances), it is decided to organize the actual radar targets into limited number of classes.

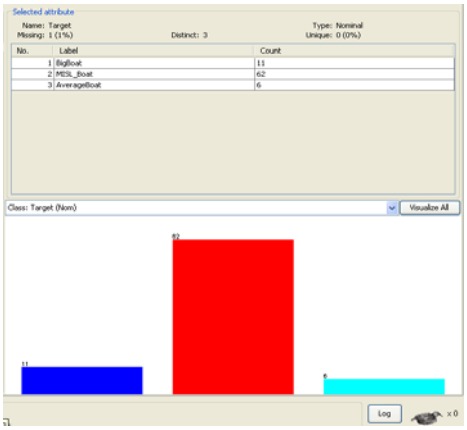

Figure 5a: Distribution of the Target Variable.

The research results presented in this paper refer to two variants of the target variable. In the first

variant the target variable contains three distinct values (Kabakchiev, Kabakchieva et al., 2011) – MISL Boat, Big Boat and Average Boat, and in the second variant, presented in this paper, the target variable contains two distinct values – MISL Boat and Other Boat. The MISL Boat class includes data records about a small rubber boat, used for the experiments by the research team from Birmingham University, and that is the reason for having the majority of instances for this class of marine targets. The other classes are formed based on the expert opinion of the participants in the real experiments, and refer to larger boats in the Big Boat class, and to smaller boats in the Average Boat class.

The distribution of instances in the different classes, for the two variants of the Target Variable, visualization from WEKA software, is presented on Fig.5a and Fig.5b respectively.

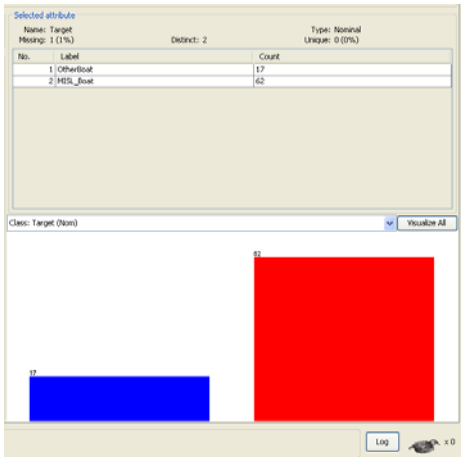

Figure 5b: Distribution of the Target Variable.

4 DATA MINING ANALYSIS

The data mining analysis for the second variant of the predicted variable is performed by using the same research approach as in (Kabakchiev, Kabakchieva et al., 2011; Kabakchieva, 2013). The data mining classification task is implemented following the CRISP-DM (Cross-Industry Standard Process for Data Mining) approach (Chapman et al., 2000), because it is a non-propriety, freely available, and application-neutral standard for data mining projects, and it is widely used by researchers in the field during the last ten years. It is a cyclic approach, including six main phases – Business understanding, Data understanding, Data preparation, Modelling, Evaluation and Deployment. There are a number of internal feedback loops between the phases, resulting from the very complex non-linear nature of the data mining process and ensuring the achievement of consistent and reliable results.

The software tool that is used for the task implementation is the open source software WEKA, offering a wide range of classification algorithms (Witten, 2005).

Several different classification algorithms are applied during the Modelling Phase, selected because they have potential to yield good results. Popular WEKA classifiers (with their default settings unless specified otherwise) are used in the experimental study, including common decision tree algorithms - J48 (based on the C4.5 algorithm) and RandomForest, two rule learners (OneR and JRip), two Bayesian classifiers (NaiveBayes and BayesNet), a Neural Network (Multilayer Perceptron), and a SimpleLogistic algorithm.

Two *decision tree classifiers* are applied – *J48* and *RandomForest*. The J48 classification filter is based on the C4.5 decision tree algorithm, building decision trees from a set of training data using the concept of information entropy. The RandomForest is an ensemble classifier that consists of many decision trees and outputs the class that is the mode of the class's output by individual trees.

Bayesian classifiers are statistical classifiers that predict class membership by probabilities, such as the probability that a given sample belongs to a particular class. The two fundamental Bayes' algorithms are applied in the research work - *Bayesian networks* and *naive Bayes*. Naive Bayes algorithms assume that the effect that an attribute plays on a given class is independent of the values of other attributes. Bayesian networks are graphical models, which can describe joint conditional probability distributions.

Two algorithms for generating classification rules are considered. The *OneR classifier* generates a one-level decision tree expressed in the form of a set of rules that all test one particular attribute. The *JRip classifier* implements the RIPPER (repeated incremental pruning to produce error reduction) algorithm. Classes are examined in increasing size and an initial set of rules for the class is generated using incremental reduced-error pruning.

The *Multilayer Perceptron* (MLP) algorithm used in the research is a feed-forward artificial neural network model that maps the input data (input variables) onto a set of appropriate output (the target variable, or the defined classes in this case). MLP utilizes a supervised learning technique called back-propagation for training the network.

Logistic Regression is a well-known statistical technique that is used for modelling binary outcomes. A simple logistic regression is used for prediction of the probability of occurrence of an event by fitting data to a logistic curve. It is a generalized linear model used for binomial regression.

The *10-fold cross validation* test option is chosen for the classification algorithms implementation, because it proves to be very effective when the available data is very limited. Every time an algorithm is run, the available data is distributed in two data sets – training data containing 9/10 of the whole dataset, and test data including the other 1/10 of the data. Each algorithm is run ten times and the final results for the algorithm evaluation are calculated as average values.

5 THE ACHIEVED RESULTS

The classification models, generated with the selected data mining algorithms, for the two variants of the Target Variable, are compared by using the following evaluation measures: % of correctly classified instances, Kappa Statistic, True Positive (TP) and False Positive (FP) Rates, and ROC Area. These are well known measures for evaluation of data mining models for classification.

The results, achieved by applying selected data mining algorithms for classification of detected radar targets for the first variant of the predicted variable (with three values) show that the received overall accuracy of the classification algorithms is near 80%, although it differs for the three target classes (Kabakchiev, Kabakchieva et al., 2011). The data attribute Energy After PC is the attribute with the highest predictive power. The classification model with the highest accuracy of prediction is achieved with the Decision tree algorithm and it is easy to interpret and understand. However, that classifier performs best for the MISL Boat class and worse for the Average Boat and the Big Boat classes. The only algorithm that performs with similar accuracy of prediction for the three classes is achieved with the NaiveBayes algorithm.

Our hypothesis is that the accuracy of prediction will increase if the number of classes is decreased, i.e. by combining the marine targets from the two less represented classes into a single class. The results from the comparison of the classification models received for the two variants of the predicted variable are presented below.

The overall classification model accuracy is evaluated based on the % of correctly classified instances, and the classification error is based on the % of incorrectly classified instances. The results from the accuracy evaluation of the generated classification models are presented on Fig.6.

The results on Fig.6 reveal that all classifiers perform with accuracy above 70%. Moreover, the classifiers' accuracy for a Target Variable with 2 classes is higher than that for a Target Variable with 3 classes.

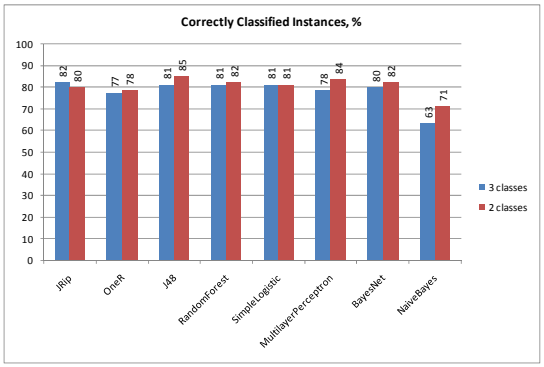

Figure 6: Accuracy evaluation of the generated classification models.

The results from the evaluation of the generated classification models, based on the Kappa Statistic evaluation measure, an index that compares correct classifications against chance classifications and taking values in the range from -1 for complete disagreement, to 1 for perfect agreement, are presented on Fig.7. Higher values are achieved again for the classifiers with the second variant of the Target Variable (with two classes). However, most of the values are quite below 0.5 which means that there is no high level of agreement between the predicted and the actual class of the targets.

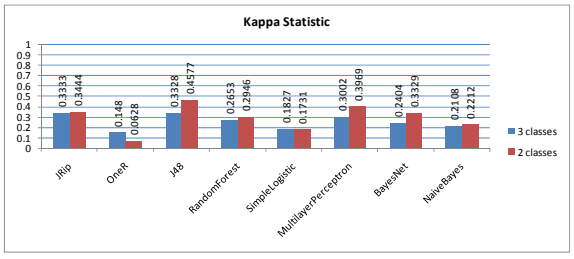

Figure 7: Evaluation of the generated classification models based on the Kappa Statistic measure.

The ROC curve plots the true positives against the false positives and the area under the curve represents the accuracy of the model – the larger the area, the more accurate the model.

Table 2: Detailed class accuracy evaluation of the generated classification models.

	Target Variable									
	Variant 1 - 3 classes						Variant 2 - 2 classes			
	BigBoat		MISL Boat		Average Boat		MISL Boat		Other Boat	
Data Mining Algorithm	TP Rate	FP Rate	TP Rate	FP Rate	TP Rate	FP Rate	TP Rate	FP Rate	TP Rate	FP Rate
JRip	0.182	0.029	0.984	0.706	0.333	0	0.903	0.588	0.412	0.097
OneR	0	0.029	0.952	0.824	0.333	0.027	0.984	0.941	0.059	0.016
J48	0.091	0.029	0.968	0.647	0.5	0.027	0.968	0.588	0.412	0.032
RandomForest	0.091	0.015	0.984	0.765	0.333	0.014	0.984	0.765	0.235	0.016
SimpleLogistic	0.091	0	1	0.882	0.167	0	1	0.882	0.118	0
MultilayerPerceptron	0.367	0.059	0.919	0.647	0.167	0.027	0.968	0.647	0.353	0.032
BayesNet	0	0.044	0.984	0.706	0.333	0.014	0.968	0.706	0.294	0.032
NaiveBayes	0.455	0.279	0.677	0.412	0.5	0.041	0.774	0.529	0.471	0.226

The achieved results for the ROC Area evaluation measure are presented on Fig.8.

For most of the classifiers the ROC Area values are slightly above 0.5 which means that they are not performing very well – slightly better than the naïve classification (random classification without the use of a classification model). The models generated with the Naïve Bayes and Random Forest algorithms seem to be the best performing classifiers (ROC Area values between 0.65-0.683), but these values are still not very high and consequently, the classifiers are not very reliable for correct prediction.

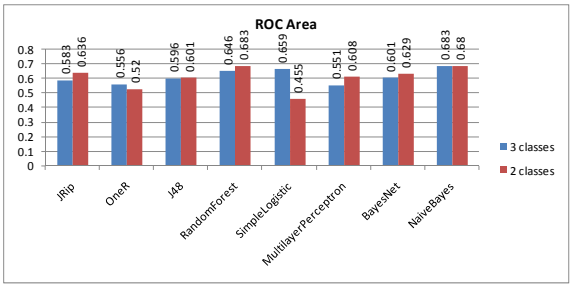

Figure 8: Evaluation of the generated classification models based on the ROC Area measure.

The results for the detailed class accuracy of the generated classification models are presented in Table 2. It is obvious that all classifiers perform with very high accuracy for the MISL boat class – the class that is most represented in the dataset, but are much less accurate in the prediction of the other classes.

6 CONCLUSIONS

All classification models generated with the selected data mining algorithms for the two variants of the target variable (with three and two values) perform with accuracies of prediction above 70% (the only exception is the NaiveBayes classifier achieved for a target variable with three values). Moreover, the classifiers received with the same data mining algorithms for a target variable with two values outperform the classifiers achieved for a target variable with three classes. All classifiers predict with very high accuracy the MISL Boat class – the class that is highly represented in the dataset, but are much less accurate in the prediction of the other (two or one) classes.

The classifiers achieved with the decision tree algorithm J48 are the best performing classification models in both cases, providing 81% prediction accuracy for a target variable with three classes and 85% prediction accuracy for a target variable with two classes. A very good classifier in the case of a target variable with two classes is also achieved with the neural network algorithm MultiLayerPerceptron – 84% accuracy, but this algorithm is not so effective in the case of a target variable with three classes. These are also the classifiers with the highest values of Kappa Statistic. However, these classifiers do not predict equally all classes, they perform much better for the prediction of the MISL Boat class, which is most represented in the data used for the data mining analysis, and are less accurate when predicting the other classes.

The classification models achieved with the NaiveBayes algorithm are the only classifiers working with closer accuracies of prediction for all classes, although these accuracies are not very high. The ROC Area values for these classifiers are also the highest received, which means that the classification models are properly working for all classes. However, the ROC Area and Kappa Statistic values achieved are still not very high and consequently, the classifiers are not very reliable for correct prediction.

The classification models achieved by applying selected data mining algorithms on the available data for FSR detected moving marine targets are similar to the results received by the research team from Birmingham University for FSR detected moving ground targets.

ACKNOWLEDGEMENTS

We would like to acknowledge the work of the University of Birmingham team who developed the equipment, experimentation technique and conducted measurements, and SELEX Galileo (Luton). This work is financially supported by the Bulgarian Science Fund DDVU 02/50/2010, and is partly supported by the project AComIn "Advanced Computing for Innovation" 2012, grant 316087, funded by the FP7 Capacity Programme (Research Potential of Convergence Regions).

REFERENCES

Chapman, P., et al. (2000). *CRISP-DM 1.0: Step-by-step data mining guide*. 2000 SPSS Inc. CRISPWP-0800. Available at: http://www.crisp-dm.org/CRISPWP-0800.pdf.

Cherniakov, M, Gashinova, M, Cheng, H, Antoniou, M, Sizov, V, Daniel, L.Y. (2007). Ultra wideband forward scattering radar: Concept and prospective. Proceedings of Int. Conf. Radar 2007, 1-5, (2007).

Cherniakov, M., Raja Abdullah, R.S.A., Jancovic, P., Salous, M. (2005). Forward Scattering Micro Sensor for Vehicle Classification. Proceedings of the IEEE International Radar Conference, Washington DC, US, pp. 184-189, 2005.

Galati, G. (edit.), 1993. *Advanced radar techniques and systems*, IEE Radar, Sonar, Navigation and Avionics Series 4, Peter Peregrinus Ltd.

Ibrahim, N.K.,. Raja Abdullah, R.S.A, Saripan, M.I. (2009). Artificial Neural Network Approach in Radar Target Classification. Journal of Computer Science 5 (1): pp.23-32, 2009, ISSN 1549-3636.

Kabakchiev, C., Garvanov, I., Cherniakov, M., Gashinova, M., Behar, V., Kabakchiev, A., 2011. *CFAR Detection and Paramiter Estimation of Moving Marine Targets using Forward Scattering Radar*, Proc. of Int. Radar Simp. IRS'11, Leipzig, Germany, (2011).

Kabakchiev, C., Garvanov, I., Cherniakov, M., Gashinova, M., Kabakchiev, A., Kiovtorov, V., Vladimirova, M., Daskalov,P, 2011. *CFAR BI Detector for Mariner Targets in Time Domain for Bistatic Forward Scattering Radar*, Pros. of Int. SPS-2011, Jachranka, Poland, 2011.

Kabakchiev, H., Kabakchieva, D., Cherniakov, M., Gashinova, M., Behar, V., Garvanov, I., 2011. *Maritime Target Detection, Estimation and Classification in Bistatic Ultra Wideband Forward Scattering Radar*. Conference Proceedings of the International Radar Symposium (IRS 2011), 7-9 September 2011, Leipzig, Germany, pp.79-84.

Kabakchieva, D. (2013). Study of Data Mining Classification Models. PhD. Thesis, Institute of Information and Communication Technologies (IICT), Bulgarian Academy of Sciences (BAS), 2013. Available at: http://www.iict.bas.bg/konkursi/2013/D_Kabakchieva/Dorina%20Kabakchieva%20avtoreferat.pdf

Raja Syamsul Azmir Bin Raja Abdulla (2005). Forward Scattering Radar for Vehicle Classification. PhD Thesis, July 2005, The University of Birmingham, UK.

Rashid, N, Antoniou, M, Jancovic, P, Sizov, V, Abdullah, R, Cherniakov, M, 2008. *Automatic Target Classification in a Low Frequency FSR Network*, Proc. of EuRAD conf. 2008, pp. 68-71.

Witten, I., Frank, E., 2005. *Data Mining: Practical Machine Learning Tools and Techniques*. Morgan Kaufmann Publishers, Elsevier Inc.

Author Index

AUTHOR INDEX

Proceedings of ICTRS 2013
Second International Conference on Telecommunications and Remote Sensing
ISBN: 978-989-8565-28-0
http: //www.ictrs.org